Norges miljø- og
biovitenskapelige
universitet

Master's Thesis 2016 60 ECTS
Institute for Mathematical Sciences and Technology

The influence of iron on the structure and properties of Ti-V based metal hydrides

Magnus Moe Nygård
Environmental physics and renewable energy

The influence of iron on the structure and properties of Ti-V based metal hydrides

Magnus Moe Nygård
Norwegian University of Life Sciences
Institute for Energy Technology

December 14, 2016

Preface

As a freshman at the Norwegian University of Life Sciences I had the pleasure of visiting the Institute for Energy Technology and get a tour inside the JEEP II reactor. This was an exciting experience for someone who just had entered the field of applied mathematics and theoretical physics, and really opened my eyes to the field of material sciences. Now, five years later, I look back at a lot of memorable moments in the university. I have had the pleasure to work together with many skilful people from whom I have learnt many things. These I have benefited from in the process of writing this thesis, and for that I am grateful. I would furthermore take this opportunity to thank Frode Myklebust and Sveinung Mjelde for encouraging me to enter mathematics and physics at an early age.

The opportunity to write my master thesis at The Physics Department at IFE has given me knowledge that complements my education. In the writing process I have found IFE and the Physics Department as an especially including environment as a student. I would like to thank all my colleagues for an exciting year! On several occasions I have had the pleasure to present my work to the staff, and I have represented the department at both UiO and NTNU. It has furthermore been very encouraging to be trusted to perform some challenging experimental tasks, such as calibrating the Sieverts apparatus in the hydrogen laboratory.

I owe a dept of gratitude to my supervisors Magnus Helgerud Sørby, Bjørn Christian Hauback and Arne Auen Grimenes for all the help and encouragement you have provided during the process of writing this thesis. I would also like to express my sincere thanks to Christoph Frommen who has skilfully advised my on numerous occasions.

I would finally like to to thank mamma, pappa and my dear Frida for always being there for me. This would not have been possible without you.

Magnus Moe Nygård, Kjeller 14/12-2016

Contents

Sammendrag

Formålet med denne oppgaven er å undersøke hvordan tilsetningen av jern påvirker krystallstrukturen og sorpsjonsegenskapene til metallhydrider som baserer seg på $Ti_{0.70}V_{0.30}$. Oppgaven er motivert utifra et ønske om å erstatte dyrt vanadium med det mye rimeligere ferrovanadium i slike titan-rike metallhydrider. Seks legeringer med sammensetningen $(Ti_{0.70}V_{0.30})_{1\text{-}z}Fe_z$ med z $\in \{0, 0.03, 0.06, 0.10, 0.20, 0.30\}$ har blitt syntetisert ved lysbuesmelting og de krystallinske fasene har blitt bestemt ved pulverdiffraksjon fra synkrotron-stråler. De termodynamiske egenskapene til legeringene ble studert i Sieverts apparat og ved kalorimetriske målinger. I enkelte tilfeller ble endringen i fasesammensetning under hydrogen-sorbsjonsreaksjonene fulgt med *in-situ* pulverdiffraksjon fra synkrotronstråler.

Legeringene danner kubisk romsentrerte krystallstrukturer for alle de undersøkte sammensetningene. Tilsetningen av jern fører til at enhetscellen til den kubisk romsentrerte fasen forminskes og gitterparameteren avtar lineært med det økende jerninnholdet. Den kubisk romsentrerte fasen oppnås sammen med en mindre andel av en heksagonal urenhetsfase som synes å være en fast oppløsningsfase av Ti, V og Fe som inngår i sorbsjonsreaksjonene. De romsentrerte legeringene danner kubisk flatesentrert-relaterte dihydrider når de utsettes for lave hydrogentrykk og jerninnholdet er lavere enn 10 at.%. Innenfor dette sammensetningsområdet påvirkes ikke hydrogenlagringskapasiteten i særlig grad av jerninnholdet og når $\sim$ 3.5 % per vekt. For høyere jerninnhold avtar kapasiteten betydelig. Absorbsjonskinetikken er rask og reaksjonen er praktisk talt over iløpet av minutter når legeringene utsettes for $\sim$ 20 bar hydrogengass. Dihydridene synes å inneholde defekter som stablingsfeil. Dette forhindrer at strukturforfining kan gjennomføres påtilfredstillende måte. Trykk-sammensetnings isotermer har blitt målt for temperaturer inntil 120 °C. Disse inneholder ett enkelt platå med platå-trykk under sensitivitetsområdet til den benyttede trykkgiveren. Jernet synes ikke å påvirke platåtrykket i målbar grad, men en økning i jerninnholdet senker entalpien, utbruddstemperaturen og aktiveringsenergiene til hydrogen desorpsjonsreaksjonen.

Abstract

The influence of iron on the crystalline structure and hydrogen sorption properties of a metal hydride system based upon $Ti_{0.70}V_{0.30}$ have been studied. The aim is to determine whether the expensive vanadium could be substituted by the much cheaper ferrovanadium in such titanium-rich metal hydrides. Six alloys of $(Ti_{0.70}V_{0.30})_{1\text{-}z}Fe_z$ with $z \in \{0, 0.03, 0.06, 0.10, 0.20, 0.30\}$ where successfully synthesised by arc melting and the crystalline phases were determined by synchrotron-radiation powder diffraction. The thermodynamic properties of the alloys were studied in Sieverts apparatus and by differential scanning calorimetry. Changes in the phase composition during hydrogen sorption were for selected systems followed by *in-situ* synchrotron-radiation powder diffraction.

The alloys form body-centred cubic crystal structures for all the considered compositions. The addition of iron cause the unit cell of the bcc phase to contract, and the lattice parameter is observed to decrease linearly with increasing iron content. The bcc phase is obtained alongside a small fraction of an hexagonal impurity phase which seem to be a solid solution of Ti,V and Fe that participate in the hydrogenation. The bcc alloys form *face-centred-cubic related* dihydrides when exposed to low pressures of hydrogen if the content of iron is less than 10 at.%. Within this range the hydrogen capacities are not significantly influenced by the addition of iron and reach ~ 3.5 wt.%. Beyond these values the capacity rapidly decrease. The absorption kinetics are fast, and the reaction is complete within minutes when exposed to modest hydrogen pressures of ~ 20 bar. The resultant dihydrides seem to contain defects such as stacking faults and twin boundaries that prohibit structural refinement to be conducted. Pressure-composition isotherms have been measured at temperatures below 120 °C. These reveal that there is a single plateau with a plateau-pressure below the sensitivity of the measurements. The iron does not seem to influence the plateau-pressure, but the increased content of iron lower the enthalpy, onset temperature and activation energies for desorption.

Chapter 1

Introduction

1.1 Background and motivation

The International Energy Agency reported in 2013 [1] that the total energy consumption of the world amounted to a staggering 156 PWh. This can be subdivided into its different sources as is illustrated in figure 1.1. It is clear that most of the energy is originating from non-renewable sources such as coal, oil and gas which basically has been the situation since the rise of the industrial revolution. The main reasons for this is that these carbon based energy carriers are technically simple to utilize and historically they have been easily accessible. Since the 1970s the world primary energy consumption has more than doubled [1]. This increase in energy consumption is expected to persist due to population growth and improved standard of living throughout the world. The development is therefore leading towards a depletion of natural resources.

The burning of carbon-based energy carriers are furthermore associated with emissions of large amounts of the greenhouse gas CO_2 into the atmosphere. A lot of scientific research has lately been directed to this issue in order to understand the global consequences of these emissions. Based on enormous amounts of data that has been collected by numerous contributors it has been found by the International Panel on Climate Change that it is extremely likely that anthropogenic emissions of greenhouse gases contribute to increase the temperature of the atmosphere and the ocean, reduce the extent of permanent ice masses and raise the sea level [2].

The severity of these changes have during the last decades urged most developed economies to invest heavily in renewable energy technologies such as wind and solar. The countries of the European Union have for instance

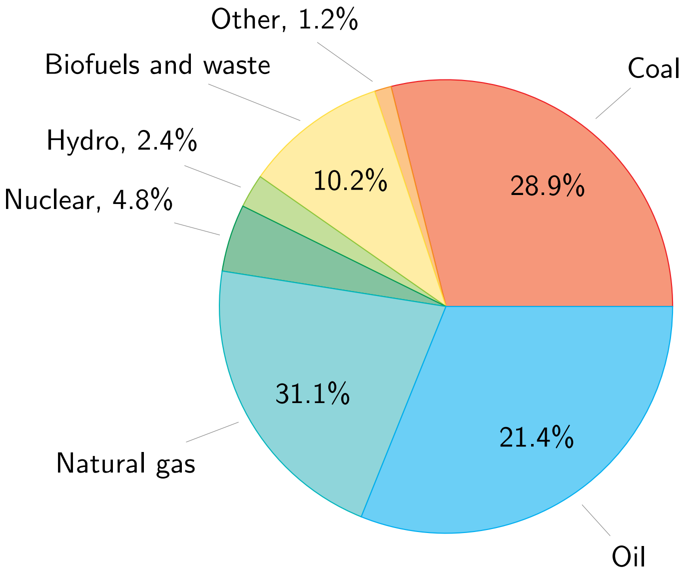

Figure 1.1: The world total primal energy consumption divided by source for 2013 as reported by the International Energy Agency [1]. Note that the "other"-block includes geothermal, solar, wind, tidal and various other energy sources that are considered renewable.

agreed that by 2030 at least 27% of their total energy consumption should originate from renewable technologies [3]. This has resulted in a significant increase in the installed units of onshore- and offshore windturbines [4] and photovoltaics [5]. The rate of energy conversion through these technologies is however heavily reliant on shifting conditions such as wind speed, cloudiness, and various other weather related phenomena. These energy sources can moreover rarely provide immediate response to the commercial demand of energy, and it is therefore necessary to implement some large-scale energy carrier into the electrical power grid. This will enable the storage of energy when conditions are favourable for energy generation for subsequent appliance when consumption again exceeds generation.

Hydrogen is considered a promising energy carrier in this context. It is the most abundant element in the universe and has a gravimetric energy density of 142 MJ/kg [6]. This mean that hydrogen has a lot of potential considering that the corresponding value for commercial gasoline is 47 MJ/kg [6]. The world annual production of hydrogen was 65 billion kg [7] in 2007. Most of this did however originate from fossil fuels through processes that give off CO_2. This means that if hydrogen is to be considered a clean, renewable energy carrier one either has to implement an effective CO_2 capture mechanism or turn to an environmentally benign alternative of production such as water electrolysis. The latter alternative has been demonstrated with commercial-type electrolysers coupled to silicon photovoltaic cells with a conversion efficiency of about 7% [8]. This is quite modest, but more expensive systems have been demonstrated to approach conversion efficiencies as high as 20% [9]. Pressurized electrolysers, such as the NEL A electrolyser [10], has furthermore been developed that enable the generation of hydrogen at highly variable power inputs. This is strictly demanded if the technology should be coupled to windturbines and solar panels to generate hydrogen from excess energy. Hydrogen can therefore be considered as available through renewable means at $99.9 \pm 0.1\%$ purity [10]. Another aspect that make hydrogen especially attractive is that its chemical energy can be extracted electrochemically by a *fuel-cell*. The efficiency of such a device is therefore not bounded by the Carnot efficiency and can reach as high as 60% [11]. At this point it is clear that there are several advantages with hydrogen from an energy perspective. The main problem is however associated with the fact that hydrogen assume a diatomic gas phase at room-temperature and atmospheric pressure with a density of 0.0813 $\mathrm{kg/m^3}$ [12]. This mean that its volumetric energy density is only 11.5 $\mathrm{MJ/m^3}$ as compared to 32000 $\mathrm{MJ/m^3}$ for gasoline. The main technological challenge is therefore associated with storage.

The holy grail of hydrogen research is a cost-efficient and safe storage unit that possess both high gravimetric and volumetric hydrogen densities without application of any toxic material. The unit should furthermore be able to release the hydrogen at temperatures close to room-temperature, and both charging and discharging should commence at reasonable time scales. Such cycling should be possible a great number of times without affecting the storage properties. Several possibilities for such a storage unit is currently being considered and a comparison between a select handful of candidates is provided by figure 1.2.

The least technologically demanding option is to store hydrogen as a gas in high pressure tanks. This is for instance how hydrogen is stored in commercially available fuel cell vehicles such as the Toyota Mirai. According to the manufacturer [14], the high-pressure hydrogen tanks possess a storage density of 5.7 wt.%. The tank must however be filled at hydrogen pressures approaching 700 bar which represent a considerable safty risk. The need of these high pressures can be eliminated if the gaseous hydrogen is condensed into a liquid. The density of the substance is in that case increased to 71.105 $\mathrm{kg/m^3}$ [12] and the hydrogen can therefore be compactly stored

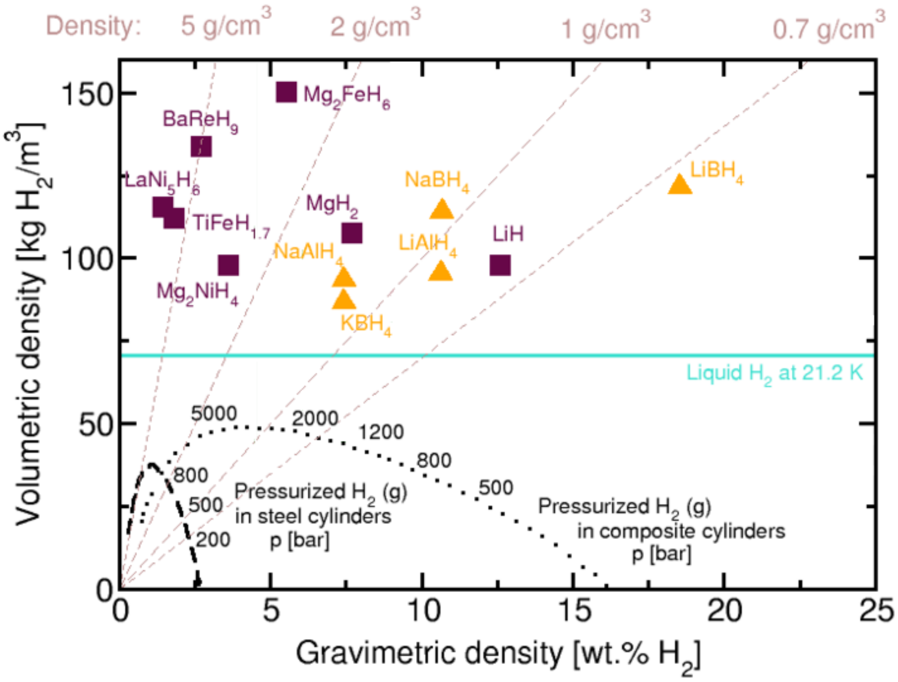

Figure 1.2: The gravimetric and volumetric hydrogen densities of a selection of possible hydrogen storage alternatives. The purple markers indicate metal hydrides while the orange markers indicate complex hydrides. Liquid and gaseous hydrogen are also indicated. The figure is adapted from [13].

without high pressures. The liquid-vapor phase transition does however occur at -252 °C at atmospheric pressure, and the vaporization enthalpy amounts to 449 kJ/kg [15]. The substance must therefore be maintained at cryogenic temperatures to prevent the resultant liquid from evaporating back into its gas phase. Liquid hydrogen has been the fuel of choice in the space industry [16] since the 1970s and the required cryogenic techniques for storage is therefore an established technology. The large amounts of energy associated with the phase-transition is however a significant drawback of this storage option.

The final alternatives involve materials in their solid state that store hydrogen through different interactions. These are often subdivided into two categories depending on the physical state of the stored hydrogen. Certain solid state compounds, such as metal organic frameworks (MOFs), are able to store molecular hydrogen through *physisorption*. In this case the hydrogen molecules adhere onto the host substance through weak van-der-Waals type forces. The hydrogen storage capacity of these materials are therefore closely linked to the materials specific surface area. The gravimetric density of hydrogen in MOFs have been reported as high as 7 wt.% [17], but this is at liquid nitrogen temperatures (-196 °C). At room-temperature the corresponding values are much lower, but the material represent a completely reversible alternative for hydrogen storage [17].

In the other scenario the hydrogen molecule dissociate into two hydrogen atoms under interaction with the storage material. This process is often referred to as *chemisorption* since the hydrogen becomes chemically bonded to the host material. The hydrogen atoms furthermore tend to diffuse into the host material to alter the structure and properties of the host. In certain cases the host compound turn ionic or covalent in the hydride phase which is appropriately referred to as a *complex hydride*. The gravimetric hydrogen densities of complex hydrides can be as high as 18 wt.% for $LiBH_4$ [18]. Such hydrides are however generally quite stable and $LiBH_4$ do for instance only partially decompose below 600 °C [19]. The sorption reactions are furthermore seldom reversible and the associated kinetics are often slow.

Reversibility is usually not the problem with metal hydrides where the hydrogen atoms enter interstitial sites in the host metal lattice. Such hydrides, like the classic formed from $LaNi_5$, generally show high volumetric hydrogen densities, but the gravimetric hydrogen densities are usually quite modest as shown in figure 1.2. Such compounds are therefore difficult to implement into hydrogen-based vehicles, but they are nevertheless interesting for stationary applications. They furthermore form a safe hydrogen storage alternative, and toxic elements can in many cases be avoided.

1.2 Research definition

A special type of metal hydrides form from body-centred cubic alloys such as solid solutions of titanium and vanadium. These hydrides can achieve decent gravimetric hydrogen densities around 3 wt.%, but suffer from slow kinetics and the demand of an activation treatment to enable absorption to commence at an appreciable rate. Vanadium is furthermore an expensive element in its purest form and is available at 99.5% purity for about $\sim$ 350 €/kg [20]. As titanium can be purchased for about $\sim$ 10 €/kg [20], vanadium is by far the most expensive part of the system. 80% purity *ferrovanadium* can however be obtained at a price of $\sim$ 15 €/kg [20]. For an alloy of $Ti_{0.70}V_{0.30}$ the substitution of vanadium by ferrovanadium represent a significant cost-reduction of $\sim 90\%$, and the price can probably be reduced even further for a large scale production. As the resultant 20% of ferrovanadium mostly consist of iron[1] it is of fundamental interest to determine how the introduction of iron influence the crystal structure and hydrogen sorption properties of the titanium rich Ti-V metal hydrides.

It has already been shown [22] that the activation treatment can be eliminated by the addition of small amounts of iron into an $Ti_{0.70}V_{0.30}$ alloy. In that case the absorption commenced at room-temperature and the absorption kinetics were described as fast. The desorption process has however not been considered, and neither have the hydrogen capacity of the material or the structural changes imposed by the iron. This study therefore aim to investigate the structure and properties of the metal hydride system $(Ti_{0.70}V_{0.30})_{1\text{-}z}Fe_z$ with different amounts of iron present in the alloy. In particular it seeks to investigate

- the synthesis of the different alloys under consideration.
- the crystal structure and phase composition of the materials in their pure and hydrogenated state.
- the hydrogen-sorption properties of the alloys.

It has furthermore been suggested that Zr_7Ni_{10} might have a catalytic effect [23] [24] on the hydrogen sorption by similar systems. In these prior studies the substance was however introduced into the alloy in small amounts during arc-melting which, strictly speaking, make it part of the main alloy. In this work it will be considered whether the Zr_7Ni_{10} exhibit truly catalytic behaviour on the sorption processes of the Ti-V-Fe system when it is mixed into the system by mild ball-milling.

---

[1] Possible elements include C (max 0.25%), Si (max 1.5%), S (max 0.05 %), P (max 0.1%) and Al (max 1.5 %) [21].

Chapter 2

Theoretical background

2.1 The solid crystalline state

2.1.1 Chemical bonding in crystals

Consider some substance that consist of atoms, molecules or ions that are bound together by attractive forces to form a solid substance. Such forces are generally of electrostatic origin and act between the negatively charged electrons and positively charged nuclei of the atoms, but the strength and nature of these attractive interactions depend on the properties of the atoms that constitute the substance under consideration. As the atoms are attracted towards each other their electron distribution will at some point start to overlap. At this instance the Pauli exclusion principle manifests itself in the form of a strong, albeit reasonably short-range, repulsive force between the atoms that act to oppose the attractive electrostatic forces. The atoms in the substance are therefore exposed to an effective potential field in which the atoms reside in the vicinity of certain equilibrium positions where their potential energy assume a minimal value as shown in figure 2.1.

At absolute zero temperature the atoms of the crystal will be at rest in these equilibrium positions and the crystal can therefore be considered as a three dimensional periodic array of identical building blocks. The periodicity can however be broken by certain crystalline imperfections or impurities that accidentally may have been included into the structure when the crystal was originally formed. If energy is added to the crystal in the form of heat or work the atoms will start to vibrate about the equilibrium positions in the effective potential and the temperature of the crystal increases. When sufficient amounts of energy is supplied the vibrations can become violent enough for the atoms to escape the effective potential. In this case the

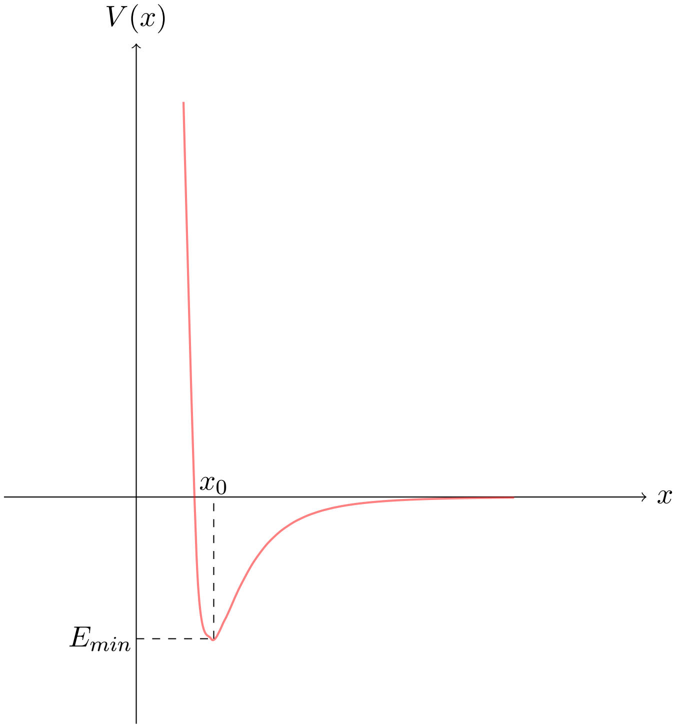

Figure 2.1: The effective potential $V(x)$ of an atom in a crystalline solid. At absolute zero temperature the atom will be positioned at a distance x_0 from its nearest neighbours in the lattice with potential energy E_{min}.

crystal starts to melt into a liquid for which there is no macroscopic ordering of the atoms which now move about freely. The energy of the atoms is however still sufficiently small for the interatomic attractive forces to have a significant effect on the bulk fluid which sticks together and occupy a constant yet moldable volume. The amplitude of such thermal oscillations is however relatively small below the melting point of the substance. The solid substance do therefore possess a highly ordered microscopic structure even at finite temperatures and it is usually referred to as a *crystal* or *crystalline solid*.

2.1.2 The direct lattice

In order to treat a crystalline solid mathematically we need to define some practical constructions. It is common to assume that the crystal extends infinitely in all directions. This assumption is acceptable for all practical

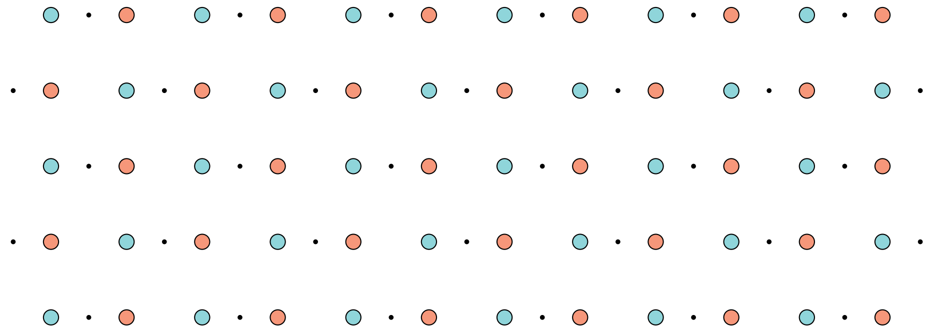

Figure 2.2: A two-dimensional crystal containing two different atoms in the basis indicated as blue and red. The Bravais lattice is also indicated as the series of black points.

purposes as the number of atoms in most bulk crystals is very large, and therefore most of the atoms are situated deep within the bulk crystal. This enables us to neglect surface effects.

The characteristic feature of a crystalline solid is that a certain unit containing one or several atoms, ions or molecules is repeated throughout the volume that is occupied by the crystal. Such a unit is known as *the basis* of the crystal and a two-dimensional example containing two different atoms is shown in figure 2.2. From this figure we see that a mathematical point can be assigned to every basis element. These points generate what is known as a *Bravais lattice* which for emphasis is rendered in figure 2.3.

Under our assumption that the crystals extent is infinite, the atomic arrangement is identical around every single lattice point and it is therefore invariant under translation by vectors

$$\vec{R} = \sum_{i=1}^{d} \{n_i \vec{a}_i\} \tag{2.1}$$

where d is the dimension of the crystal[1], $\{n_i\}_{i=1}^{d} \in \mathbb{Z}$ and $\{\vec{a}_i\}_{i=1}^{d}$ is a set of d vectors referred to as *the primitive vectors* that generate the Bravais lattice. It should be noted that these vectors are not uniquely defined and different choices are possible for a given lattice as is illustrated for a two dimensional Bravais lattice in figure 2.3.

Next we define a *primitive unit cell* as the volume that enclose a single lattice point such that the total volume occupied by the crystal is spanned by translating this unit cell by any of the primitive unit vectors chosen through

---

[1] A physical crystal is three dimensional and henceforth we shall set $d = 3$.

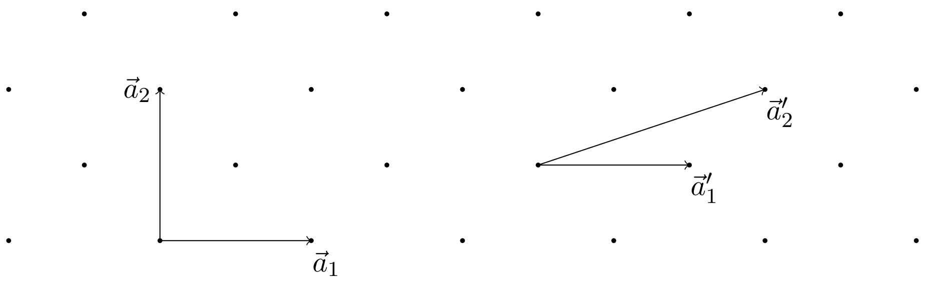

Figure 2.3: A two dimensional Bravais lattice alongside two different choices of primitive vectors, $\{\vec{a}_1, \vec{a}_2\}$ and $\{\vec{a}'_1, \vec{a}'_2\}$.

the lattice without overlap. For a three dimensional crystal this volume V is given as

$$V = \vec{a}_1 \cdot (\vec{a}_2 \times \vec{a}_3) \tag{2.2}$$

where $\{\vec{a}_i\}_{i=1}^3$ are the primitive vectors. Any point within such a unit cell can be represented by

$$\vec{r} = x_1\vec{a}_1 + x_2\vec{a}_2 + x_3\vec{a}_3 \tag{2.3}$$

where $\{\vec{a}_i\}_{i=1}^3$ are the primitive lattice vectors that have been chosen, but in this case $\{x_i\}_{i=1}^3 \in [0,1]$[2]. For certain lattices there is however more useful to apply a so called *conventional unit cell* that contain more than one lattice point to indicate the symmetry of the lattice more clearly. It is however customary to choose the smallest unit-cell that is able to render the full symmetry of the lattice.

A *lattice plane* is any plane that contains at least three different lattice points that cannot be connected by a single straight line. If the lattice plane is shifted in parallel one obtains a series of parallel lattice planes. A given plane can be characterized by its interceptions with the axes defined by the primitive vectors as is illustrated in figure 2.4 or by the inverse interceptions which is more practical.

This serves to define *the Miller-indices* of a lattice plane which is a set of three integer numbers h, k, l that is inversely proportional to the interceptions x_1, x_2, x_3 with the respective primitive vectors

---

[2] To simplify the notation in this chapter I have chose the notation $\{\vec{a}_i\}_{i=1}^3$ for the primitive vectors. In the rest of this work I will however switch to the more widespread notation of $\vec{a}_1 = \vec{a}$, $\vec{a}_2 = \vec{b}$ and $\vec{a}_3 = \vec{c}$ and $x_1 = x$, $x_2 = y$ and $x_3 = z$

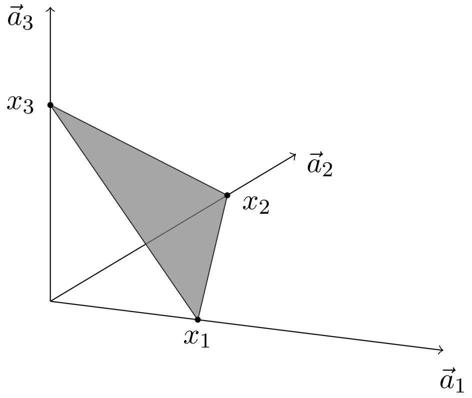

Figure 2.4: A lattice plane can be characterized by the three points $(x_1, 0, 0)$, $(0, x_2, 0)$ and $(0, 0, x_3)$ where the lattice plane intercepts the three lattice vectors $\{\vec{a}_i\}_{i=1}^3$.

$$h : k : l = \frac{1}{x_1} : \frac{1}{x_2} : \frac{1}{x_3} \tag{2.4}$$

The plane is then referred to as (hkl). It should be noted that the Miller indices h, k, l assume integer values.

The crystal structure is defined by the basis and the Bravais lattice. All crystals have translational symmetry per definition, but a rotation[3] about an axis or a reflection through a plane might also map the crystal onto itself. There might also be more complicated symmetries, but these can always be represented by a combination of translations, rotations and reflections[4] and henceforth we refer to these as the three fundamental operations of symmetry. The international system for the nomenclature of the operations of symmetry for crystals is known as the Hermann-Mauguin symbols in which a rotation axis is represented by $n \in \{2, 3, 4, 6\}$, an inversion axis by $p \in \{\overline{1}, \overline{3}, \overline{4}, \overline{6}\}$ and a mirror plane by m. A rotation and a mirror reflection is distinguished from translation by the fact that they keep at least one of the lattice points in the associated Bravais lattice at rest. Therefore we refer

---

[3] Since the rotational symmetry of a rotation by an angle $\Phi = 2\pi$ is trivial the rotations of symmetry can be represented by $\Phi = \frac{2\pi}{n}$ where $n \in \mathbb{Z}$. The translational symmetry does however impose a restriction on the allowed angles of rotation that might map a Bravais lattice onto itself and one can show that the allowed values of n is restricted to $2, 3, 4$ or 6.

[4] A rotation about a two-fold rotation axis followed by a reflection through a plane containing the rotation axis yields for instance an inversion.

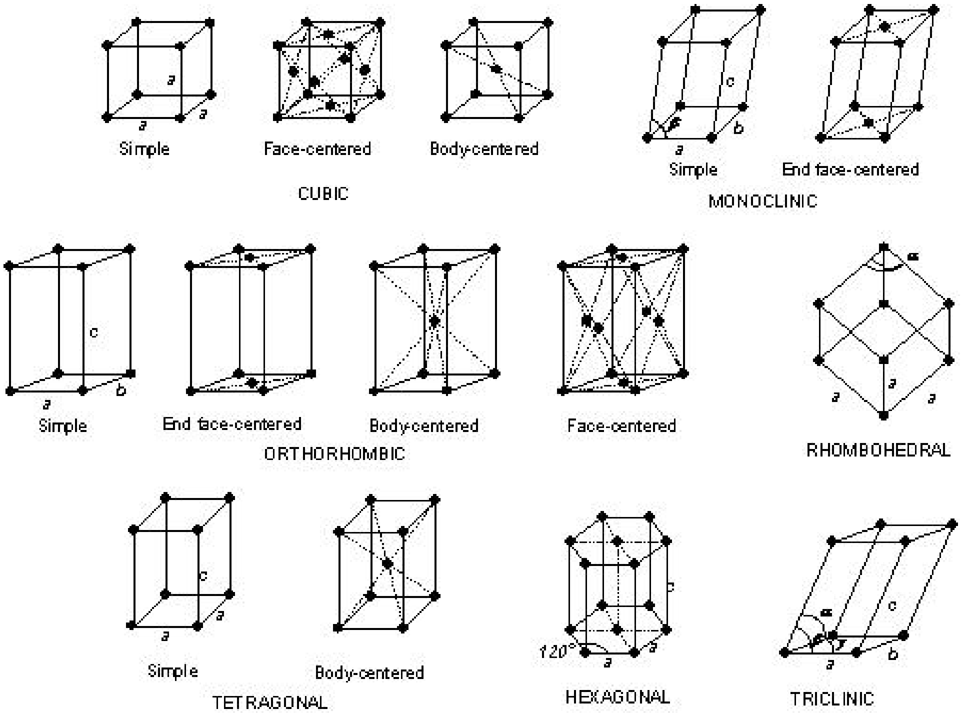

Figure 2.5: The seven crystal systems (capital letters) holding the fourteen Bravais lattices (lower case letters). It should be noted that the angle between two axes is 90° unless the angle is marked specifically. The figure is adapted from [25].

to these operations of symmetry and their combinations as *point operations*. The collection of all possible operations of symmetry for a given structure is known as the structures *space group*. Of these it is often expedient to single out the operations of symmetry that only includes point operations, the collection of which is referred to as the structures point group. For a three dimensional crystal it can be showed that there exists a total of 230 different space groups while the total number of point groups are 32. These properties of symmetry might furthermore serve as a criteria for classification of crystal structures. In this respect it has been shown that any given crystal structure can be classified by the 14 Bravais lattices and seven crystal systems that are rendered in figure 2.5. In accordance with this figure we shall henceforth denote a *primitive unit cell* by P, a *body-centred unit cell* by I, a *face-centred unit cell* by F and a *end face-centred unit cell* by C.

2.2 Diffraction of waves by crystals

The short interatomic spacing and periodicity of the constituents in a crystalline solid makes it an ideal diffraction grating for studying interference by short wavelength radiation in the Angstrom-regime. Waves with suitable wavelength can therefore be applied to probe crystals to investigate their properties. An obvious choice of such probes are the quantum of electromagnetic radiation, the photon, with wavelength λ given by the relation

$$\lambda = \frac{c}{\nu} \tag{2.5}$$

where c is the speed of light and ν is the frequency of the photon. Other possibilities include neutrons and electrons, but as X-rays are applied exclusively in this work the emphasis is in the following subsection placed upon this probe. It should however be stressed that the established scattering theory is similar for the other possibilities[5].

2.2.1 Interactions between photons and matter

There are three substantial processes by which photons interact with matter. These are the *photoelectric effect*, *pair-production* and *Compton scattering* [27]. The probability per second per incident photon for the respective processes to occur can be derived from quantum mechanics as differential cross-sections $d\sigma/d\Omega$.

In the photoelectric effect a photon with energy $E_\gamma = h\nu$ is incident upon an atom with atomic number Z and knocks out an electron from one of the bound states within the atom. In its final state the electron is given a momentum p in the continuous spectrum of the atom. A half-classical treatment, such as the one given by Hemmer [28], show that the photoelectric effect become increasingly probable when the scattering angle increases and when the photon interacts with an atom of larger atomic number Z. The probability is on the other hand diminished as the incoming photon becomes more energetic. It is usually the most tightly bound electron of the $1s$-state in the K-shell of the atom that is subjected to this effect. The excitation of this so-called *photoelectron* introduce a vacancy in the atom and, since this represent an unstable state, electrons from the outer shells are transferred towards the vacancy to return the atom to its most stable configuration. The energy difference between the binding energy of the electrons in their initial and final states are given off as a photon that is characteristic of the

---

[5] See for instance [26] for an excellent treatment of thermal neutron scattering.

atomic element. Such photons are usually referred to as *fluorescence* and the effect is significantly increased if the initial energy of the incident photon coincides with the energy difference between two bound states within the atom.

In pair-production the incident photon interacts with the field of an atom to generate an electron-positron pair. Through conservation of energy there is a lower threshold for the incident energy of the photon that is required to enable this process to occur. This is equal to two electron rest-masses $E_{\gamma,min} = 2m_e c^2 = 1.022$ MeV. The excess energy of the photon is converted to kinetic energy of the electron and positron. As the positron is the anti-particle of the electron it will be attracted towards an electron once it slows down. The two particles are subsequently annihilated in such a way that the electron and positron are converted into two photons, both with energy equal to the electron rest-mass of 512 MeV, which are emitted in opposite directions to conserve momentum.

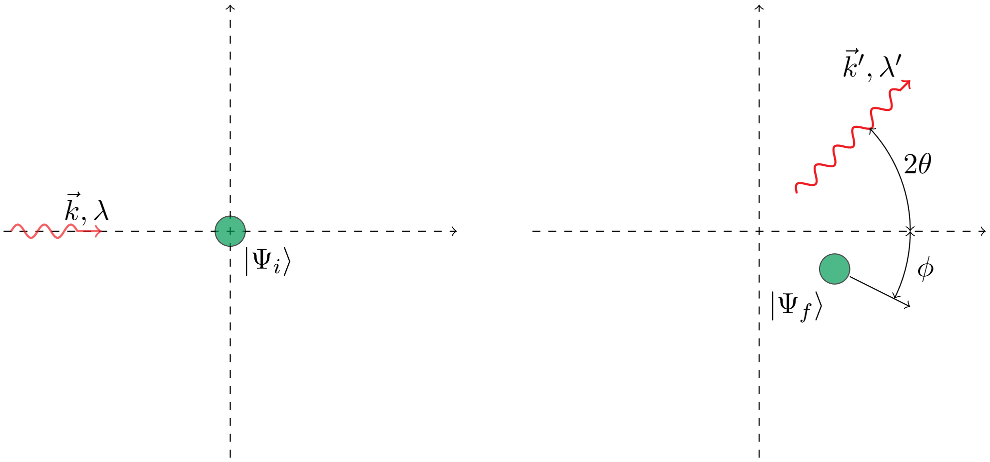

Figure 2.6: A photon with wave-vector $\vec{k}$ and wavelength λ is incident upon a free electron in the state $|\Psi_i\rangle$ and scattered into a state with wave-vector $\vec{k}'$ and wavelength λ'. In the final state $|\Psi_f\rangle$ the electron moves in the direction defined by the angle ϕ relative to the direction of the incident photon. The scattering angle between the incident and scattered photon is similarly 2θ.

In the Compton scattering process a photon with wavelength λ and wavevector $\vec{k}$ is incident upon some charged particle, say an electron with charge e and mass m_e, and scattered into the state with wavelength λ' and wave-vector $\vec{k}'$. The situation is shown in figure 2.6. The differential cross-section for this process is given from quantum electrodynamics by the Klein-

Nishina formula[6]. It is however only a special case of Compton scattering that is able to yield coherent photons that are able to interfere with one another. This occur in the non-relativistic limit where $E_\gamma \ll m_e c^2$ and the scattering is elastic $\lambda = \lambda'$. The differential cross-section is then reduced to the Thompson differential cross-section $(d\sigma/d\Omega)_{Thompson}$ given as

$$\left(\frac{d\sigma}{d\Omega}\right)_{Thompson} = \frac{1}{2} r_0^2 \left(1 + \cos^2(\theta)\right) \tag{2.6}$$

where r_0 is the Bohr radius and θ the scattering angle. It is interesting that this differential cross-section is independent of the incident energy of the photon. If the photon should be able to probe a crystalline solid it must however possess a wavelength in the X-ray regime. Such energies do fortunately lie within the non-relativistic limit as $E_{\gamma,X-ray} \sim 0.01$ MeV $\ll$ 512 MeV $= m_e c^2$. Another fortunate effect is that such energies also lie below the pair-production threshold prohibiting this effect to occur. Fluorescence due to the photoelectric effect is however unavoidable, but as these photons are incoherent in their nature it will manifest itself as a background that is superimposed upon the coherent Compton scattering[7].

2.2.2 The reciprocal lattice

Let us consider the elastic scattering of a beam of photons with wavelength λ that is incident upon some crystalline solid and neglect all the other interactions that has been discussed above. Such a treatment is motivated from the final argument that was made in the prior subsection. Any photon can be represented as a plane wave with wave-vector $\vec{k}$ and angular frequency ω as $\exp\left(i(\vec{k}\cdot\vec{r} - \omega t)\right)$. The condition for observing constructive interference between two such waves is that the difference between their traversed distances is an integer number of wavelengths. When X-rays with incident wavelength λ and wave-vector $\vec{k}$ is incident upon some crystalline and scattered elastically off the family of lattice planes having Miller indices (hkl) the condition could be formulated mathematically as

$$2d_{hkl}\sin(\theta) = n\lambda \qquad n \in \mathbb{Z} \tag{2.7}$$

where 2θ is the scattering angle and d_{hkl} is the inter-planar distance of the lattice planes. The situation is illustrated in figure 2.7 and the result is

---

[6] See for instance [29]

[7] With a qualified choice of the X-ray wavelength λ, the fluorescence can however be reduced to insignificant values.

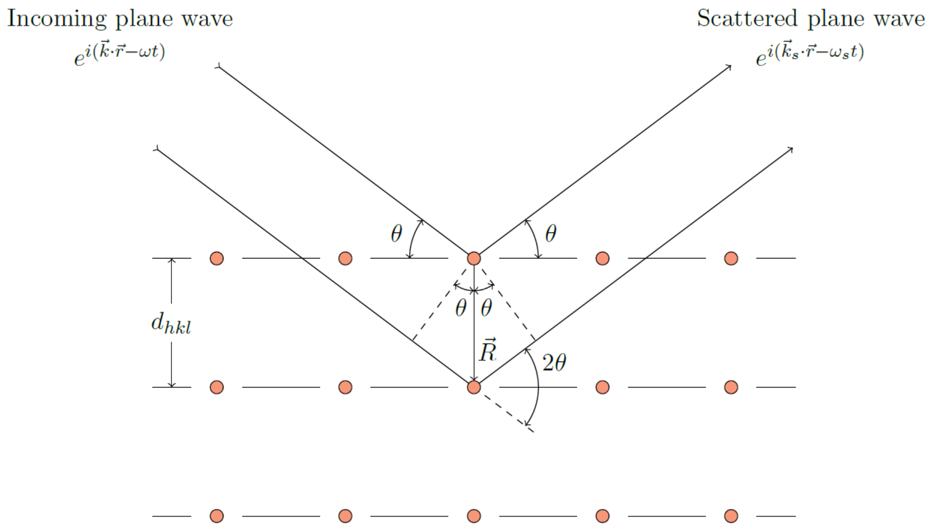

Figure 2.7: An incoming plane wave with wave-vector $\vec{k}$ and angular frequency ω is scattered from two basis elements in some crystal situated at the two points separated by the lattice vector $\vec{R}$ to yield a scattered wave with wave-vector $\vec{k}_s$ and angular frequency ω_s. The angle between the incoming and scattered wave is denoted 2θ and the two basis-elements belong to the family of lattice planes having Miller-indices (hkl) and an interplanar distance d_{hkl}.

known as the *Bragg law*. If $\vec{R}$ is a lattice vector between two scattering agents the condition could alternatively be formulated as

$$\vec{R}\cdot\frac{\vec{k}}{|\vec{k}|}-\vec{R}\cdot\frac{\vec{k}_s}{|\vec{k}_s|}=n\lambda \qquad n\in\mathbb{Z} \tag{2.8}$$

where $\vec{k}_s$ is the wave-vector of the scattered photon with angular frequency ω_s. The situation is shown in figure 2.7. If the scattering process is elastic the absolute values of the incoming and scattered wave-vector will be equal $|\vec{k}|=|\vec{k}_s|=2\pi/\lambda$. If equation 2.8 is multiplied through by a factor $2\pi i/\lambda$ with subsequent exponentiation we see that

$$e^{i\vec{R}\cdot\vec{Q}}=e^{i\vec{R}\cdot(\vec{k}-\vec{k}_s)}=e^{i(2\pi n)}=1 \qquad n\in\mathbb{Z}$$

where $\vec{Q}=\vec{k}-\vec{k}_s$ and the last equality follows by exploiting Eulers formula. Due to the translational symmetry of the Bravais lattice there will be an infinite amount of points for which the interference condition is satisfied and the scattered plane wave must therefore be invariant against translation by any lattice vector $\vec{R}'$ so that

$$e^{i\vec{Q}\cdot(\vec{R}+\vec{R}')} = e^{i\vec{Q}\cdot\vec{R}}$$

which means that $\exp(i\vec{Q}\cdot\vec{R}') = 1$ for any lattice vector $\vec{R}'$ and hence we must have that

$$\vec{Q}\cdot\vec{R}' = 2\pi n \qquad n \in \mathbb{Z} \tag{2.9}$$

This has to hold for any lattice vector $\vec{R}'$ and therefore we must impose some conditions on the difference between the incoming and scattered wavevectors $\vec{Q}$ for constructive interference to occur. Since any lattice vector $\vec{R}'$ can be represented as in equation 2.1 we can construct the vectors

$$\begin{aligned}\vec{b}_1 &= \frac{2\pi}{V}\vec{a}_2 \times \vec{a}_3 \\ \vec{b}_2 &= \frac{2\pi}{V}\vec{a}_3 \times \vec{a}_1 \\ \vec{b}_3 &= \frac{2\pi}{V}\vec{a}_1 \times \vec{a}_2\end{aligned} \tag{2.10}$$

where V is the unit cell volume in the direct lattice given by equation 2.2 for which the relation $\vec{a}_i \cdot \vec{b}_j = 2\pi\delta_{ij}$ hold[8]. If the vectors $\vec{Q}$ are restricted to

$$\vec{Q} = m_1\vec{b}_1 + m_2\vec{b}_2 + m_3\vec{b}_3 \tag{2.11}$$

with $\{m_i\}_{i=1}^3 \in \mathbb{Z}$ it is clear that the relation 2.9 holds for all lattice vectors $\vec{R}'$ so that we have constructive interference. A consequence of this result is that of all the possible incoming plane waves the ones that yield constructive interference is represented by a point given by equation 2.11 in the so called *reciprocal lattice* of the crystalline solid under consideration that is spanned by the vectors $\{\vec{b}_i\}_{i=1}^3$.

A property of the reciprocal lattice vectors $\vec{Q} = h\vec{b}_1 + k\vec{b}_2 + l\vec{b}_3$ is that they are orthogonal to the lattice plane (hkl). One can furthermore show that the distance, d_{hkl}, between two adjacent lattice planes with Miller indices (hkl) is given by

$$d_{hkl} = \frac{2\pi}{|h\vec{b}_1 + k\vec{b}_2 + l\vec{b}_3|} \tag{2.12}$$

---

[8] δ_{ij} is the Kronecker delta.

2.2.3 Powder diffraction

A consequence of the mathematical treatment in the former section is that any family of lattice planes can be represented by a mathematical point in the reciprocal lattice that is associated with the Bravais lattice of the crystal. Constructive interference occur whenever the difference between the incoming wave-vector $\vec{k}$ and the scattered wave-vector $\vec{k}_s$ is equal to some reciprocal lattice vector $\vec{Q}$ that fulfil

$$\vec{Q} = \vec{k} - \vec{k}_s = \vec{R} \tag{2.13}$$

where $\vec{R}$ is a lattice vector. This result is known as *Laues interference condition.* This condition can be further clarified by a geometrical construction in the reciprocal space known as a Ewald sphere. In this construction the incoming wave-vector $\vec{k}$ terminates on an arbitrary reciprocal lattice point and the other end of the wave-vector then define the center of the Ewald-sphere which has radii $|\vec{k}| = 2\pi/\lambda$. The wave-vector is now located on the surface of the sphere and Laues interference condition states that we will have constructive interference *if and only if* another reciprocal lattice point can be found on the surface. The reciprocal space of a *single crystal* can therefore be observed in direct space as distinct points. If the direction of the incoming photons are held fixed and the crystal is made to rotate the lattice can be observed in its entirety. It is however quite common that the material is only available as a powder. If diffraction is performed on such a powdered sample the effect of rotating the crystal is achieved instantaneously. As the powder crystallites are oriented at random the corresponding reciprocal lattices will also be randomly oriented. The distance from the origin of the reciprocal lattices to the lattice point that yield constructive interference is however the same. The result is therefore that the scattered waves with wave-vectors $\vec{k}_s$ from the crystalline powder will be oriented along the surface of a cone[9] whose base define what is known as a *Debye-Scherrer ring* as illustrated in figure 2.8. The result of a powder diffraction measurement is therefore a one-dimensional projection of the directions of constructive interference from the crystallites. If the amount of randomly oriented crystallites approach infinity the density of scattered wave-vectors $\vec{k}_s$ on the Debye-Scerrer rings will be constant and it is customary to only measure on a small rectangular portion of the rings.

---

[9] The apex of this cone is the origin of the so-called *Ewald-sphere* and its base lies in the plane that is orthogonal to the incoming wave-vector $\vec{k}$.

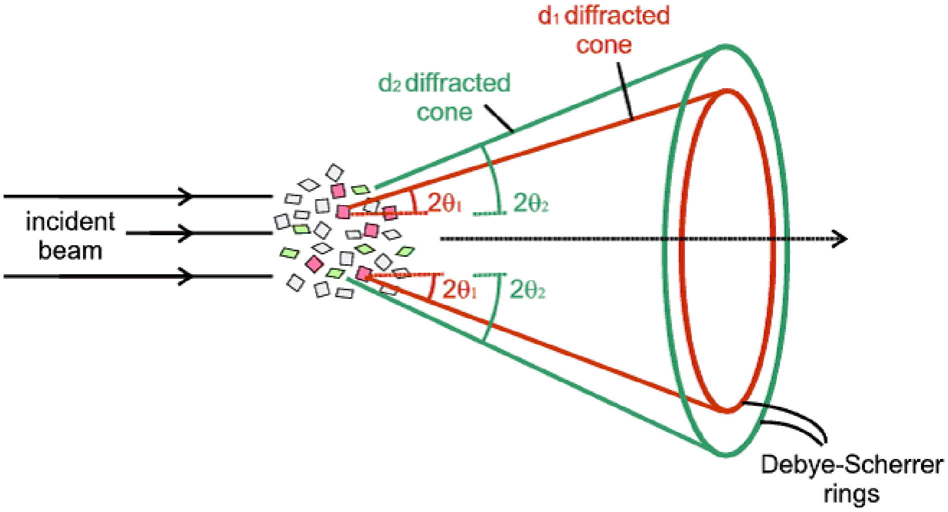

Figure 2.8: A beam of photons is incident on a crystalline powder and scattered from the crystalline grains with suitable orientation into an angle 2θ to generate a diffracted cone. The figure is adapted from [30].

2.2.4 The intensities of the Bragg peaks

So far we have only considered the allowed scattering directions from a crystalline solid. These are solely determined from equation 2.7 and is independent of what is contained within the crystalline basis and whether the applied probes are photons, neutrons or electrons. The observed intensities of the Bragg peaks having Miller indices (hkl) is however dependent on these matters. The observed intensity I_{hkl} of the Bragg peak having Miller indices (hkl) is proportional to the squared modulus of the so-called *structure factor* $F(\vec{Q})$ which is given as

$$F(\vec{Q}) = \sum_{j=1}^{N} \left\{ f_j(\vec{Q}) e^{i\vec{Q}\cdot\vec{r}_j} e^{-\frac{1}{2}Q^2\langle u_j^2\rangle} \right\} \tag{2.14}$$

where $\vec{Q}$ is the scattering vector and the sum is over all N atoms that are centred at positions $\{\vec{r}_j\}_{j=1}^{N}$ within the unit cell. The final exponential in this expression is known as the Debye-Waller factor and take into account that the atoms oscillate through thermal vibration about their centred positions with a temperature T and time t dependent amplitude $u(T,t)$. $\langle u_j \rangle$ is the thermal average of the oscillation of atom j. The exponential prefactor $f_j(\vec{Q})$ depends on the interaction between the probe and the scattering agents. For photons these are charged particles of which there are two, both holding a charge $e = 1.602 \cdot 10^{-19}$ C, present in the atom, namely the proton and the electron. The protons are however situated in the atomic nuclei and as the electrons are situated about this entity it is essentially the latter particles that scatter. The electrons are furthermore situated in an *electron-cloud* about the atomic nuclei at positions specified by a probability distribution given from their quantum mechanical wave-functions. As analytical expressions for most real-world systems are unavailable it is common to treat $f_j(\vec{Q})$ as a Fourier transform of a spatial density $\rho_j(\vec{r})$ of the electron-cloud about its center of mass $\vec{r} = 0$ as

$$f_j(\vec{Q}) = \int \rho_j(\vec{r}) e^{i\vec{Q}\cdot\vec{r}} d^3r \tag{2.15}$$

where $\vec{Q}$ is the scattering vector[10]. In this case $f_j(\vec{Q})$ is referred to as the *atomic form factor* and it is not surprising that it depends on the number of electrons present in the atom Z. Photons are therefore unable to probe lighter elements such as hydrogen. This is all very different if the applied probes are neutrons. The neutron acts as a point scatterer as it is uncharged[11] and therefore interacts with the atomic nucleus itself. The ability of the different atoms to scatter neutrons must however be determined experimentally in the absence of any complete theory of nuclear forces. The exponential pre-factor is therefore taken as a so-called *scattering length* $f_j(\vec{Q}) \to b_j$ which have been measured experimentally and compiled into extensive tables. From such tables it can be seen that neutron scattering are similar in magnitude for all elements. These scattering lengths are furthermore dependent on the nuclear isotope and spin relative to that of the neutron. Neutrons therefore provide a valuable alternative to photons as it is able to probe lighter elements, magnetic structures and allow for so-called *contrast variation.*

---

[10] It should be noted that the atomic form factor is generally a complex property $f_j(\vec{Q}) \in \mathbb{C}$.

[11] It does however possess a magnetic moment and is therefore able to probe magnetic structures.

2.3 Physical and chemical properties of metal hydrides

2.3.1 Thermodynamics of sorption reactions

Let us consider the configuration where a single hydrogen molecule H_2 is situated infinitely far away from the surface of some metal M. The reference energy level E_0 is chosen as the energy of this infinitely separated "H_2+M"-system. The two hydrogen atoms comprising the hydrogen molecule are bound together by a covalent bond that can be broken if an energy of $E_D = 218\,\mathrm{kJ/mol\,H}$ is supplied. The potential energy difference between the "H_2+M"- and the "2H+M"-systems is therefore equal to this heat of dissociation E_D when the hydrogen atoms and molecule is situated infinitely far away from the metal surface. As the hydrogen molecule is brought towards the metal attractive van der Waals forces enable the molecule to *adsorb* onto the metal surface to lower the potential energy of the "H_2+M"-system in the process referred to as *physisorption*. At some point the repulsive forces associated with the Pauli exclusion principle will however become dominant so that the potential energy of the system once again increase. There is therefore a characteristic energy minimum given by the *heat of adsorption* E_P as shown in figure 2.9. Under the assumption that the metal surface has an affinity for electrons the situation is entirely different when the two hydrogen atoms are brought towards it. In this case it will at some point be energetically favourable for the two electrons to bond chemically to the metal surface which mean that the potential energy of the "2 H+M"-system must decrease as illustrated in figure 2.9. At some distance from the metal surface the potential energy of the two systems will therefore intersect so that $E_{\mathrm{H_2+M}} = E_{\mathrm{2\,H+M}}$ and beyond this point the molecular hydrogen will dissociate into two hydrogen atoms under interaction with the metal surface. If this event occur above the reference energy E_0, as indicated by the red and blue lines in the figure, the dissociation is an endothermic reaction and an *activation energy* E_A must be supplied to enable the reaction to commence. If the intersection occurs below the reference energy, as indicated by the green and yellow lines, the dissociation is on the contrary exothermic and will therefore commence spontaneously with the release of an energy E_{NA}. At this point the electrons of the two hydrogen atoms are shared with the metal and the two hydrogen atoms are therefore more tightly bound to the surface than was the case for physisorption. This enable a new set of interactions to occur that are collectively referred to as *chemisorption*. Initially the hydrogen atoms are situated on the metal surface with a minimal potential energy E_C that is referred to as the *heat of chemisorption.* At some point the hydrogen atoms might diffuse into the bulk of the metal. In this process the hydrogen atoms move between energetically favourable positions with potential energy E_S relative to the reference energy E_0 inside the effective potential field that is set up by the atoms that constitute the metal. These interstitial sites are separated by potential energy barriers with energy E_{DIFF} that are characteristic of the atoms that constitute the metal.

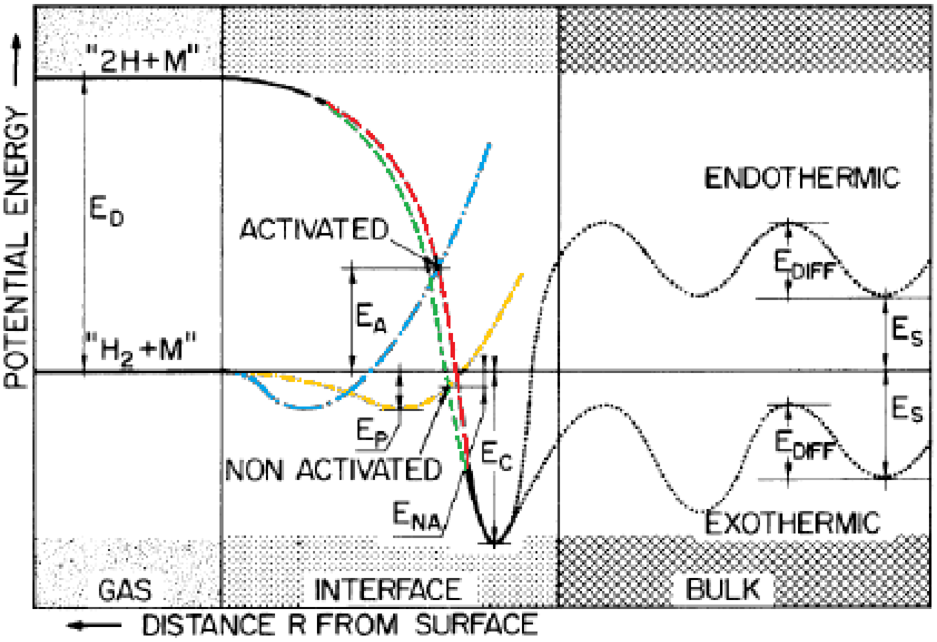

Figure 2.9: A schematic overview of the potential energies $E_{\mathrm{H_2+M}}$ and $E_{\mathrm{2\,H+M}}$ of the hydrogen molecule and metal system "$\mathrm{H_2+M}$" and the two hydrogen atoms and metal system "$\mathrm{2\,H+M}$" as a function of the distance R between the hydrogen and the surface of the metal. The red and blue lines correspond to a system where an activation energy E_A is necessary to initiate the dissociation of molecular hydrogen while the green and yellow lines correspond to a system where the dissociation commence spontaneously. The figure is adapted from Gross et al. [31].

Next we assume the chemists point of view and consider the reaction where $\frac{1}{2}$x moles of hydrogen gas react with some solid state metal M through the reaction

$$\mathrm{M(s)} + \frac{\mathrm{x}}{2}\mathrm{H_2(g)} \rightleftharpoons \mathrm{MH_x(s)} \tag{2.16}$$

to form a metal hydride $\mathrm{MH_x}$. It can be shown [32] that the equilibrium constant K of this reaction when it commence in an environment of constant pressure P and temperature T is given as

$$K = \left(\frac{P}{P^\circ}\right)^{\frac{\mathrm{x}}{2}} = e^{-\frac{\Delta G^\circ}{RT}} \tag{2.17}$$

where P° is any convenient reference pressure, R is the universal gas constant and ΔG° is the standard Gibbs free energy of the reaction giving the hypothetical change in G when one mole of metal M reacts with $\frac{\mathrm{x}}{2}$ moles of pure $\mathrm{H_2}$ gas to form one mole of the metal hydride $\mathrm{MH_x}$ at pressure $P^\circ = 1$ bar.

As the chemical reaction 2.16 commence more and more hydrogen atoms diffuse into the metallic bulk to increase the concentration of hydrogen x within the metal. The structural phase of the metal typically change during this process. Initially the hydrogen atoms enter the solid solution alongside the metal to occupy interstitial sites of minimal potential energy E_S within the metal lattice. This phase is often denoted by α. Once interactions between the different hydrogen atoms start to become important a second phase - often denoted as β - is formed locally. This β-phase is also referred to as the hydride phase. As the phase-transition from the α- to the β-phase commence the equilibrium pressure between the $\mathrm{H_2}$-gas and the metal hydride ideally assume a constant value which often is referred to as *the plateau pressure*[12]. This *plateau-region* is usually studied through so-called *pressure-composition-isotherms* which are two-dimensional projections of the metal-hydride phase diagram onto an isotherm where the hydrogen-to-metal ratio is plotted as a function of the equilibrium $\mathrm{H_2}$-gas pressure P. For applications it is usually deemed beneficial that the phase-transition commence over an as large as possible range of hydrogen-to-metal ratios since this enable relatively large amounts of hydrogen to be absorbed and subsequently released with only modest changes in the equilibrium pressure. The thermodynamic regions where such phase-transitions occur in metal-hydrides are hence of fundamental importance.

The equilibrium constant K can be applied to estimate the standard enthalpy ΔH° and standard entropy ΔS° of phase-transitions in metal-hydrides as the pressure P assume a constant value throughout the transition. When such analyses are to be conducted equation 2.17 is usually rewritten by taking the natural logarithm of both sides and expanding the standard Gibbs free energy ΔG° of the right-hand side into its standard

---

[12] In practice this plateau pressure might be sloped.

enthalpy related term and its standard entropy related term as

$$\frac{\mathrm{x}}{2}\ln(\frac{P}{P^{\circ}}) = -\frac{1}{RT}\Delta H^{\circ} + \frac{1}{R}\Delta S^{\circ} \tag{2.18}$$

If several equilibrium constants K are collected at different temperatures T and $\ln(K)$ is plotted as a function of the inverse temperature the standard enthalpy ΔH° and standard entropy ΔS° of the reaction can respectively be extracted from the slope and the point of interception by the resultant line with the second axis. A typical phase diagram for a metal hydride is shown in figure 2.10 with three different pressure-composition-isotherms and a corresponding van't Hoffs plot.

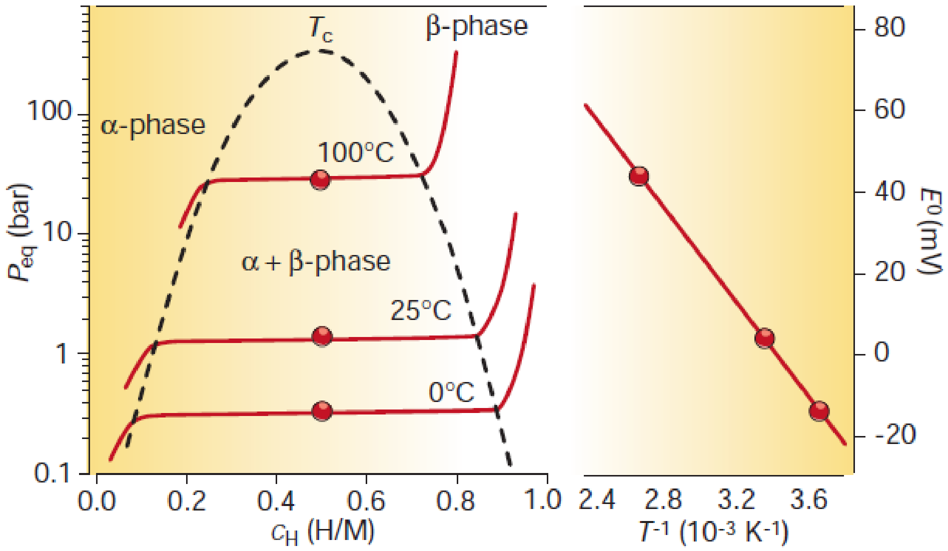

Figure 2.10: A general phase diagram depicting the hydrogen-to-metal ratio as a function of the equilibrium H_2-gas pressure P for three pressure-composition-isotherms (left) and the corresponding van't Hoff diagram (right) for the classic metal hydride system $LaNi_5$. The dashed line indicate the domain of the $\alpha-$ to β-phase transition which above the critical temperature T_c occurs instantly. The figure is adapted from Schlapbach and Züttel [18].

2.3.2 The kinetics of sorption reactions

From the prior subsection it is clear that the thermodynamics of the hydrogen and metal system dictates that it might be energetically feasible for the metal to sorb hydrogen. Thermodynamics is however unable to state anything about how fast such a reaction would commence. For that purpose one need to consider the system kinetically. There are a wide variety of factors that might slow the kinetics of the sorption. A common limiting factor is the formation of thin, passivated layers of oxide on the surface of the metal preventing the chemisorption of atomic hydrogen to commence. The reaction is in this case unable to commence until the passivated layer has been reduced. Another reaction limiting possibility is the formation of a *hydride barrier* on the surface of the material preventing further diffusion into the bulk. Sample properties such as the particle size, packing density, the shape of the sample and the thermal contact between the sample and its enclosing environment might also affect the kinetics of the reaction. It is however difficult to separate out the rate-limiting interaction.

When considering the kinetics of the sorption reaction 2.16 one usually consider the *extent of conversion* ξ which is given by

$$\xi = \frac{\mathrm{x}_t}{\mathrm{x}_{t=\infty}} \tag{2.19}$$

where x_t is the *molar hydrogen-to-metal ratio* in the metal hydride $\mathrm{MH_x}$ at time t while $\mathrm{x}_{t=\infty}$ is ditto when the chemical reaction 2.16 is completely finished. The rate of the reaction $d\xi/dt$ can generally be modelled as a function of the extent of reaction ξ, temperature T and pressure P as

$$\frac{d\xi}{dt} = f(\xi)k(T)h(P) \tag{2.20}$$

The temperature dependence has been observed empirically to follow the Arrhenius relation which state that

$$k(T) = Ae^{-\frac{E_A}{RT}} \tag{2.21}$$

where E_A is the activation energy of the system, R is the universal gas constant and A is a pre-exponential factor. The pressure dependence can according to Ron [33] be taken as

$$h(P) = \frac{|P_{eq} - P|}{P_{eq}} \tag{2.22}$$

for brittle metal hydrides where P_{eq} is the equilibrium pressure of the hydride. It is however possible that the pressure dependent term can take on more complicated forms and it is therefore fortunate that it can be taken as constant $h(P) = B$ if a large excess of molecular hydrogen is supplied in a hydrogenation experiment or if the desorbed gas is effectively removed from the sample during a desorption experiment [34]. The extent of reaction dependent term $f(\xi)$ is finally taken as a reaction model for which several theoretical expressions have been derived.

We now strictly assume that the pressure dependent term can be taken as constant $h(P) = B$ so that the reaction rate $d\xi/dt$ is given by

$$\frac{d\xi}{dt} = \widetilde{A}e^{-\frac{E_A}{RT}} f(\xi) \tag{2.23}$$

where $\widetilde{A} = AB$, E_A is the activation energy, R is the universal gas constant, T is the temperature and $f(\xi)$ is some reaction model describing how the extent of reaction ξ varies with time t. The reaction rate will assume its maximal value once $d^2\xi/dt^2 = 0$ giving

$$\left.\frac{d^2\xi}{dt^2}\right|_m = \left.\frac{d\xi}{dt}\right|_m \left[\frac{E_A\beta}{RT_m^2} + \widetilde{A}e^{-\frac{E_A}{RT_m}} \dot{f}(\xi_m)\right] = 0 \tag{2.24}$$

where $\beta = dT/dt$ is the heating rate, and the index m denote a property measured at the point where the reaction rate assume its maximal value. If this expression is massaged somewhat further we wind up at the final result that is known as the *Kissinger equation* which is given as

$$\ln\left(\frac{\beta}{T_m^2}\right) = \ln\left(-\frac{\widetilde{A}R}{E_A}\dot{f}(\xi_m)\right) - \frac{E_A}{R}\frac{1}{T_m} \tag{2.25}$$

From this equation it is possible to achieve an estimate of the activation energy from the slope of the line of regression that is established based on several recorded measurements at constant heating rates β where the right-hand side is plotted as a function of $1/T_m$. It should however be noted that in so doing one strictly assume that $\dot{f}(\xi_m)$ is independent of the heating rate. If this assumption is not satisfied one should observe a significant and systematic deviation from linearity. Such analyses are in the following referred to as *Kissinger analyses.*

2.4 Prior studies of Ti-V based hydrides

2.4.1 The raw materials

Selected properties of the applied raw-materials in their elemental form are shown in table 2.1 while the crystallographic data for their crystalline phases are shown in table 2.2.

Elemental titanium Ti is present in many mineral deposits such as rutile (TiO_2) and ilmenite ($FeTiO_3$) which are widely distributed throughout the

Table 2.1: Selected properties of elemental titanium, vanadium and iron. The melting- and boiling points are measured at a pressure $P = 101.325$ kPa and the electro-negativity is measured on the Pauling scale. The values are taken from [35].

		Element			
		Ti	V	Fe	
Property	Symbol	Value			Unit
Atomic number	Z	22	23	26	-
Relative atomic mass	M	47.88	50.94	55.85	$\frac{\text{g}}{\text{mol}}$
Density	ρ	4.506	6.0	7.87	$\frac{\text{g}}{\text{cm}^3}$
Melting point	T_M	1668	1910	1538	°C
Boiling point	T_B	3287	3407	2861	°C
Atomic radius, non bonded	r_{nb}	2.11	2.07	2.04	Å

Table 2.2: The space group, lattice parameters a, b and c, unit cell volume V and fractional coordinates (x, y, z) for the crystallographic phases of the Ti, V and Fe raw-materials. A reference to the respective data is also indicated.

Phase	Space group	a [Å]	b [Å]	c [Å]	V [Å^3]	(x, y, z)	Ref.
α-Ti	$P6_3/mmc$	2.9511	2.9511	4.6843	35.33	$(\frac{1}{3}, \frac{2}{3}, \frac{1}{4})$	[36]
β-Ti	$Im\bar{3}m$	3.3111	3.3111	3.3111	36.30	$(0, 0, 0)$	[37]
α-V	$Im\bar{3}m$	3.0278	3.0278	3.0278	27.76	$(0, 0, 0)$	[38]
α-Fe	$Im\bar{3}m$	2.8665	2.8665	2.8665	23.55	$(0, 0, 0)$	[39]
γ-Fe	$Fm\bar{3}m$	3.6544	3.6544	3.6544	48.80	$(0, 0, 0)$	[40]
δ-Fe	$Im\bar{3}m$	2.9315	2.9315	2.9315	25.19	$(0, 0, 0)$	[41]

Earths crust and upper mantle. Titanium can therefore be purchased at a rather low price of about $\sim$ 10 €/kg [20]. The element crystallize in a hexagonal-close-packed structure denoted α-Ti below 882 °C where it undergo a phase transition to a body-centred cubic phase denoted β-Ti. This phase persist until it melts at 1668 °C. It is a quite ductile material and has the highest strength to density ratio of any metallic element. This make it ideal for lightweight, high-strength applications such as medical implants, sporting goods, mobile phones, jet-engines and airframe components. It is also characterized by a very high corrosion resistance which is due to a protective film of titanium oxide that spontaneously form on the surface of the material if the least trace of oxygen or water is present in its environment.

Elemental vanadium crystallize in a body-centred cubic phase denoted α-V that is stable until it melts at 1910 °C. Like titanium it is present in many crustal minerals such as vanadinite ($Pb_5(VO_4)_3Cl$), patronite (VS_4)

and carnotite ($K_2(UO_2)_2(VO_4)_2{\cdot}3\,H_2O$). The element is however significantly more expensive to isolate and is therefore available at 99.5% purity for about ∼ 350 €/kg [20]. It is by far the most expensive component in the Ti-V-Fe system, but 80% purity *ferrovanadium* can interestingly be purchased at about ∼ 15 €/kg [20]. Due to its high price vanadium is primarily used as an alloying additive to steel, aluminium and titanium to increase the strength of the materials. Such materials can be found in bicycle frames, crankshafts, airframe components, surgical instruments and tools. Vanadium is also applied in the nuclear sector as it is nearly transparent to neutrons and hence ideal for containing samples during scattering experiments.

At room temperature and atmospheric pressure elemental iron crystallize in a body-centred cubic phase that is commonly referred to as *ferrite* and denoted by α-Fe. At 910 °C the structure undergoes a phase transition into a face-centred cubic phase that is commonly referred to as *austenite* and denoted γ-Fe. At 1394 ° there is yet another phase transition back into a body-centred cubic phase that is denoted δ-Fe before the crystal melts at 1538 °C. Elemental iron do like titanium react readily with oxygen, but the oxides that tend to form are remarkably different. They tend to form porous oxide layers that easily penetrate into the bulk of the substance making it extremely prone to corrosion. Elemental iron is therefore only found naturally as iron oxide in crustal minerals such as hematite (Fe_2O_3), magnetite (Fe_3O_4) and limonite ($\sim 2\,Fe_2O_3{\cdot}3\,H_2O$). It is the most abundant element in the Earth's crust and can be purchased for about ∼ 0.20 €/kg [20].

2.4.2 Prior studies of vanadium hydride

It has been known since the late 1920s and early 1930s that vanadium reacts with hydrogen at appreciable temperatures and pressures to form hydrides. The successful synthesis of vanadium hydride was reported by Maeland et al. in 1961 [42] with the highest observed composition $VH_{1.77\pm0.05}$. The structure of these hydrides were determined through powder X-ray diffraction as a body-centred tetragonal mono-hydride phase that for the highest hydrogen contents was accompanied by a face-centred cubic phase in a multiphase composition. The hydrogen atoms was for the face-centred cubic phase inferred by Maeland et al. to occupy the tetrahedral interstitial sites.

Maelands investigations were extended in 1964 [43] when X-ray diffraction was applied to established a tentative phase diagram for the vanadium-hydrogen system. The hydrides that were studied by Maeland could be subdivided into three different aliquots depending on the applied raw materials and preperation of the hydrides. This compromise a granular vanadium based aliquot, an aliquot based on crystal bar vanadium and an aliquot of hydrides prepared under high hydrogen pressures as described in Maelands prior paper of 1961 [42]. Maelands original result is rendered in figure 2.11 alongside pressure-composition isotherms that were measured later by Reilly and Wiswall [44]. When the primary body-centred cubic vanadium samples were exposed to pressurized hydrogen gas Maeland observed through X-ray diffraction that, depending on the temperature and absorbed amount of hydrogen, either a body-centered tetragonal phase or a face-centered cubic phase was formed. As is clear from figure 2.11, these two phases were observed to coexist in certain regions. In these regions it was observed that the lattice parameters of the phases were constant but in the body-centered tetragonal single phase region the lattice parameters were observed to increase linearly with respect to the hydrogen-to-metal ratio x = H/V. The maximum hydrogen content reported by Maeland is for the $VH_{1.80}$ system which corresponds to a hydrogen content of $\eta_{\mathrm{VH}} = 3.44$ wt.%.

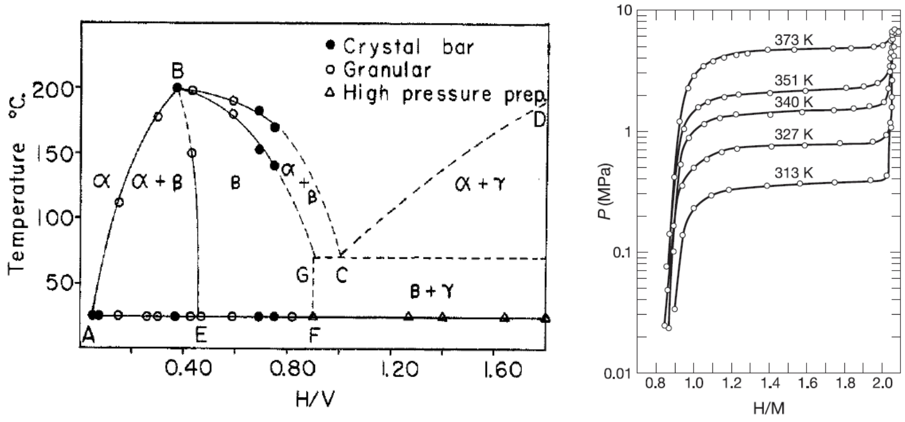

(a) (b)

Figure 2.11: A tentative phase diagram (a) as prepared by Maeland [43] and pressure-composition isotherms (b) from Reilly and Wiswall [44] for vanadium hydride. The primary body-centred-cubic phase is denoted by α while the β designates a body-centred tetragonal hydride and the γ is assigned to a face-centred-cubic hydride. The markers shown as an inlet of Maelands figure represent the three different aliquots of samples that was prepared.

2.4.3 Prior studies of ternary titanium vanadium hydrides

Hexagonal-close packed α-Ti do, like α-V, react with hydrogen to form a face-centred cubic hydride [45]. When the composition approach TiH_2 the cubic unit cell has been observed [45] to deform into a tetragonal configuration. The reaction rate is also in this case modest at room temperature and significant only at elevated temperatures [22]. For titanium it has furthermore been shown [46] that the body-centred cubic β-Ti phase of table 2.2 can be stabilized through alloying with vanadium and subsequently quenching the melt. The phase diagram for this binary $Ti_{1\text{-}y}V_y$ system is shown in part (a) of figure 2.12. The system has been reported to absorb hydrogen to form ternary hydrides $Ti_{1\text{-}y}V_yH_x$, but extensive activation procedures are also in this case necessary to enable the absorption to commence. A phase diagram for this ternary hydride system has been determined from a crystallographic investigation performed with X-ray diffraction at 295 K by Hagi et al. [47]. The resultant phase diagram is shown in part (b) of figure 2.12. As can be seen from the figure there are five stable phases, a hexagonal-close packed phase denoted by α, a body-centred cubic phase denoted by β, a face-centred cubic phase denoted by γ, a face-centred tetragonal phase[13] denoted by δ and a body-centred tetragonal phase denoted ϵ. The hexagonal α-phase is claimed by the authors to be α-Ti that segregates out of the body-centred cubic β-phase matrices as the hydrogen free samples are obtained from the hydrides by degassing at 1073 K. This is motivated from observing through X-ray diffraction that the extent of the α-phase increased with the number of hydrogenation/dehydrogenation-cycles that the substance was exposed to. It should also be noted that the $\beta + \gamma / \epsilon + \gamma$ phase transition has been confirmed by the authors through "*further experiments*" to exist somewhere between y=0.40 and y=0.45 but the nature of these experiments are not discussed any further and neither are the corresponding data. It is finally stressed that there exist some conflicting results in the literature concerning the δ-phase as it was found to be body-centred tetragonal in an *in-situ* SR-PXD study that was conducted by Suwarno et al. in 2013 [48].

The thermodynamic properties of the ternary $Ti_{1\text{-}y}V_yH_x$ in the vanadium rich region were investigated in a 1995 paper by Akio Kagawa [49]. Desorption pressure-composition isotherms were collected for five different samples with molar ratios y $\in \{0.80, 0.85, 0.90, 0.95, 1.0\}$ and the obtained results are shown in figure 2.13. From these measurements Kagawa was led to conclude that

---

[13] The face-centred tetragonal phase is associated with a tetragonal distortion of the face-centred cubic γ phase.

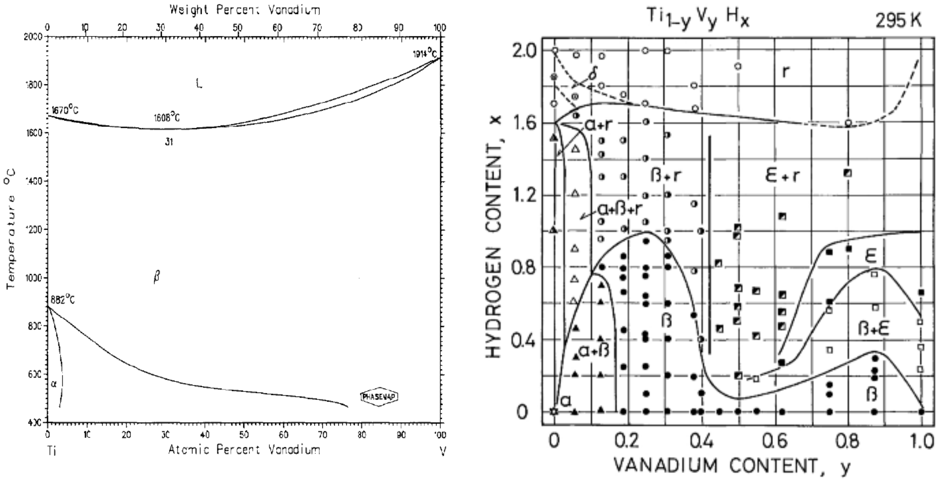

(a) (b)

Figure 2.12: Phase diagrams for the binary titanium-vanadium system (a) and the associated ternary hydride $Ti_{1\text{-}y}V_yH_x$ at temperature T = 295 K (b). The binary phase diagram is adapted from Murray [46] while the ternary phase diagram is taken from Hagi et al. [47].

- a homogenization heat-treatment at 1373 K for 1 week followed by cooling the samples in a furnace gave no detectable influence on the pressure-composition isotherms.
- activation was easily attained by degassing at 723 K in vacuum.
- there was no apparent traces of pulverization observed after the performed hydrogenation/dehydrogenation-cycles.
- the plateau pressure is reduced with increasing content of titanium in the alloy.
- there seem to be no significant reduction in the hydrogen absorption capacity or the plateau pressure of the pressure-composition isotherm for the y=0.90 sample even after 100 hydrogenation/dehydrogenation-cycles.
- the absolute values of enthalpy change $|\Delta H|$ increased with increasing titanium content for both the formative and dissociative reaction while the associated absolute values of entropy change $|\Delta S|$ increased gently with increasing titanium content.

- the slope of the plateau pressure increase gradually with titanium concentration until y=0.90 before it increase steeply for the higher titanium concentrations that were considered.

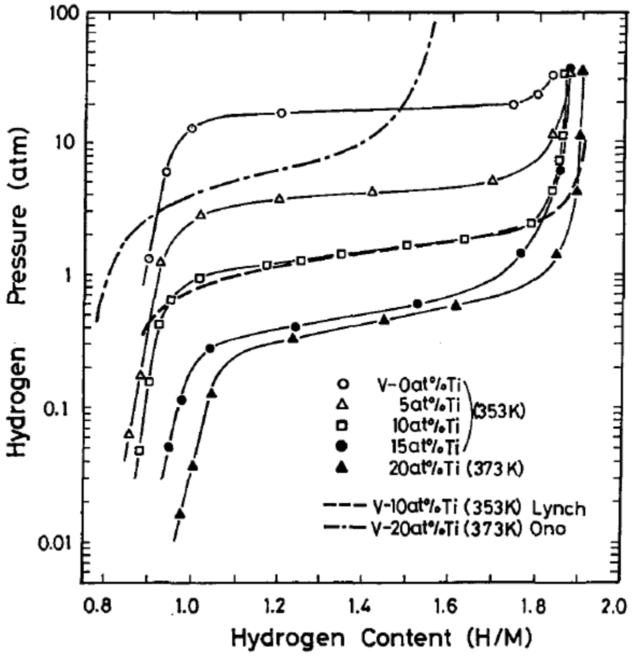

Figure 2.13: Desorption pressure-composition isotherms for $Ti_{1\text{-}y}V_yH_x$ hydrides with different stoichiometric coefficients y. The figure is adapted from the 1995 paper by Kagawa [49] while the reproduced data from Lynch and Ono is adapted from [50] and [51] respectively.

A broader range of molar compositions for the ternary system $Ti_{1\text{-}y}V_yH_x$ were furthermore studied by Matsuda and Akiba in 2013 [52]. The pressure-composition isotherms were collected at elevated temperatures to counter the effect of a decreasing plateau pressure with increasing titanium content and the results are rendered in figure 2.14. As can be seen from the figure, the plateau region for the highest considered titanium contents have relatively low equilibrium pressures even at the high temperatures that were considered. The figure also show that the hydrogen uptake by the vanadium rich samples seem rather stable over two absorption/desorption-cycles while the hydrogen uptake for the titanium rich samples decrease from the first to the second cycle.

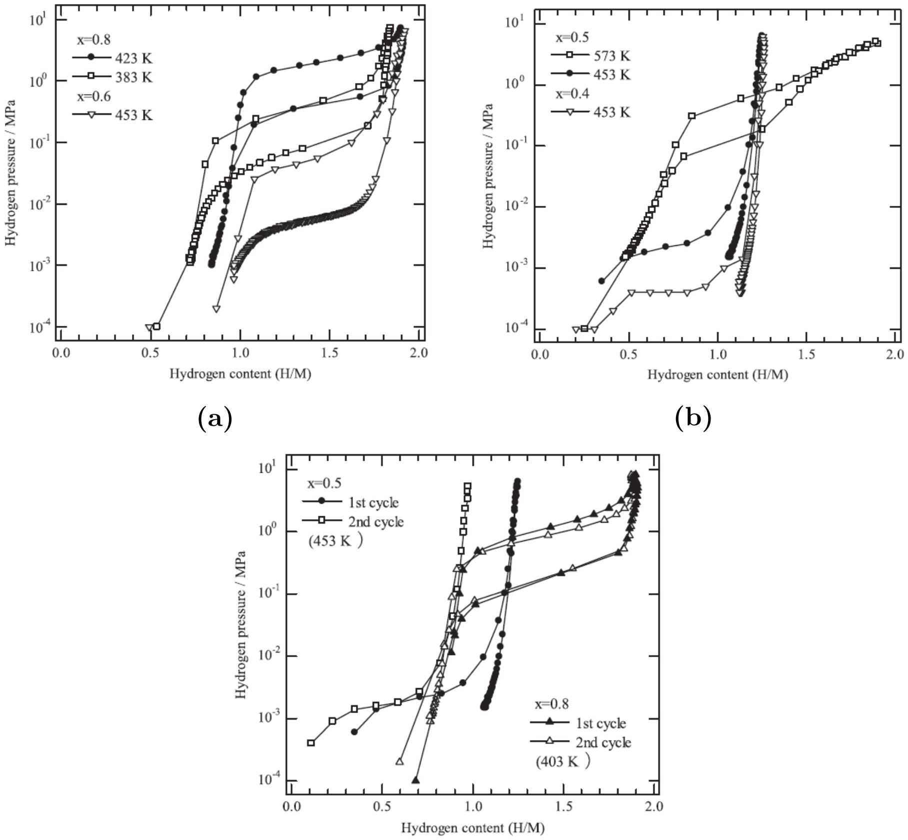

(a) **(b)**

(c)

Figure 2.14: Pressure-composition isotherms for $Ti_{1\text{-}x}V_xH_y$ with (a) x=0.6 and x=0.8 and (b) x=0.4 and x=0.5. The pressure-composition isotherms for two consecutive cycles are also shown in (c) for $Ti_{1\text{-}x}V_xH_y$ with x=0.5 and x=0.8. The figure is adapted from [52]. Note that the curves are collected at different temperatures and that the notation in this figure differ from that adapted in the rest of the text as the molar ratios are switched y↔x.

The microstructure of these ternary titanium vanadium hydrides were investigated through *transmission electron microscopy* (TEM) by Matsuda and Akiba in 2013 [52]. It was found that *twin boundaries* and *stacking faults* seem to be introduced into the alloy during the first hydrogenation/dehydrogenation cycle. The density of the twin boundaries were observed to be higher for the titanium rich part of the alloy than for the vanadium rich part.

2.4.4 Eliminating the dependency on activation

Extensive activation procedures were needed in the above mentioned studies to enable the absorption of hydrogen by bcc alloys to commence at room-temperature. If we take Maelands 1964 study [43] as an example such activation involved out-gassing the sample under vacuum at 700 °C before the sample was exposed to 1 bar of gaseous hydrogen at 400 °C. The sample was then cooled to room-temperature under the hydrogenous atmosphere. Without such an activation procedure it was observed for a pure vanadium sample that no reaction commenced for a 24 hour period under exposure to 55 bar pressure of hydrogen at room temperature [53]. In this paper it was however found that the kinetics of the reaction could be greatly enhanced at comparable experimental conditions by introducing a small amount of a second metal M, such as Fe, Co or Ni, with radii at least 5 % smaller than that of vanadium to produce alloys $V_{1-y}M_y$. Similar investigations were made for body-centred cubic $Nb_{1-y}M_y$ alloys and for a series of hexagonal and face-centred cubic phases exposed to the same constraint. As a similar enhancement in the hydrogen absorption kinetics occurred for the Nb-based system, but not for any hexagonal or face-centred cubic phase, the authors were led to conclude that the effect was reserved to body-centred cubic phases. To verify this hypothesis Maeland et al. added 10 at.% of Fe, Mn, Cr and Co respectively to a body-centred cubic $Ti_{0.70}V_{0.30}$ alloy [22]. With such additions the absorption was observed to be complete within minutes without any activation treatment of the samples. No reaction was observed for the unaltered $Ti_{0.70}V_{0.30}$ alloy during the first 24 hours of exposure to hydrogen at room temperature.

2.4.5 Some relevant considerations of quaternary Ti−V based hydrides

Several studies have been made of the quaternary Ti-V-Cr and Ti-V-Mn hydrides. It has for instance been shown [54] that the addition of chromium to titanium rich Ti-V cause

- the unit cell of both the body-centred cubic alloy and face-centred cubic dihydride to contract
- the hydrogen absorption kinetics to slow down.
- the incubation time before hydrogenation initiates to increase.
- a reduction in the apparent activation energy for desorption.

The Ti-V-Mn system has been shown to crystallize in a body-centred cubic and C14 Laves multiphase composition [55]. Such a multiphase composition has been shown by Akiba and Iba [56] to enhance

- the activation procedure.
- the flatness of the plateau pressure.
- the sorption kinetics.

Relatively little attention has however been paid to the quaternary Ti-V-Fe hydrides. The few relevant studies that are known to the author has been directed towards the vanadium rich part of the system. It has for instance been observed by Kagawa et al. [57] that the presence of iron within the vanadium-rich alloy impose a significant decrease in the reversible hydrogen storage capacity of the material as the number of hydrogenation cycles is increased. An extensive study of the lattice parameter variation and thermodynamics of the dihydride formation in the vanadium-rich $(\mathrm{Ti}_{1\text{-}y}\mathrm{V}_y)_{1\text{-}z}\mathrm{Fe}_z\mathrm{H}_x$ system has also been undertaken by Lynch et al. in 1985 [50]. This study indicate that the addition of iron to the system seem to

- increase the plateau pressure.
- decrease the reaction enthalpies $|\Delta H|$ and entropies $|\Delta S|$ of both the absorption and desorption reactions in a linear fashion.
- cause a linear contraction of the lattice parameters of both the body-centred cubic phase of the pure alloy and the face-centred cubic phase of the dihydrides.

It was furthermore observed that an annealing treatment of the alloys seemed to have no significant effect on the measured pressure-composition isotherms. In this final study it was also indicated that it seems to be a critical electron to atom ratio of $(e/a)_c = 5.1$ that indicate whether a dihydride is able to form or not. The dihydride is observed to form below this critical value while it is absent above it.

2.4.6 Addition of catalysts

For the Ti-V-Cr system it has been shown [23] [24] that the hydrogen sorption kinetics could be enhanced if a small weight percentage of $\mathrm{Zr}_7\mathrm{Ni}_{10}$ is introduced in the alloy. The $\mathrm{Zr}_7\mathrm{Ni}_{10}$ were in the cited studies introduced into the alloys by arc melting, and it is believed [23] that the enhanced kinetics is due to the formation of a C14 Laves phase. An investigation of the microstructure in these samples indicated that the Zr and Ni dopants were only present in an intergranular phase that formed a network distributed throughout the body-centred cubic matrix.

Chapter 3

Experimental

3.1 The instruments

Unless it is specified explicitly the equipment that are presented in this section are owned and maintained by the Institute for Energy Technology.

3.1.1 The balances

Quantitative measurements of mass are in the present work performed with three different balances shown in figure 3.1.

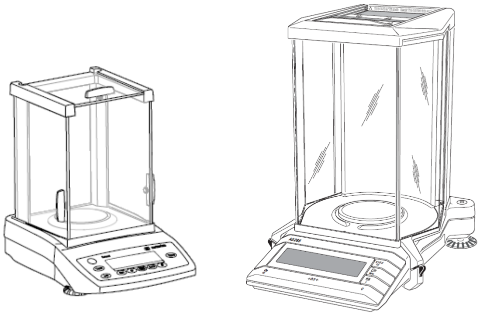

(a) (b) (c)

Figure 3.1: The Sartorius Extend ED124S balance (a), the Mettler Toledo AG204 DeltaRange balance (b) and the Mettler PM460 DeltaRange balance (c). The drawings are taken from [58] (a), [59] (b) and [60] (c).

3.1.2 The electric arc furnace

An electric arc furnace is a construction that applies an intense electric current to heat charged materials. Due to the high temperatures that can be achieved it is a common method for the synthesis of intermetallic phases with high melting points. A schematic drawing of the furnace that is applied in the present work is shown in figure 3.2. The system can be considered to consist of an electric circuit (black line), a gas circuit (green line) and a cooling system (blue line) which are brought together under a glass dome that define an enclosed volume. The sample that is to be melted is placed in one of the cavities in the copper crucible that is located within the glass dome. The dome can be put under vacuum and filled with argon gas by operating a gas tank, two butterfly-valves and an Edwards RV12 oil filter pump that is connected in the gas circuit. The current flowing in the electric circuit can be operated by a WECO Discovery 160T advanced inverter power source which is connected to a wolfram tip acting as a cathode and the

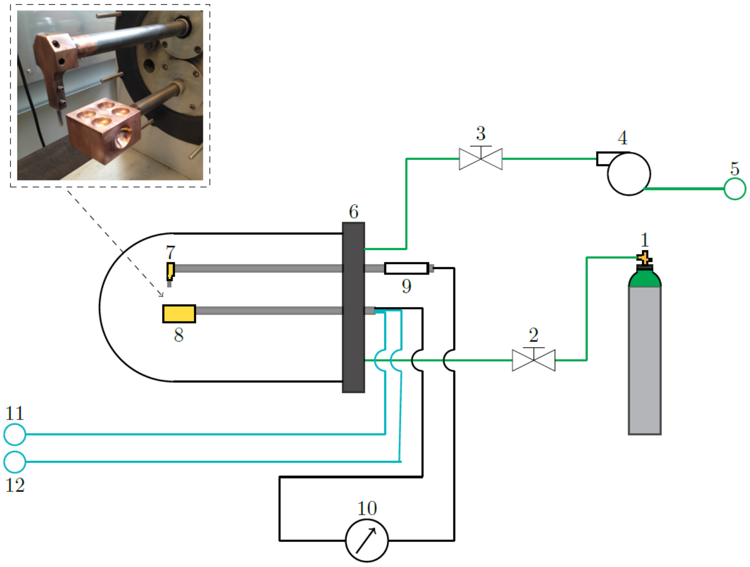

Figure 3.2: A schematic drawing of the electric arc furnace that is applied in the present work. The constituents of the apparatus are: 1) argon gas bottle, 2-3) valves, 4) pump, 5) exhaust outlet, 6) mounting stand with connected glass dome, 7) wolfram tip (cathode), 8) copper crucible (anode), 9) steering handle, 10) current source, 11) cooling water inlet, 12) cooling water outlet. The inserted image shows the wolfram tip above the copper crucible with its four cavities tilted upwards.

copper crucible which act as an anode. The position of the cathode can be altered by operating a handle situated outside the glass dome that also hold a switch which allow the closure of the electric circuit. As the current is increased a voltage is built up across the argon gap between the cathode and anode and eventually the voltage enables dielectric breakdown to occur. When this happens an electric arc flows from the cathode to the anode through the material placed in the cavity which is necessarily exposed to ohmic heating. The crucible is at the same time prevented from overheating by water flowing in the cooling circuit situated inside it.

3.1.3 The ball mill

Another frequently applied solid state processing technique is ball milling. When material synthesis is performed by this technique the different materials are placed inside a vial alongside a number of balls of some hard material such as ceramic, flint or stainless steel. The vial is then sealed off by a lid and placed in an external frame that is mounted to a rotational mechanism. The vials are then made to rotate causing its contents to be energetically slung around. The materials are hence exposed to numerous impacts with the balls attritionally grinding the materials to a fine powder. By altering design parameters such as the rotational speed, milling time, the amount and type of balls, milling atmosphere and the temperature under which the milling occurs both amorphous and crystalline materials can be synthesised.

A wide range of ball mills are commercially available and in this work a Fritsch GmbH Planetary Micro Mill Pulverisette 7 was applied. This ball mill is based on a planetary rotational geometry where two vials are mounted to external frames rotating circularly about the rotational origin. The vials and the balls are made of tempered steel. When the lid is sealed to the vial a teflon gasket is inserted to ensure that the vials are closed hermetically.

3.1.4 The X-ray diffractometer

X-ray diffraction patterns can be collected in the laboratory from an X-ray diffractometer. This instrument can be considered to consist of an X-ray source and an X-ray detector which are mounted to a mechanical construction referred to as a *goniometer* by two arms. These arms can be stationary or made to rotate about the goniometer axis where the sample that is under investigation is placed either in a cavity in a plate or inside a capillary which is mounted to a goniometer head. This enables a wide range of operational geometries for the diffractometer. A simple schematic of a goniometer is

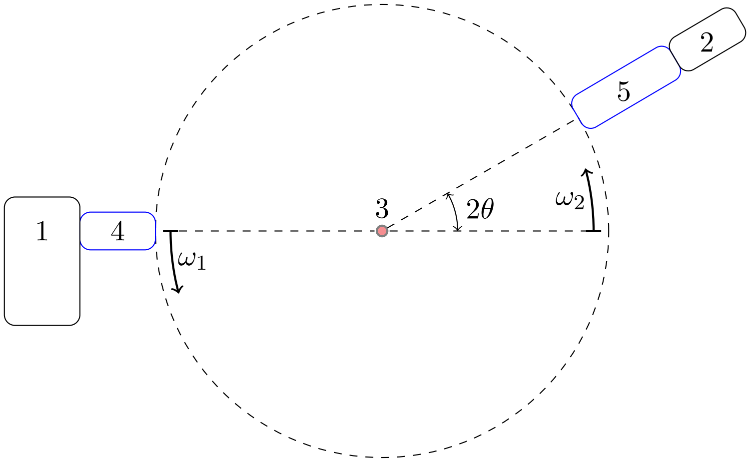

Figure 3.3: A simple schematic of the diffractometer hardware known as a goniometer. The X-ray tube (1) and the X-ray detector (2) are mounted to the goniometer arms which both can be made to rotate about the goniometer axis (3) going out of the paper plane by angles ω_1 and ω_2 respectively. The polychromatic beam of X-rays which are generated in the X-ray source is collimated by a system of divergence and Soller slits both after the X-ray tube (4) and before the detector (5). The angle between the two goniometer arms is 2θ.

shown in figure 3.3.

In the present study a Bruker AXS D8 Advance diffractometer was applied which utilize the Debye-Scherrer geometry. This mean that the goniometer arms rotates symmetrically about the goniometer axis[1]. The X-ray source of the diffractometer is a copper anode supplying X-rays of wavelength

$$\lambda_{Cu-K\alpha 1} = 1.54060 \text{ Å} \tag{3.1}$$

and

$$\lambda_{Cu-K\alpha 2} = 1.54444 \text{ Å} \tag{3.2}$$

The detector of the instrument is a Lynx-Eye silicon strip detector.

---

[1] This imply that if the X-ray tube is situated at an angle ω_1 the detector is situated at an angle given by $\omega_2 = -\omega_1$ with respect to figure 3.3

3.1.5 The BM01A beamline at ESRF

The synchrotron radiation source

It is a fundamental principle of physics that an accelerated charged particle emit electromagnetic radiation in accordance with Larmors radiation formula

$$P = -\frac{q^2}{6\pi\epsilon_0 m^2 c^3}\frac{dp_\mu}{d\tau}\frac{dp^\mu}{d\tau} \tag{3.3}$$

where P is the radiated power, q is the charge of the accelerated particle, m is the mass of the particle, ϵ_0 is the permittivity of free space, c is the speed of light and $\underline{\mathrm{p}}$ is the relativistic four-momentum of the particle. Hence a facility utilizing this principle, such as a *synchrotron*, might replace the X-ray tube of the diffractometer discussed in the previous subsection if the parameters of equation 3.3 are chosen appropriately. In a synchrotron the charged particles are electrons with charge $e = 1.602 \cdot 10^{-16}$ C and mass $m_e = 9.11 \cdot 10^{-31}$ kg and the electrons move at velocities approaching the speed of light for the emitted electromagnetic radiation to have X-ray wavelength. To achieve this experimentally the electrons are accelerated by exposing them to an assembly of strong magnetic fields which cause the electrons to precess about the axis normal to both the magnetic field and the electrons direction of movement.

A schematic drawing of a synchrotron facility is depicted in figure 3.4. The electrons are produced in bunches by an *electron gun* and accelerated to 6 GeV energies by a *linear particle accelerator*[2] coupled to a *booster synchrotron* before they are injected into the *storage ring*. Here the electrons precess in a tube that is maintained at very low pressures about an axis normal to the plane in which the synchrotron is situated. The precession is governed by a series of strong dipole magnets situated around the ring known as *bending magnets* causing the electrons to emit electromagnetic radiation by equation 3.3[3]. The electromagnetic radiation are subsequently directed away from the bending magnets towards a hutch known as a *beamline* where the experimental set-up is situated.

In the present study the synchrotron experiments where conducted at the Swiss-Norwegian Beamline (SNBL) BM01A which is situated at a bending magnet source at the European Synchrotron Radiation Facility (ESRF) in Grenoble, France.

---

[2] The linear particle accelerator is often abbreviated LINAC.

[3] The electromagnetic radiation can also be generated by more complex magnetic arrengements known as *wigglers* and *undulators*.

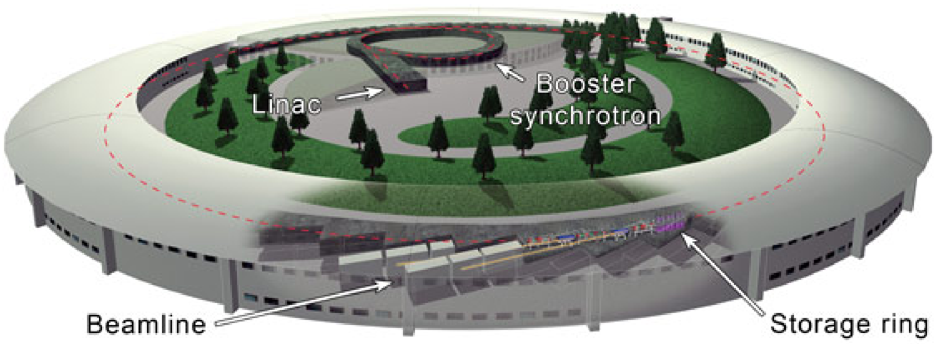

Figure 3.4: A schematic drawing of a synchrotron. The figure is adapted from [61].

The powder diffractometer

The X-ray beam enters the beamline hutch through a beamline channel of fixed orientation and is incident upon the goniometer and the detector. The diffractometer is based on the Dectris Pilatus 2M detector [62] which is a fast and low-noise area detector that can be tilted and translated both horizontally and vertically. The horizontal range of the detector is $\Delta x \in [146 \text{ mm}, 700 \text{ mm}]$ with respect to the goniometer axis while the vertical range is $\Delta z \in [0 \text{ mm}, 500 \text{ mm}]$ where 0 mm corresponds to the case where the beam nearly hits the center of the detector. The detector tilt is currently limited to $\phi = 35°$.

The blower

The temperature of the sample can be controlled by a hot blower which has been developed locally at the ESRF and operates in the temperature regime $T \in [25\ °\text{C}, 500\ °\text{C}]$. The blower consist of a heating element that is situated at the end of a metallic cylinder which is open at the other end. A fan blows the heated air through the cylinder and out onto the sample that is subsequently heated. The temperature of the blower is measured by a thermocouple that is situated at the center of the tube in the cylinder opening. A calibration must be performed to know the temperature at the sample position as the hot stream of air cools when it flows out of the blower towards the sample. The blower should be mounted close to the sample to reduce their temperature difference, but if the they are mounted too close the blower will project its shadow onto the detector and hence reduce its resolution. A compromise must therefore be made when considering these issues.

The hydrogen gas rig

By placing the sample in sapphire capillaries that can be mounted to a high pressure cell the sample can be exposed to either H_2-gas or some inert gas under high pressures. To achieve this the high pressure cell is connected to a gas circuit as is shown schematically in figure 3.5. By operating the valves (1-8) the gases can be made to flow through the circuit. The pressure in the circuit can be measured by a pressure sensor that is situated at (17). When hydrogen gas is filled into the circuit it is customary to do this indirectly through the volume (21). A rotationally operated pump (22) enables the circuit to be emptied of gas and put under dynamic vacuum.

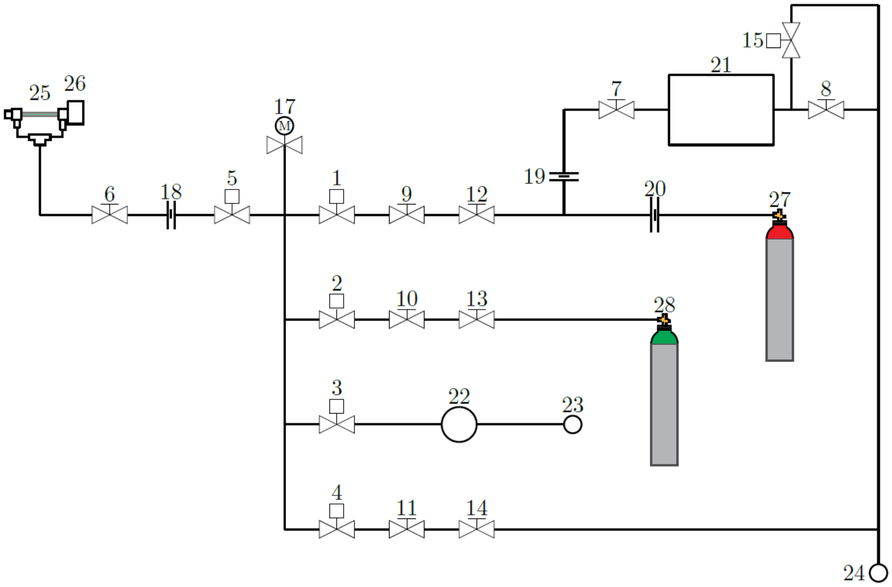

Figure 3.5: A schematic diagram of the hydrogen gas rig at the BM01A beamline. 1-5) user operated pneumatic valves, 6-8) manually operated valves, 9-11) flow restricting needle valves, 12-14) check valves, 15-16) safety relief valves, 17) pressure sensor, 18-20) Swagelok VCR gaskets, 21) reservoir volume, 22) pump, 23-24) exhaust outlets, 25) sapphire capillary holding the sample, 26) goniometer mounting point, 27) H_2-gas inlet, 28) Ar-gas inlet.

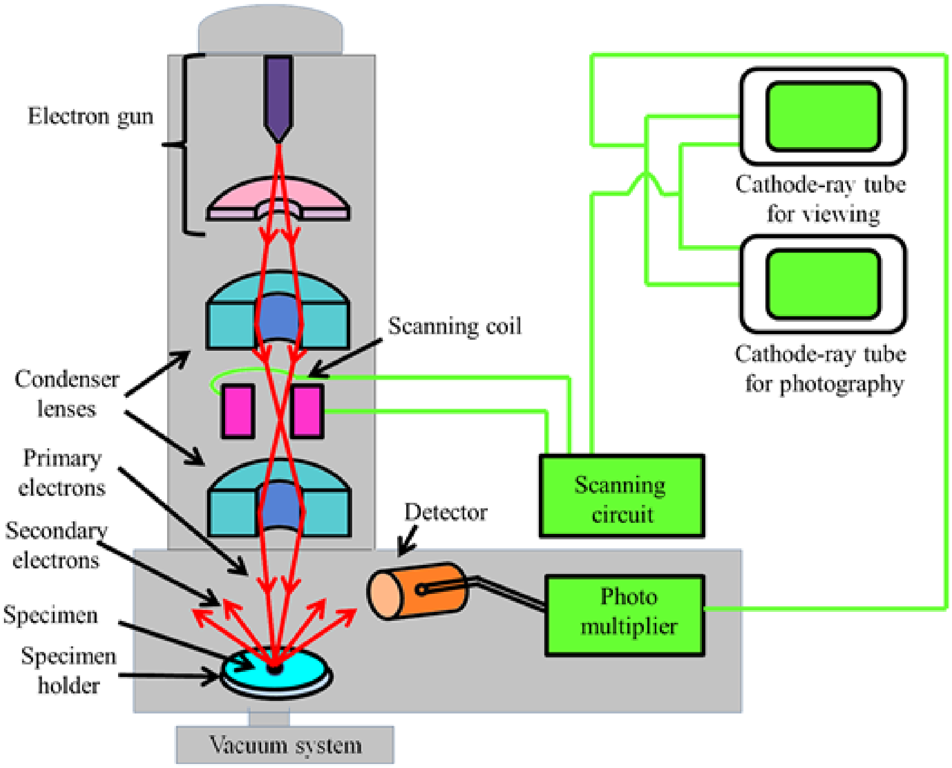

Figure 3.6: A simplified schematic drawing of a scanning electron microscope. The figure is adapted from [63].

3.1.6 The scanning electron microscope

Figure 3.6 show a simplified schematic drawing of a scanning electron microscope. The instrument applies an intense beam of electrons to study the composition and topography of subjected samples. Since electrons are charged particles they are prohibited from penetrating deep into the subjected specimen. This restrict the technique to studies of the sample composition and topography in the close proximity of the sample surface.

The electrons are produced by an *electron gun* in the uppermost part of the instrument and directed downwards towards a series of electromagnets. These generate magnetic fields that the charged electrons interact with in such a way that the beam can be controlled and focused[4]. The elec-

---

[4] In a typical measurement the electromagnets are operated in such a way that the electron beam scan an area of the surface which is why the instrument is called a scanning electron microscope.

tromagnets therefore act as the *condenser lenses* of the microscope. The *primary electrons* from the electron gun are subsequently incident upon the sample which it interacts with through a variety of processes. Certain electrons are back-scattered off the sample, while others are absorbed by it. If this happen in the closest proximity of the surface, the excited surface atom might emit one of its own electrons. These electrons are referred to as the *secondary electrons* and are detected by the instrument to generate two-dimensional images of the sample surface. If absorption occur deeper down in the specimen the absorbed energy is given off as photons instead. These photons can provide information about the elemental composition of the sample since each element has its own distinct electromagnetic emission spectrum. The photons are therefore detected by an energy-dispersive spectrometer and the elemental composition of the sample is deduced through a so-called Energy-Dispersive X-ray spectroscopy (EDX) analysis.

3.1.7 The Sieverts apparatus

A Sieverts apparatus is an instrument that enable the exposure of different samples to gas pressures in ambient or heated environments. To achieve this experimentally a supply of gas and a container holding the sample, that is henceforth referred to as a *sample-holder*, are connected by a circuit of several pipelines. The circuit is subdivided into numerous parts by pneumatically actuated valves that can be operated from a computer program. The gas flow through the circuit can therfore be arranged for specific experiments. A detailed description of the instrument and its different components are provided elsewhere [64] but a simplified schematic of the main part of the rig is shown in figure 3.7. As can be seen from this figure the rig can be considered to consist of four volumes of which V_1, V_2 and V_3 constitute the instrument manifold while the final volume V_4 is the sample-holder that accommodate the sample and must be mounted to manifold by a mechanical connection. The volumes are often gathered together and referred to as the large volume, $V_{large} = V_1 + V_2 + V_3$, or the small volume, $V_{small} = V_2 + V_3$. An oven is mounted to a sliding rack underneath the assembly point of the sample-holder. As the oven can be set to temperatures as high as 538 °C and lifted to partially surround the sample-holder the temperature of the sample environment can be designed to the experiment. The temperature is measured by two thermal resistors that are coupled to the sample-holder and instrument manifold respectively while the pressure within the system is monitored by a pressure transducer connected to the volume V_2.

There are currently two such Sieverts apparatuses in the hydrogen labo-

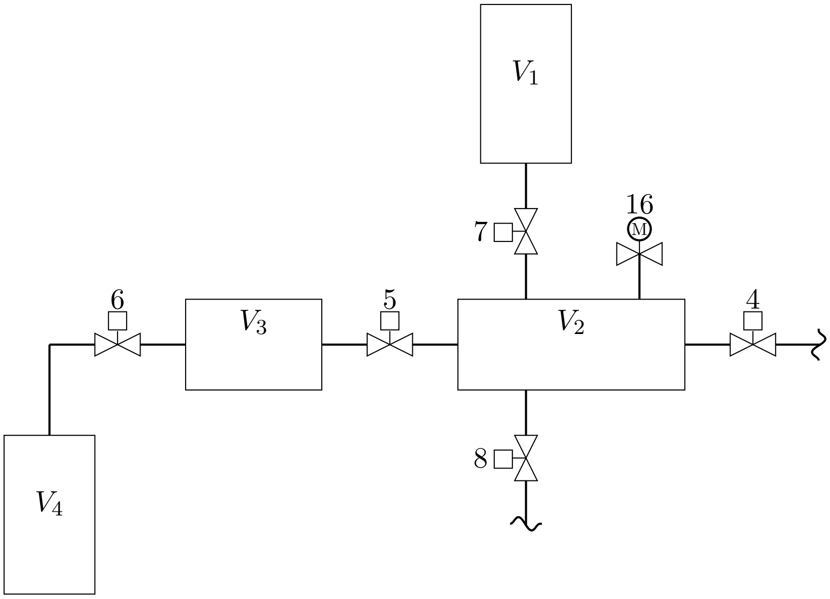

Figure 3.7: The main part of the Sieverts apparatus holding the different volumes V_1, V_2, V_3 and V_4. The valves (4-8) are pneumatically actuated and the pressure transducer (16) is custom made by Presens. The pipelines continue towards the rest of the rig that is described in [64].

ratory at IFE that is henceforth referred to as the B-side and C-side rig. Each of these have their own sample-holder that is respectively referred to as #10B and #12B. The different volumes were determined volumetrically through several volumetric measurements performed during the calibration [64] that was performed by the author. Based upon these measurements the resultant mean values were taken as the best estimates and the corresponding standard deviation as the measurement uncertainties. The final estimates are given in table 3.1. It should be noted that the measurement uncertainty of the pressure transducer δP has been found to be

$$\delta P = 0.04 \text{ bar} \tag{3.4}$$

while the thermal resistors were calibrated to an internal standard [64] so that their measurement uncertainties δT fulfil

$$\delta T = 0.3\ ^{\circ}\text{C} \tag{3.5}$$

Table 3.1: The different volumes within the B-side and C-side Sieverts apparatus and the two sample-holders #10B and #12B that was determined in the calibration [64].

Rig/Sample-holder	B/#10B	C/#12B
$V_{rig,1}$ [mL]	152.08 ± 0.02	301.29 ± 0.55
$V_{rig,2}$ [mL]	9.97 ± 0.08	9.93 ± 0.08
$V_{rig,3}$ [mL]	6.24 ± 0.05	6.18 ± 0.07
$V_{sample-holder,4}$ [mL]	13.04 ± 0.04	12.89 ± 0.21

3.1.8 The TG/DSC

Thermal analysis is a set of experimental techniques for investigating different properties of a sample as it is exposed to a predefined temperature program. It is the property of interest that dictates which technique one has to apply. Differential scanning calorimetry (DSC) is for instance applied to investigate the heat of reaction as the sample undergoes a physical or chemical change while thermogravimetric analysis (TGA) monitors the mass of the sample.

In the present work TGA and DSC are performed simultaneously with a Netzsch STA 449 F3 Jupiter apparatus. A schematic drawing of the operational principle of such a heat flux type DSC is rendered in figure 3.8. The sample is placed within a small crucible which is sealed by a perforated lid and placed upon a thermally conducting disc. An identical albeit empty reference crucible is placed alongside the crucible holding the sample. The property that is monitored is hence a differential between the properties of the two crucibles. With regard to this principle two thermocouples are mounted inside the disc underneath the respective crucibles so that the temperature difference ΔT between the sample T_S and reference crucible T_R can be monitored. The disc is furthermore situated on the top of a pedestal which is mounted to a high precision weight that enable TGA to be performed *in-situ*. A cylindrical oven is mounted above the pedestal which can be lowered to enclosed the system as it is heated. The cylindrical volume is furthermore connected to a gas circuit through pipe entries at the top and bottom of the cylinder. This is implemented so that an inert gas can be made to flow through the system to fix its pressure and atmosphere and remove gases that are desorbed from the sample. As the disc that carries the crucibles are made of a material with good thermal conductivity the heat from the oven is primarily transported to the sample and reference

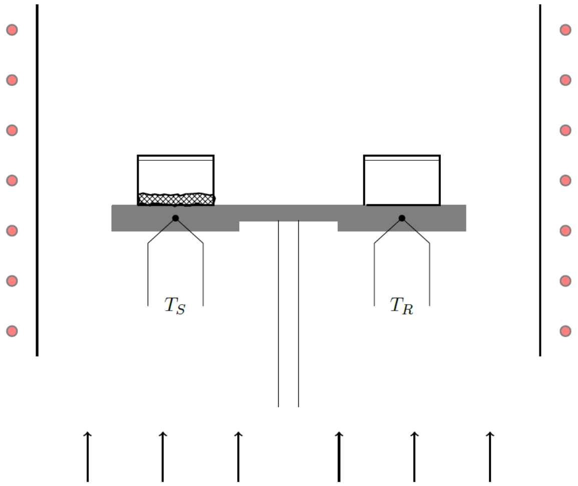

Figure 3.8: A schematic drawing of the operational principle behind a heat flux type DSC. The sample is situated inside the crucible on the left side of the thermally conducting disc. An empty reference crucible is placed next to the sample and the temperature difference $\Delta T = T_S - T_R$ between the two crucibles is measured by two thermocouples. The system is placed upon a pedestal that is mounted on a high precision weight within a cylindrical oven through which an inert gas can be made to flow as indicated by the arrows.

by thermal conduction through Fouriers law of heat conduction. During steady-state conditions the measured temperature difference between the sample and reference is ideally zero but if the sample undergo a physical or chemical change the rate of heat transfer to the sample will differ from that of the reference. This effect is manifested through the measured temperature difference through which the heat of reaction can be determined from Fouriers law of heat conduction

$$\Phi = \frac{\Delta T}{R} \tag{3.6}$$

where $\Phi = dQ/dt$ is the heat flow into or out of the sample, ΔT is the measured temperature difference between the sample and the reference and R is the thermal resistance. If the apparatus is properly calibrated and the so-called baseline[5] is known the heat flux into or out of the sample can be assigned to any temperature difference ΔT that is measured *in-situ*.

---

[5] This is the background contribution to the heat flux signal that is generated in the DSC at steady-state conditions by the empty crucibles and the differences in heat capacities of the sample and reference crucible.

3.2 Methodology

3.2.1 Sample preparation

All the samples that have been prepared in the present work have been handled under an argon atmosphere inside an MBraun Unilab glove-box. During the preparation of a sample the number of necessary moles n of each element present in the sample is determined from the desired molar relationship of the different constituents and the corresponding masses m are determined from the relation

$$m = nM \tag{3.7}$$

where M is the molar mass of the element. The different masses are determined with either the Sartorius Extend ED124S balance or the Mettler Toledo AG204 DeltaRange balance depending on which glove-box the preparation is handled within. Selective specifications for the different balances that are relevant for our investigations are rendered in tables 3.2, and 3.3. An unsuccessfull effort were also made to track down the datasheet of the Mettler PM460 DeltaRange. This prevent error analysis to be performed for this balance.

The measurement uncertainties δm can be determined with application of the technical specifications given in tables 3.2 and 3.3 following the strategy outlined in a technical doument from Mettler Toledo [66]. This document state that under the assumption that the balance measurement deviation is normally distributed the uncertainty δm of a single measurement can be taken as the normalized standard deviation that is given by

Table 3.2: Selective specifications from the Sartorius Extend ED124S datasheets [58] [65].

Property	Symbol	Value
Readability	s_{READ}	0.0001 g
Repeatability	s_{REP}	0.0001 g
Non-linearity	s_{N-L}	0.0002 g
Temperature coefficient	s_{TEMP}	$2.0 \cdot 10^{-6}\ \frac{1}{\mathrm{K}}$
External calibration weight	m_{CAL}	100 g
Tolerance	s_{CAL}	0.001 g
Calibration weight tolerance	$s_{CAL,\ REL}$	$1.0 \cdot 10^{-5}$

Table 3.3: Selective specifications from the Mettler Toledo AG204 DeltaRange datasheet [59].

Property	Symbol	Value
Readability	s_{READ}	0.0001 g
Repeatability	s_{REP}	0.0001 g
Non-linearity	s_{N-L}	± 0.0002 g
Temperature coefficient	s_{TEMP}	$1.5 \cdot 10^{-6}\ \frac{1}{\mathrm{K}}$
Internal calibration weight	m_{CAL}	200 g
Tolerance	s_{CAL}	0.006 g
Calibration weight tolerance	$s_{CAL,\ REL}$	$3.0 \cdot 10^{-5}$

$$\delta m = \sqrt{\frac{1}{m^2}\left(s_{REP}^2 + \frac{2}{3}s_{N-L}^2\right) + \frac{1}{3}\left(s_{CAL,\ REL}^2 + \frac{1}{3}\left(s_{TEMP} \cdot d_t\right)^2\right)} \quad (3.8)$$

where s_{REP}, s_{N-L}, $s_{CAL,\ REL}$ and s_{TEMP} are the specified *repeatability*, *non-linearity*, *calibration weight tolerance* and *temperature coefficient* respectively in the data-sheet of the balance while m is the measured mass. d_t is the width of the temperature band in which the temperature of the balance environment might fluctuate and in this work it is assumed as $d_t = 2$ K.

After preparation, the samples are brought out of the glove-box inside sealed argon-filled glass vessels and loaded into one of the crucibles in the arc-melter. A titanium piece is also loaded into another crucible. In this loading-manoeuvre the samples are exposed to air for a short amount of time until a vacuum of $\sim 10^{-2}$ mbar is drawn inside the glass dome of the arc-melter. The system is subsequently flushed with argon gas to a final pressure of 0.75 bar on three occasions before the titanium piece is melted under argon at a pressure of 0.75 bar to purify the atmosphere inside the dome even further. The sample is then melted under similar conditions. To prevent the powdered raw-materials from bursting out of the cavity the set current is ramped in increments of 20 A from an initial current of 30 A to a final current of 70 A. At the final set current the sample is turned and remelted five times to ensure homogeneity before the glass dome again is dismantled from the arc-melter. The sample is then in the shape of a spherical button that is crushed by application of an anvil and hammer before it is brought back into the glove-box for storage. From the sample is brought out of the glove-box its mass is monitored by application of the Mettler PM460 DeltaRange balance throughout the preparatory steps outlined above. The observed changes are due to measurement errors and losses associated with raw-materials bursting out of the cavity in the arc-melter or pieces that are lost when the sample is crushed.

The micro-structure of some samples might subsequently be altered by ball-milling in the Fritsch GmbH Planetary Micro Mill Pulverisette 7. For this purpose the mass of the sample is measured initially inside the glove-box before it is loaded into a vial alongside an appropriate number of tempered steel balls. The vials are sealed under argon and loaded out of the glove-box before they are mounted inside the ball-mill. Care is taken so that two vials are always situated inside the planetary ball-mill to ensure symmetry. After the milling is complete vials are transported back into the glove-box where the sample is retrieved and its mass measured once again to assure that the mass losses over the process are insignificant.

3.2.2 X-ray diffraction studies

Laboratory X-ray diffraction pattern

Preliminary structure analysis is performed on the Bruker AXS D8 Advance diffractometer at IFE. In a typical experiment the diffractometer is in the Debye-Scherrer geometry and the powdered sample is placed inside 0.5 mm inner diameter Hilgenberg borosilicate glass capillaries. The sample is aided into such a capillary with application of 0.3 mm glass rod until the powder occupy at least 3 cm of the capillarys vertical extent. The capillary is then cut with a nail-clipper approximately 1 cm above the powder surface and the open end is glued shut with Precision Super Glue delivered by Loctite. When the glue is dry the capillary is brought out of the glove-box and mounted to the diffractometers goniometer-head in a lump of beeswax. The goniometer head is then levelled and mounted at the goniometer axis of the instrument before the experimental parameters are set in the Bruker software and the diffraction pattern is collected. The resultant laboratory powder diffraction (lab PXD) patterns will however have much lower signal-to-noise ratio than synchrotron measurements and it is therefore only applied for preliminary structure analysis and phase determination in this work.

Synchrotron X-ray diffraction pattern

Synchrotron radiation powder X-ray diffraction (SR-PXD) patterns is obtained on the Swiss-Norwegian beam-line at the European Synchrotron Radiation Facility in Grenoble, France. The applied wavelength λ_{SNBL} of the X-rays was set to

$$\lambda_{SNBL} = 0.6973 \text{ Å} \tag{3.9}$$

throughout the entire beam time and several *ex-situ* and some *in-situ* measurements were conducted.

In the typical *ex-situ* measurement the powdered sample is loaded into 0.5 mm inner diameter Hilgenberg borosilicate glass capillaries following the exact same procedure as when the lab PXD patterns were collected. The sample is then brought out of the glove-box and embedded in beeswax inside a small metal tube that is subsequently mounted through a magnetic coupling to a goniometer head. The assembly is then brought into the beam-line hutch, mounted on the goniometer axis and properly levelled before the hutch can be sealed off and the measurement recorded.

In the typical *in-situ* measurement the powdered sample is placed in the center of a sapphire capillary with 0.8 mm inner diameter that is open in both ends. The handling is done under an argon atmosphere inside a glove-box. The powder is compacted with application of two 0.6 mm diameter glass rods from both ends of the capillary. The rods are eventually left inside the capillary as to prevent the sample from blowing away when it is exposed to a dynamic vacuum or a H_2-gas pressure. The rods are then cut approximately 1 cm outside the extent of the capillary before the entire assembly is mounted to the pressure-cell by tightening two bolts - one in each end of the capillary. The pressure-cell is then brought out of the glove-box and into the beam-line hutch where it is mounted at the goniometer axis. The pressure-cell is connected to the high pressure gas rig shown in figure 3.5 and exposed to a dynamic vacuum and if a sufficient level of vacuum is reached the hutch is sealed off. A temperature program is then set for the blower and the measurement is started. Depending on whether an absorption or a desorption process is studied the sample can be exposed to H_2-gas by operating the high pressure gas rig software.

In either case the detector is set at $\Delta x = 246.38$ mm and $\Delta z = 490$ mm and the measured raw-data is in either case integrated to a powder pattern by the pyFAI-based tool *Bubble* [62].

Rietveld refinement

In the present work selected PXD patterns have been exposed to a *Rietveld refinement* using the General Structure Analysis System (GSAS) [67]. This is a structural refinement technique that was originally developed by the Dutch crystallographer Hugo M. Rietveld over two papers published in 1967 [68] and 1969 [69] respectively. The technique was originally developed for neutron powder diffraction but can equally well be applied when considering diffraction patterns measured with X-rays. Such a pattern generally consist of a finite amount of N data-points $\{i\}_{i=1}^{N}$ giving the measured intensities of scattered photons $I_{i,meas}$ as a function of the scattering angle $2\theta_i$. As elaborated in subsection 2.2.3 it is clear that the random orientation of the crystallites in a powder diffraction experiment inflict a projection of the full diffraction pattern of the crystalline samples three-dimensional structure into a one-dimensional recording. An inevitable consequence of such a projection is the loss of information associated with the overlap of originally independent peaks in the three-dimensional diffraction pattern. In the years before Rietveld developed his technique it was not possible to distinguish overlapping peaks from each other and refinement had to rely on the integrated intensities of the observed Bragg-peaks in the measured powder diffraction pattern. Rietvelds ground-breaking idea was to fit a calculated profile with intensities $I_{i,calc}$ to the measured pattern by means of a non-linear regression to minimize the expression

$$M = \sum_{i=1}^{N} \{w_i M_i^2\} = \sum_{i=1}^{N} \{w_i |I_{i,meas} - I_{i,calc}|^2\} \tag{3.10}$$

where $\{I_{i,meas}\}_{i=1}^{N}$ are the measured intensities, $\{I_{i,calc}\}_{i=1}^{N}$ are the calculated intensities predicted by the model and w_i is a statistical weight that is often taken as the statistical squared inverse standard deviation of $M_i = |I_{i,meas} - I_{i,calc}|$ so that

$$w_i = \frac{1}{\sigma_{M_i}^2} \tag{3.11}$$

One therefore considers the entire pattern as opposed to the integrated intensities of the observed Bragg-peaks separately. The advantage of such a strategy is that overlapping Bragg-peaks can be considered without attempting to deconvolute them into separately, observed integrated intensities.

The theoretical model giving the calculated intensities $\{I_{i,calc}\}_{i=1}^{N}$ in our N data-points is given in accordance with the discussion of section 2.2 as

$$I_{i,calc} = S \sum_{h,k,l} \left\{ m_{hkl} L_{hkl} P_{hkl} A_i |F_{hkl}|^2 f(2\theta_i^{hkl}) \right\} + I_{i,background} \tag{3.12}$$

where S is a scaling factor[6], the sum is over all the Bragg peaks with Miller indices h, k, l that contribute to the measured intensity in measurement point

---

[6] The scaling factor S is dependent on the wavelength λ of the incident photons, the

i, m_{hkl} is a multiplicity factor, L_{hkl} is the Lorentz factor, P_{hkl} is a factor taking into account the preferred orientation of the sample, A_i is a factor taking into account the absorption of photons within the sample, F_{hkl} is the structure factor and $f(2\theta_i^{hkl})$ is some function describing the profile of the contributing peak with Miller indices h, k, l in the measurement point i due to instrumental and sample broadening. These peak profiles can in general be described by a so-called *Pseudo-Voigt function* that is a linear combination of a normalized *Gaussian-* and a normalized *Lorentzian function* so that

$$f(2\theta_i^{hkl}) = \frac{2}{\pi}\frac{\Gamma_{hkl}}{\Gamma_{hkl}^2 + (2\Delta 2\theta^{hkl})^2} + \frac{4}{\sqrt{\pi}}\sqrt{\frac{\ln(2)}{H_{hkl}^2}}e^{-2\ln(2)\left(\frac{\Delta 2\theta^{hkl}}{H_{hkl}}\right)^2} \tag{3.13}$$

where $\Delta 2\theta^{hkl} = 2\theta^{hkl} - 2\theta_i^{hkl}$ with $2\theta^{hkl}$ as the centred position of the Bragg peak with Miller-indices h, k, l, H_{hkl} is the Gaussian full-width at half maximum of the peak that is given by *the Cagliotti equation*[7] as

$$H_{hkl}^2 = G_U \tan^2(\theta_i^{hkl}) + G_V \tan(\theta_i^{hkl}) + G_W \tag{3.14}$$

with G_U, G_V and G_W as adjustable parameters and Γ_{hkl} is the Lorentzian full-width at half maximum given by

$$\Gamma_{hkl} = L_X \tan(\theta_i^{hkl}) + \frac{1}{\cos\theta_i^{hkl}} L_Y \tag{3.15}$$

with L_X and L_Y as refineable parameters that are related to the crystallite size and the strain within the sample respectively. $I_{i,background}$ is finally a polynomial describing the background radiation that contributes to the measured diffraction pattern.

---

volume of the irradiated sample, the intensity of the incoming beam of photons, the distance between the sample and the detector, the area of the detector and the unit-cell volume within the sample.

[7] This equation was originally established by Cagliotti et al. [70] through a detailed treatment of the dependence of the observed full-width at half-maximum H_{hkl} of the Bragg-peaks in powder neutron diffraction patterns on the divergence of the incident neutron beam that was introduced between the neutron source and the monochromator, the monochromator and the sample and finally between the sample and the detector. The influence of the mosaic spread of the monochromator was also taken into consideration. When the technique is applied with X-rays there is however no corresponding physical explanation for the parameters G_U, G_V and G_W and they must be viewed as empirical constants.

The ability of the theoretically determined model to explain the measured intensities is finally quantified through application of three different measures. The first two of these are the weighted profile R-factor and the weighted profile R-factor that are given by

$$R_p = \frac{\sum_{i=1}^{N} \{|I_{i,meas} - I_{i,calc}|\}}{\sum_{i=1}^{N} \{I_{i,meas}\}} \tag{3.16}$$

and

$${}_wR_p = \sqrt{\frac{\sum_{i=1}^{N} \{w_i |I_{i,meas} - I_{i,calc}|^2\}}{\sum_{i=1}^{N} \{w_i |I_{i,meas}|^2\}}} \tag{3.17}$$

with $I_{i,meas}$ as the measured intensities, $I_{i,calc}$ as the calculated intensities, N as the total amount of measurements, P as the number of refined parameters and w_i as a statistical weight. For the weighted profile R-factor it might furthermore be advantageous to consider the limit where all the observed discrepancy between the measured and calculated intensities are statistical so that the average $M_i = |I_{i,meas} - I_{i,calc}|$ equals the statistical standard deviation σ_{M_i}. In this case the weighted R-factor is reduced to

$${}_wR_p \to \sqrt{\frac{\sum_{i=1}^{N} \left\{w_i \sigma_{M_i}^2\right\}}{\sum_{i=1}^{N} \{w_i |I_{i,meas}|^2\}}} = \sqrt{\frac{N}{\sum_{i=1}^{N} \{\frac{1}{\sigma_{M_i}^2} |I_{i,meas}|^2\}}} \tag{3.18}$$

where the statistical weight has been chosen as the squared statistical standard deviation $w_i = \frac{1}{\sigma_{M_i}^2}$. It is furthermore customary to correct the total number of measurements N by subtracting the number of refined parameters P so that we can define a statistically expected profile R-factor ${}_eR_p$ as

$${}_eR_p = \sqrt{\frac{N - P}{\sum_{i=1}^{N} \{\frac{1}{\sigma_{M_i}^2} |I_{i,meas}|^2\}}} \tag{3.19}$$

The final measure of quality on the theoretically calculated intensities is then given by the so-called reduced χ^2 which is defined as the fraction between the squared weighted profile R-factor and the squared statistically expected profile R-factor as

$$\chi^2 = \frac{{}_wR_p}{{}_eR_p} = \frac{\sum_{i=1}^{N} \{\frac{1}{\sigma_{M_i}^2}|I_{i,meas} - I_{i,calc}|^2\}}{N - P} \tag{3.20}$$

where the statistical weight w_i has been taken as the squared inverse statistical standard deviation σ_{M_i}.

3.2.3 Thermodynamic analysis in Sieverts-apparatus

The main goal of the thermodynamic analysis within the Sieverts-apparatus is to determine the hydrogen content in some subjected sample by volumetric techniques. Such analyses are heavily reliant on the ideal gas law which is given from simple thermodynamics as

$$PV = Nk_BT \tag{3.21}$$

which through the relations $N = nN_A$ and $k_B = R/N_A$ also can be expressed as

$$PV = nRT \tag{3.22}$$

where N_A is Avogadros number, R is the universal gas constant and n is the number of moles of gas in our system. It should be stressed that the fundamental assumptions that has been imposed on the system in arriving at this result is that it has to be in thermodynamic equilibrium with its environment and that the gas is sufficiently dilute so that the gas molecules won't interact with each other. A question then arises naturally: *what constitutes sufficiently diluted?* Or put another way: *how much does a real gas at a temperature T and pressure P deviate from ideal gas behaviour?* To account for this we introduce the so-called compressibility factor $Z(P, T)$ which is defined as

$$Z(P, T) = \frac{PV}{nRT} \tag{3.23}$$

From the definition it is clear that a purely ideal gas would have $Z(P, T) = 1$ and that the deviation from unity for the compressibility factor is a measure of the actual deviation of the real gas from ideal gas behaviour.

Several empirical models describing the compressibility factor of hydrogen gas $Z(P, T)$ has been developed over the years and throughout this work we will apply the model that was developed by Lemmon et al. in 2008 [71] to provide consistency with the calculations from the NIST Standard Reference Database. The resulting expression for the compressibility factor is

$$Z(P,T) = 1 + \sum_{i=0}^{8} \{a_i \left(\frac{100\text{ K}}{T}\right)^{b_i} \left(\frac{P}{10\text{ bar}}\right)^{c_i}\} \tag{3.24}$$

where T is the temperature measured in K and P is the pressure measured in bar while $\{a_i\}_{i=0}^{8}$, $\{b_i\}_{i=0}^{8}$ and $\{c_i\}_{i=0}^{8}$ are dimensionless constants that has been fitted to the experimental data. All the relevant constants are given in table 3.4. This model has been reported to agree with the current standard of within 0.01% throughout the temperature range 220 K to 1000 K with H_2-pressures as high as 120 MPa which means that the uncertainty δZ must be taken as the worst case scenario which is given by

$$\frac{\delta Z}{Z(P_{max} = 1200\text{ bar}, T_{min} = 220\text{ K})} = 0.0001 \quad \Rightarrow \quad \delta Z = 0.0002 \tag{3.25}$$

Table 3.4: Constants $\{a_i\}_{i=0}^{8}$, $\{b_i\}_{i=0}^{8}$ and $\{c_i\}_{i=0}^{8}$ associated with the compressibility factor $Z(P,T)$ for normal hydrogen given in equation 3.24.

i	a_i	b_i	c_i
0	0.05888460	1.325	1.0
1	−0.06136111	1.87	1.0
2	−0.002650473	2.5	2.0
3	0.00271125	2.8	2.0
4	0.001802374	2.938	2.42
5	−0.001150707	3.14	2.63
6	$0.9588528 \cdot 10^{-4}$	3.37	3.0
7	$-0.1109040 \cdot 10^{-6}$	3.75	4.0
8	$0.1264403 \cdot 10^{-9}$	4.0	5.0

Based upon the results of the calibration [64] and the theoretical framework that is established in appendix A the amount of hydrogen that is sorbed by a sample that is situated inside one of the sample-holders of the Sieverts apparatus can be determined.

Kinetics measurements

In the typical kinetics measurement a pressure P_i is filled into either the small V_{small} or the large volume V_{large} while a vacuum is drawn inside the sample-holder volume V_j holding the sample of volume V_{sample}. After thermodynamic equilibrium is reached the valve separating the two volumes are opened allowing the gas to interact with the sample and the sorbed amount of moles after k recordings n_k are calculated through either equation A.9 or A.23 depending on whether the sample is at ambient or elevated temperature. The measurement uncertainty in the sorbed amount of moles δn_k is calculated as described in appendix A where it is assumed that all the measurement uncertainties are independent and randomly distributed.

Pressure-composition-isotherm measurements

The typical measurement of a pressure-composition isotherm can be considered as several kinetics measurements that are collected consecutively. As for the kinetics measurement a pressure P_i is filled into either the small V_{small} or the large volume V_{large} while a pressure P_j is established inside the sample-holder volume V_j holding the sample of volume V_{sample}. After thermodynamic equilibrium is reached the valve separating the two volumes are opened allowing the gas to interact with the sample and the absorbed amount of moles after k recordings n_k are calculated through either equation A.9 or A.23 depending on whether the sample is at ambient or an elevated temperature. The measurement uncertainty in the sorbed amount of moles δn_k is calculated as described in appendix A where it is assumed that all the measurement uncertainties are independent and randomly distributed. It should be noted that the measurement uncertainty will increase as a function of the number of data-points that are collected on the pressure-composition isotherm since the measurement uncertainty of the sorbed amount of moles at measurement k is dependent on the measurement uncertainty at step $k-1$.

3.2.4 Thermodynamic analysis by TG/DSC

In the present work all samples have been placed inside alumina (Al_2O_3) crucibles with masses $m_{crucible} = 299 \pm 8$ mg when TG/DSC measurements have been conducted. As the standard deviation of these masses only amounts to ~ 3 % of the total mass it was concluded that the same baselines could be applied for all measurements. Five baseline signals having temperature programs consisting of a linear heating segment at different heating rates β from room temperature to 800 °C followed by a one hour isotherm at 800 °C were therefore measured once with an alumina crucible of mass $m_{crucible}^{baseline} = 322.57$ mg. The heating rates were chosen as $\beta \in [2, 5, 10, 15, 20]$ $\frac{\mathrm{K}}{\mathrm{min}}$ to enable apparent activation energies E_A to be determined through Kissinger analyses of the collected datasets. The isotherm was included to ensure that all the hydrogen was removed from the sample. To prevent the introduction of further measurement errors the same reference crucible with mass $m^{ref}_{crucible} = 322.44 \pm 0.13$ mg was applied for all measurements. A typical measurement for the experimental set-up described above is shown in figure 3.9 for a sample of m_{sample}= 21.896 mg of $\mathrm{Ti}_{0.70}\mathrm{V}_{0.30}\mathrm{H}_{\mathrm{x}}$. Several interesting properties can be extracted from such a measurement such as the mass percentage of hydrogen that is present in the sample, η, that is given by

$$\eta = \frac{\Delta m}{m_{tot}} \cdot 100\% \tag{3.26}$$

where Δm is the absolute change in the mass of the sample through the desorption and m_{tot} is the initial mass of the sample. In so doing it is strictly assumed that no other substance is added or removed from the sample during the experiment so that the mass of hydrogen initially present in the sample was $m_{\mathrm{H}} = \Delta m$.

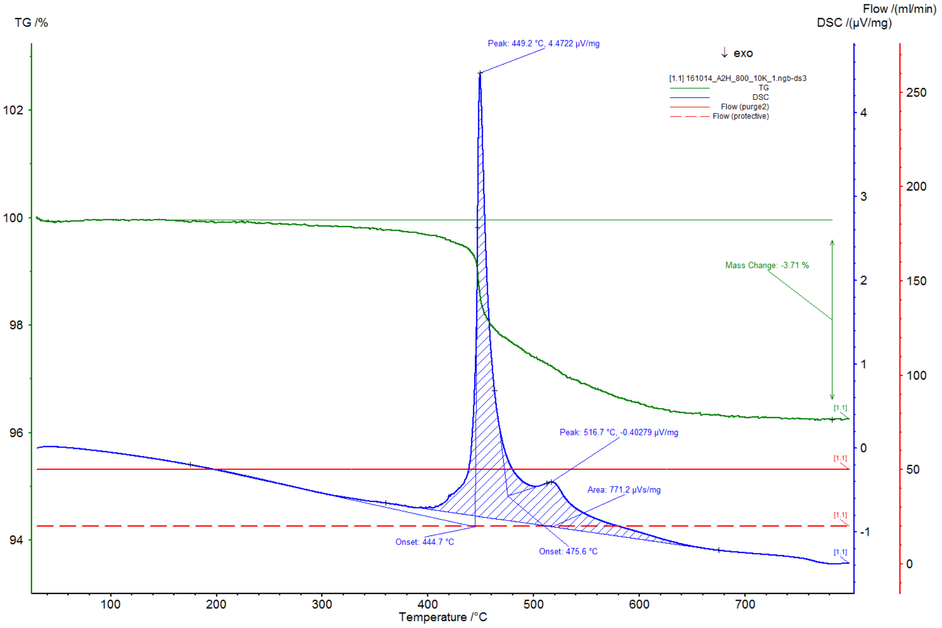

Figure 3.9: Measured TG/DSC signal for a linear heating at $\beta = 10$ K/min from room temperature to 800 °C followed by an hour long isotherm (not shown) at the final temperature for m_{sample}= 21.896 mg of $\mathrm{Ti}_{0.70}\mathrm{V}_{0.30}\mathrm{H}_{\mathrm{x}}$.

By integrating the measured heat flow into the sample Φ_m from the desorption is initiated at time $t_{\xi=0}$ to it is complete at time $t_{\xi=1}$ one can furthermore determine the reaction enthalpy of desorption ΔH. In the present work the integration was performed in the Netzsch PROTEUS evaluation software. The determined enthalpies are however given in μVs/mg and a calibration constant C must be determined to convert these into the desired unit of J/mol. In the present configuration of the Netzsch STA 449 F3 Jupiter TG/DSC instrument such a calibration constant is however undetermined and therefore we can only compare the desorption enthalpies on a relative basis. For our purposes it is natural to choose the desorption enthalpy of the iron-free compound $\Delta H_{\mathrm{z=0}}$ as the reference value so that the property that can be compared is $\Delta H_{\mathrm{z}}/\Delta H_{\mathrm{z=0}}$ with z as the content of iron in the system $(\mathrm{Ti}_{0.70}\mathrm{V}_{0.30})_{1\text{-z}}\mathrm{Fe}_{\mathrm{z}}$. Thus qualitative considerations of the influence of iron on the desorption enthalpies can still be made.

When performing a Kissinger analysis the temperatures T_m must be extracted from the measured heat-flow signals. These are associated with peaks in the heat-flow. In certain cases these peaks might be overlapping, and the measured signal must in those cases be *deconvoluted* to extract the peak positions. This has in the present work been done using gaussian functions in the Fityk software [72]. Once the peaks are extracted a linear regression is performed and the activation energy can be obtained from the slope of the resultant line. The associated uncertainty is furthermore proportional to the uncertainty of the slope which has been determined through standard error analysis [73].

Chapter 4

Results and discussion

4.1 Sample preparation

Six samples of $(Ti_{0.70}V_{0.30})_{1\text{-}z}Fe_z$ one for each of the iron contents $z \in \{0, 0.03, 0.06, 0.10, 0.20, 0.30\}$ were initially prepared from -200 mesh powders of titanium and iron (Alfa Aesar, 99.5% purity; metal basis) and vanadium cut from a 0.5 mm thick sheet (Aldrich Chemistry 99.7% purity; metal basis) following the procedure outlined in subsection 3.2.1 with the Sartorius Extend ED124S balance. The measured masses can be found in table C.1 and the corresponding amount of moles are given in table C.2. Based upon these measurements the stoichiometric coefficients of the prepared samples were determined as indicated in table 4.1. Four batches of Zr_7Ni_{10} were also prepared from zirconium (ABCR, 99.5% purity; metal basis) and nickel (Goodfellow, 99.99% purity; metal basis) powders following the same procedure as for the $(Ti_{0.70}V_{0.30})_{1\text{-}z}Fe_z$ alloys albeit with the Mettler Toledo AG204 DeltaRange balance. The measured properties can be found in tables C.3 and C.4 and the corresponding stoiciometric relations are given in table 4.1. As annealing treatments seem to have little influence upon the pressure-composition isotherms of similar systems [49] [50] it was decided against exposing the samples to such treatments.

$\sim$ 1 g batches of the as-cast $(Ti_{0.70}V_{30})_{1\text{-}z}Fe_z$ were subsequently loaded into the Sieverts apparatus and exposed to the treatments outlined in table 4.2. The samples were activated through two consecutive cycles of dynamic vacuum and 20 bar H_2 gas at 350 °C. The samples were finally exposed to a 20 bar pressure of H_2 gas at room temperature before the resultant hydrides were loaded out of the Sieverts apparatus and into the glove-box where they were easily ground to a fine powder with an agate mortar and pestle. Since

Table 4.1: The stoichiometric coefficients y and z for the different samples $(\mathrm{Ti}_{1\text{-}y}\mathrm{V}_{y})_{1\text{-}z}\mathrm{Fe}_{z}$ and the measured number of moles of the elements present within the sample given in table C.2. The corresponding stoichiometric coefficient w = $\frac{n_{\mathrm{Zr}}}{n_{\mathrm{Ni}}}$ for the four prepared batches of $(\mathrm{Zr}_{w}\mathrm{Ni})_{10}$ that were determined from the measured amount of moles given in table C.4 are also shown.

Sample	Batch	y [$\emptyset$]	z [$\emptyset$]	w [$\emptyset$]
$\mathrm{Ti}_{0.70}\mathrm{V}_{0.30}$	#1	0.30014	-	-
		± 0.00010	-	-
$\mathrm{Ti}_{0.70}\mathrm{V}_{0.30}$	#2	0.30000	-	-
		± 0.00010	-	-
$(\mathrm{Ti}_{0.70}\mathrm{V}_{0.30})_{0.97}\mathrm{Fe}_{0.03}$	#1	0.29995	0.0300	-
		± 0.00010	± 0.0011	-
$(\mathrm{Ti}_{0.70}\mathrm{V}_{0.30})_{0.94}\mathrm{Fe}_{0.06}$	#1	0.29994	0.0601	-
		± 0.00010	± 0.0004	-
$(\mathrm{Ti}_{0.70}\mathrm{V}_{0.30})_{0.90}\mathrm{Fe}_{0.10}$	#1	0.30004	0.1000	-
		± 0.00011	± 0.0003	-
$(\mathrm{Ti}_{0.70}\mathrm{V}_{0.30})_{0.80}\mathrm{Fe}_{0.20}$	#1	0.29998	0.20002	-
		± 0.00017	± 0.00014	-
$(\mathrm{Ti}_{0.70}\mathrm{V}_{0.30})_{0.70}\mathrm{Fe}_{0.30}$	#1	0.30005	0.30006	-
		± 0.00018	± 0.00010	-
$\mathrm{Zr}_{7}\mathrm{Ni}_{10}$	#1	-	-	0.7013
		-	-	± 0.02
$\mathrm{Zr}_{7}\mathrm{Ni}_{10}$	#2	-	-	0.7009
		-	-	± 0.02
$\mathrm{Zr}_{7}\mathrm{Ni}_{10}$	#3	-	-	0.7015
		-	-	± 0.02
$\mathrm{Zr}_{7}\mathrm{Ni}_{10}$	#4	-	-	0.7014
		-	-	± 0.02

the as-cast materials were very ductile it was impossible to crush these directly into fine powders. The powdered alloys were therefore obtained from the powdered hydrides by subjecting these to an additional desorption in the Sieverts-apparatus under dynamic vacuum at 500 °C as outlined in table 4.3. The resultant powders were retrieved from the Sieverts-apparatus and loaded back into the glove-box for storage.

Preliminary phase identification of the respective materials were performed *ex-situ* on the Bruker AXS D8 Advance diffractometer at IFE. The data was collected as described in subsection 3.2.2 and the resultant PXD-patterns that were measured for the Ti-V(-Fe) alloys, hydrides and catalyst

Table 4.2: Conditions for hydrogenation in the Sieverts apparatus. Note that the logger was accidentally stopped for the measurement where the duration is marked by a question mark.

Sample	Treatment	Duration
$Ti_{0.70}V_{0.30}$	dyn. vac. at 350 °C	22.4 hrs
	20 bar H_2 at 350 °C	4.42 hrs
	dyn. vac. at 350 °C	18.1 hrs
	20 bar H_2 at 350 °C	7.09 hrs
	dyn. vac. at 350 °C	17.0 hrs
	20 bar H_2 at RT	5.55 hrs
$(Ti_{0.70}V_{0.30})_{0.97}Fe_{0.03}$	dyn. vac. at 350 °C	18.6 hrs
	20 bar H_2 at 350 °C	5.4 hrs
	dyn. vac. at 350 °C	18.2 hrs
	20 bar H_2 at 350 °C	5.67 hrs
	dyn. vac. at 350 °C	17.2 hrs
	20 bar H_2 at RT	1.87 +? hrs
$(Ti_{0.70}V_{0.30})_{0.94}Fe_{0.06}$	dyn. vac. at 350 °C	23.3 hrs
	20 bar H_2 at 350 °C	6.23 hrs
	dyn. vac. at 350 °C	16.2 hrs
	20 bar H_2 at 350 °C	8.02 hrs
	dyn. vac. at 350 °C	17.6 hrs
	20 bar H_2 at RT	5.82 hrs
$(Ti_{0.70}V_{0.30})_{0.90}Fe_{0.10}$	dyn. vac. at 350 °C	22.5 hrs
	20 bar H_2 at 350 °C	9.76 hrs
	dyn. vac. at 350 °C	17.6 hrs
	20 bar H_2 at 350 °C	6.27 hrs
	dyn. vac. at 350 °C	14.7 hrs
	20 bar H_2 at RT	7.23 hrs
$(Ti_{0.70}V_{0.30})_{0.80}Fe_{0.20}$	dyn. vac. at 350 °C	13.4 hrs
	20 bar H_2 at 350 °C	10.1 hrs
	dyn. vac. at 350 °C	14.0 hrs
	20 bar H_2 at 350 °C	11.3 hrs
	dyn. vac. at 350 °C	15.5 hrs
	20 bar H_2 at RT	5.72 hrs
$(Ti_{0.70}V_{0.30})_{0.70}Fe_{0.30}$	dyn. vac. at 350 °C	23.7 hrs
	20 bar H_2 at 350 °C	7.40 hrs
	dyn. vac. at 350 °C	15.9 hrs
	20 bar H_2 at 350 °C	6.87 hrs
	dyn. vac. at 350 °C	19.2 hrs
	20 bar H_2 at RT	3.95 hrs

Table 4.3: Conditions for dehydrogenation of hydrides in the Sieverts apparatus.

Sample	Treatment	Duration
$Ti_{0.70}V_{0.30}$	dyn. vac. at 500 °C	22.3 hrs
$(Ti_{0.70}V_{0.30})_{0.97}Fe_{0.03}$	dyn. vac. at 500 °C	21.4 hrs
$(Ti_{0.70}V_{0.30})_{0.94}Fe_{0.06}$	dyn. vac. at 500 °C	23.4 hrs
$(Ti_{0.70}V_{0.30})_{0.90}Fe_{0.10}$	dyn. vac. at 500 °C	19.3 hrs
$(Ti_{0.70}V_{0.30})_{0.80}Fe_{0.20}$	dyn. vac. at 500 °C	16.5 hrs
$(Ti_{0.70}V_{0.30})_{0.70}Fe_{0.30}$	dyn. vac. at 500 °C	22.1 hrs

materials are shown in figure 4.1, 4.2 and 4.3 respectively. From the PXD patterns of the alloys it was inferred through a PDF-search in the EVA software that the main phase is body-centred cubic regardless of the amount of iron z present in the alloy $(Ti_{0.70}V_{0.30})_{1\text{-}z}Fe_z$. There is however an observable hexagonal *impurity phase* present in all the alloys. Such an impurity phase has earlier been observed by numerous authors in similar systems and there exist some controversy in the literature concerning its nature. There has for instance been proposed that it might be

- an oxide.
- a solid solution of Ti and V [48].
- α-Ti that segregates out of the BCC phase matrices as the hydrogen free samples are obtained from the hydrides by degassing [47].

It should be noted that the hexagonal phase is hexagonal-closed packed for the alloys with an iron content $z \leq 0.20$ while it is Laves C14 for the system with $z = 0.30$. The phase composition discussed above were later confirmed through a Rietfeld refinement performed on the measured laboratory PXD patterns of the different samples. The results from these refinements can be found in appendix D.1.

It is interesting to observe that there is no trace of the hexagonal phase in the PXD patterns of the hydrides with iron content $z \leq 0.20$ which seem to be single phase structures at a first glance. An explanation can be posed for either proposition stated above as

- the oxide is mainly situated on the surface of the material and is reduced through interaction with hydrogen.
- the structure form a γ-Ti-like hydride that is hidden underneath the diffraction peaks of the main phase.

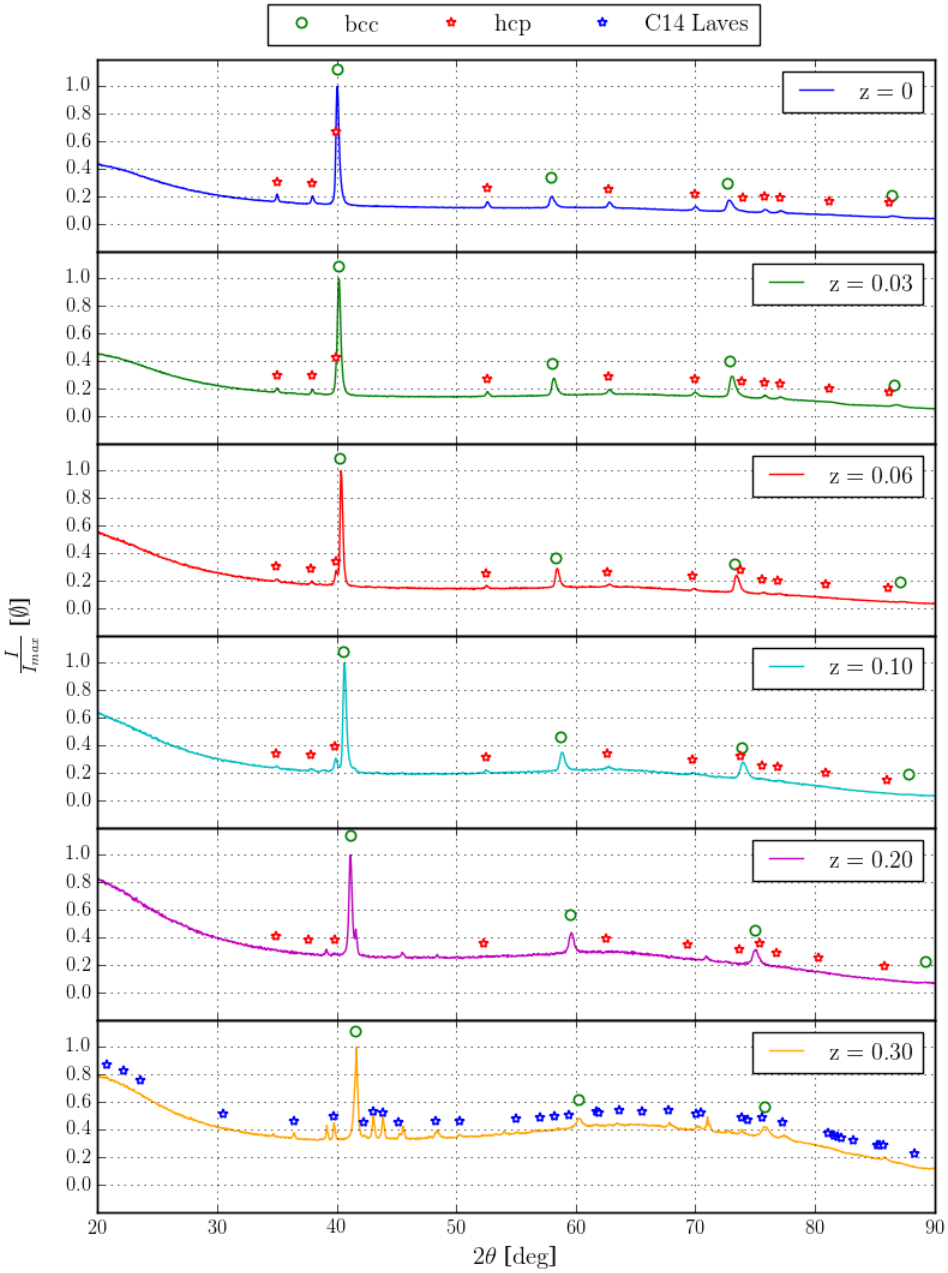

Figure 4.1: The normalized Cu-Kα PXD patterns of the $(\mathrm{Ti}_{0.70}\mathrm{V}_{0.30})_{1\text{-z}}\mathrm{Fe}_{\mathrm{z}}$ samples that was prepared following the procedure outlined in table 4.2. The patterns were measured on the Bruker AXS D8 Advance diffractometer at IFE with an X-ray wavelength of $\lambda = 1.5406$ Å.

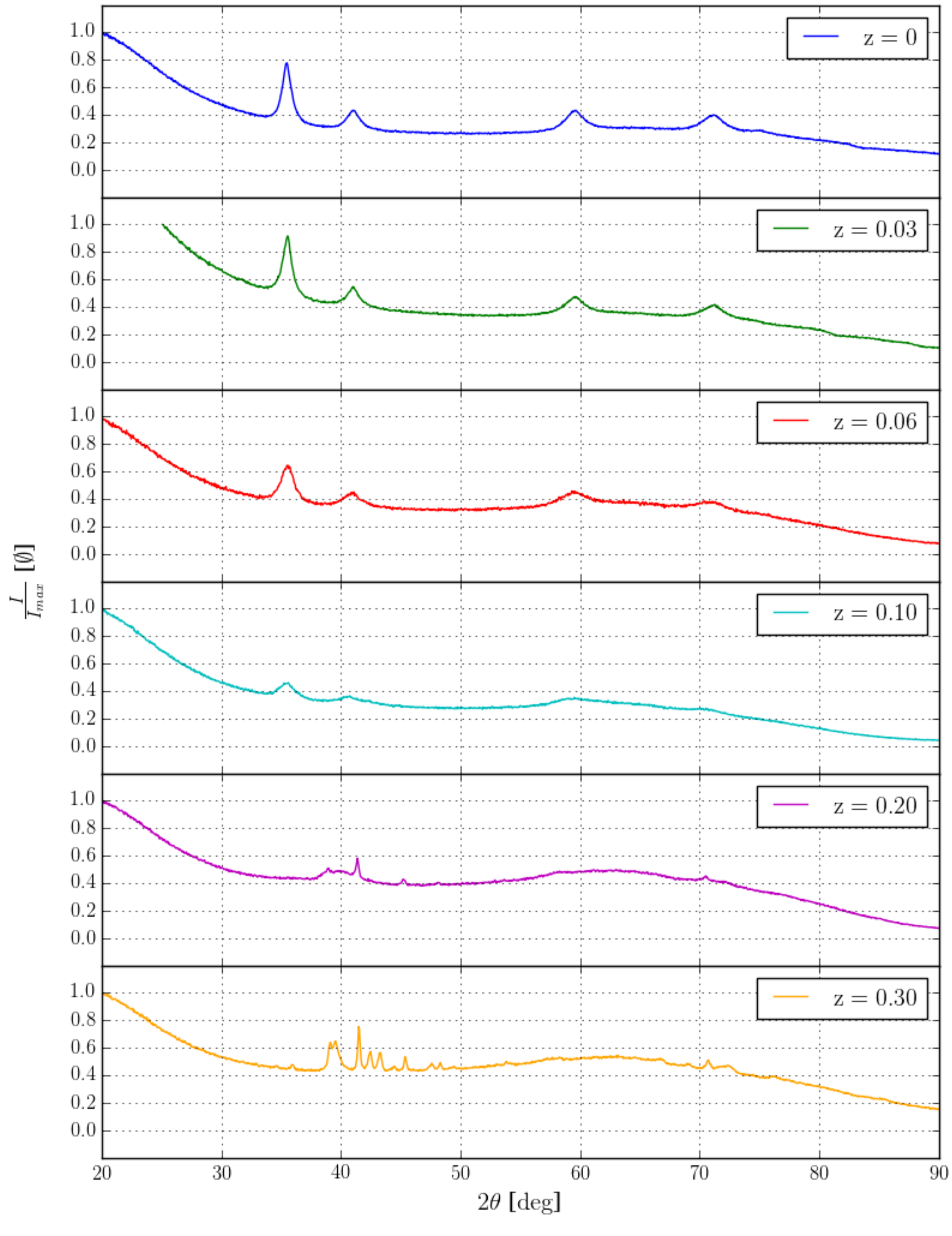

Figure 4.2: The normalized Cu-Kα PXD patterns of the $(Ti_{0.70}V_{0.30})_{1\text{-}z}Fe_zH_x$ samples that was prepared following the procedure outlined in table 4.2. The patterns were measured on the Bruker AXS D8 Advance diffractometer at IFE with an X-ray wavelength of $\lambda = 1.5406$ Å.

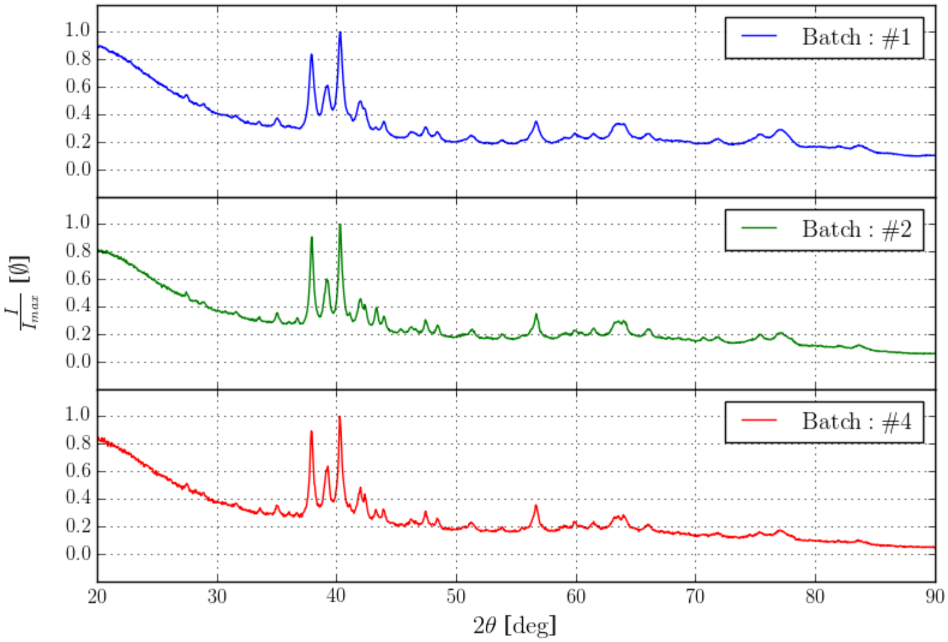

Figure 4.3: The normalized Cu-Kα PXD patterns of three batches of Zr_7Ni_{10} with the measured compositions shown in table 4.1. The patterns were measured on the Bruker AXS D8 Advance diffractometer at IFE with an X-ray wavelength of $\lambda = 1.5406$ Å.

- same as above.

For the samples having iron concentrations z = 0.20 and z = 0.30 the body-centred cubic phase of the alloy is however still present in the PXD patterns of the corresponding hydrides. This might indicate that the applied H_2 pressure during synthesis lies on or below the plateau pressure of the system, but it might also result from a reduction in the potential hydrogen storage capacity of the material. The diffraction peaks in the the hydride PXD patterns are quite broad which complicates the analysis of the material as it is demanding, especially for laboratory PXD measurements, to deduce what is hidden underneath such peaks. As it is expected that the systems with low concentrations of iron show a similar hydrogenation behaviour as that of the reference system $Ti_{0.70}V_{0.30}$ it is clear that we might expect the presence of twin boundaries and stacking faults. This is based upon the TEM study that was reported by Matsuda and Akiba [52]. The phase diagram in figure 2.12 do furthermore indicate that we should expect a two-phase region with a bcc and fcc hydride before the single phase fcc dihydride is formed. It is therefore possible that small amounts of the body-centred cubic hydride might be hidden underneath the broad peaks of the dihydride. It was however found through a Rietveld refinement performed on the laboratory PXD pattern of the $\mathrm{Ti_{0.70}V_{0.30}H_x}$ hydride that a reasonable fit could be achieved under the assumption that the structure is single phase face-centred cubic. The results of this analysis can be found in appendix D.2.

The composition of the as-cast $\mathrm{Ti_{0.70}V_{0.30}}$, $\mathrm{(Ti_{0.70}V_{0.30})_{0.90}Fe_{0.10}}$ and $\mathrm{(Ti_{0.70}V_{0.30})_{0.70}Fe_{0.30}}$ systems were furthermore investigated through EDX analyses performed on the SEM micrographs depicted in figure 4.4. From this figure it can be seen that the composition of the alloys are close to the nominal composition. It is however observed that some contaminating Al seem to be present in the $\mathrm{Ti_{0.70}V_{0.30}}$ system and that certain oxygen-rich areas are found on the surface of the investigated $\mathrm{(Ti_{0.70}V_{0.30})_{0.90}Fe_{0.10}}$ particle[1]. The Al signal might be due to the block the samples were mounted on during the analysis while the latter observation is expected considering that the samples were exposed to air as they were loaded into the scanning electron microscope.

Several EDX analyses were also undertaken for the second batch of prepared $\mathrm{Zr_7Ni_{10}}$ of which one measurement is shown in figure 4.5. The analysis seem to indicate that there is a slight surplus of Zr in the sample and since the other measurements yield similar results they have been omitted from the figure. It must however be kept in mind that such EDX analyses are only able to give a rough indication of the sample composition as the limited penetrability of the electrons only enable the parts of the sample in vicinity of the surface to be probed. Furthermore only selective parts of the sample are actually studied and hence there is no guarantee that the observed result is representable for the sample as a whole. It is however reassuring that no other element than Zr and Ni are observed in the analysis. From the SEM micrographs of figure 4.5 it seems to be a distribution of particle sizes with characteristic lengths ranging from about 1 μm to 70 μm. It is furthermore clear that the characteristic lengths lie mostly in the large part of this range.

The size and shape of the crystallites constituting the metal powders were investigated in the set of SEM micrographs shown in figure 4.6. The distribution in particle sizes range from smaller than 1 μm to about 60 μm and their morphology seem arbitrary and do not seem to vary with the iron

---

[1] This was observed in the area marked 2 in the SEM micrograph of the as-cast $\mathrm{(Ti_{0.70}V_{0.30})_{0.90}Fe_{0.10}}$ particle. The EDX analysis of this area has been omitted from the figure for brevity.

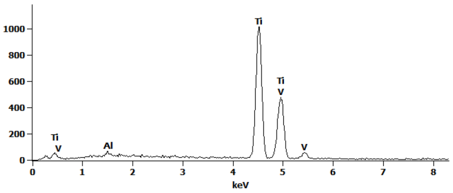

	Al	Ti	V
wt.%	0.60	68.67	30.73
	±0.08	±0.86	±0.55
at.%	1.08	69.62	29.30
	±0.14	±0.87	±0.53

(a)

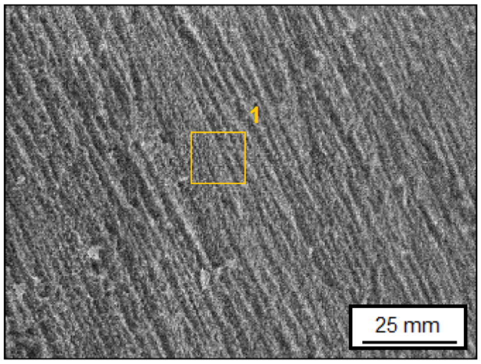

(b)

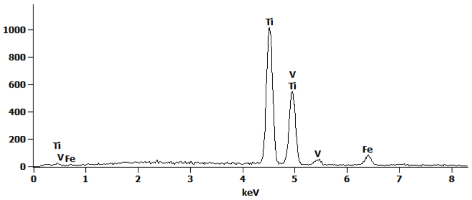

	Ti	V	Fe
wt.%	60.69	29.03	10.27
	±0.80	±0.72	±0.46
at.%	62.70	28.20	9.10
	±0.83	±0.70	±0.41

(c)

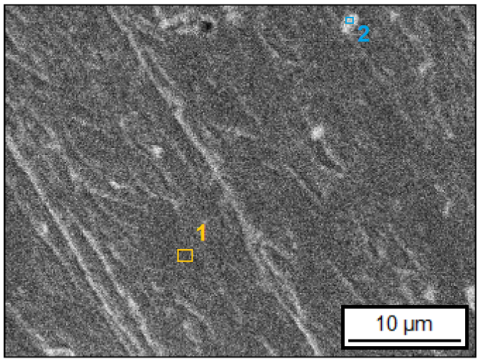

(d)

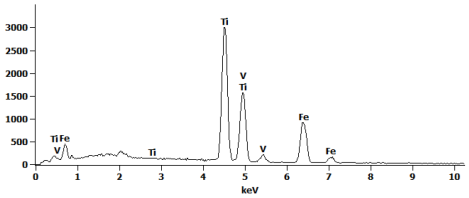

	Ti	V	Fe
wt.%	47.21	21.83	30.96
	±0.38	±0.34	±1.30
at.%	50.07	21.77	28.16
	±0.40	±0.34	±1.18

(e)

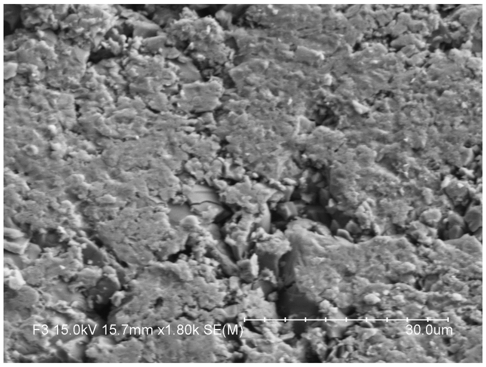

(f)

Figure 4.4: EDX analyses of the areas marked 1 in the SEM micrographs of the surface of a large as-cast particle of $Ti_{0.70}V_{0.30}$ (a)+(b), $(Ti_{0.70}V_{0.30})_{0.90}Fe_{0.10}$ (c)+(d) and $(Ti_{0.70}V_{0.30})_{0.70}Fe_{0.30}$ (e)+(f).

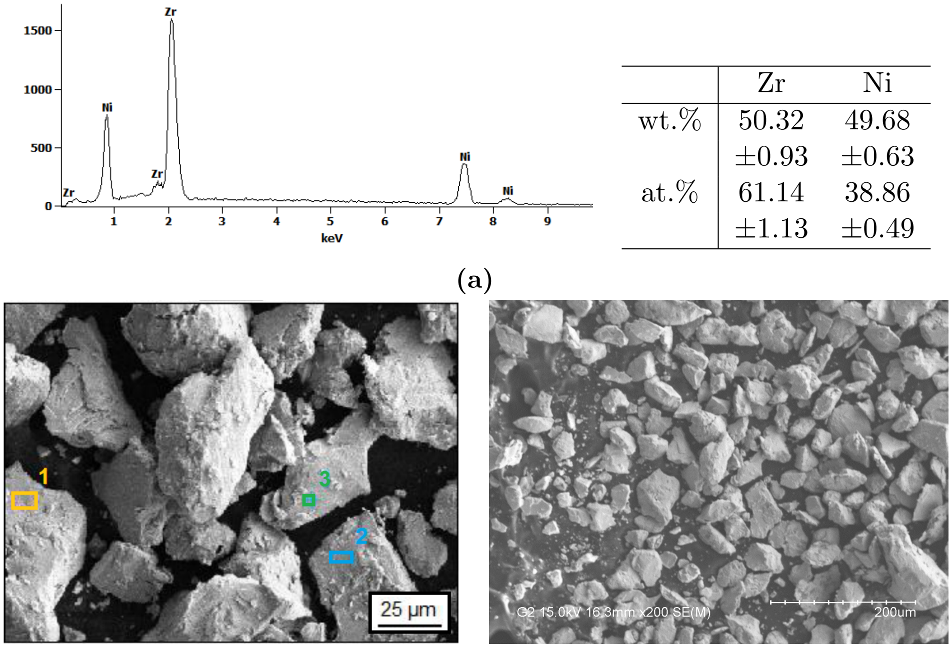

	Zr	Ni
wt.%	50.32	49.68
	±0.93	±0.63
at.%	61.14	38.86
	±1.13	±0.49

(a)

(b) (c)

Figure 4.5: EDX analysis (a) of the area marked 1 in the SEM micrograph (b) of the surface of a powdered particle of Zr_7Ni_{10}. The particle size distribution is shown in the SEM micrograph (c).

content. It is however clear that the majority of alloy particles are smaller than the general Zr_7Ni_{10} particles displayed in figure 4.5.

The obtained alloy and hydride powders were finally ball-milled with 5wt.% of Zr_7Ni_{10} from the second batch that was prepared. The milling was performed as described in subsection 3.2.1 with 7 tempered steel balls for 1 hour and at a rotational speed of 360 rpm. The mass of the samples were measured both before and after the milling and the obtained results can be found in table C.5. From this table it should also be noted that the amount of catalyst that was added to the samples were below the measurement uncertainty of the balance and therefore the exact amount of catalyst present in the ball-milled products are very uncertain.

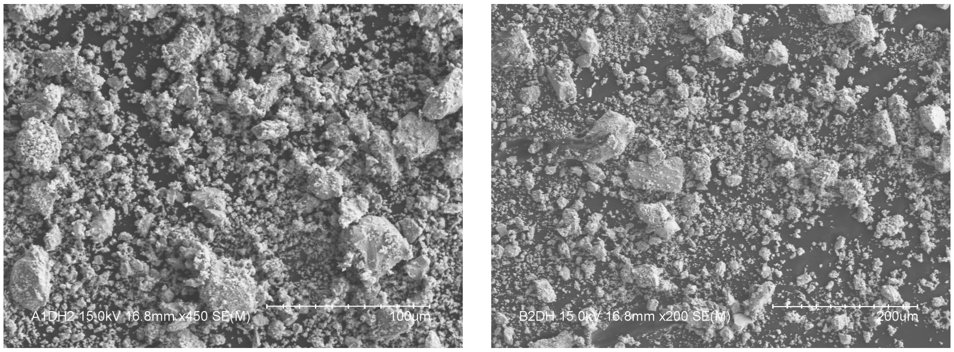

(a) z = 0 **(b)** z = 0.03

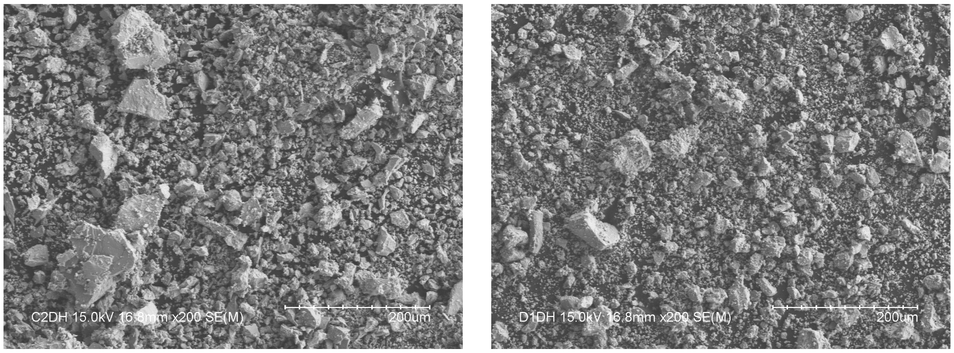

(c) z = 0.06 **(d)** z = 0.10

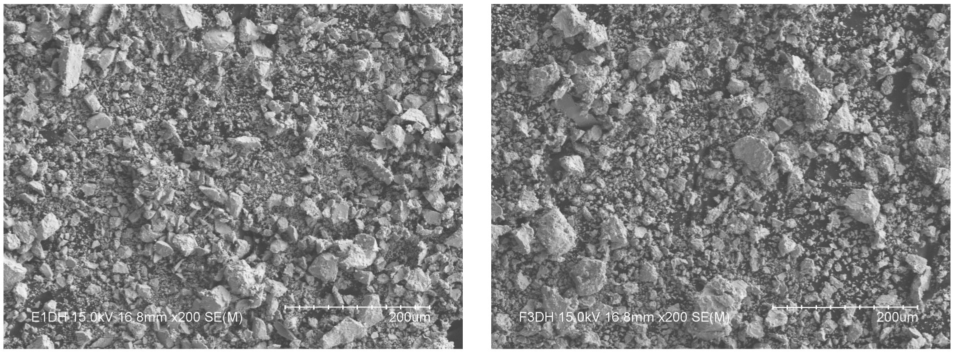

(e) z = 0.20 **(f)** z = 0.30

Figure 4.6: SEM micrographs of the powdered $(Ti_{0.70}V_{0.30})_{1\text{-}z}Fe_z$ samples that was prepared as described in table 4.3. Notice that the magnification is twice as large as the other micrographs in micrograph (a).

4.2 Ex-situ SR-PXD structural analysis

Measurements conducted following the strategy outlined in subsection 3.2.2 at SNBL enabled a more extensive analysis to be performed. The measured SR-PXD patterns of the alloy materials and the hydrides are shown in figure 4.7 and 4.8 respectively. From these measurements it was readily found through a PDF-search in the EVA software that another fcc phase is present in the two systems with the highest content of iron $z = 0.20$ and $z = 0.30$ in addition to the bcc and hexagonal structures that were observed in the preliminary phase identification. This fcc phase seem to be the oxide Ti_4Fe_2O which is consistent with the fact that the phase is also present in the corresponding hydrides. The presence of this oxide in the two most iron-rich systems indicate that we should not be surprised if oxides have formed on the other alloys as well since the samples were handled similarly. There are several possible sources for such a contamination such as leakage into the arc-melter, Sieverts apparatus or glove-box. Some oxides might even have been present in the starting materials. Apart from these possible sources the materials were exposed directly to air during synthesis. Oxides does however tend to reside in nm thick layers on the surface of titanium-rich compounds impeding detection through X-ray diffraction. Following this line of reasoning the hypothesis of the hexagonal-close packed impurity phase being an oxide seem to weaken. This could be verified through transmission-electron microscopy which is beyond the scope of this work.

The SR-PXD patterns of the alloy materials were subsequently analysed by Rietveld refinement to accurately determine the lattice parameters of the different phases. The refinement results and obtained fits are rendered in appendix D.5 and the lattice parameter variation as a function of the amount of iron present in the alloy z is shown in figure 4.9 for the bcc and hcp phases. From this figure it is clear that the lattice parameter of the bcc phase, a_{BCC}, decrease linearly with increasing amount of iron present in the alloy. This is similar to what was observed for the vanadium-rich part of the $(\mathrm{Ti}_{1\text{-}y}\mathrm{V}_y)_{1\text{-}z}\mathrm{Fe}_z$ alloy by Lynch et al. [50] and for the titanium-rich Ti-V-Cr system by Suwarno et al. [54]. It should also be observed that the lattice parameters of the hexagonal-close-packed structure, a_{hcp} and c_{hcp}, varies with the concentration of iron and that there is a significant difference between these and the α-Ti lattice parameters $a_{\alpha\text{-Ti}}$ and $c_{\alpha\text{-Ti}}$ even for the system with no iron present in the alloy. This exclude the possibility of the impurity phase being α-Ti that has segregated out of the bcc phase which leave the hypothesis that the hexagonal close-packed structure is a solid solution of Ti, V and Fe as the most likely candidate.

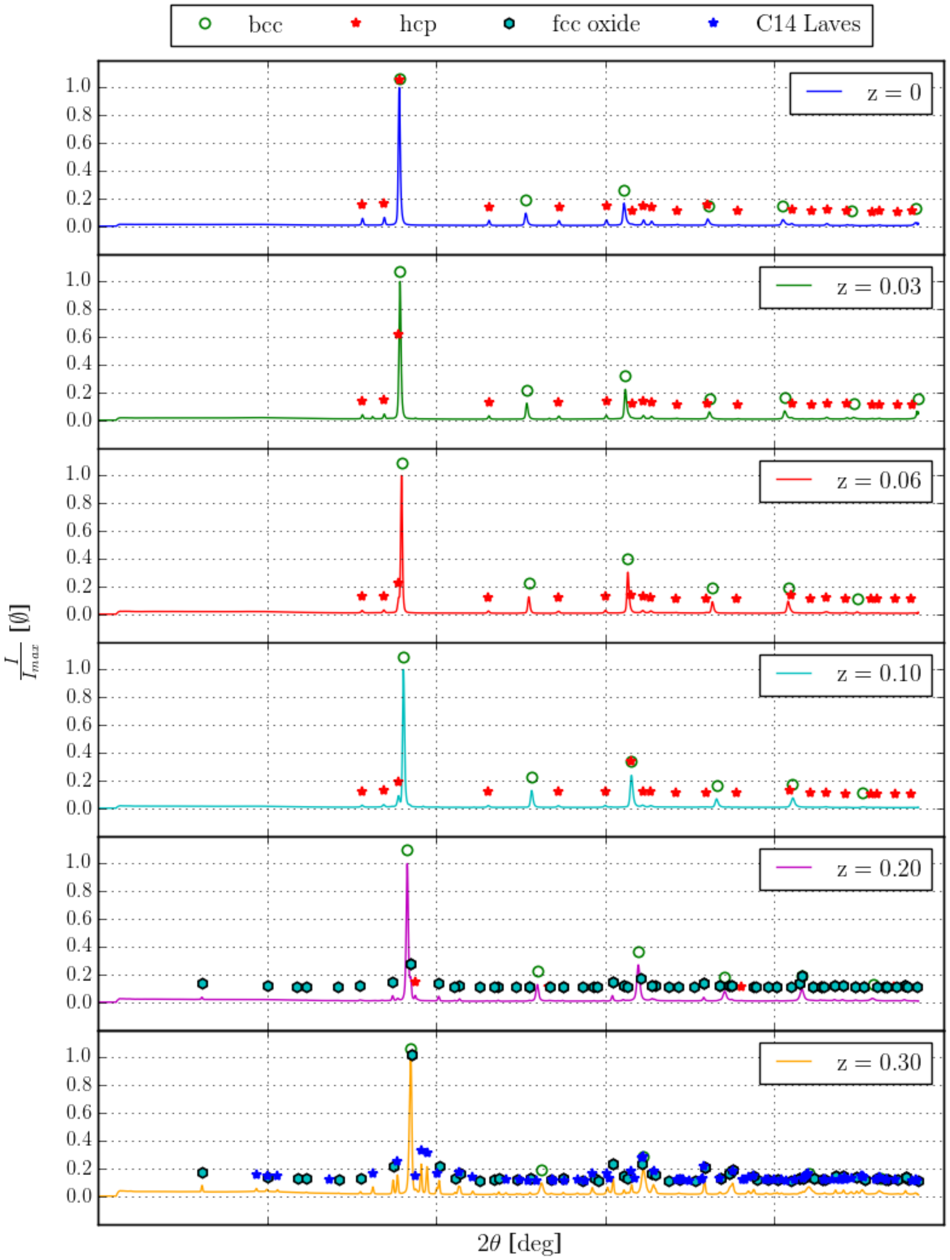

Figure 4.7: The normalized SR-PXD patterns of the $(Ti_{0.70}V_{0.30})_{1\text{-}z}Fe_z$ samples that was prepared following the procedure outlined in table 4.3. $\lambda = 0.6973$ Å

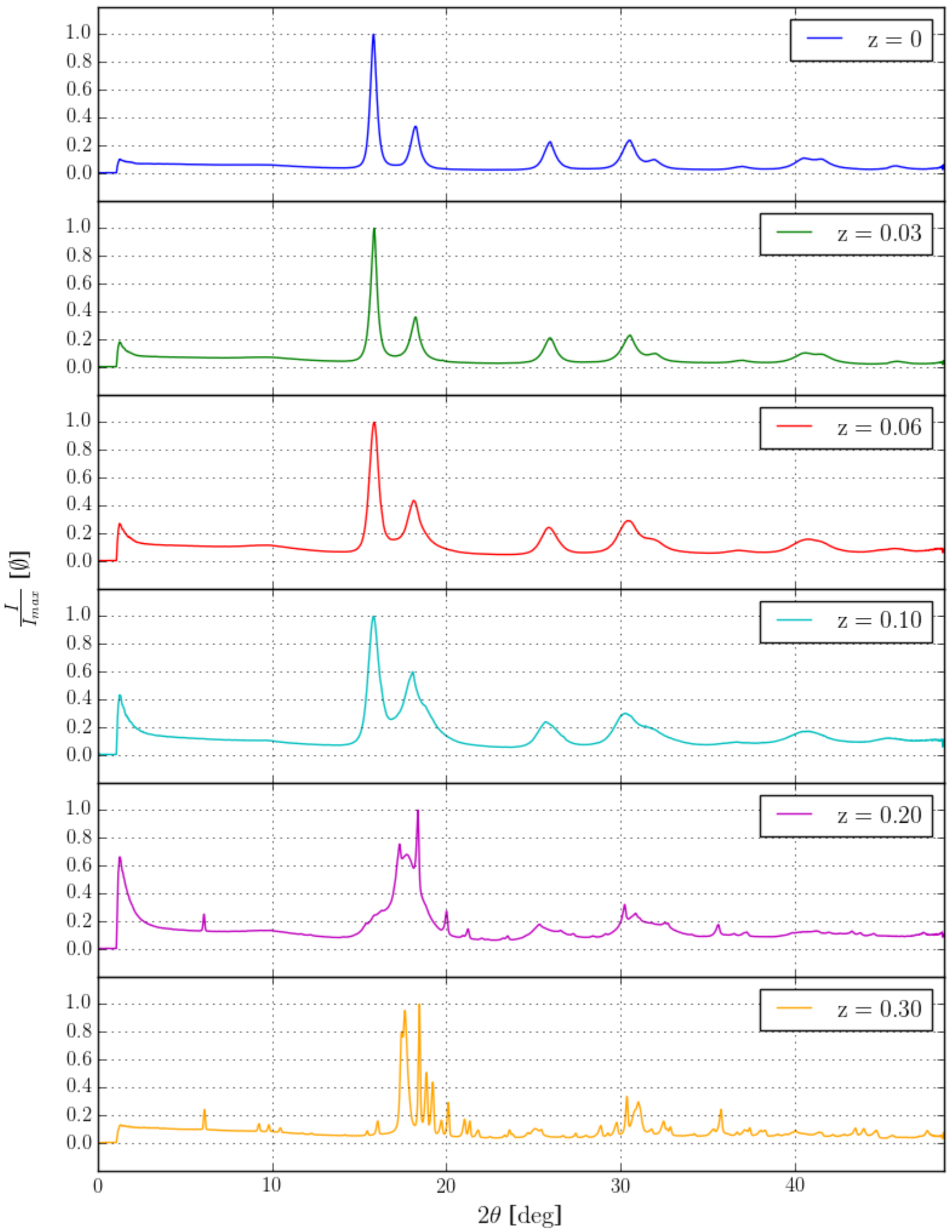

Figure 4.8: The normalized SR-PXD patterns of the $(Ti_{0.70}V_{0.30})_{1\text{-}z}Fe_zH_x$ samples that was prepared following the procedure outlined in table 4.2. $\lambda = 0.6973$ Å.

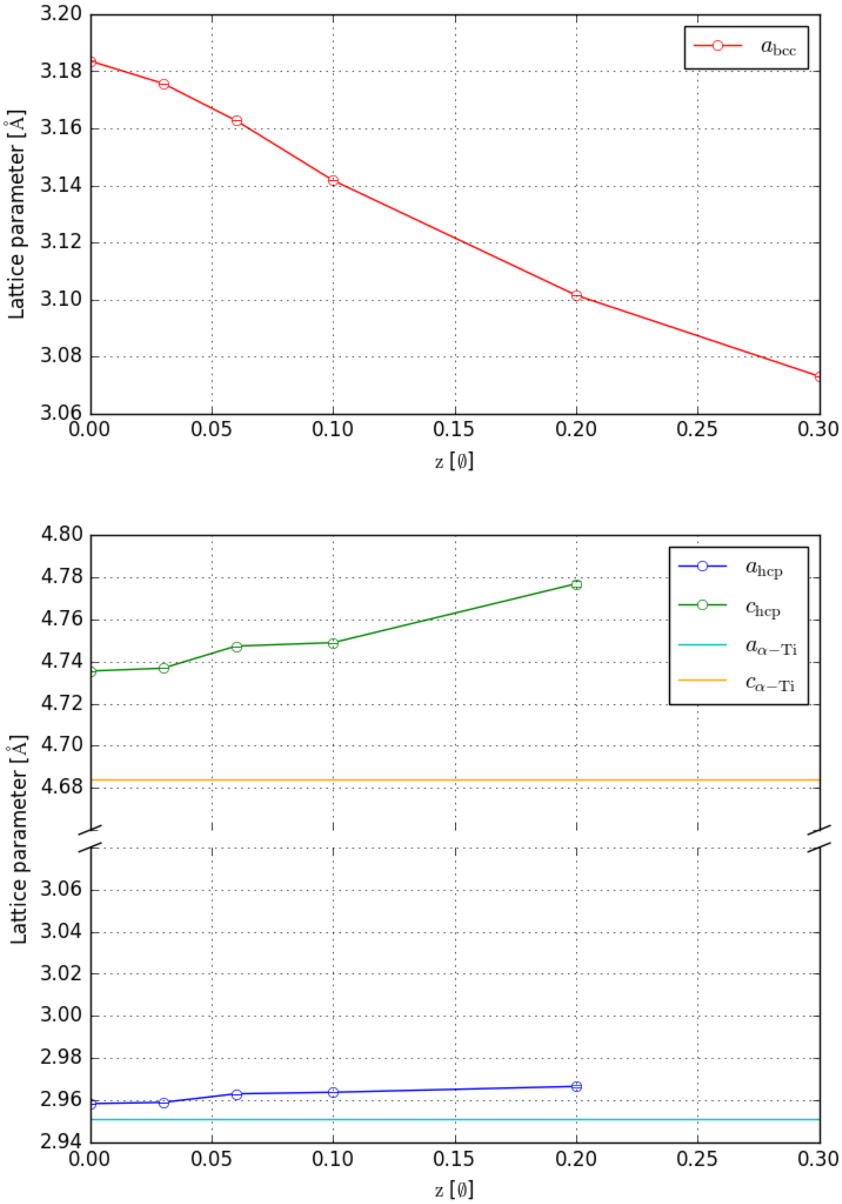

Figure 4.9: The lattice parameters for the BCC phase, a_{bcc}, and the HCP phase, a_{hcp} and c_{hcp}, as a function of the iron content z present in the alloy $(\mathrm{Ti}_{0.70}\mathrm{V}_{0.30})_{1\text{-}z}\mathrm{Fe}_{z}$. The lattice parameters of pure α-Ti from table 2.2 are displayed for comparison in the latter figure. The numerical values of the different lattice parameters were determined by Rietveld refinement on the collected SR-PXD patterns shown in figure 4.7. It should be noted that the vertical axis of the lower figure is broken to render the detailed variation of the lattice parameters more clearly.

Several attempts were made to perform a structural refinement of the hydride $\mathrm{Ti_{0.70}V_{0.30}H_x}$ with different plausible phases present in the model. The observed deviation between the measured intensity I_{meas} and the calculated intensity I_{calc} are shown for several solution candidates in figure 4.10 alongside the background $I_{background}$ and the measured SR-PXD pattern. The statistical parameters R_p, ${}_wR_p$ and χ^2 of the Rietveld refinement are somewhat improved with increasing number of parameters in the model but it is still clear from the difference plots that the models do not fully describe the SR-PXD pattern. Similar analyses were performed on the $\mathrm{(Ti_{0.70}V_{0.30})_{1\text{-}z}Fe_zH_x}$ systems with $\mathrm{z} \in \{0.03, 0.06, 0.10\}$ and as can be seen from figure D.20 and D.21 we observe similar deviations from the measured intensities for the $\mathrm{z} = 0.03$ and $\mathrm{z} = 0.06$. For the $\mathrm{z} = 0.10$ system it is apparent from figure 4.11 that the simplest models give a very poor fit to the measured intensities. For the two final systems; a body-centred cubic hydride is furthermore visible in the diffraction pattern. In fact no other hydride can be observed for the most iron rich system which also lack the characteristic broadening of the diffraction peaks that is present in the other hydrides. The Laves C14 phase is however still present.

The structural problem of $\mathrm{Ti_{0.70}V_{0.30}}$ treated in figure 4.10 is most readily observed in the first two peaks having Miller-indices (111) and (200). From the intensity deviations it seems that the measured (111) peak is slightly shifted towards a higher scattering angle than what is suggested by the calculated profiles while the (200) peak seem to be shifted in the opposite direction. According to Warren [74] such deviations are exactly what one would observe for face-centred cubic structures[2] with stacking faults which has later been verified through a series of computer simulations [76]. It is furthermore discussed by Balogh et al. [77] that such planar defects might cause the diffraction peaks to take on asymmetric and broadened profiles. Similar observations were also made in the TEM analysis conducted by Matsuda and Akiba for the $\mathrm{Ti_{1\text{-}y}V_y}$ hydrides [52]. Hence planar defects seem to explain the difficulties that were encountered during the structural refinement of the synthesised hydrides. As the deviations from an undistorted face-centred cubic profile increase with increasing amounts of iron present in the alloy it seems that the iron has an aggravating effect on the planar defects and eventually the *face-centred cubic related* phase is unable to form for the most iron rich compound. A Rietveld refinement performed on this latter hydride revealed that the unit-cell volume of the Laves C14 phase

---

[2] According to Dupraz et al. [75] this is a *fairly common* problem encountered in face-centred cubic metals.

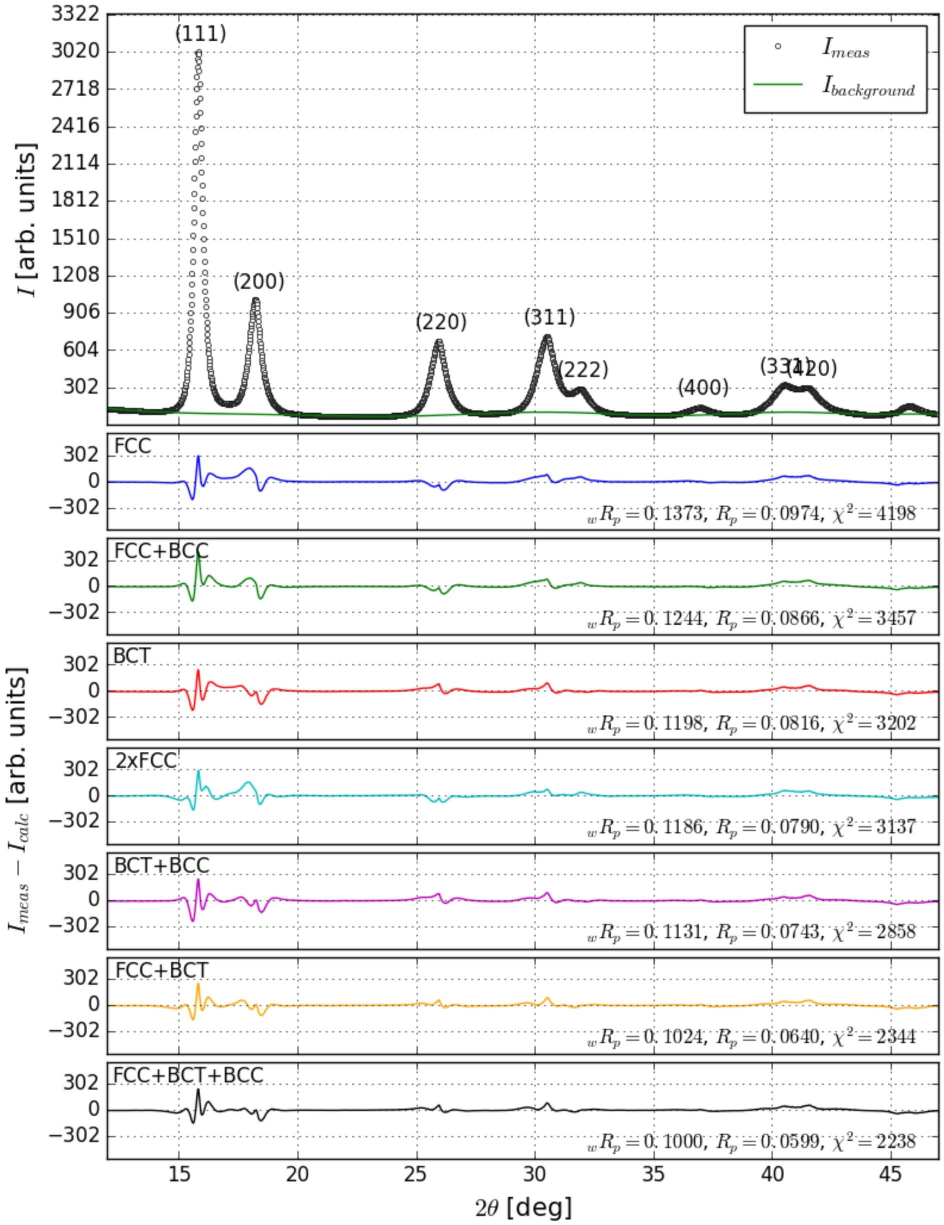

Figure 4.10: The measured SR-PXD pattern of the hydride $\mathrm{Ti}_{0.70}\mathrm{V}_{0.30}\mathrm{H}_{\mathrm{x}}$ that was synthesised following the procedure outlined in table 4.2 shown alongside the background $I_{background}$ and the intensity deviation $I_{meas} - I_{calc}$ between the measured scattering intensity I_{meas} and the calculated intensity I_{calc} determined through Rietveld refinement for several different solution candidates. The statistical parameters R_p, $_wR_p$ and χ^2 of the refinements are indicated.

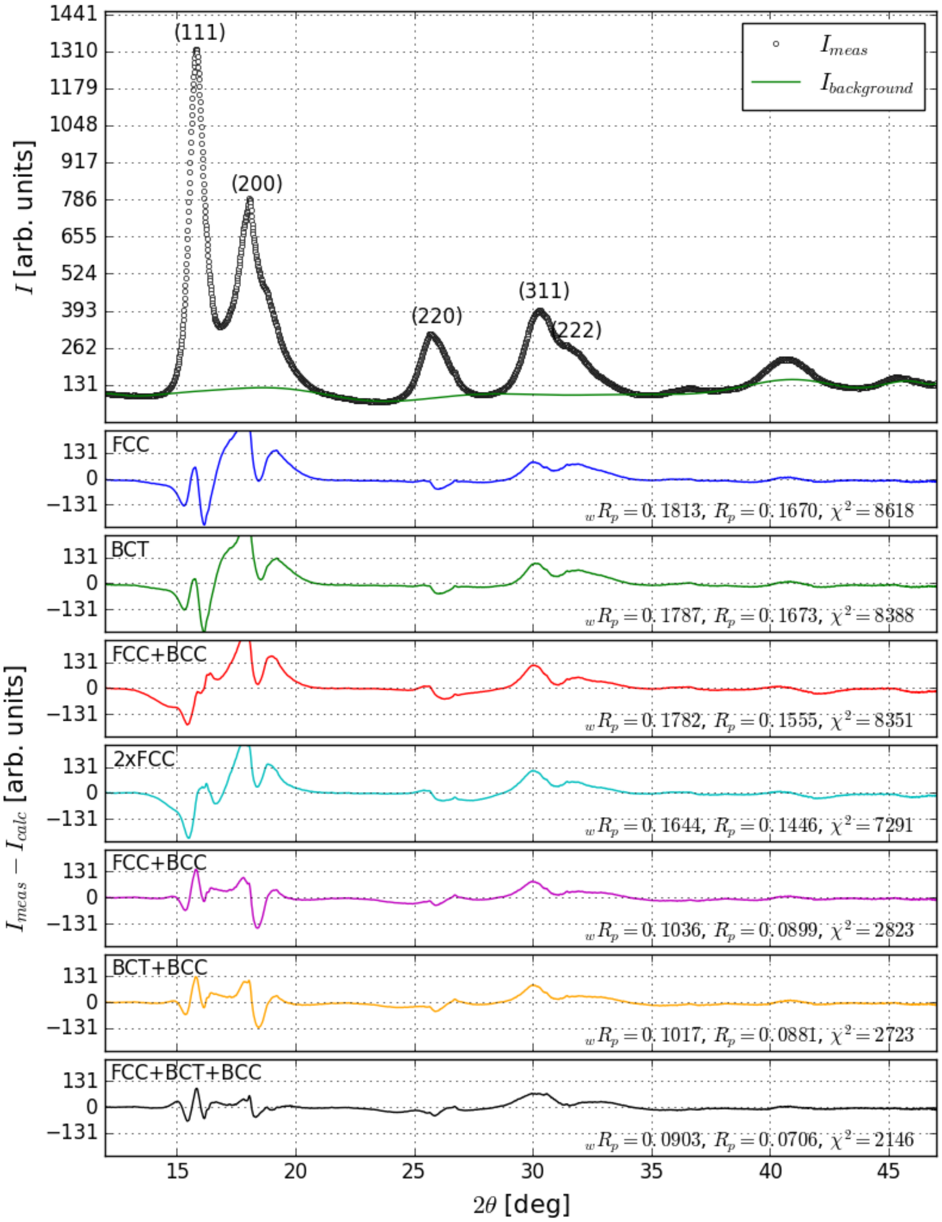

Figure 4.11: The measured SR-PXD pattern of the hydride $(Ti_{0.70}V_{0.30})_{0.90}Fe_{0.10}H_x$ that was synthesised following the procedure outlined in table 4.2 shown alongside the background $I_{background}$ and the intensity deviation $I_{meas} - I_{calc}$ between the measured scattering intensity I_{meas} and the calculated intensity I_{calc} determined through Rietveld refinement for several different solution candidates. The statistical parameters R_p, $_wR_p$ and χ^2 of the refinements are indicated.

increased during hydrogenation indicating the accommodation of hydrogen within the structure. It was also observed that the unit cell of the face-centred cubic phase assumed to be the oxide Ti_4Fe_2O also expanded. A similar observation was made for the $(Ti_{0.70}V_{0.30})_{0.80}Fe_{0.20}H_x$ hydride.

A Rietveld refinement was also performed on the SR-PXD pattern of Zr_7Ni_{10} from the batch that was ball-milled with the different samples. The refinement is shown in figure 4.12 and it is clear that a small fraction of an unidentified impurity phase is present. The bulk of the catalyst does however seem to possess the desired phase which is reassuring considering the excess of Zr that was indicated by the EDX analyses discussed in the prior section. SR-PXD patterns were finally measured of the ball-milled alloys and hydrides to verify the presence of the added catalyst in the final powders. The $2\theta \in [10°, 30°]$ region of the results are given in figures 4.13 and 4.14 for the alloys and hydride materials respectively. In these figures the measured pat-

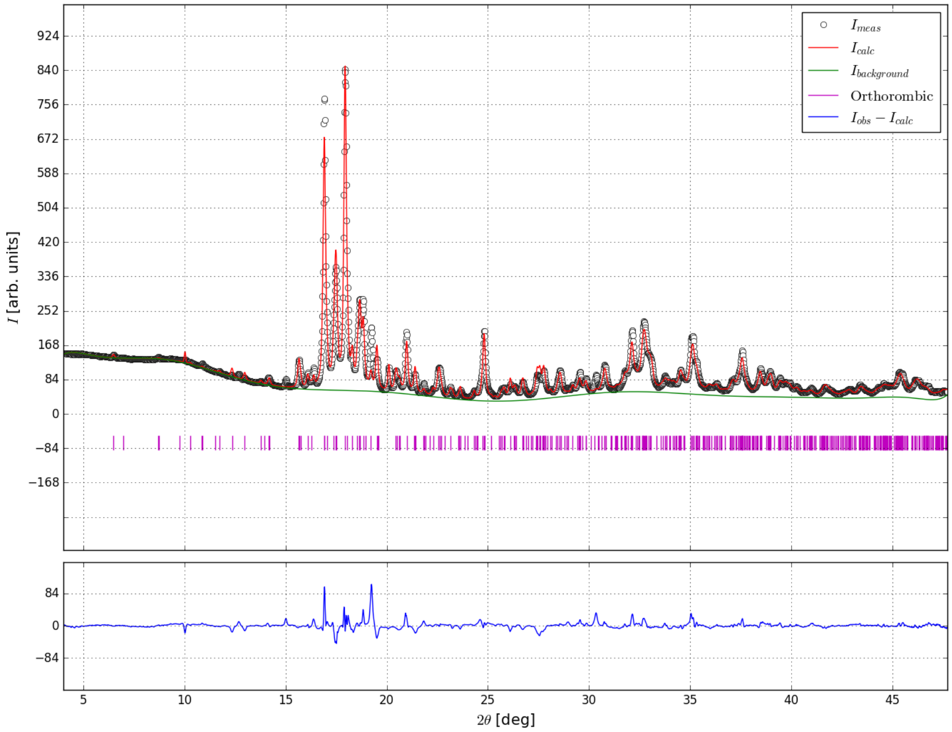

Figure 4.12: Rietveld refinement on the SR-PXD pattern of the second batch of prepared Zr_7Ni_{10} that were subsequently ball-milled together with the different alloys and hydrides. $\lambda = 0.6973$ Å.

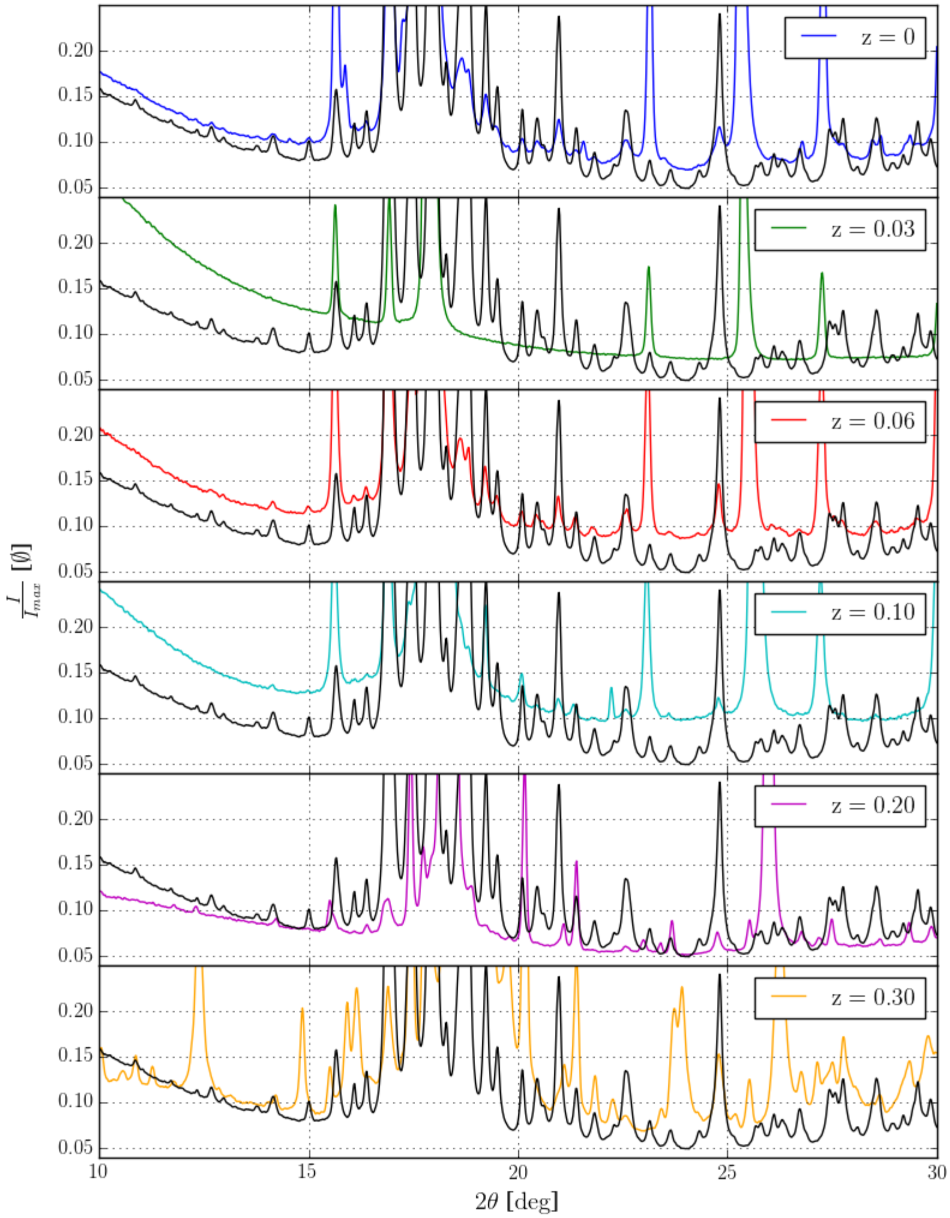

Figure 4.13: SR-PXD patterns of the $(Ti_{0.70}V_{0.30})_{1\text{-}z}Fe_z$ + 5wt.% Zr_7Ni_{10} samples. The data has been normalized to the corresponding SR-PXD pattern of Zr_7Ni_{10} that is shown for comparison as the solid black line. $\lambda = 0.6973$ Å.

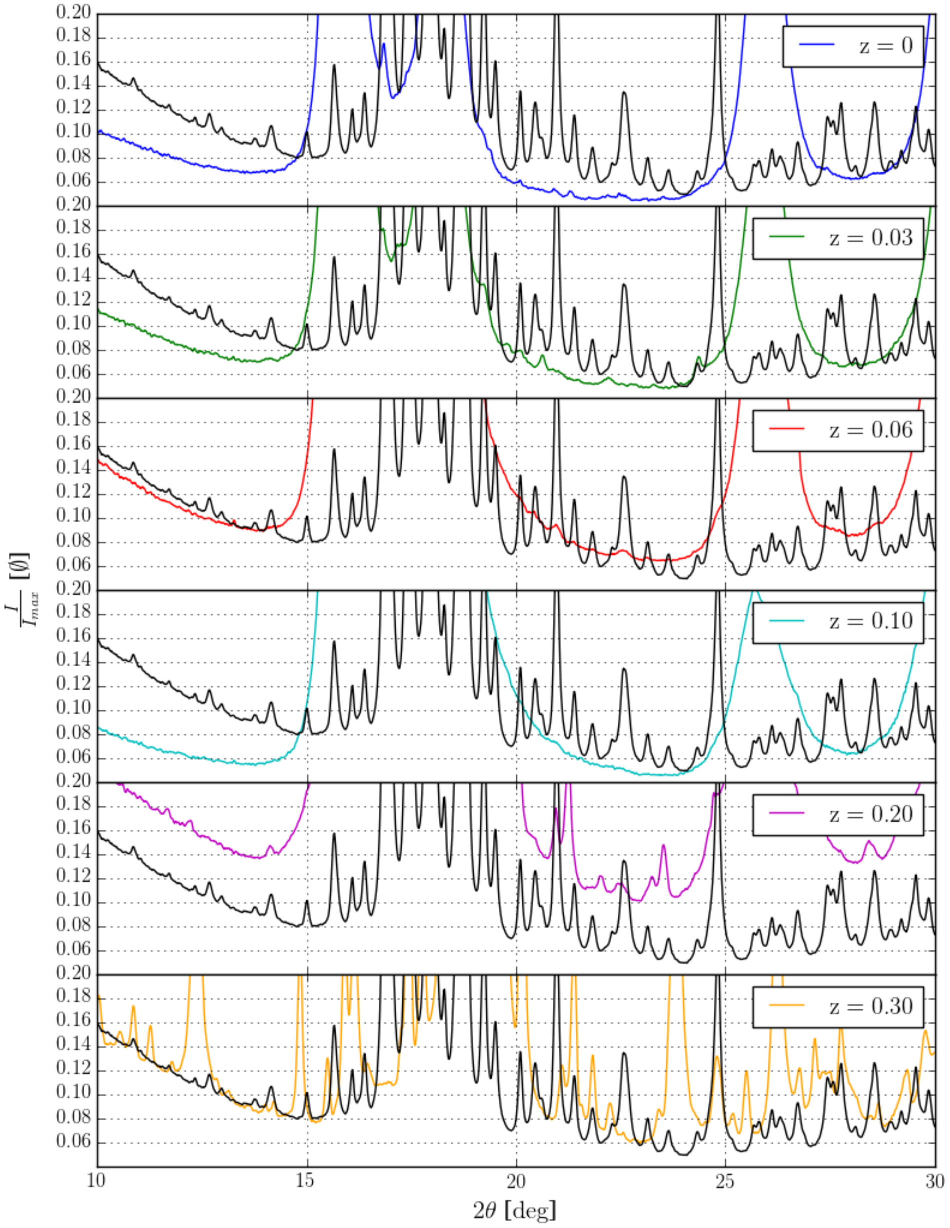

Figure 4.14: SR-PXD patterns of the $(Ti_{0.70}V_{0.30})_{1\text{-}z}Fe_zH_x$ + 5wt.% Zr_7Ni_{10} samples. The data has been normalized to the corresponding SR-PXD pattern of Zr_7Ni_{10} that is shown for comparison as the solid black line. $\lambda = 0.6973$ Å.

terns have been normalized to the maximum intensity observed in the measured SR-PXD pattern of Zr_7Ni_{10} to facilitate the comparison between the catalyst and the ball-milled samples. The Zr_7Ni_{10} can be readily observed in certain measurements like that of $(Ti_{0.70}V_{0.30})_{0.94}Fe_{0.06}$ and $Ti_{0.70}V_{0.30}H_x$ while it is apparently absent in others like that of $(Ti_{0.70}V_{0.30})_{0.97}Fe_{0.03}$. Furthermore only a selected few Zr_7Ni_{10} peaks are observed. The final issue might indicate certain preferred orientations of the Zr_7Ni_{10} crystallites inside the borosilicate glass capillaries when the measurements were conducted. This is plausible as the average catalyst-crystallite is larger than the average sorbent or hydride particle as indicated in the SEM micrographs of the prior section. It should be stressed that the added amount of catalyst is very low and hence there is no guarantee that significant amounts are exposed to the 400 μm broad region that is probed by the X-ray beam to yield a sufficiently intense signal in the SR-PXD pattern.

4.3 In-situ SR-PXD structural analysis

The structural transformation of selected systems during hydrogen sorption were studied through *in-situ* SR-PXD at SNBL. The experiments were prepared as outlined in subsection 3.2.2 and the observed phases throughout the sorption processes are presented in table 4.4 where they are associated with distinct labels.

Table 4.4: The different phases that are observed in the sorption processes studied bt *in-situ* SR-PXD at SNBL. The phases are associated with distinct labels and the corresponding space groups are also shown.

Label	Phase	Space group
α	body-centred cubic alloy	$Im\bar{3}m$
β	body-centred cubic hydride	$Im\bar{3}m$
β'	body-centred cubic hydride	$Im\bar{3}m$
γ	face-centred cubic related hydride	$Fm\bar{3}m$
δ	hexagonal-close packed alloy	$P6_3/mmc$
ϵ	face-centred cubic hydride	$Fm\bar{3}m$

Figure 4.15 show an *in-situ* SR-PXD measurement conducted during desorption of hydrogen from the $(Ti_{0.70}V_{0.30})_{0.97}Fe_{0.03}H_x$ system under dynamic vacuum. From the figure it is readily visible that the intensity in the high scattering angle regime diminish as the temperature is increased. This is due to the blower that upon heating expands thermally to partially cover

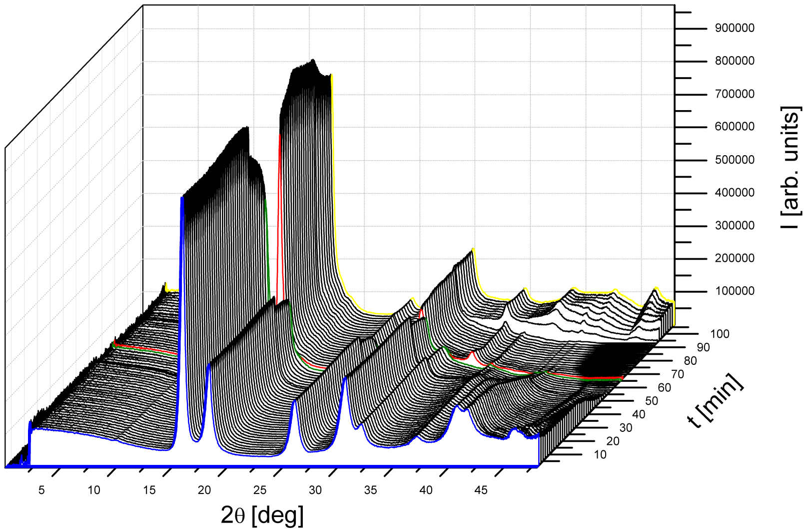

(a)

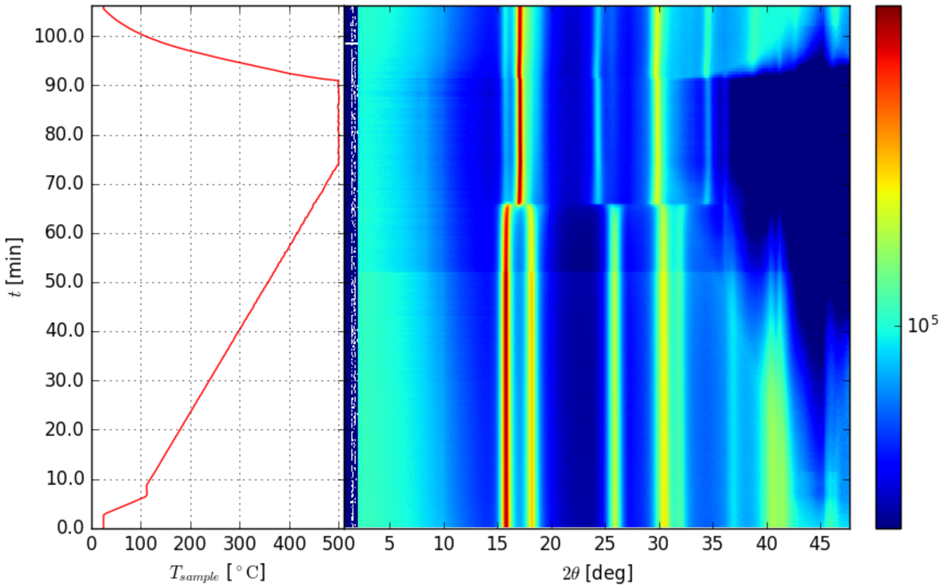

(b)

Figure 4.15: *In-situ* SR-PXD during desorption of hydrogen from $(Ti_{0.70}V_{0.30})_{0.97}Fe_{0.03}H_x$ visualized by a waterfall diagram (a) and a contour plot for which the colorbar yield the logarithmic intensity (b). The known phases are indicated for four selected measurements (c) that is also marked in the waterfall diagram. The heating rate was set to 20 K/min in the first heating segment while it was changed to 5 K/min in the second. The temperature of the sample T_{sample} was determined from the measured temperatures through the calibration curve displayed in figure B.2.

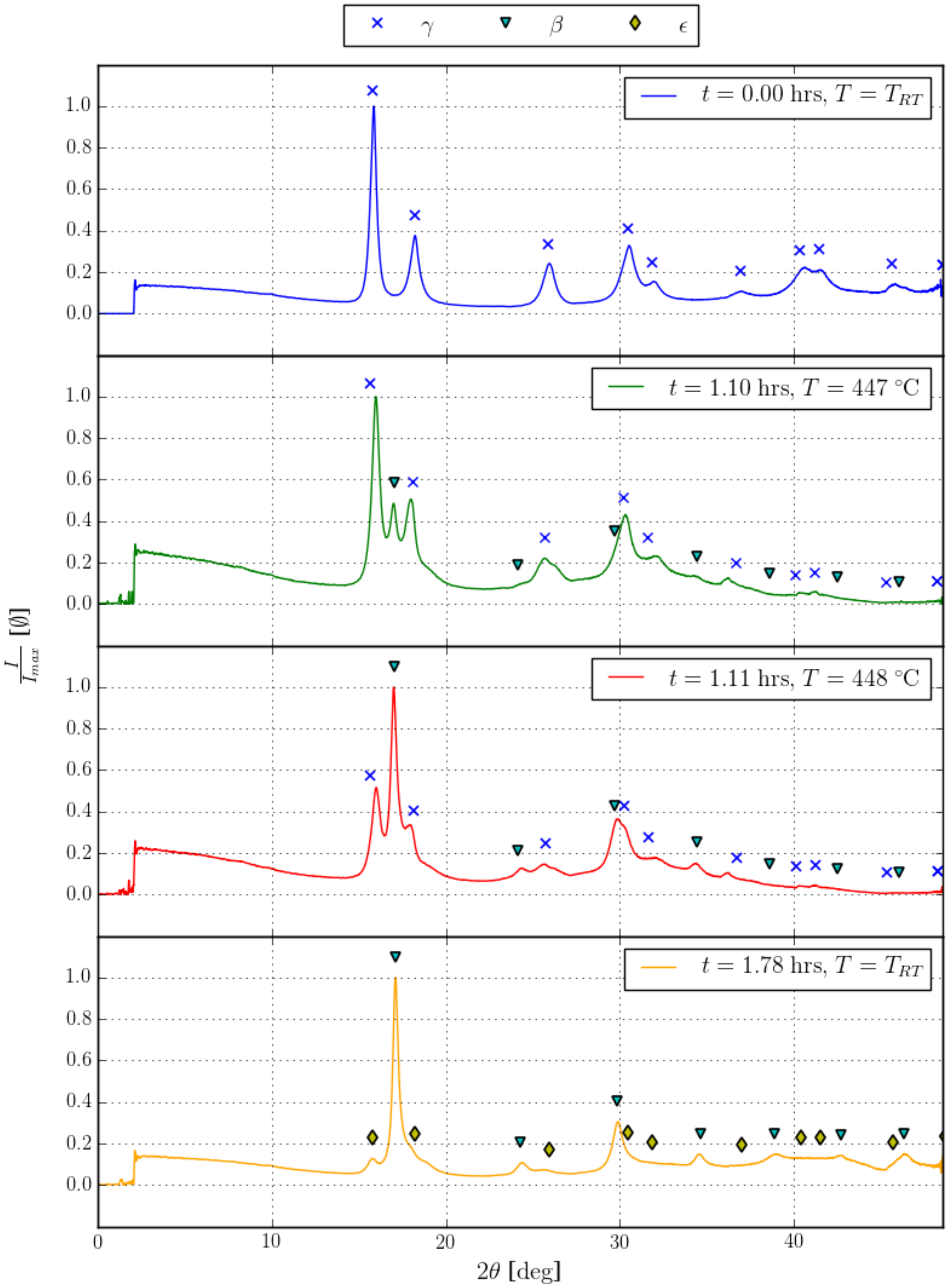
× γ
▼ β
◆ ϵ
$t = 0.00$ hrs, $T = T_{RT}$
$t = 1.10$ hrs, $T = 447$ °C
$t = 1.11$ hrs, $T = 448$ °C
$t = 1.78$ hrs, $T = T_{RT}$
$\frac{I}{I_{max}}$ [∅]
0.0
0.2
0.4
0.6
0.8
1.0
0
10
20
30
40
2θ [deg]

(c)

the detector. Once cooling is initiated the intensity recovers back to normal values. Nothing seem to happen to the system before the temperature reach 432 °C where the γ-fcc-related peaks of the hydride phase suddenly disappear and strong β-bcc peaks appear instead. The high temperature of hydrogen desorption indicate that the sample has been passivated by a thin oxide layer residing on the the particle surfaces which is reduced once the temperature reach sufficient values enabling the reaction to initiate abruptly. If this is the case one should expect different processes to occur in parallel which is supported by the data. The different peaks were traced through the measurements and were subsequently indexed with reference to table 4.4 in part (c) of figure 4.15. Attempts were made to perform Rietveld refinements with the selected measurements shown in the figure but no unambiguous solution were obtained. A portional misfit in the β-bcc and γ-fcc phases were however discovered in the attempt at $t = 1.10$ hrs and $t = 1.11$ hrs. As discussed in the prior section this might be due to stacking faults, twin boundaries and other planar defects present in the material. Eventually a second face-centred cubic phase denoted by ϵ emerge with a lattice parameter that is slightly larger than that of the initial γ-fcc phase. It is possible that this is the hydride phase of the hexagonal-close packed δ phase but this hypothesis can not be confirmed based on this measurement alone. It is finally evident when one compare the lattice parameter of the β-bcc phase in the final measurement to that of the pure α-bcc alloy that some hydrogen is still left inside the system. The blower is therefore unable to reach sufficient temperatures to completely desorb the hydrogen and the SR-PXD measurement can only provide a partial picture of the desorption process.

An *in-situ* SR-PXD measurement was also conducted during absorption of hydrogen by the system $(Ti_{0.70}V_{0.30})_{0.90}Fe_{0.10}$ + 5 wt.% Zr_7Ni_{10} as shown in figure 4.16. The H_2-gas was introduced in small pulses to prevent the powder from blowing out of the beam. It should be noted that the pressure signal shown in the figure is based on handwritten notes and therefore only serve as a rough indication of the true experimental condition under which the sample resides. As can be seen from the six highlighted measurements the hydrogenation consist of several sequential steps. The different phases were traced through the reaction, indexed with reference to table 4.4 and successful Rietveld refinements were finally obtained for some of the highlighted measurements in the figure. These refinements can be found in appendix D. From the first three highlighted measurements it is observed that the lattice parameter of the body-centred cubic α phase increase slightly. This indicate that the hydrogen first enter interstitial sites in this phase to form a solid solution. Figure 4.17 show an enlarged section of

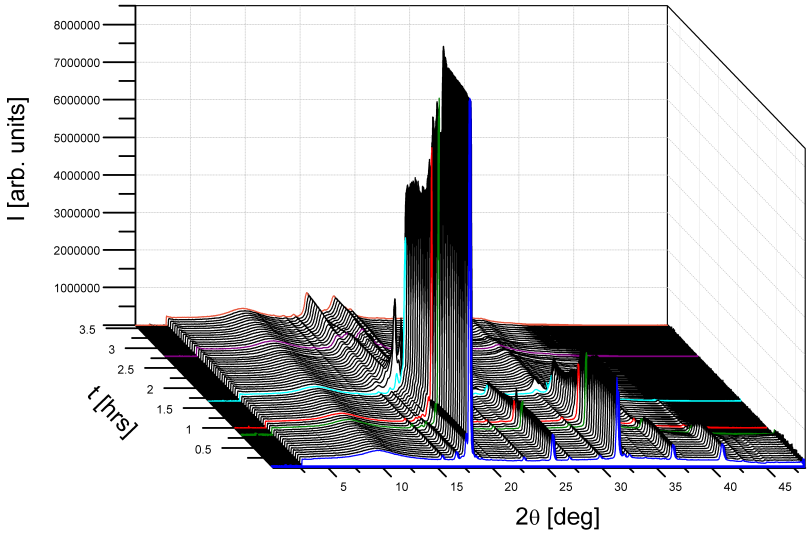

(a)

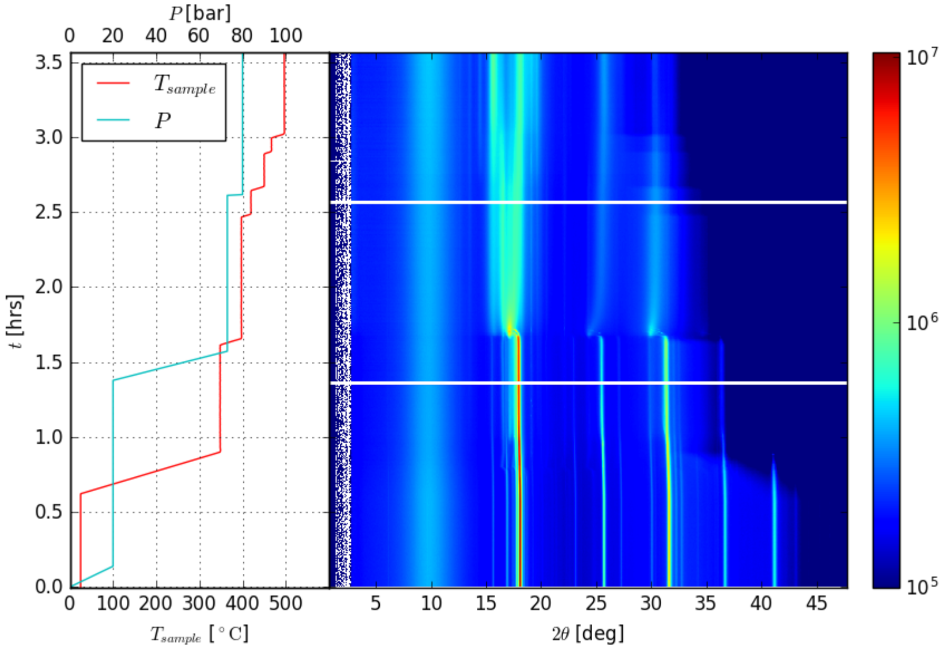

(b)

Figure 4.16: *In-situ* SR-PXD during absorption of hydrogen by $(Ti_{0.70}V_{0.30})_{0.90}Fe_{0.10}$ + 5 wt.% Zr_7Ni_{10} visualized by a waterfall diagram (a) and a contour plot for which the colorbar yield the logarithmic intensity (b). The known phases are indicated for six selected measurements (c) that are also marked in the waterfall diagram. The heating rate was in all linear temperature regions set to 20 K/min and the temperature of the sample T_{sample} was determined from the measured temperatures through the calibration curve displayed in figure B.3. Notice that the experiment was paused on two occasions in order to raise the H_2-pressure within the reservoir volume of the high-pressure gas rig.

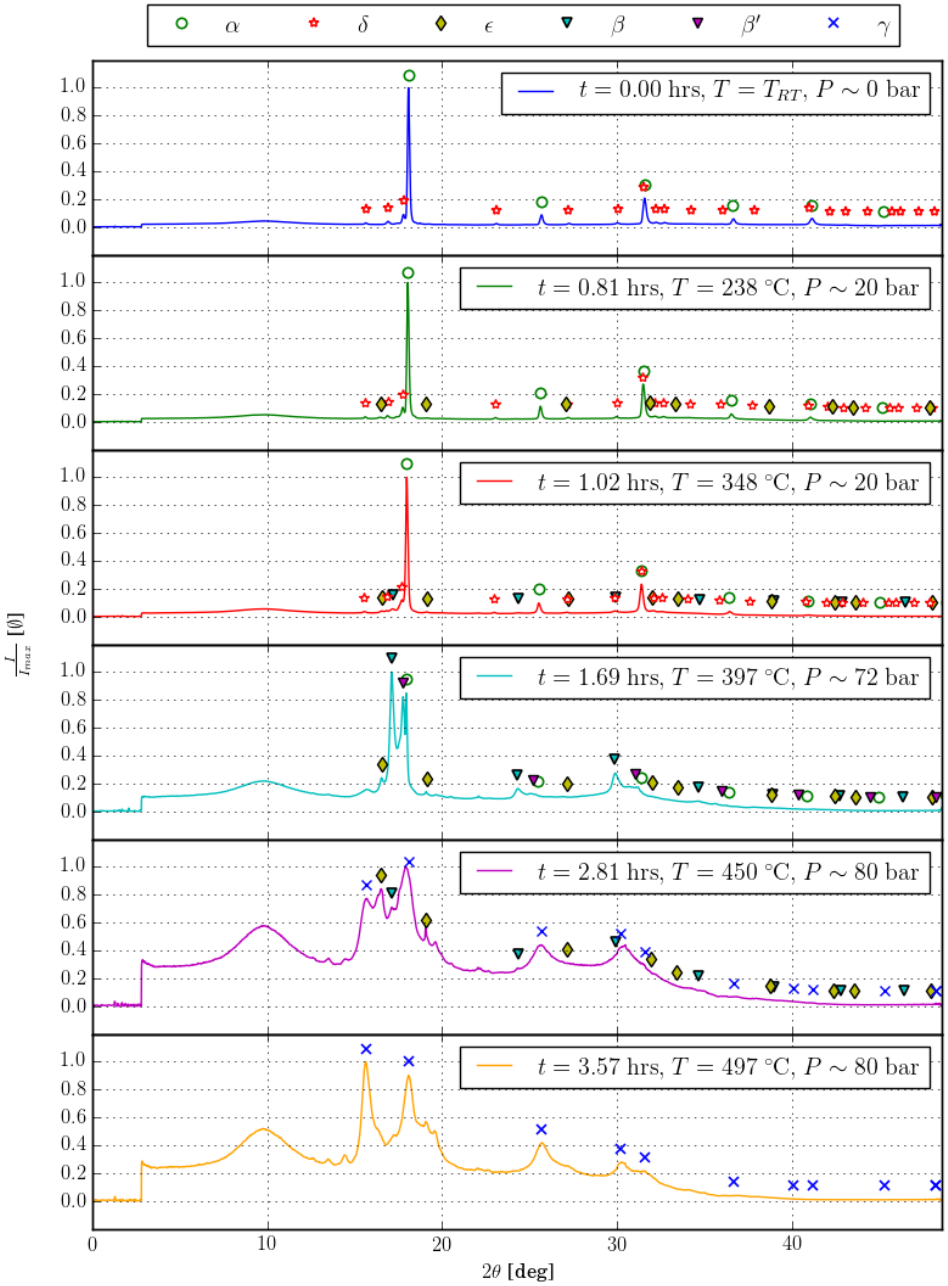
α
δ
ϵ
β
β′
γ
$t = 0.00$ hrs, $T = T_{RT}$, $P \sim 0$ bar
$t = 0.81$ hrs, $T = 238$ °C, $P \sim 20$ bar
$t = 1.02$ hrs, $T = 348$ °C, $P \sim 20$ bar
$t = 1.69$ hrs, $T = 397$ °C, $P \sim 72$ bar
$t = 2.81$ hrs, $T = 450$ °C, $P \sim 80$ bar
$t = 3.57$ hrs, $T = 497$ °C, $P \sim 80$ bar
$\frac{I}{I_{max}}$ [∅]
0.0
0.2
0.4
0.6
0.8
1.0
0
10
20
30
40
2θ [deg]

(c)

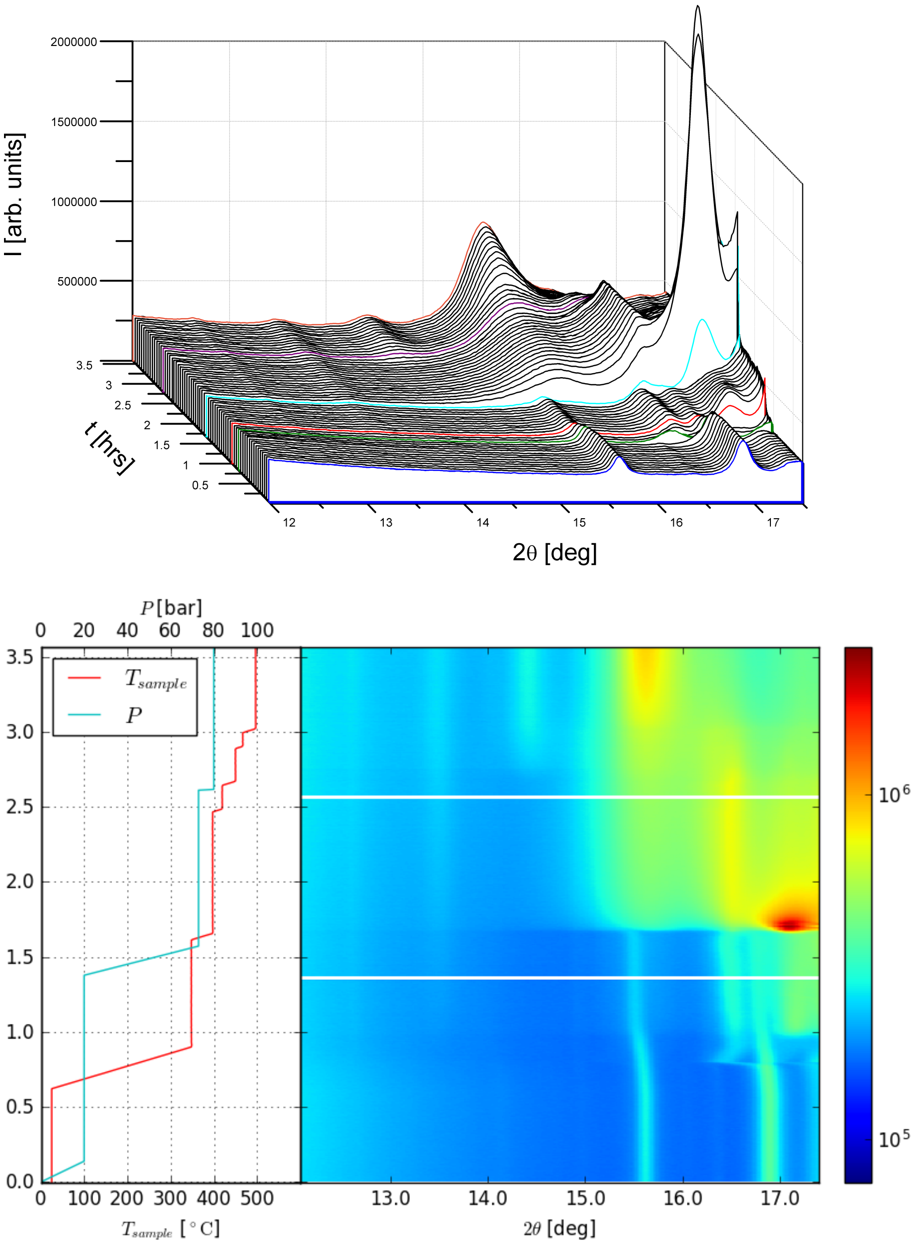

Figure 4.17: The enlarged $2\theta \in [12.0°, 17.5°]$ range of the *in-situ* SR-PXD absorption of hydrogen by $(Ti_{0.70}V_{0.30})_{0.90}Fe_{0.10}$+5 wt.% added Zr_7Ni_{10} shown in figure 4.16.

the $2\theta \in [12°, 17.5°]$ range of the absorption measurement. From this figure it is readily observed at about $t = 0.81$ hrs that the hexagonal-close packed δ phase is shifted towards lower scattering angles. This corresponds to an increase in the unit cell volume V_δ which might either be due to thermal expansion or that the phase is absorbing hydrogen. On closer inspection it can however be observed that the expansion continues past the first linear heating segment which exclude the possibility of the expansion being solely due to thermal expansion. It is furthermore interesting to observe that the ϵ-fcc phase appear at about the same time as the unit cell volume of the δ-hcp phase start to increase. With respect to this observation it seem rather probable that the δ-hcp phase could be a α-Ti like solid solution of Ti, V and Fe that form a γ-Ti like ϵ-fcc hydride phase upon hydrogenation. From figure 4.18 it can furthermore be seen that the δ-hcp phase disappear altogether at about $t = 1.69$ hrs when the sample temperature reach $T_{sample} = 397$ °C and the hydrogen pressure is about 72 bar. At this point the peaks of the β-bcc-phase appear and its intensity grow rapidly over the next couple of minutes. The sudden initiation of the reaction can once again be explained by a thin layer of oxide that has formed on the particle surfaces to prevent the absorption to initiate. The peaks of the ϵ-fcc-phase also increase significantly as can be seen from figure 4.17 before it again diminish at about $t = 2.81$ hrs when the sample temperature is $T_{sample} = 450$ °C and the hydrogen pressure is about 80 bar. It is interesting to observe that a new diffraction peak appear and start to grow at about 14.5° at about the same time as the ϵ-fcc phase diminish which seem to link the two events. This peak has however not been associated with any phase. It is probable that other peaks might be hidden underneath the main diffraction peaks which at this point has broadened and assumed odd profiles as observed in the *ex-situ* SR-PXD measurements discussed in the prior section. It is possible that the observed peak might be due to a deformation in the ϵ-fcc phase to a tetragonal structure as was reported by Sidhu et al. [45] to occur in the face-centred cubic γ-Ti deuteride when the composition approach TiD_2. Figure 4.19 does finally show the enlarged $2\theta \in [18.8°, 22.5°]$ region. In this part of SR-PXD pattern there are several minor diffraction peaks that fit reasonably well with the added Zr_7Ni_{10} as illustrated in the figure. The peaks are furthermore shifted towards lower scattering angles as the sample is heated indicative of thermal expansion.

When the absorption seemed to have finished the hydrogen was removed from the cell and replaced by a dynamic vacuum in an attempt to desorb the sample back to its initial state. The collected SR-PXD measurement of the process is rendered in figure 4.20. The unidentified peak discussed above

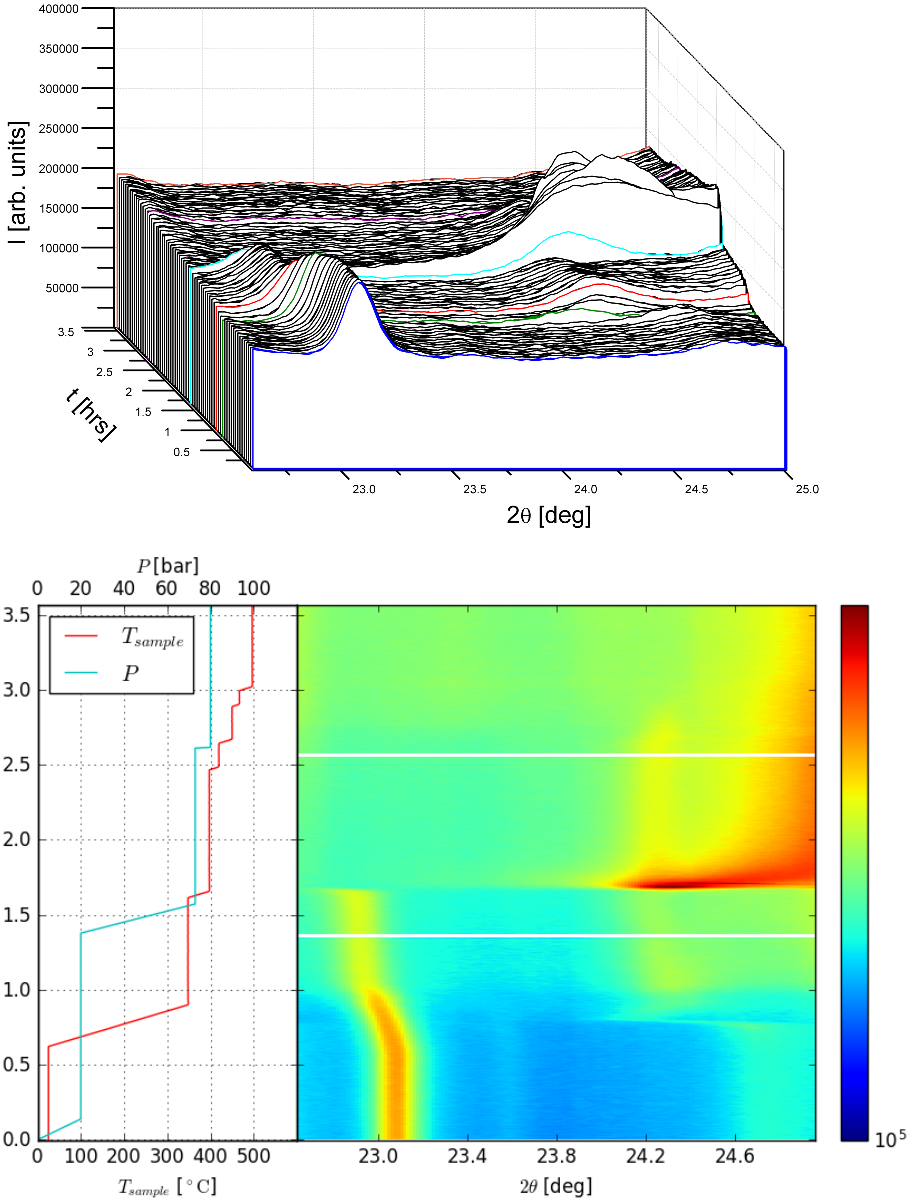

Figure 4.18: The enlarged $2\theta \in [22.6°, 25.0°]$ range of the *in-situ* SR-PXD during absorption of hydrogen by $(Ti_{0.70}V_{0.30})_{0.90}Fe_{0.10}$+5 wt.% added Zr_7Ni_{10} shown in figure 4.16.

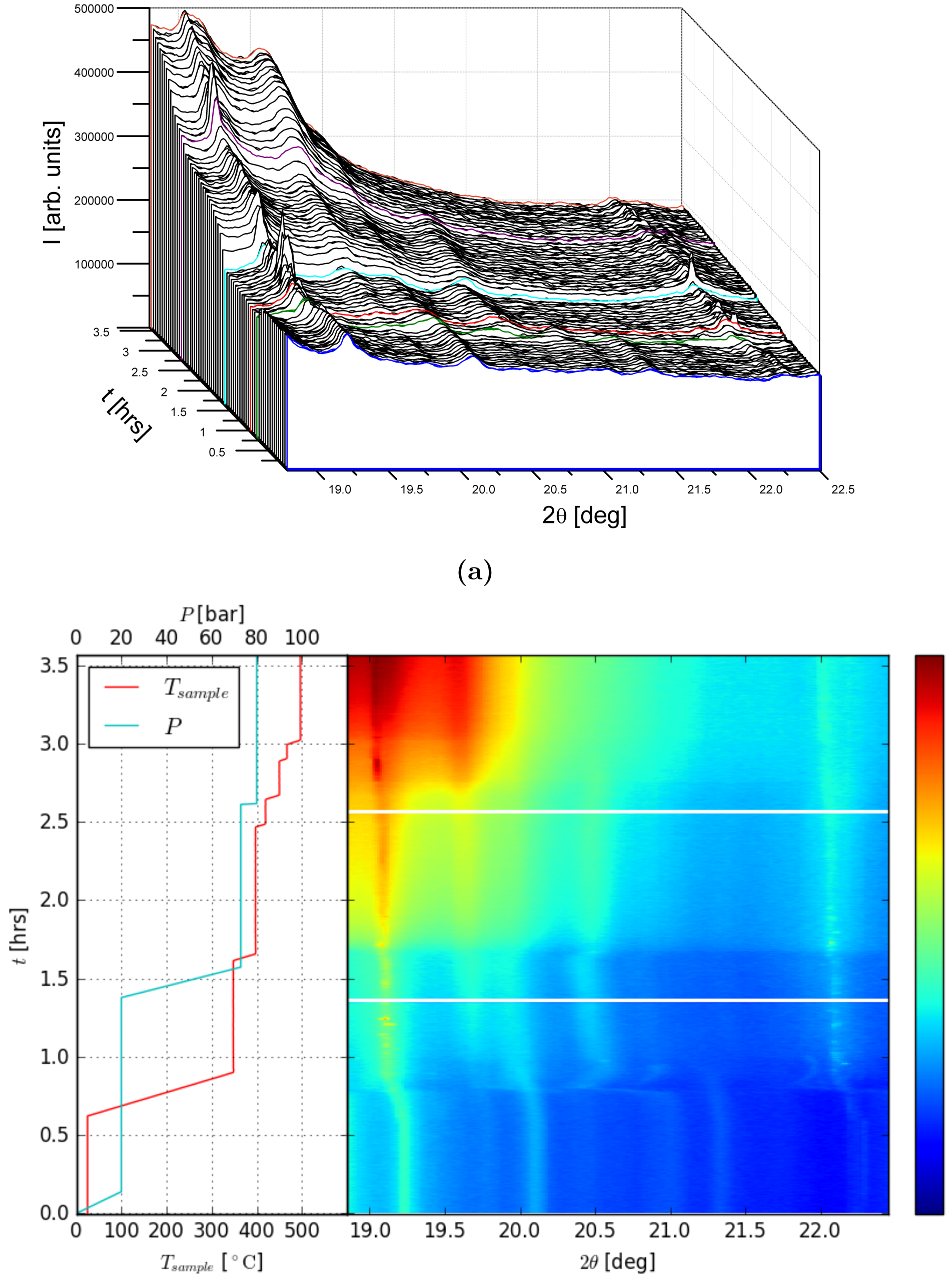

(a)

(b)

Figure 4.19: The enlarged $2\theta \in [18.8°, 22.5°]$ range of the *in-situ* SR-PXD absorption of hydrogen by $(Ti_{0.70}V_{0.30})_{0.90}Fe_{0.10}$+5 wt.% added Zr_7Ni_{10} shown in figure 4.16. The Zr_7Ni_{10} also seem to be present in the sample as indicated in (c) where the measurement at t = 0.00 hrs (blue) is shown alongside the *ex-situ* SR-PXD pattern of Zr_7Ni_{10} (black). The signals have been normalized to their observed maximum intensities in the region to facilitate the comparison.

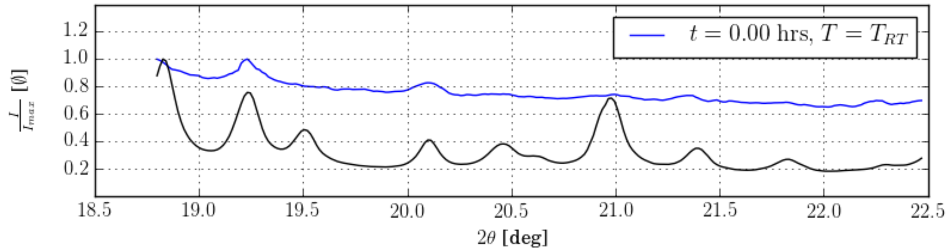

(c)

disappeared once the desorption was initiated. This indicate that the phase is an unstable hydride. Another set of diffraction peaks did furthermore appear that unfortunately has been identified as rutile (TiO_2). This reveal that the system is not completely sealed and that the sample have oxidized. As an overpressure of hydrogen inside the cell prevent air from entering the system the problem did not unfold until the sample was exposed to a dynamic vacuum and it is therefore recommended that the desorption is carried out under a slight hydrogen back-pressure in the future.

To summarize this subsection we state that the hydrogen sorption seem to follow

$$\alpha \xrightleftharpoons{\mathrm{H_2}} \beta \xrightleftharpoons{\mathrm{H_2}} \gamma \tag{4.1}$$

$$\delta \xrightleftharpoons{\mathrm{H_2}} \epsilon \tag{4.2}$$

where α is the bcc-alloy, β is the bcc hydride, γ is the fcc-related hydride, δ is the hcp impurity phase and ϵ is an fcc hydride that form from the δ phase.

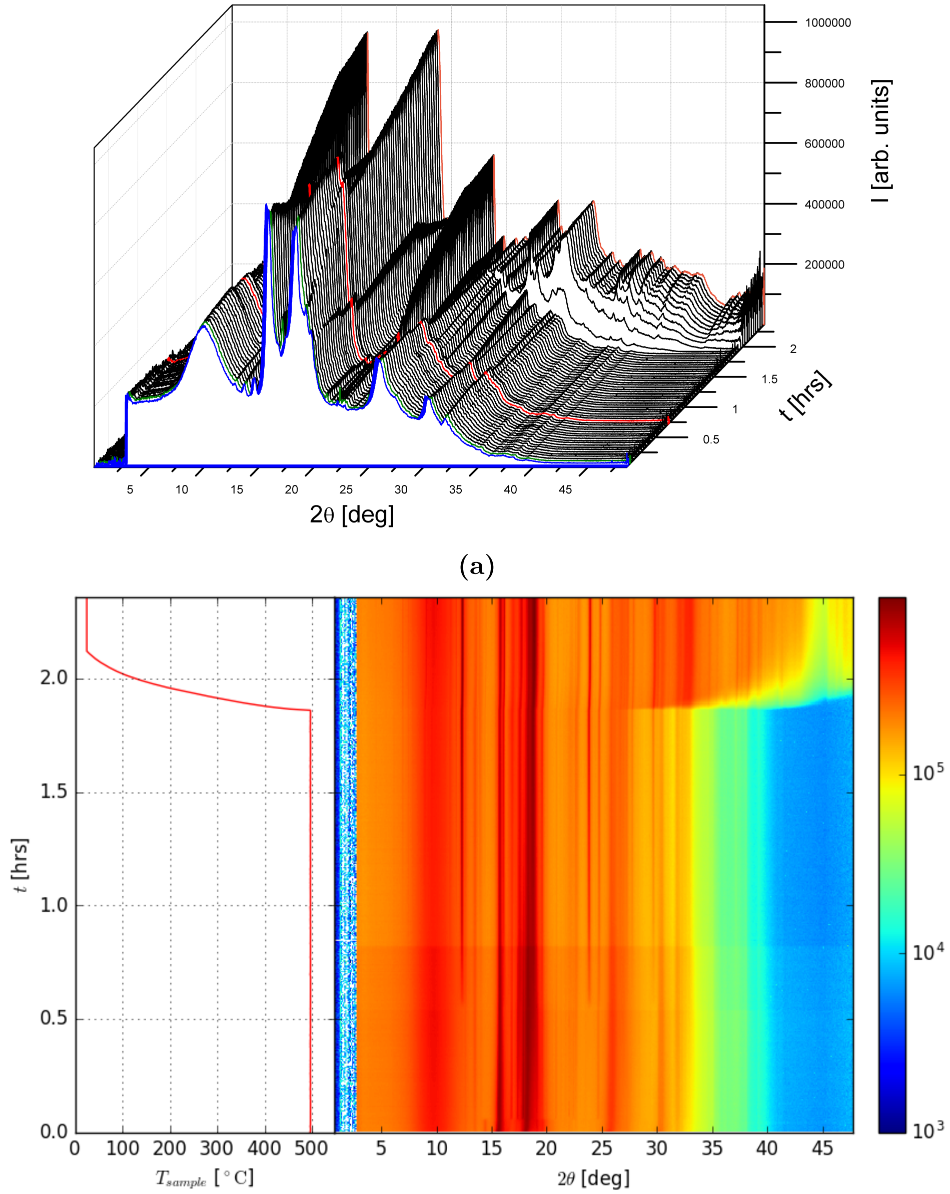

(a)

(b)

Figure 4.20: *In-situ* SR-PXD during desorption of hydrogen from $(Ti_{0.70}V_{0.30})_{0.90}Fe_{0.10}$ + 5 wt.% Zr_7Ni_{10} that was hydrogenated during the measurement displayed in figure 4.16. (a) show a waterfall diagram while (b) yield the corresponding contour plot for which the colorbar yield the logarithmic intensity. The known phases are indicated for four selected measurements (c). The temperature of the sample T_{sample} was determined from the measured temperatures through the calibration curve displayed in figure B.3.

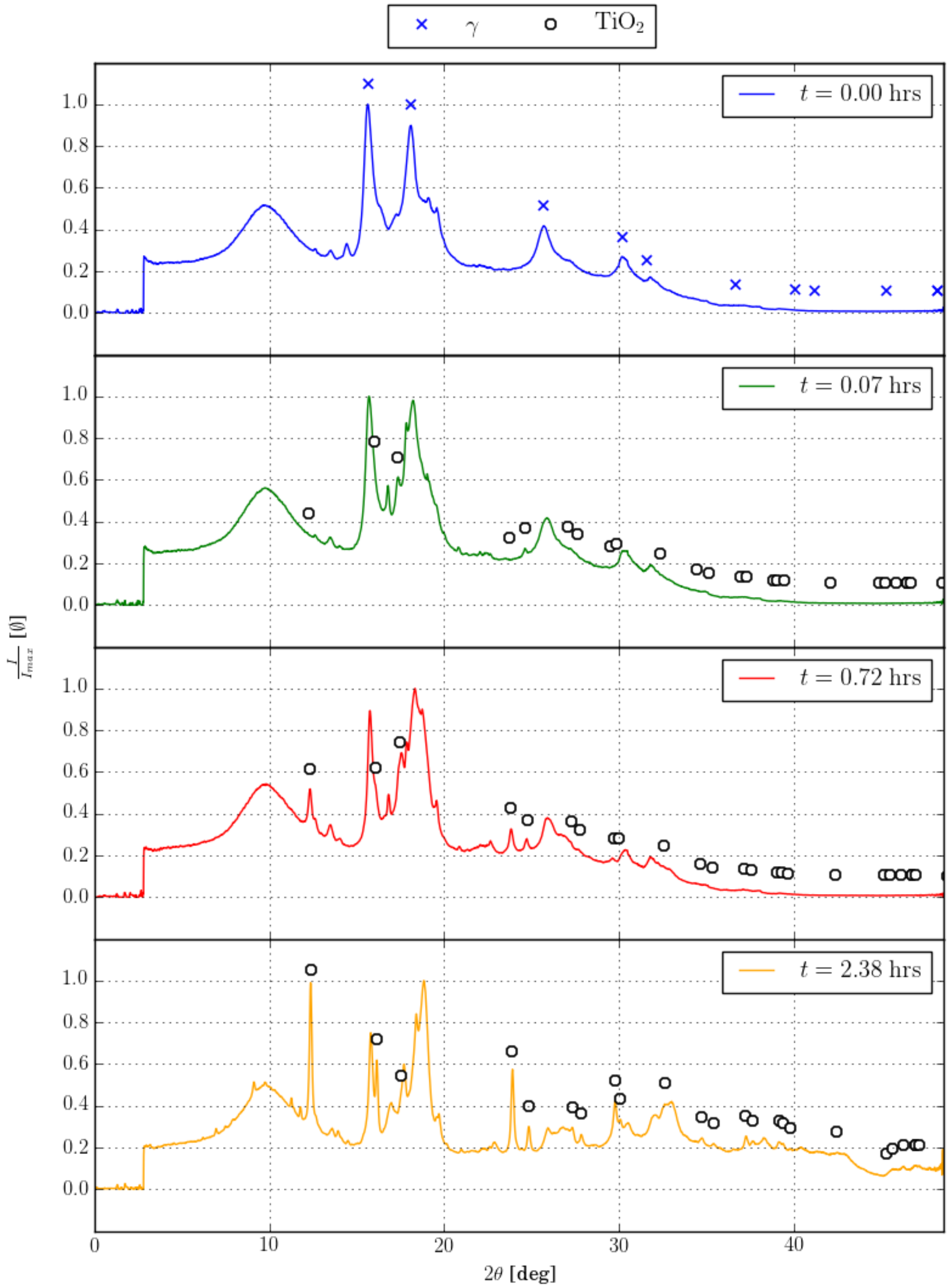
× γ
○ TiO_2
$t = 0.00$ hrs
$t = 0.07$ hrs
$t = 0.72$ hrs
$t = 2.38$ hrs
$\frac{I}{I_{max}}$ [∅]
2θ [deg]
0.0
0.2
0.4
0.6
0.8
1.0
0
10
20
30
40

(c)

4.4 Thermodynamic analysis in Sieverts apparatus

4.4.1 Kinetic analysis

Two measurement series were conducted in the Sieverts apparatus to explore the hydrogen absorption kinetics of $(Ti_{0.70}V_{0.30})_{1\text{-}z}Fe_z$. In the first series ~ 190 mg of the as-cast samples were placed inside the sample-holder and mounted Sieverts apparatus. A detailed description of the masses and particle morphology of the considered samples are rendered in table 4.5.

The samples were initially exposed to an activation treatment consisting of dynamic vacuum and a temperature of 500 °C. The samples were left to dwell in this environment for at least 8 hours before they were cooled to room-temperature and exposed to ~ 20 bar[3] of H_2-gas once the valve separating the small volume within the Sieverts apparatus and the sample-holder was opened at time $t = 0$ hrs. The small volume was applied to maximize the pressure reduction associated with absorption by the sample to facilitate the analysis. After the absorption was complete the hydrogen was removed from the sample by re-exposing it to the dynamic vacuum and 500 °C environment for at least 8 hrs. This procedure was repeated three times and the extent of reaction ξ during each of these absorption cycles are shown in figure 4.21. From this figure it can readily be observed that the hydrogen absorption kinetics of the system is very fast. For the samples with $z \leq 0.10$ there is a notable improvement in the kinetics between the first and two subsequent cycles which is probably due to an increase in the metal surface through which the hydrogen can diffuse into the bulk metals. This is supported by observing that the relatively large sample particles that were initially loaded into the sample-holder had been decomposed into fine powders after the third absorption was complete. In the two final cycles it can be observed that the introduction of iron seem to have an enhancing effect on the absorption kinetics. It is however interesting to notice that the hydrogen absorption by the $(Ti_{0.70}V_{0.30})_{0.97}Fe_{0.03}$ sample commence at a slower rate than that of the reference system $Ti_{0.70}V_{0.30}$ during the first two cycles. This effect might be explained by the deviant particle morphology of $(Ti_{0.70}V_{0.30})_{0.97}Fe_{0.03}$ as opposed to the particle morphology of the other systems.

Figure 4.22 show the development of the molar hydrogen-to-metal ratio x within the hydride $(Ti_{0.70}V_{0.30})_{1\text{-}z}Fe_zH_x$ during the first hour of the mea-

---

[3] It should be noted that the $(Ti_{0.70}V_{0.30})_{0.80}Fe_{0.20}$ system were exposed to molecular hydrogen at ~ 70 bar in the first cycle as opposed to 20 bar.

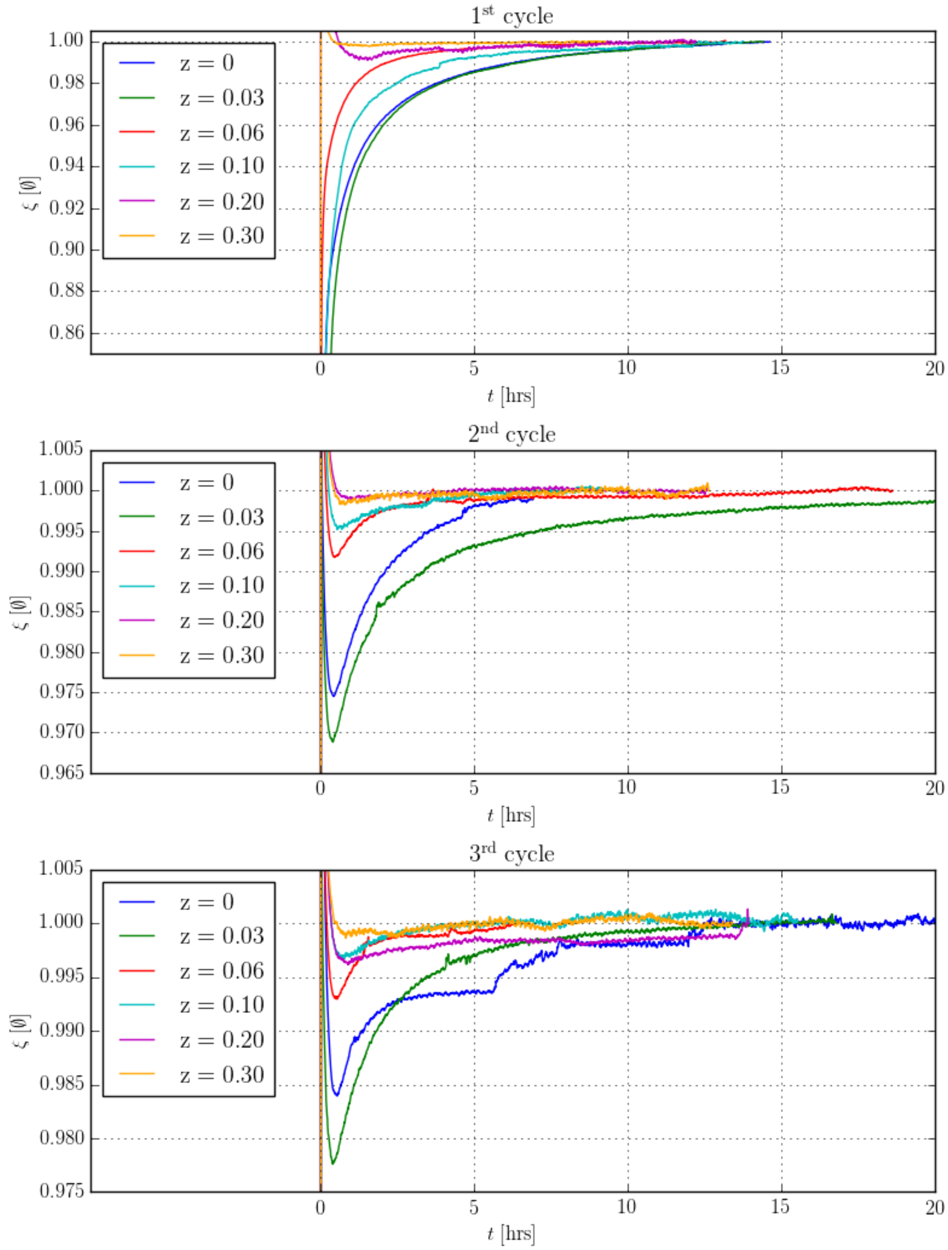

Figure 4.21: The extent of reaction ξ for the three consecutive hydrogen absorption cycles by as-cast $(\mathrm{Ti}_{0.70}\mathrm{V}_{0.30})_{1\text{-}z}\mathrm{Fe}_z$ when exposed to an initial hydrogen pressure of $\sim$ 20 bar. Note that the extent of the reaction initially assume values $\xi > 1$ because of the temperature development associated with the exothermic reaction and the Joule-Thompson effect.

Table 4.5: The masses m_{sample} and particle morphology of the samples that were loaded into sample-holder #12B on the Siverts apparatus C-side in the first series of hydrogen absorption kinetics measurements.

Sample (Batch)	Rig	m_{sample} [mg]	Particle morphology
$Ti_{0.70}V_{0.30}$ (2)	C	191.7	Mostly small particles
$(Ti_{0.70}V_{0.30})_{0.97}Fe_{0.03}$ (1)	C	195.2	Plate-like particles
$(Ti_{0.70}V_{0.30})_{0.94}Fe_{0.06}$ (1)	C	198.4	Mostly small particles
$(Ti_{0.70}V_{0.30})_{0.90}Fe_{0.10}$ (1)	C	197.3	Mostly small particles
$(Ti_{0.70}V_{0.30})_{0.80}Fe_{0.20}$ (1)	C	189.7	Mostly small particles
$(Ti_{0.70}V_{0.30})_{0.70}Fe_{0.30}$ (1)	C	190.2	Mostly small particles

surements in figure 4.21 alongside the associated temperature development. From this figure it is readily observed that there is a significant temperature development associated with the reaction. This is partly due to the exothermicity of the reaction and partly due to the Joule-Thompson effect[4] when the hydrogen expands into the sample-holder. As can be seen from figure 4.21 it is simply not possible to consider the absorption kinetics until the developed heat has been transferred away from the sample. It is this heat-development that cause the extent of reaction ξ to take on values $\xi > 1$ in figure 4.21. It can be seen from figure 4.22 that this take about 30 min after which the reaction is almost complete.

The maximal hydrogen-to-metal ratio x_{max} at the end of each cycle are shown in figure 4.23 for the respective systems. The measurement uncertainties are quite large but it is apparent that there is no significant reduction in the hydrogen capacity of the hydrides until the iron content exceed $z > 0.10$. The hydrogen content do furthermore seem reasonably stable during the first three cycles with the exception of the first cycle of $(Ti_{0.70}V_{0.30})_{0.80}Fe_{0.20}$. The measurement uncertainty is also quite large for this measurement which is due to the fact that the applied pressure was 70 bar instead of 20 bar.

A second measurement series were also conducted to determined whether the theoretical maximal hydrogen-to-metal ratio of $x \sim 2$ could be reached

---

[4] The Joule-Thompson effect describe the temperature change of a real gas or liquid when it is forced through a valve adiabatically in a throttling process. At first the reasoning presented in the text might be surprising as most real gases at room-temperature cool when they expand through a valve, but hydrogen, helium and neon deviates from this common behaviour at room temperature and warms instead as they are throttled. It should however be noted that also hydrogen, helium and neon experience the same behaviour as the other gases at lower temperatures.

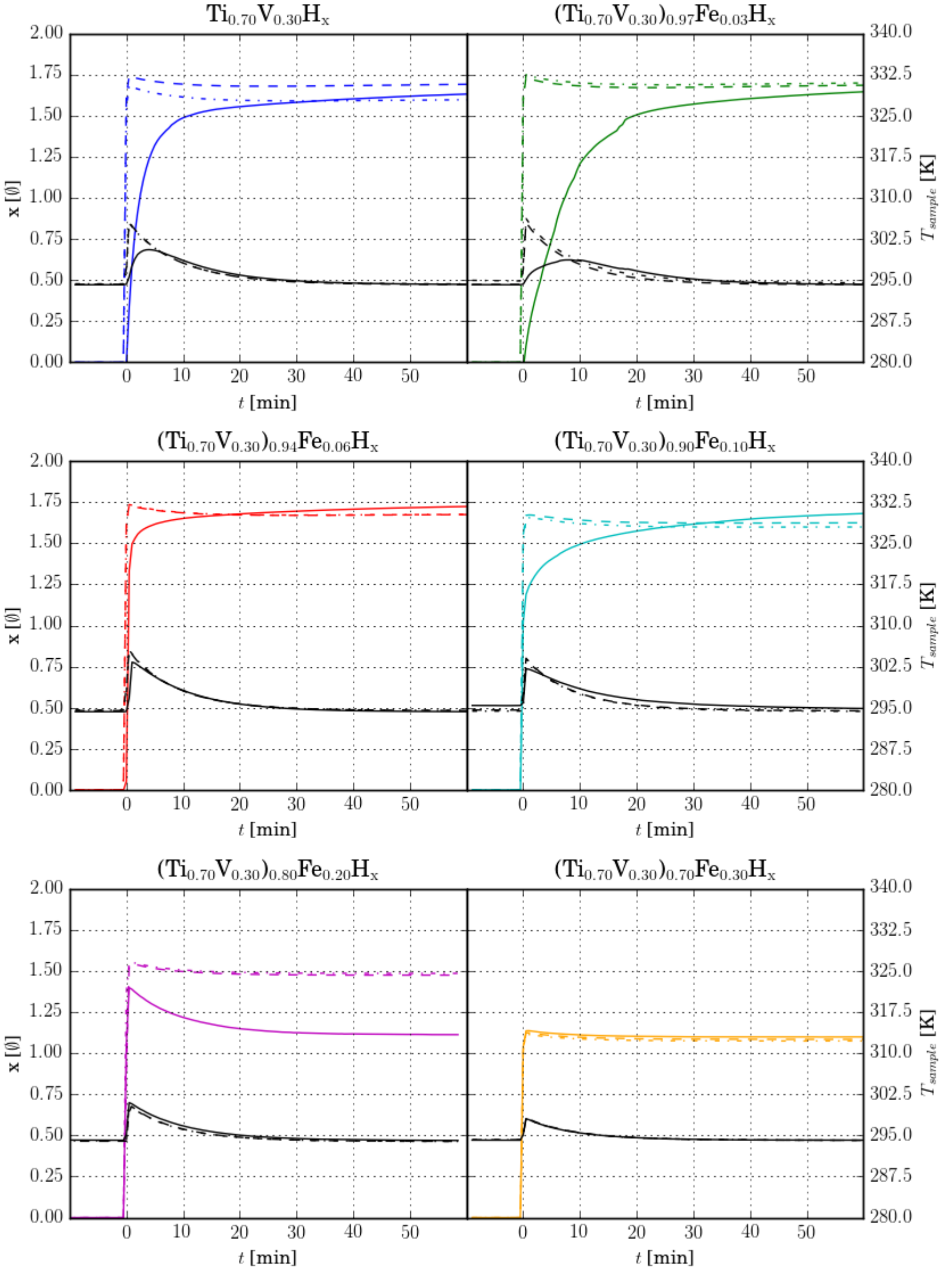

Figure 4.22: The development of the molar hydrogen-to-metal ratio x within the hydride $(Ti_{0.70}V_{0.30})_{1\text{-}z}Fe_zH_x$ during three consecutive hydrogen absorption cycles conducted at room-temperature by exposing the samples to an initial pressure of ~ 20 bar. The solid lines correspond to the first measurement, the dashed lines to the second and the dashed dotted to the third. The associated black lines give the corresponding temperature development as measured by the thermistor coupled to the sample-holder.

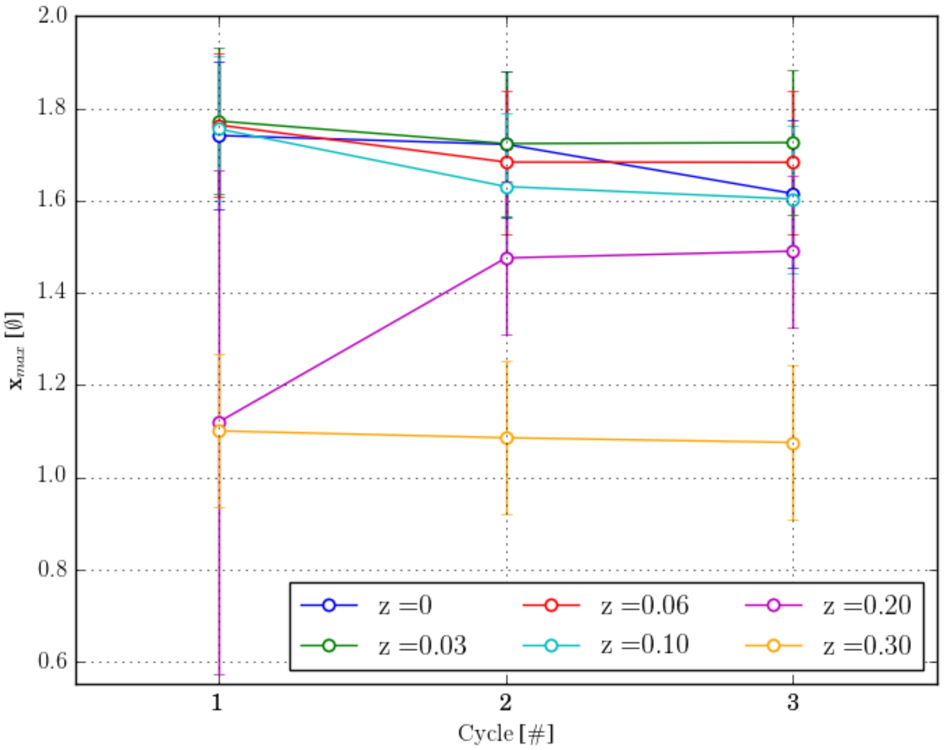

Figure 4.23: The maximal hydrogen-to-metal ratio x_{max} observed in the three consecutive H-absorption cycles displayed in figure 4.21 for the system $(Ti_{0.70}V_{0.30})_{1\text{-}z}Fe_zH_x$.

for the hydrides $(Ti_{0.70}V_{0.30})_{1\text{-}z}Fe_zH_x$ within the allowed pressure-range of the Sieverts apparatus. The maximal pressure that can be achieved is $\sim$ 190 bar but such large pressures would cause unreasonable measurement uncertainties for the molar hydrogen-to-metal ratio δx as was the case in the first absorption cycle of $(Ti_{0.70}V_{0.30})_{0.80}Fe_{0.20}$ when it was exposed to 70 bar of molecular hydrogen. Appendix A.4 does however show that $\delta x \propto 1/n_M \propto 1/m_M$ and the applied sample mass was therefore increased to $\sim$ 600 mg to counter the increasing measurement uncertainty imposed on the system by the high hydrogen pressure. The samples that are described in table 4.6 were loaded into either the #10B sample-holder and mounted to the B-side Sieverts apparatus or #12B sample-holder and mounted to the C-side Sieverts apparatus. Three sorption cycles were measured following the same procedure as for the first measurement series with the exception that the applied pressure was set to $\sim$ 190 bar. The large volume within the Sieverts apparatuses were also applied to decrease the drop in pressure during absorption[5]. The extent of reaction ξ during each of these sorption cycles are shown in figure 4.24. From this measurement it is readily observed that the measured signals are more stable on the B-side than on the C-side. This is likely due to differences between the pressure transducers applied in the two apparatuses and it seems that the C-side transducer has either been broken or that the applied pressure is outside its range of stability. This behaviour is also apparent in figure 4.25 which show the development of the molar hydrogen-to-metal ratio x during the first two hours of the measurements alongside the associated temperature development. It should be noted that the temperature increase is much higher than was the case for the measurements with initial pressures of $\sim$ 20 bar shown in figure 4.22. The maximal hydrogen-to-metal ratio x_{max} observed at the end of the measurements are shown in figure 4.26. The measurement uncertainties are as expected quite large but the maximal hydrogen-to-metal ratio seem to approach the expected limit of $\mathrm{x}_{max} = 2$ for the $\mathrm{z} = 0$ and $\mathrm{z} = 0.06$ systems. It is however interesting that the $\mathrm{z} = 0.03$ system seem to have a lower capacity than even the $\mathrm{z} = 0.10$ system. This might however be explained by considering that the measurement uncertainties are larger for the C-side than for the B-side and recalling that this system was measured under the apparent problems with the pressure transducer discussed above.

Table 4.6: The masses m_{sample} and particle morphology of the samples that were loaded into the sample-holder of the specified Sieverts apparatus rig during the second series of hydrogen absorption kinetics measurements.

Sample (Batch)	Rig	m_{sample} [mg]	Particle morphology
$\mathrm{Ti}_{0.70}\mathrm{V}_{0.30}$ (2)	B	638.0	Mostly large particles
$(\mathrm{Ti}_{0.70}\mathrm{V}_{0.30})_{0.97}\mathrm{Fe}_{0.03}$ (1)	C	584.0	Mostly large particles
$(\mathrm{Ti}_{0.70}\mathrm{V}_{0.30})_{0.94}\mathrm{Fe}_{0.06}$ (1)	B	581.7	Mostly large particles
$(\mathrm{Ti}_{0.70}\mathrm{V}_{0.30})_{0.90}\mathrm{Fe}_{0.10}$ (1)	B	631.4	Mostly small particles
$(\mathrm{Ti}_{0.70}\mathrm{V}_{0.30})_{0.80}\mathrm{Fe}_{0.20}$ (1)	C	593.6	Mostly small particles
$(\mathrm{Ti}_{0.70}\mathrm{V}_{0.30})_{0.70}\mathrm{Fe}_{0.30}$ (1)	C	587.5	Mostly small particles

---

[5] The small volume was however applied for the first cycles of the $\mathrm{Ti}_{0.70}\mathrm{V}_{0.30}$ and $(\mathrm{Ti}_{0.70}\mathrm{V}_{0.30})_{0.80}\mathrm{Fe}_{0.20}$ systems

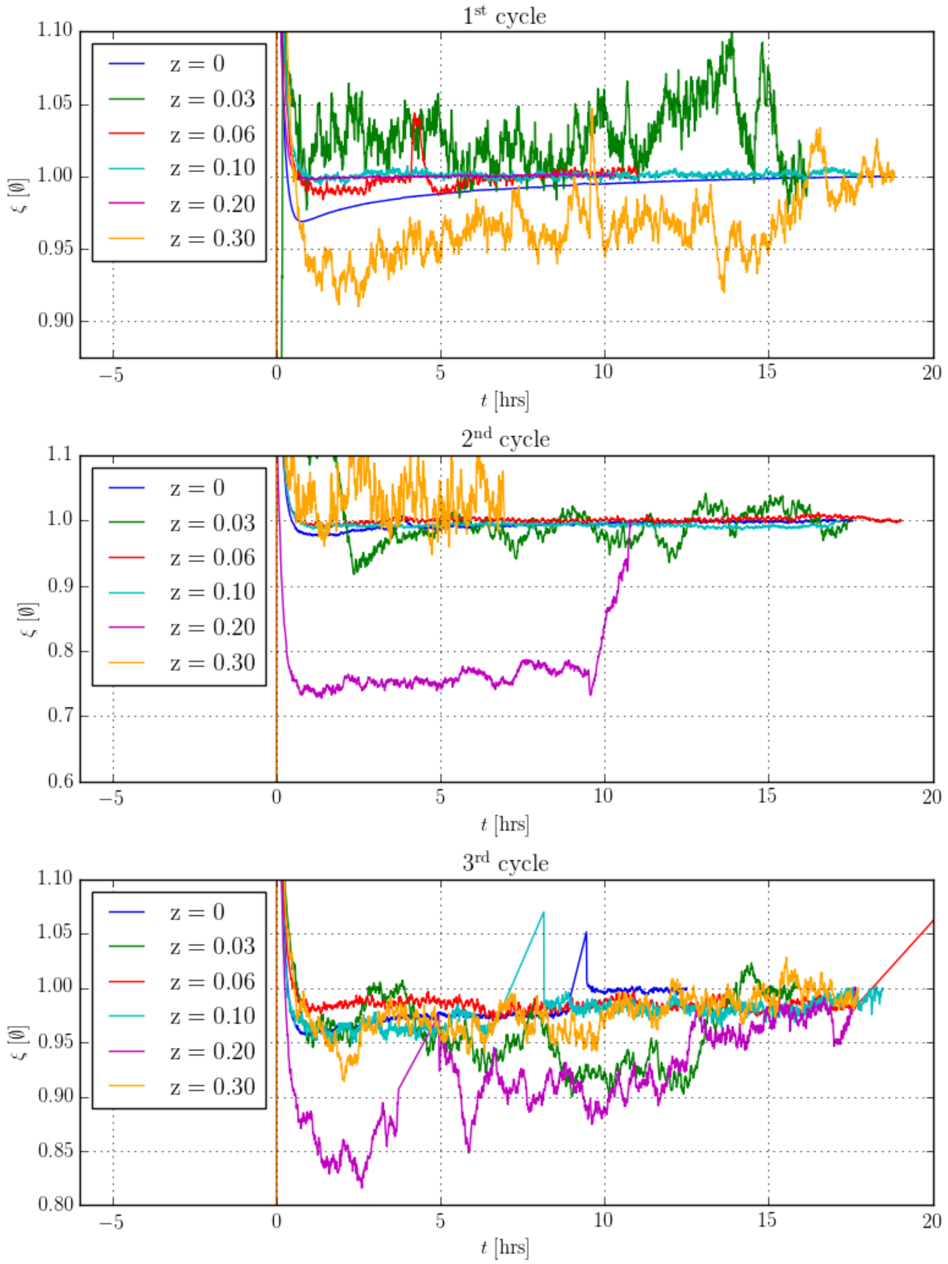

Figure 4.24: The extent of reaction ξ for the three consecutive hydrogen absorption cycles by as-cast $(\mathrm{Ti}_{0.70}\mathrm{V}_{0.30})_{1\text{-}z}\mathrm{Fe}_z$ when exposed to an initial hydrogen pressure of $\sim$ 190 bar. Note that the extent of the reaction initially assume values $\xi > 1$ because of the temperature development associated with the exothermic reaction and the Joule-Thompson effect.

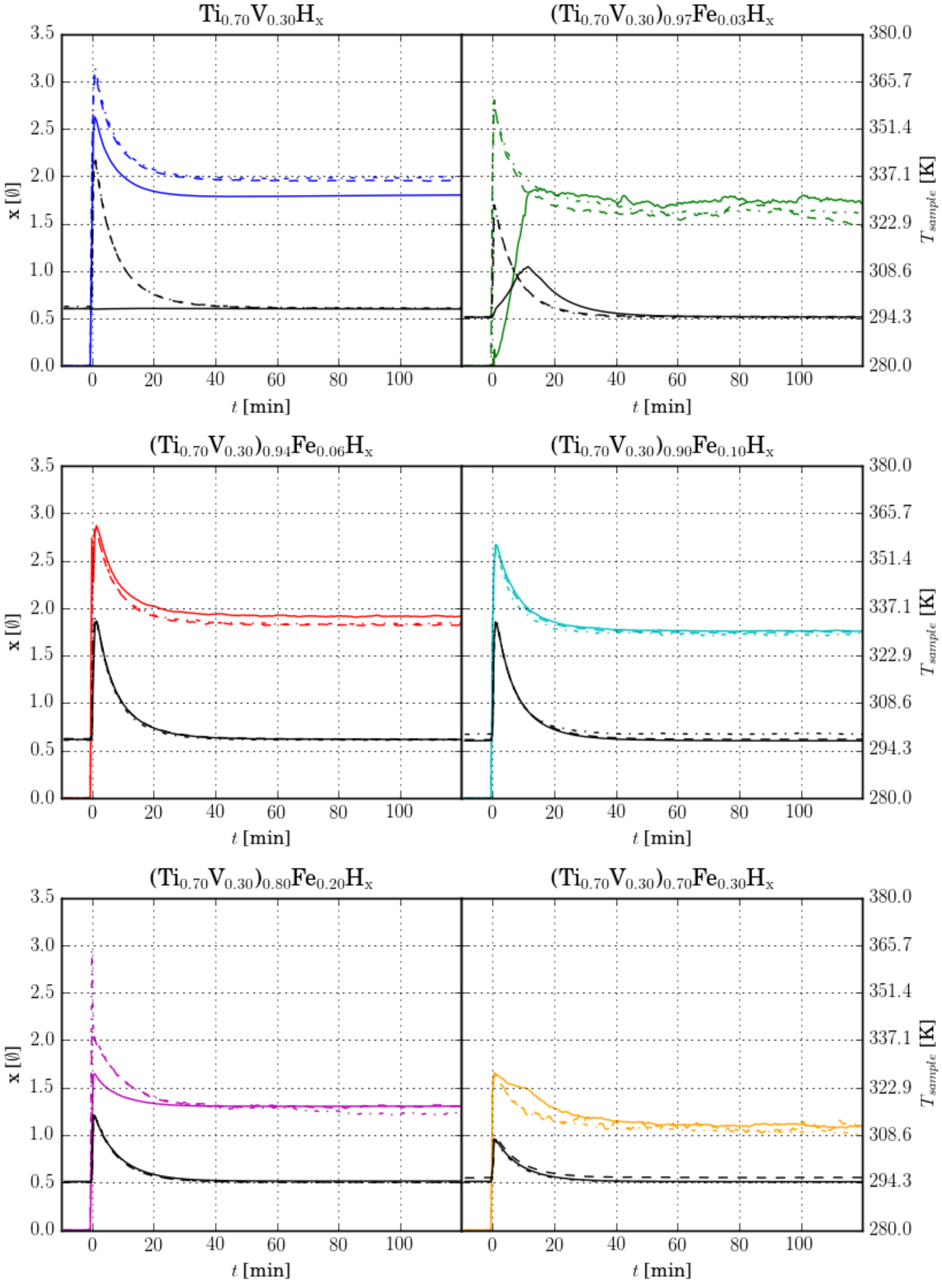

Figure 4.25: The development of the molar hydrogen-to-metal ratio x within the hydride $(Ti_{0.70}V_{0.30})_{1\text{-}z}Fe_zH_x$ during three consecutive hydrogen absorption cycles conducted at room-temperature by exposing the samples to an initial pressure of ∼ 190 bar. The solid lines correspond to the first measurement, the dashed lines to the second and the dashed dotted to the third. The associated black lines give the corresponding temperature development as measured by the thermistor coupled to the sample-holder.

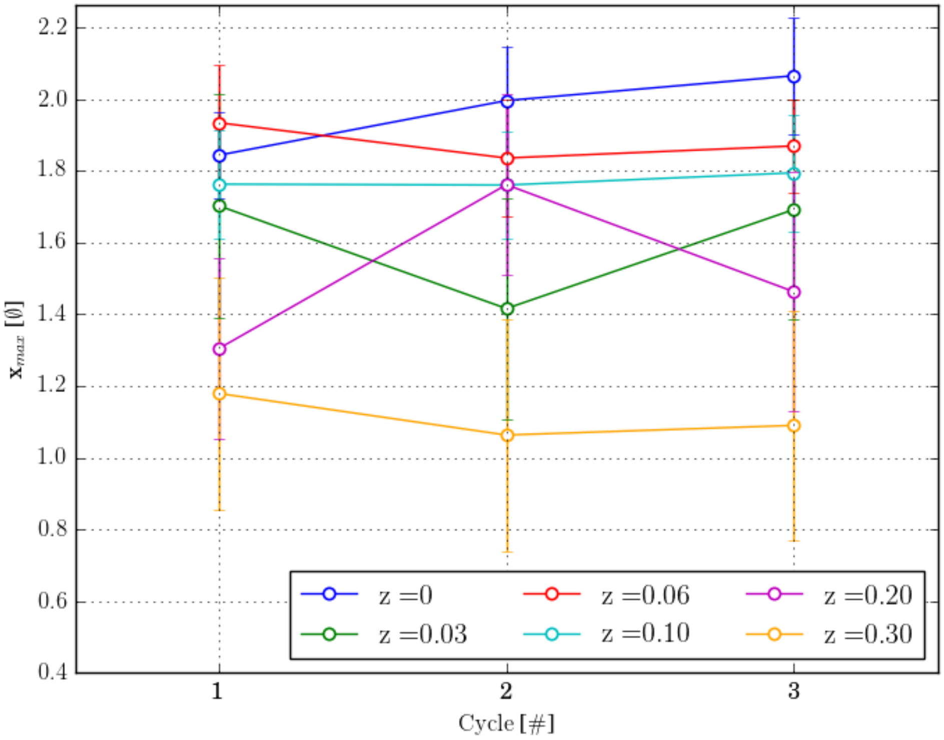

Figure 4.26: The maximal hydrogen-to-metal ratio x_{max} observed in the three consecutive H-absorption cycles displayed in figure 4.24 for the system $(Ti_{0.70}V_{0.30})_{1\text{-}z}Fe_zH_x$.

4.4.2 Pressure-composition isotherms

Pressure-composition isotherms (PCI) were measured for selected systems. As there is no computerized set-up to enable automatic data-collection all measurements had to be conducted manually. The upper part of figure 4.27 show a PCI curve measured at room-temperature for the $Ti_{0.70}V_{0.30}H_x$ system. From this curve it seems that the system hold a plateau that is below the detection limit of the pressure transducer until the molar hydrogen-to-metal ratio reach about x $\sim$ 1.05. The equilibrium pressure then seem to increase but when the initial pressure were set to $P = 1.28$ bar in the ninth absorption the pressure followed the trend shown in the lower part of figure 4.27. As the equilibrium pressure at the end of this measurement lies below the earlier values it seem that something has happened to the sample. A possible explanation is that the surfaces of a fraction of the particles had been passivated by an oxide layer and that the hydrogen was able to reduce this layer once the pressure reached a sufficiently high value. Another attempt was therefore made to measure the room-temperature PCI for this system as shown in figure 4.28. It is however clear that something similar has happened to the system during this measurement. As the equilibrium pressure was increased way beyond what seemed to be necessary for the system to reach a molar hydrogen-to-metal ratio of x $\sim$ 1.54, and the sample did not absorb more than a molar hydrogen-to-metal ratio of 1.21 ± 0.18. The hydride was subsequently desorbed in the TG/DSC apparatus and it was revealed that its weight percentage of hydrogen was $\eta = 2.30\%$. This correspond to a molar hydrogen-to-metal ratio of 1.14. This is considerably less than what was observed in the kinetics measurements, but it is reassuring that the value is within the uncertainties in the PCI. The resultant hydride was also studied by lab XRD where it was observed that both the β-bcc and γ-fcc-related hydrides were present. At this point it seem rather likely that the oxidation discussed in the 4.1, 4.2 and 4.3 sections might have occurred in the Sieverts apparatus.

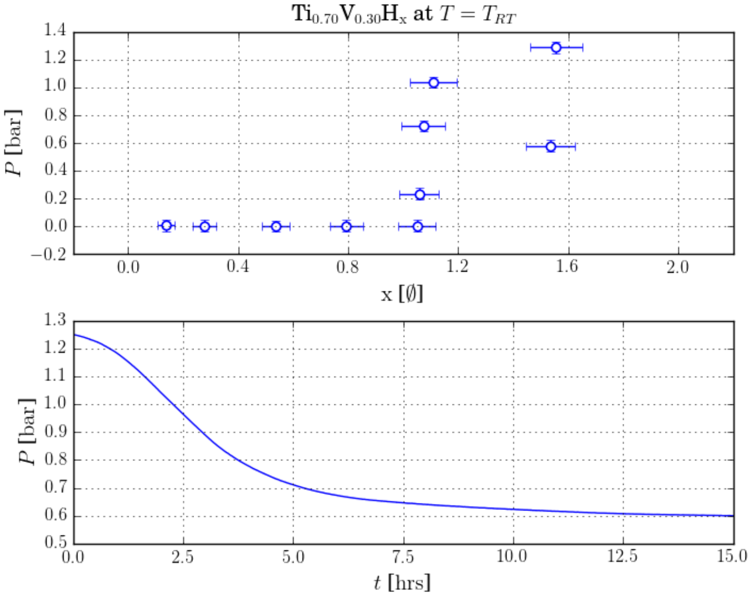

Figure 4.27: The upper figure show the pressure-composition isotherm for the $Ti_{0.70}V_{0.30}H_x$ system at room-temperature T_{RT}. The lower figure show the measured pressure from the valve was opened during the ninth absorption. The measurement was conducted on the B-side Sieverts apparatus.

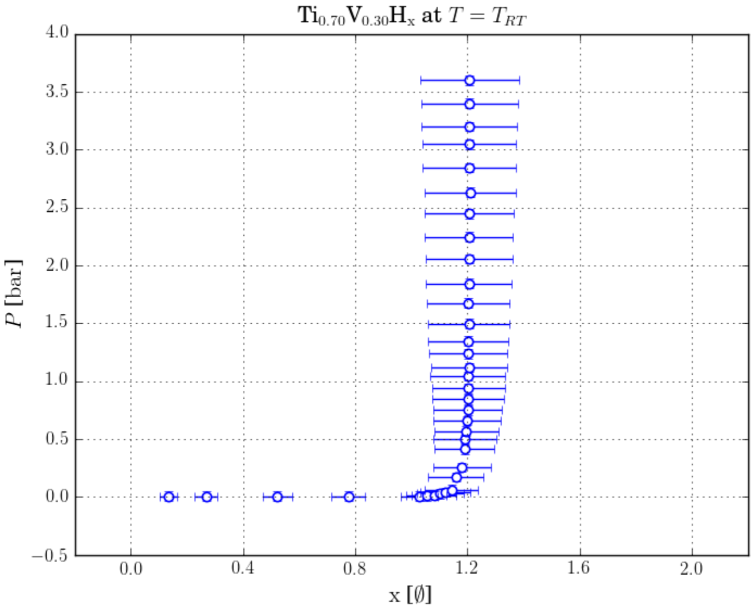

Figure 4.28: Pressure-composition isotherm for the $Ti_{0.70}V_{0.30}H_x$ system at room-temperature T_{RT}. The measurement were conducted on the B-side Sieverts apparatus.

Following this line of reasoning one should expect something similar to happen to the other systems. A PCI curve was therefore measured at room-temperature for the $(Ti_{0.70}V_{0.30})_{0.80}Fe_{0.20}H_x$ as shown in figure 4.29. From this figure it can be seen that this system also inhibit a plateau below the detection limit of the pressure transducer. This plateau seem to end when the molar hydrogen-to-metal ratio reach about x $\sim$ 1.56, which is close to the maximal value that was observed in the first series of kinetics measurements. It is therefore clear that the effect that prevented the hydrogenation of the $Ti_{0.70}V_{0.30}$ system to commence further is not present for the $(Ti_{0.70}V_{0.30})_{0.80}Fe_{0.20}$ system. It does furthermore seem to be another plateau in the range x $\in [1.56, 1.67]$ but the measurement uncertainty has increased significantly at this point in the data accumulation. It is furthermore surprising that the molar hydrogen-to-metal ratio seemingly starts to decrease at the end of this region towards a final value of x $= 1.39$, which is below the observed maximal values in either of the kinetics measurements, at an equilibrium pressure of $P = 171.7$ bar. The measurement uncertainties are however unreasonably large in these final measurements making precise considerations difficult to achieve. As can be seen from the

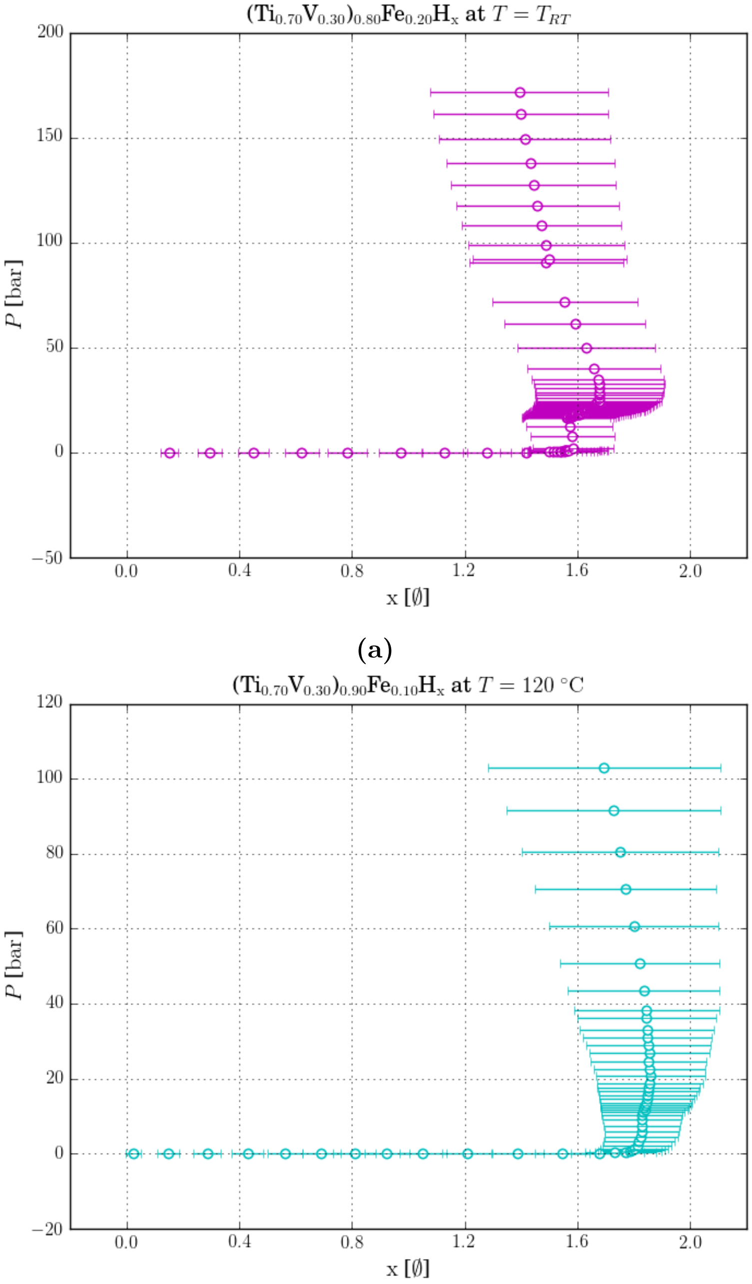

(a)

(b)

Figure 4.29: Pressure-composition isotherms for the $(\mathrm{Ti}_{0.70}\mathrm{V}_{0.30})_{0.80}\mathrm{Fe}_{0.20}\mathrm{H}_\mathrm{x}$ system at room-temperature T_{RT} (a) and the $(\mathrm{Ti}_{0.70}\mathrm{V}_{0.30})_{0.90}\mathrm{Fe}_{0.10}\mathrm{H}_\mathrm{x}$ system at $T = 120$ °C (b). The measurements were conducted on the C-side and B-side Sieverts apparatus respectively.

figure similar observations can be made from the PCI at $T = 120$ °C for the $(\mathrm{Ti}_{0.70}\mathrm{V}_{0.30})_{0.90}\mathrm{Fe}_{0.10}$ system.

The two hydrides were subsequently desorbed in the TG/DSC apparatus to reveal their hydrogen contents. The weight percentage of hydrogen was found to be 2.87% for the $(\mathrm{Ti}_{0.70}\mathrm{V}_{0.30})_{0.80}\mathrm{Fe}_{0.20}$ hydride, and 3.70% for the $(\mathrm{Ti}_{0.70}\mathrm{V}_{0.30})_{0.90}\mathrm{Fe}_{0.10}$. These values correspond to a molar hydrogen-to-metal ratio of $\mathrm{x} = 1.47$ and $\mathrm{x} = 1.89$ respectively. Once again it is reassuring that these values is within the measurement uncertainties in the pressure-composition isotherms. Lab XRD patterns were also measured which revealed that the hydrides were similar to the ones shown in figure 4.2.

It is clear that the plateau pressure associated with the phase transition from the β-bcc hydride phase to γ-fcc-related hydride phase is below atmospheric pressure for the system $(\mathrm{Ti}_{0.70}\mathrm{V}_{0.30})_{1\text{-}\mathrm{y}}\mathrm{Fe}_{\mathrm{y}}\mathrm{H}_{\mathrm{x}}$. In subsection 2.4.3 it was shown that the plateau pressure of the $\mathrm{Ti}_{0.6}\mathrm{V}_{0.4}$ assumed a low value even for high temperatures [52]. With respect to Kagawas observation that increasing titanium contents tend to lower the plateau pressure [49] we should expected a low value also for our $\mathrm{Ti}_{0.70}\mathrm{V}_{0.30}$ system. According to Lynch et al. [50] we should however expect that the iron might raise the plateau pressure. This does not seem to be the case at the considered temperatures. It might however be possible that such observations can be made at higher temperatures, but this has not been pursued further in this work. We are therefore unable to obtain standard enthalpies and entropies of the hydride phase transition from the strategy outlined in subsection 2.3.1. These values are therefore yet to be determined.

4.5 Thermodynamic analysis by TG/DSC

4.5.1 The hydrogen capacity

Three batches of hydrides have been synthesised at this point; the batch that was prepared initially (first batch), the end product from the kinetics measurements with a hydrogen pressure of ∼ 20 bar (second batch) and the end product from the final kinetics measurements (third batch). The hydrogen content of these hydrides were determined gravimetrically by TG/DSC following the procedure outlined in subsection 3.2.4. The determined mass percentage of hydrogen, η, that is present in the different hydrides are shown in figure 4.30. The volumetric estimates from the kinetics measurements following the procedure outlined in appendix A are also shown for comparison.

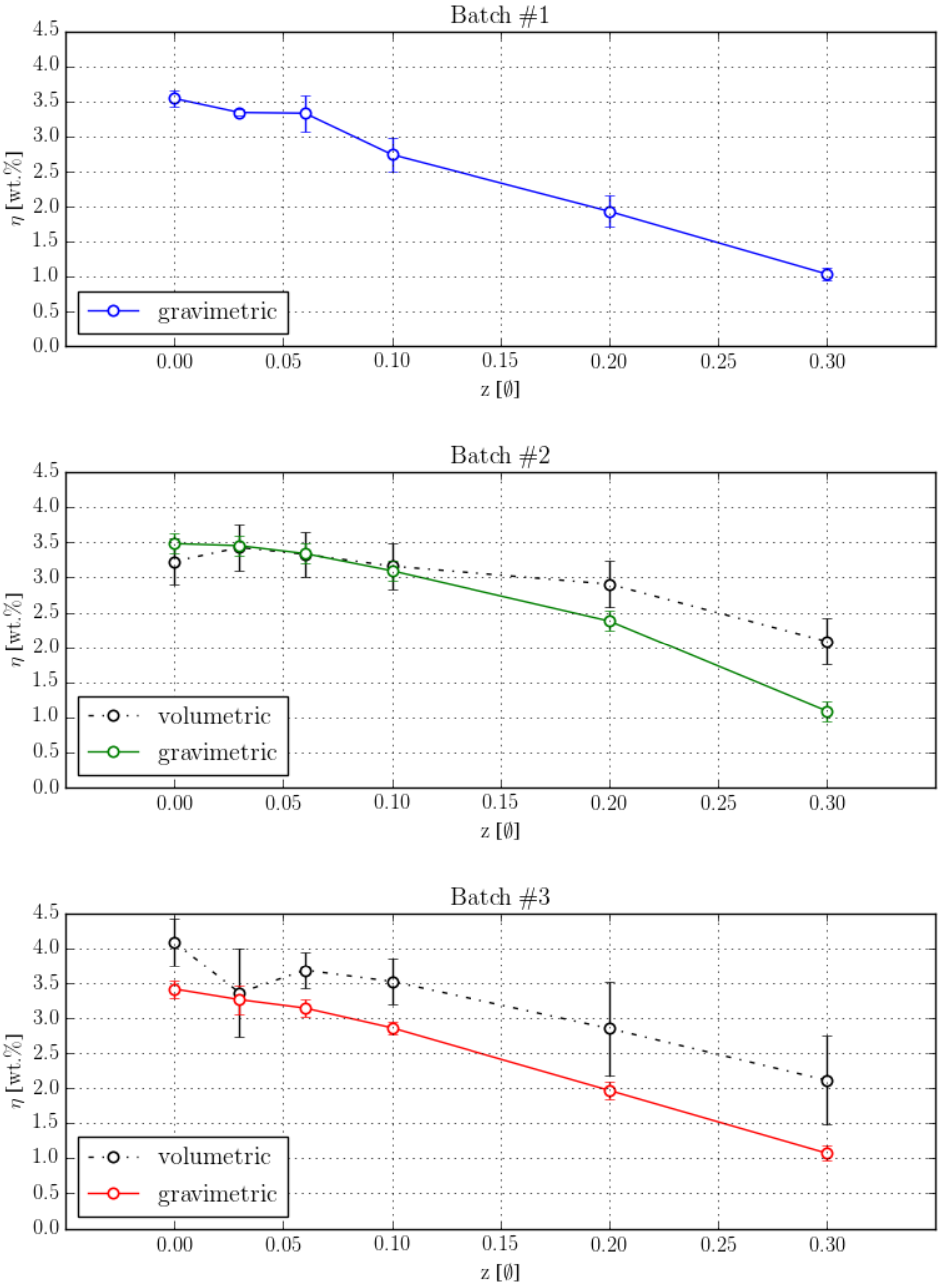

Figure 4.30: The mass percentage of hydrogen η present in the hydrides $(Ti_{0.70}V_{0.30})_{1\text{-}z}Fe_zH_x$ determined by TGA in the TG/DSC apparatus and volumetrically from the kinetics measurements conducted in the prior subsection.

From the figure it is clear that the hydrogen content decrease with increasing amount of iron present in the alloy. It is also clear that the gravimetric estimates for the three different batches are similar. The volumetric estimates of the hydrogen content in the samples with z ≤ 0.10 from the second batch agree with the gravimetric estimates. This is reassuring considering that the new Sieverts apparatus calibration [64] is yet to be tested on well known systems. The volumetric estimates for the samples of higher iron contents in this batch are higher than the gravimetric estimates. This might be due to out-gassing from the samples when they were removed from the high pressure hydrogen atmosphere in the Sieverts apparatus. Another possibility is that the samples are oxidized during transport to or inside the TG/DSC apparatus. If this is the case, and the oxide is reasonably stable, it could be able to trap the hydrogen inside the samples. Oxidation would increase the sample mass so that the hydrogen content seems lower than it really is. PXD-patterns were measured of the samples after desorption in the TG/DSC and the results are shown in figure 4.31. As the lattice parameters in this case are similar to the ones of the pure alloys it is clear that no hydrogen is left inside the samples after desorption. It is however also apparent that the samples have oxidized. Figure 4.32 show two series of desorption measurements in the TG/DSC conducted at different heating rates. From this figure it is readily observable that the mass of the samples increase linearly towards the end of the linear heating segment when the heating rate is 2 K/min. This is indicative of oxidation. When the heating rate is 10 K/min the samples behaves differently and there is no linear increase in the sample mass during the heating segment. It therefore seems that oxidation only have an observable impact upon the relative mass changes of the sample if it is exposed to high temperatures over longer time scales. As a final test, a sample of $(\mathrm{Ti}_{0.70}\mathrm{V}_{0.30})_{0.80}\mathrm{Fe}_{0.20}$ was exposed to a linear heating at 10 K/min in the TG/DSC apparatus. As the sample mass did not increase over the linear heating segment it was concluded that oxidation effects could safely be neglected if the heating rate is $\beta \geq 10$ K/min. Moreover, figure 4.33 show that there is no apparent trend between the mass loss of the sample during the measurement and the applied heating-rate. No measurement has therefore been excluded from the collected statistics that are shown in figure 4.30.

It is interesting that the volumetric estimates of the hydrogen content of the hydrides in batch 3 systematically exceed the gravimetric estimates. This is also the case in the range of low iron contents. A possible explanation is again that the missing hydrogen is out-gassed from the hydrides when they are retrieved from the high-pressure hydrogen atmosphere within

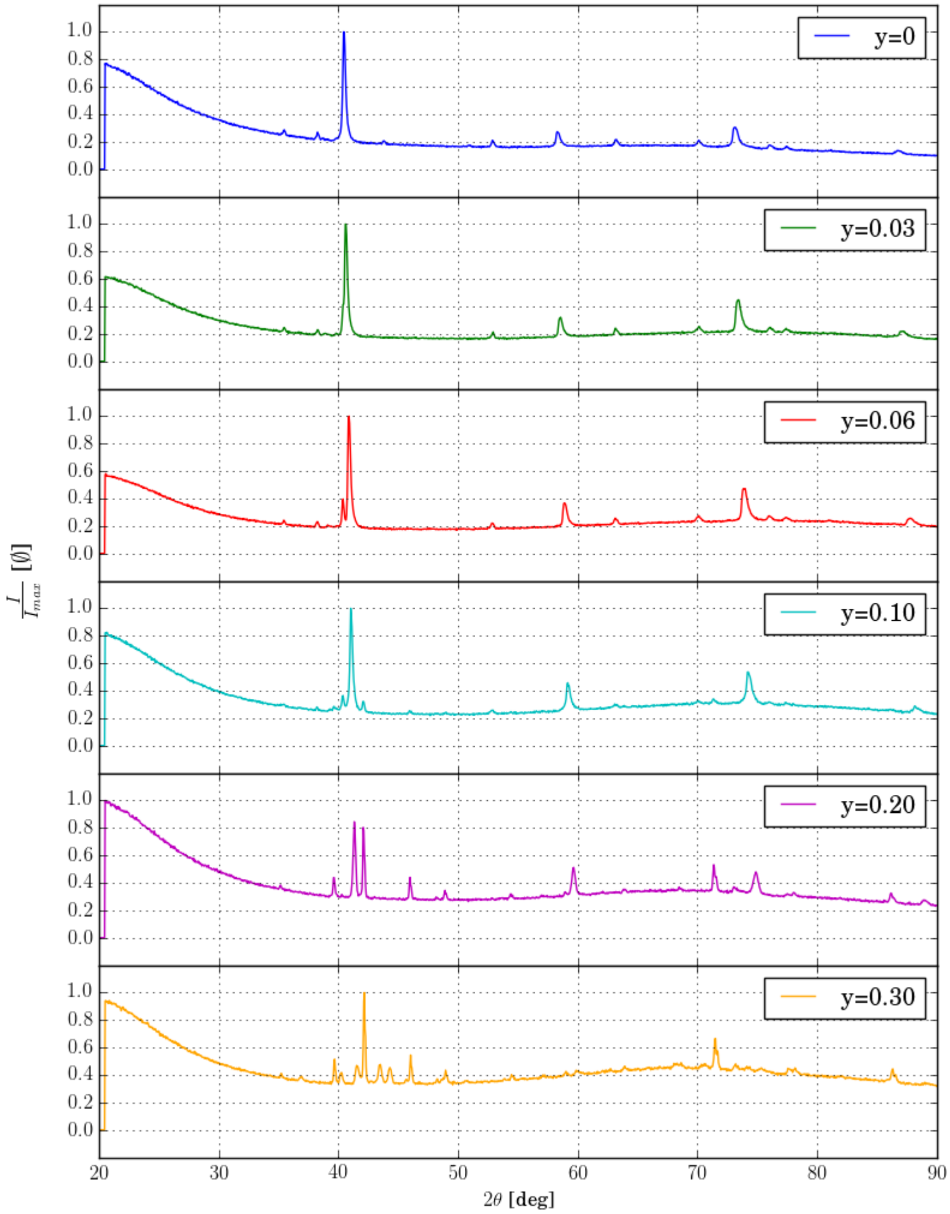

Figure 4.31: The normalized Cu-Kα PXD patterns of the $(Ti_{0.70}V_{0.30})_{1\text{-}z}Fe_z$ samples that were desorbed in the TG/DSC apparatus after they had been synthesised in the series of kinetics measurements with an initial hydrogen pressure of ∼ 20 bar.

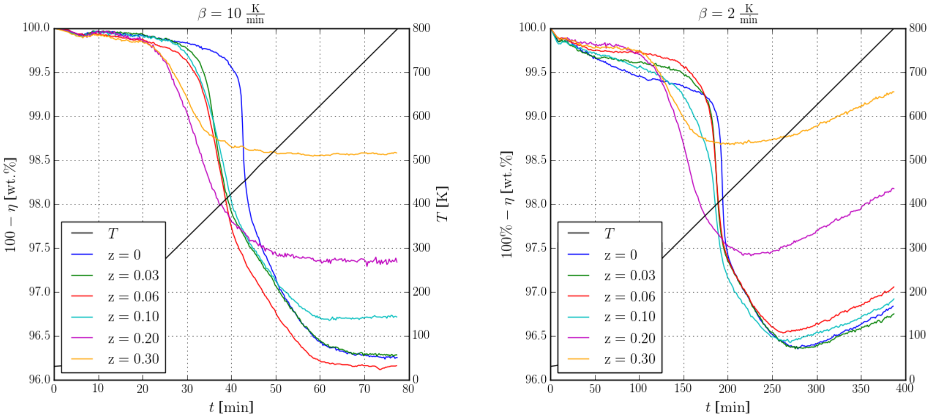

Figure 4.32: The relative mass percentage change of the sample $100\% - \eta$ during TG/DSC at two different heating rates, $\beta = 10$ K/min and $\beta = 2$ K/min. The measured samples were synthesised during the series of kinetics measurement with an initial pressure of ~ 20 bar.

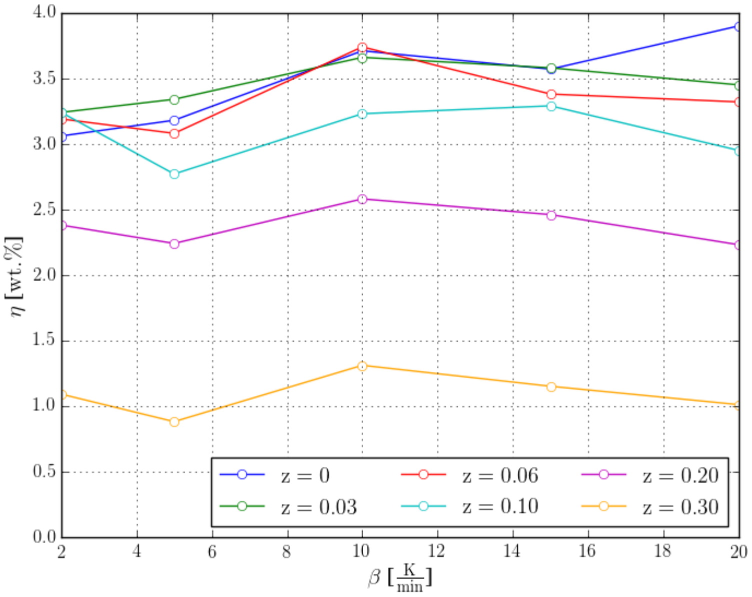

Figure 4.33: The mass percentage of hydrogen η shown as a function of the applied heating rate β. The measured samples were synthesised during the series of kinetics measurement with an initial hydrogen pressure of ~ 20 bar.

the Sieverts apparatus. In the pressure-composition isotherms of figure 4.29 there were some indications of a sloped region at the end of the plateaus. The large measurement uncertainties did however make it impossible to unambiguously determine whether this is a real effect or not. Out-gassing is however possible if such a sloped region extend down to a pressure of about ∼ 1 bar. The final hydrogen content of the resultant hydrides were in subsection 4.4.2 determined to $\eta = 2.87\%$ for $(\mathrm{Ti}_{0.70}\mathrm{V}_{0.30})_{0.80}\mathrm{Fe}_{0.20}\mathrm{H}_{\mathrm{x}}$ and $\eta = 3.70\%$ for $(\mathrm{Ti}_{0.70}\mathrm{V}_{0.30})_{0.90}\mathrm{Fe}_{0.10}\mathrm{H}_{\mathrm{x}}$. These values are close to the volumetric estimates in figure 4.30. This observation is interesting if we consider that the volumetric estimates tend to exceed their gravimetric counterparts. The main difference between this sample and the ones having hydrogen contents shown in figure 4.30 is the time they spent in the Sieverts apparatus. The typical measurement of a pressure-composition isotherm lasts several weeks while the typical kinetics measurement only last a couple of days. This mean that if oxides are able to form on the sample surfaces within the Sieverts apparatus one should expect the effect to be enhanced if the sample is present in the apparatus for a longer time period. It is therefore possible that such an oxide has formed on the surface of the "PCI-samples" while it did not form, or at least not to the same extent, on the samples originating from the kinetic measurements. Following this line of reasoning the oxide layer on the surfaces of the "PCI-samples" traps the hydrogen. The out-gassing is thereby prohibited from these samples as opposed to the others when they are retrieved from the high pressure hydrogen atmosphere within the Sieverts apparatus.

From figure 4.30 it is clear that the deviation between the volumetric and gravimetric estimates increase with the amount of iron. If the observed discrepancies are due to out-gassing from the samples we should expect the iron to destabilize the hydrides. The desorption enthalpies were therefore determined following the procedure outlined in subsection 3.2.4. This was done for all three batches of hydrides to enable comparison. Figure 4.34 show the estimates from the 10 K/min heating rate TG/DSC measurements for all three batches. These results clearly indicate that an increasing amount of iron in the alloy lower the desorption enthalpy of the hydrides. This is as expected from the discussion above. It therefore seem likely that the observed discrepancies between the volumetric and gravimetric estimates shown in figure 4.30 are due to out-gassing from the sample.

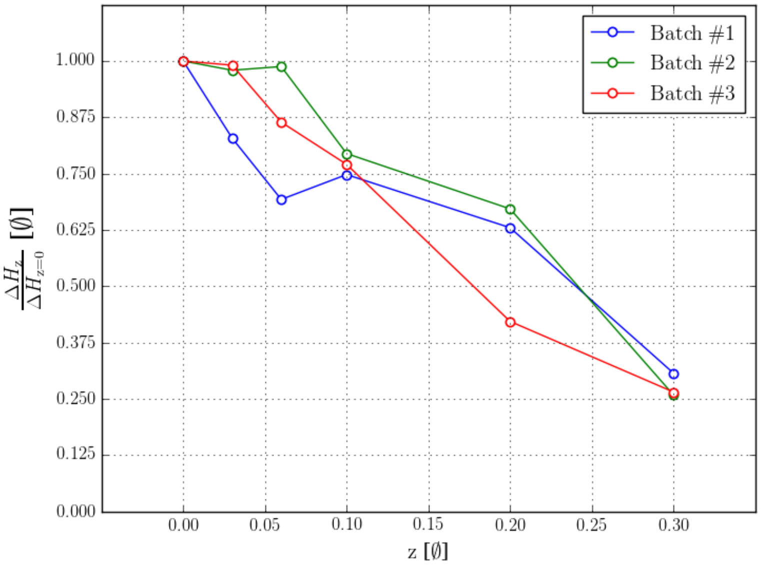

Figure 4.34: Hydrogen desorption enthalpies ΔH_{z} for the system $(\mathrm{Ti}_{0.70}\mathrm{V}_{0.30})_{1\text{-}z}\mathrm{Fe}_z\mathrm{H}_x$ normalized to the desorption enthalpy $\Delta H_{\mathrm{z}=0}$ of the iron-free compound $\mathrm{Ti}_{0.70}\mathrm{V}_{0.30}\mathrm{H}_x$. The desorption enthalpies for either sample in any of the three batches are taken from the TG/DSC measurements that were conducted at a constant heating rate of 10 K/min.

4.5.2 Kissinger analyses

In the metal hydride the hydrogen atoms are bonded to the metal at interstitial sites. If the hydrogen is to be desorbed from the metal hydride these bonds must be broken. This is often an endothermic reaction. The strength of these bonds depend on the properties of the neighbouring atoms and the distance between these and the hydrogen. If the hydrogen atoms occupy tetrahedral sites in the dihydrides they are bonded to four neighboring atoms. In our Ti-V-Fe solid solution alloys these neighbouring atoms can be any combination of the metallic constituents. The binding energies of the hydrogen atoms within the metal hydride must therefore be described by an energy spectrum. It is however possible that certain configurations of neighbouring atoms are more probable than others. The desorption from such interstitial sites will in that case manifest itself as easily distinguished peaks in the heat flow during a TG/DSC measurement.

Figure 4.35 show the onset temperatures T_{onset} for the desorption process for the three different batches of hydrides. The onset temperature of the reference system in the second batch is significantly higher than what is observed for the other batches. It therefore seem that something prohibit the sample from desorbing when this process is thermodynamically possible. The other estimates are however in good agreement and it is clear that the increased amount of iron present in the alloy tend to lower the onset temperature. This trend is in accordance with the decreasing desorption enthalpy with increasing iron content.

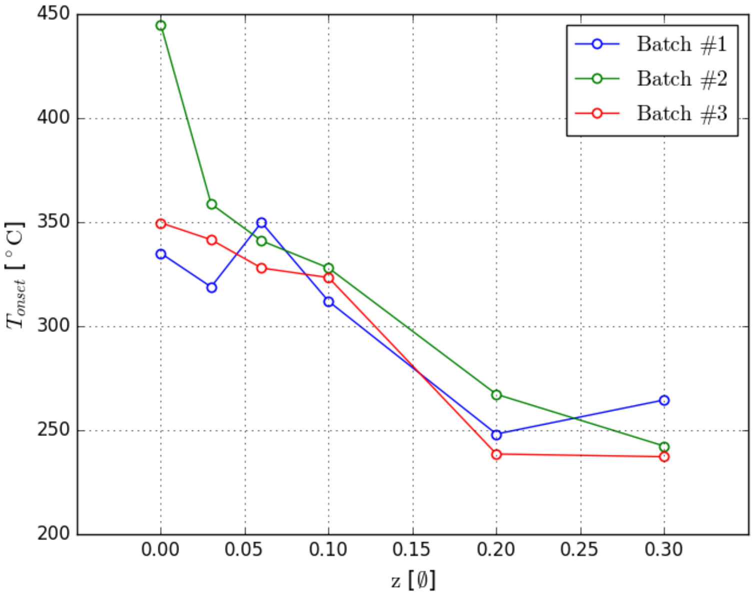

Figure 4.35: The onset temperature T_{onset} for desorption of hydrogen from the three different batches of $(\mathrm{Ti}_{0.70}\mathrm{V}_{0.30})_{1\text{-}z}\mathrm{Fe}_z\mathrm{H}_x$. The values are taken from the TG/DSC measurements with a constant heating rate of 10 K/min.

Figure 4.36 show the DSC heat flow, Φ_m, and the corresponding Kissinger analyses of two hydrides, $\mathrm{Ti}_{0.70}\mathrm{V}_{0.30}\mathrm{H}_x$ and $(\mathrm{Ti}_{0.70}\mathrm{V}_{0.30})_{0.90}\mathrm{Fe}_{0.20}\mathrm{H}_x$, from the third batch. For the iron-free sample it seem to be two major events in the desorption process, as indicated by the two peaks in the heat flow signal. One of these occur at a significantly higher temperature than the other. The main part of the desorption is however represented by the first peak. When iron is introduced into the alloy this main event splits into two. Such a splitting is observed for all the iron containing hydrides from the third batch hydrides, regardless of the amount of iron that is present in the alloy. This can be seen in the figures E.1-E.6. The corresponding Kissinger analyses are also shown in these figures. The apparent activation

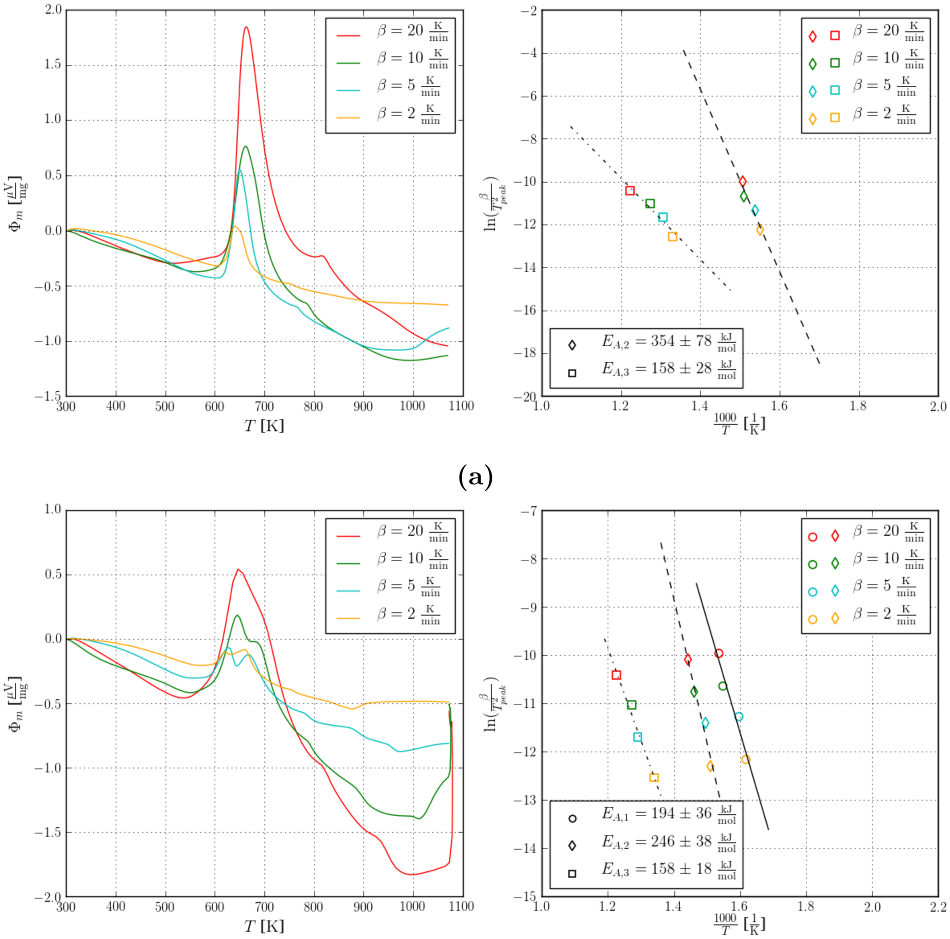

(a)

(b)

Figure 4.36: Kissinger analysis performed on the DSC measurements of $Ti_{0.70}V_{0.30}H_x$ (a) and $(Ti_{0.70}V_{0.30})_{0.90}Fe_{0.10}H_x$ hydrides from the third batch at different heating rates β. The left part of the figures show the measured heat flow signals Φ_m while the right parts show the corresponding Kissinger plot with a simple linear regression fit for the observed events. The *apparent* activation energies $(E_{A,1},)$ $E_{A,2}$ and $E_{A,3}$ were determined following the procedure outlined in subsection 3.2.4. It should be noted that the peaks are endothermic reactions.

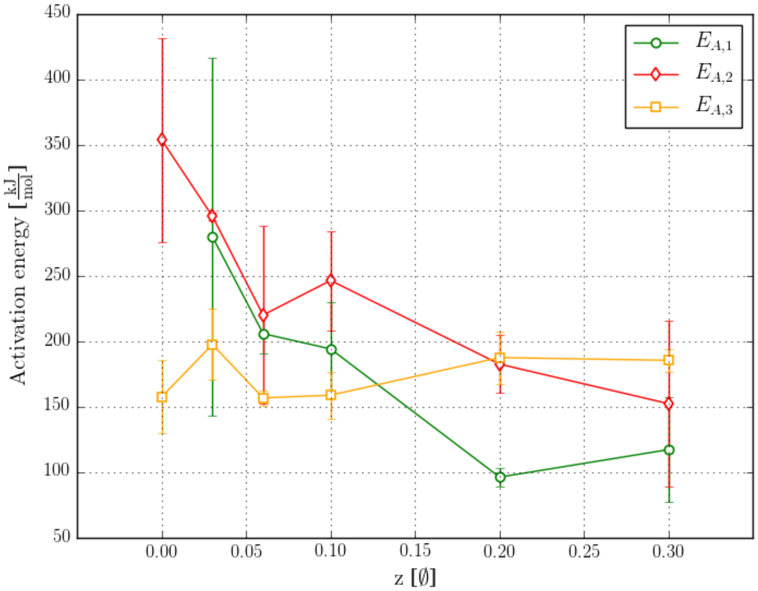

Figure 4.37: *Apparent* activation energies E_A for the three different events that was observed by TG/DSC during desorption of hydrogen from the system $(\mathrm{Ti}_{0.70}\mathrm{V}_{0.30})_{1\text{-}z}\mathrm{Fe}_z\mathrm{H}_x$. The numerical values were determined in the Kissinger analyses of figures E.1-E.6.

energies from the Kissinger analyses are shown in figure 4.37. There are considerable uncertainties associated with certain measurements, but at the same time some clearly visible trends. The apparent activation energy of the main event, $E_{A,2}$, tend for instance to decrease with increasing iron content. A similar trend is observed for the event that splits out of it, and the apparent activation energy, $E_{A,1}$, is generally below that of the main event. The decreasing activation energies with increasing iron content is similar to what was observed for the titanium-rich Ti-V-Cr system by Suwarno et al. [54] under addition of chromium to the alloy. The activation energy of the high-temperature event, $E_{A,3}$, finally seem to assume a rather constant value regardless of content of iron. This final observation indicate that the third event is associated with hydrogen desorption from iron-free interstitial sites in the metal hydride. As the event occur at a higher temperature than the others it seems that this kind of interstitial site bind the hydrogen atoms stronger than those affected by the iron.

It should be mentioned that an attempt was made to determine whether the $\mathrm{Zr}_7\mathrm{Ni}_{10}$ had any influence on the activation energies of the desorption.

The results are however inconclusive and has therefore been omitted for the sake of brevity.

In section 4.3 it was observed by *in-situ* SR-PXD that the hydrogen was not completely desorbed from the $(\mathrm{Ti_{0.70}V_{0.30}})_{0.97}\mathrm{Fe_{0.03}H_x}$ hydride when it was exposed to a maximum temperature of 500 °C. From the DSC heat flow signals of figure E.2 it can be seen that the on-set temperature of the high-temperature event for this hydride is in the proximity of the applied maximum temperature during the *in-situ* SR-PXD measurement. As the final state of the $(\mathrm{Ti_{0.70}V_{0.30}})_{0.97}\mathrm{Fe_{0.03}H_x}$ hydride in the *in-situ* SR-PXD measurement was a body-centred cubic hydride it seems that the high temperature event can be associated with the final desorption of hydrogen from this phase. It was furthermore observed by *in-situ* SR-PXD that the reaction did not initiate until the temperature reached about 432 °C when the sample was heated to the maximum temperature at a linear heating rate of 5 K/min. This is higher than any of the observed onset temperatures for that heating rate in the TG/DSC apparatus[6]. It therefore seems likely that the SR-PXD sample was indeed passivated as proposed in section 4.3.

---

[6] For the $(\mathrm{Ti_{0.70}V_{0.30}})_{0.97}\mathrm{Fe_{0.03}H_x}$ hydride of batch 2 the onset temperature was for instance $T_{onset} = 377$ °C in the TG/DSC.

Chapter 5

Concluding remarks

The synthesis, crystal structure and hydrogen sorption properties of titanium rich, body-centred cubic solid solutions of titanium, vanadium and iron have been studied. The considered system was chosen as $(\mathrm{Ti}_{0.70}\mathrm{V}_{0.30})_{1\text{-z}}\mathrm{Fe}_{\mathrm{z}}$ with $\mathrm{z} \in \{0, 0.03, 0.06, 0.10, 0.20, 0.30\}$. The ability of $\mathrm{Zr}_7\mathrm{Ni}_{10}$ to act as a sorption catalyst has also been considered.

The alloys were synthesised by arc melting and a body-centred cubic main phase, α, was obtained for all the considered systems by quenching the melt. A small amount of impurity phase is however observed alongside the main phase. This is an hexagonal-close packed phase, δ, for $\mathrm{z} \leq 0.20$ while it is a C14 Laves phase for $\mathrm{z} = 0.30$. The former seems to be a solid-solution of Ti, V and Fe. The addition of iron cause the α-bcc unit cell to contract and the lattice parameter is observed to decrease linearly with increasing iron content. The lattice parameters of the δ-hcp phase increase slightly with the addition of iron. Upon hydrogenation the system assume a *face-centred cubic related* dihydride phase, γ, for iron contents below 10%. The term *related* is utilized to emphasize that it seem to be exposed to planar defects such as stacking faults and twin boundaries. The peaks in the X-ray diffraction patterns therefore slightly shift positions and assume odd profiles which prevent the achievement of a proper structural refinement. The δ-hcp phase is not readily visible in the X-ray diffraction patterns, but *in-situ* SR-PXD measurements indicate that it might form a face-centred cubic hydride, ϵ, of its own. *In-situ* SR-PXD measurements furthermore indicate that the α-bcc phase initially transform into a body-centred cubic hydride, β, before the γ-fcc-related hydride form. The hydrogen sorption therefore seem to follow

$$\alpha \xrightleftharpoons{H_2} \beta \xrightleftharpoons{H_2} \gamma$$

$$\delta \xrightleftharpoons{H_2} \epsilon$$

A pure dihydride phase for the highest contents of iron seem to be unreachable under the experimental conditions that has been considered in this work.

The hydrogen absorption kinetics are fast for all the considered compounds and the reaction is practically finished within minutes when exposed to an initial hydrogen pressure of $\sim$ 20 bar at room-temperature. The ability of Zr_7Ni_{10} to enhance this further has therefore not been considered. The hydrogen capacities of the different compounds seem to be stable during the first three hydrogenation/dehydrogenation cycles. Both volumetric and gravimetric estimates of the final hydrogen contents have been obtained, and the hydrogen capacity reach $\sim$ 3.5 wt.% for the iron-free compound. The capacity decrease with the addition of iron, but it is still around 3.0 wt.% when the iron content reach 10 at.%. The volumetric and gravimetric estimates agree reasonably well, but the volumetric estimate tend to exceed the gravimetric for higher contents of iron. In this respect it has been found that the desorption enthalpy decrease as the content of iron in the alloy is increased. Hence, the iron destabilize the hydride and the observed discrepancies between the volumetric and gravimetric estimates seem to be due to out-gassing from the sample. Such deviations become the general trend when the hydrides are synthesised with an initial hydrogen pressure of $\sim$ 190 bar. In this case the volumetric estimate for the iron-free hydride approach the expected maximum of 4 wt.%, but the gravimetric estimate is similar to those obtained for the hydrides that were synthesised at milder experimental conditions. This is once again thought to be due to out-gassing when the sample is retrieved from the high pressure hydrogenous atmosphere.

Pressure-composition isotherms have furthermore been measured for selected systems. These hold a single plateau with plateau-pressure below the detection limit of the applied pressure-transducer. The iron does not influence this at temperatures below 120 °C within the sensitivity of the measurements.

The desorption process were finally studied by differential scanning calorimetry. The hydrogen desorption process from the iron-free hydride seem to be composed of two major events. The first of these have an onset temperature around 350 °C and can be associated with the desorption from the γ-fcc-related hydride. The second occur at a higher temperature and can be associated with the final desorption from the β-bcc hydride. The first event splits into two for the iron-containing alloys and the onset temperature of the desorption process decrease with the increasing iron content. The splitting is thought to be due to local differences between the interstitial sites that accommodate the hydrogen atoms. Apparent activation energies for the three different events have been determined through Kissinger analyses. The activation energies of the two lower temperature events seem to decrease as the amount of iron in the alloy increase. The activation energy of the high temperature event is on the contrary independent of the of iron content in the alloy. This indicate that it can be associated with hydrogen desorption from interstitial sites that are not surrounded by iron. These sites furthermore seem to bind the hydrogen atoms stronger than those affected by the iron.

This work was motivated by the possibility to replace the expensive vanadium by the much cheaper ferrovanadium. This study has shown that an alloy of $Ti_{0.70}V_{0.30}$ actually benefit from the addition of up to 10 at.% iron. With only a modest reduction in hydrogen capacity, the iron eliminate the need for activation procedures [22], lower the onset temperature for desorption and the hydrogen capacity seems stable over the first three hydrogenation/dehydrogenation cycles. However, ferrovanadium contain smaller amounts of other impurities, such as silicon and aluminium and it is therefore recommended that further studies investigate the influence of these elements upon the structure and hydrogen sorption properties of the titanium rich Ti-V-Fe alloys. The long-term cyclability of the material should also be studied in further detail.

Appendices

Appendix A

Sorption experiments in the Sieverts apparatus

A.1 Summary of calibration

There are two different scenarios under which measurements are conducted in the Sieverts apparatus. In the simplest case the oven is turned off and the entire apparatus can be considered as situated inside a large thermal reservoir at room temperature T_{RT} as shown in figure A.1. In the more complicated scenario the oven is set at a temperature T_{oven} and raised to surround part of the sample-holder volume V_4 as shown in figure A.2. The thermistor that is coupled to the sample-holder hence measure a temperature $T_{sample} \neq T_{RT}$. The rest of the apparatus is however still at room temperature T_{RT} and it will therefore be a temperature gradient somewhere within the rig. In a typical measurement H_2-gas is filled into either the large volume

$$V_{large} = V_1 + V_2 + V_3 \tag{A.1}$$

or the small volume

$$V_{small} = V_2 + V_3 \tag{A.2}$$

to a pressure P_i. The sample is situated inside the sample-holder volume V_4 where it is assumed to be in equilibrium with the H_2-gas at a pressure P_j. The two volumes are separated by the valve labelled 6 which is closed. As the valve 6 is opened the environment of the sample is disturbed from its former equilibrium condition and the sample will - depending on the pressure P that sets in inside the combined volume - either release or absorb hydrogen until a new equilibrium is reached. It is therefore possible to determine the amount of moles of hydrogen that is released or absorbed by the sample if the pressure P that would ensue if the sample was not present is known. Two equations - one for the isothermal case and another for the situation where the oven is turned on - have therefore been established in the calibration [64] that predict the final pressure P that would ensue within two volumes V_i and V_j accommodating gas at pressures P_i and P_j if the valve that initially separated the volumes are opened and no sample were present inside the volume V_j.

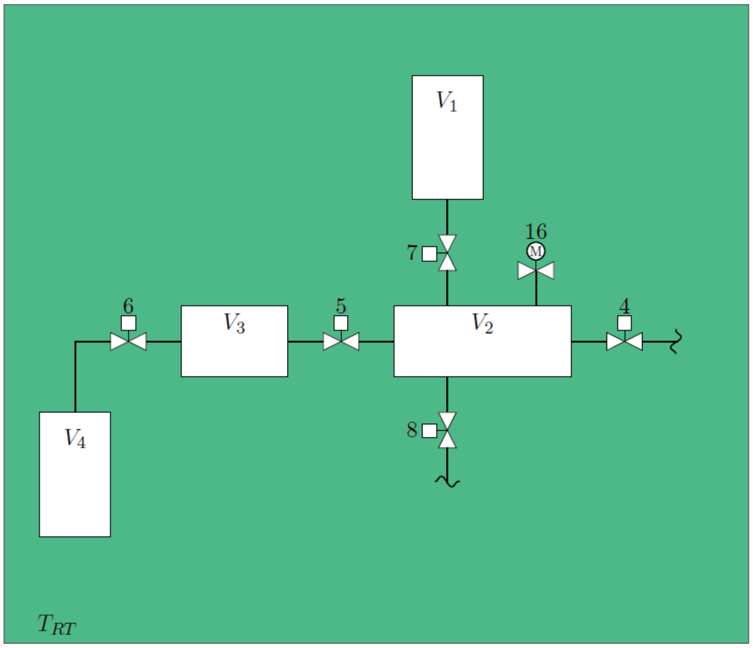

Figure A.1: The simplified Sieverts apparatus schematic. The volume V_1 is the pre-calibrated volume, V_2 is the volume of the Sieverts manifold situated inside the temperature cabinet, V_3 is the volume of the manifold between the temperature cabinet and the sample-holder volume V_4. All four volumes are at room temperature T_{RT}. The pressure is monitored by a pressure transducer labelled 16. Note how the numbering of the valves corresponds to the global schematic of figure 3.7.

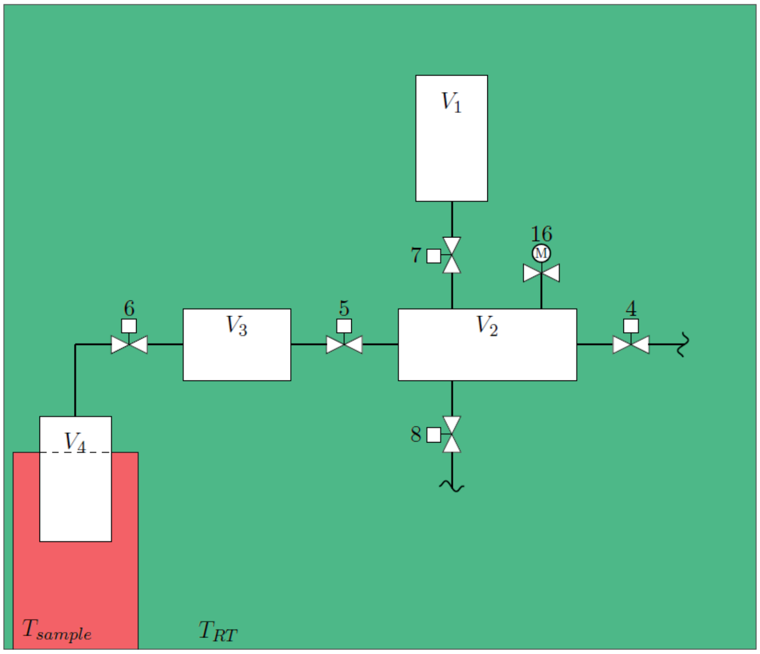

Figure A.2: The simplified Sieverts apparatus schematic. The volume V_1 is the pre-calibrated volume, V_2 is the volume of the Sieverts manifold situated inside the temperature cabinet, V_3 is the volume between the manifold and the oven and V_4 is the volume of the sample-holder. The volumes V_1, V_2 and V_3 are at room temperature T_{RT} and the volume V_4 can be divided into one part at temperature T_{RT} and another at temperature T_{sample}. The temperature gradient between the respective parts is indicated by the dashed line in accordance with the assumptions of the model. The pressure is monitored by the pressure transducer labelled 16. Note how the numbering of the valves corresponds to the global schematic of figure 3.7.

The isothermal model

For the isothermal scenario it can be shown [64] that the final pressure P is given as

$$P = \left(\frac{Z_i' Z_j'}{Z_i Z_j}\right)\left(\frac{T_i' T_j'}{T_i T_j}\right)\left[\frac{Z_j T_j V_i P_i + Z_i T_i V_j P_j}{Z_j' T_j' V_i + Z_i' T_i' V_j}\right] \tag{A.3}$$

where V_i and V_j are the two volumes, $Z_i = Z(P_i, T_i)$ and $Z_j = Z(P_j, T_j)$ are the initial compressibility factors of the gas within the two volumes at pressures P_i and P_j and temperatures T_i and T_j while $Z_i' = Z(P, T_i')$ and

$Z'_j = Z(P, T'_j)$ are the final compressibility factors for the gas within the combined volume $V = V_i + V_j$ at pressure P and temperatures T'_i and T'_j. It should be noted that the following assumptions has been made upon arriving at the equation A.3:

- Initially both volumes V_i and V_j are at thermodynamic equilibrium with the thermal reservoir at temperature T.
- The final combined system with volume $V = V_i + V_j$ is similarly allowed to reach thermodynamic equilibrium before any measurements are recorded. This includes thermal equilibrium with the thermal reservoir.
- The thermal reservoir is sufficiently large so that its temperature can be considered as relatively constant.
- The gas inside the volumes obey the ideal gas law - possibly with a compressibility factor different from unity - in both the initial and final state of the systems.
- The system is completely sealed so that there is no leakage of gas from the system.

The model with a first order temperature gradient

For the heated scenario a model implementing a first order temperature gradient was assumed and through this approach it was shown [64] that the final pressure P is given by

$$P = \frac{1}{\Lambda}\frac{Z_-}{Z_i}\frac{T_a}{T_{a,i}}\frac{V_i}{V_i + V_j}P_i + \frac{\Lambda_j}{\Lambda}\frac{Z_-}{Z_{j,-}}\frac{T_a}{T_{a,j}}\frac{V_j}{V_i + V_j}P_j \tag{A.4}$$

where we have introduced the dimensionless parameter Λ_{label} as

$$\Lambda_{label} = 1 - x_{label}\left(1 - \frac{Z_{label,-}}{Z_{label,+}}\frac{T_{a,label}}{T_{b,label}}\right) \tag{A.5}$$

where the *label* is either blank or j, and with V_i and V_j as the volumes accommodating the gas, $Z_i = Z(P_i, T_{a,i})$, $Z_{j,+} = Z(P_j, T_{b,j})$ and $Z_{j,-} = Z(P_j, T_{a,j})$ as the initial compressibility factors of volume V_i and the heated and cool part of V_j at pressures P_i and P_j and temperatures T_a and T_b respectively while $Z_+ = Z(P, T_b)$ and $Z_- = Z(P, T_a)$ are the final compressibility factors of the hot and cold volumes at pressure P and respective temperatures T_b and T_a. x is furthermore the heated fraction of the total volume

$$x = \frac{V_{heated}}{V_i + V_j - V_{sample}} \tag{A.6}$$

and x_j is the heated fraction of the sample-holder volume given as

$$x_j = \frac{V_{heated}}{V_j - V_{sample}} \tag{A.7}$$

It should be noted that the following assumptions has been made upon arriving at equation A.4:

- Initially the the volume V_i is at thermodynamic equilibrium with the thermal reservoirs at relatively constant temperature T_a.
- Initially the parts of the volume V_j - $V_{j,cool}$ and $V_{j,heated}$ - are at thermodynamic equilibrium with their respective thermal reservoirs at relatively constant temperatures T_a and T_b.
- The final combined system with volume $V = V_i + V_j$ is in mechanical and diffusive equilibrium but the two volumes are still in thermal equilibrium with their respective thermal reservoirs. Hence there is a temperature gradient at the interstice between the two volumes.
- The extent of the temperature gradient between the volumes is negligible.
- Both thermal reservoirs are very large so that their temperatures T_a and T_b remain relatively constant.
- The gas inside the volumes obey the ideal gas law - possibly with a compressibility factor different from unity - in both the initial and final state of the system.
- The system is completely sealed so that there is no leakage of gas from the system.

It is finally comforting to verify that the expression A.4 is reduced to the isothermal result of the equation A.3 when $T_a = T_b$ which means that $Z_- = Z_+ = Z$ and $Z_{j,+} = Z_{j,-} = Z_j$.

The heated volume V_{heated} was determined in the calibration for the sample-holder labelled #12B at the B-side Sievert apparatus through a simple linear regression performed on data that was collected as

$$V_{heated} = 7.364 + (0.002244\frac{1}{\mathrm{K}}) \cdot T_{sample} \pm 0.313 \text{ mL} \tag{A.8}$$

where T_{sample} is the temperature measured in kelvin by the thermal resistor that is coupled to the sample-holder. It was also shown that this relation yield acceptable results on the C-side Sieverts apparatus with the sample-holder labelled #10B. This enable the determination of the heated fractions x and x_j for different volumes V_i and V_j where V_i can be either the small volume V_{small} or the large volume V_{large} while V_j is the sample-holder volume. There is however still another obstacle that must be worked around before we can apply these equations since final pressure P is needed for computing the compressibility factors $Z_i' = Z(P, T_i')$, $Z_j' = Z(P, T_j')$, $Z_+ = Z(P, T_b)$ and $Z_- = Z(P, T_a)$ that are contained in the expressions A.3 and A.4. The best way to work around this is to perform an iteration of J steps starting from the assumption that $P \to \widetilde{P}_1 = P_i$ in the compressibility factors and with application of the final expressions for calculating the pressures P determining more and more accurate values for the final pressures $\{\widetilde{P}_\alpha\}_{\alpha=1}^{J}$ to compute more and more accurate values for the compressibility factors $\widetilde{Z}_i' = Z(\widetilde{P}_\alpha, T_i')$, $\widetilde{Z}_j' = Z(\widetilde{P}_\alpha, T_j')$, $\widetilde{Z}_+ = Z(\widetilde{P}_\alpha, T_b)$ and $\widetilde{Z}_- = Z(\widetilde{P}_\alpha, T_a)$. With the implementation of such an iteration procedure the proposed set of equations A.3 and A.4 have been thoroughly tested and the calibration document [64] show that the results can be considered as satisfactory.

A.2 Sorption at ambient temperatures

Let us consider the situation where two volumes V_i and V_j' are filled with H_2-gas to respective pressures of P_i and P_j and placed within a large isothermal reservoir of temperature T_{RT}. We assume that a sample occupies the volume V_{sample} within the volume V_j' so that $V_j = V_j' - V_{sample}$. A typical measurement consist of a series of $N+1$ data-points $\{k\}_{k=0}^{N}$ that are collected at time intervals $\Delta t = 30$ s. A H_2-gas pressure P_j is initially established inside the sample-holder volume V_j. The volume V_i is on the other hand filled with H_2-gas to a pressure P_i and the two volumes are separated by a closed valve. When the valve is opened the gas will flow towards the sample that will sorb some of the H_2 molecules if it is activated. The pressure that would establish itself within the combined volume $V_i + V_j - V_{sample}$ in the absence of any sorbing sample can in turn be predicted from equation A.3. Let us therefore determine the sorbed amount of moles of hydrogen by the sample $n_{k,\,iso}$ after k data-points has been collected. If the molar amount of H_2

molecules present within the system before the valve is opened is n_0 and the amount of moles present when the k'th data-point is collected is n_k we have that the absorbed molar amount of hydrogen by the sample $n_{k,\, iso}$ is given as

$$\begin{aligned} n_{k,\, iso} &= 2(n_0 - n_k) \\ &= 2\left(\frac{P_0^{calc} V_i}{Z_{i,\,0}^{calc} R T_{i,0}} + \frac{P_0^{calc} V_j}{Z_{j,0}^{calc} R T_{j,0}} - \frac{P_k^{meas} V_i}{Z_{i,k}^{meas} R T_{i,k}} - \frac{P_k^{meas} V_j}{Z_{j,k}^{meas} R T_{j,k}} \right) \end{aligned} \tag{A.9}$$

where the pre-factor 2 is introduced to account for the fact that there are two hydrogen atoms in a H_2 molecule and we in the second step have utilized the ideal gas law 3.22. It should be noted that P_0^{calc} is the calculated pressure given by equation A.3, P_k^{meas} is the measured pressure at data-point k, $T_{i,k}$ is the temperature measured by the thermistor within the manifold at data-point k, $T_{j,k}$ is the temperature measured by the thermistor coupled to the sample-holder at data-point k, R is the universal gas constant and $Z_{i,0}^{calc} = Z(P_0^{calc}, T_{i,0})$, $Z_{j,0}^{calc} = Z(P_0^{calc}, T_{j,0})$, $Z_{i,k}^{meas} = Z(P_k^{meas}, T_{i,k})$ and $Z_{j,k}^{meas} = Z(P_k^{meas}, T_{j,k})$ are the associated compressibility factors.

Error analysis

Under the assumption that all the measurement errors are independent and randomly distributed the uncertainty in the absorbed amount of moles $\delta n_{abs,iso}$ is given by

$$\begin{aligned} \delta n_{abs,iso} = \Bigg[& \left(\frac{\partial n_{abs,iso}}{\partial P^{calc}} \delta P^{calc} \right)^2 + \left(\frac{\partial n_{abs,iso}}{\partial P^{meas}} \delta P \right)^2 + \left(\frac{\partial n_{abs,iso}}{\partial T_i} \delta T \right)^2 \\ & + \left(\frac{\partial n_{abs,iso}}{\partial T_j} \delta T \right)^2 + \left(\frac{\partial n_{abs,iso}}{\partial Z_i^{calc}} \delta Z \right)^2 + \left(\frac{\partial n_{abs,iso}}{\partial Z_j^{calc}} \delta Z \right)^2 \\ & + \left(\frac{\partial n_{abs,iso}}{\partial Z_i^{meas}} \delta Z \right)^2 + \left(\frac{\partial n_{abs,iso}}{\partial Z_j^{meas}} \delta Z \right)^2 + \left(\frac{\partial n_{abs,iso}}{\partial V_i} \delta V_i \right)^2 \\ & + \left(\frac{\partial n_{abs,iso}}{\partial V_j} \delta V_j \right)^2 \Bigg]^{\frac{1}{2}} \end{aligned} \tag{A.10}$$

where the uncertainties δP, δT and δZ are given by relations 3.4, 3.5 and 3.25 respectively, while the uncertainty in the pressure δP^{calc} is determined as in the calibration document [64] and the derivatives are given as

$$\frac{\partial n_{abs,iso}}{\partial P^{calc}} = \frac{2}{R}\left[\frac{V_i}{Z_i^{calc}T_i} + \frac{V_j}{Z_j^{calc}T_j}\right] \tag{A.11}$$

$$\frac{\partial n_{abs,iso}}{\partial P^{meas}} = -\frac{2}{R}\left[\frac{V_i}{Z_i^{meas}T_i} + \frac{V_j}{Z_j^{meas}T_j}\right] \tag{A.12}$$

$$\frac{\partial n_{abs,iso}}{\partial T_i} = \frac{2V_i}{RT_i^2}\left[\frac{P^{meas}}{Z_i^{meas}} - \frac{P^{calc}}{Z_i^{calc}}\right] \tag{A.13}$$

$$\frac{\partial n_{abs,iso}}{\partial T_j} = \frac{2V_j}{RT_j^2}\left[\frac{P^{meas}}{Z_j^{meas}} - \frac{P^{calc}}{Z_j^{calc}}\right] \tag{A.14}$$

$$\frac{\partial n_{abs,iso}}{\partial Z_i^{calc}} = -2\frac{P^{calc}V_i}{(Z_i^{calc})^2RT_i} \tag{A.15}$$

$$\frac{\partial n_{abs,iso}}{\partial Z_j^{calc}} = -2\frac{P^{calc}V_j}{(Z_j^{calc})^2RT_j} \tag{A.16}$$

$$\frac{\partial n_{abs,iso}}{\partial Z_i^{meas}} = 2\frac{P^{meas}V_i}{(Z_i^{meas})^2RT_i} \tag{A.17}$$

$$\frac{\partial n_{abs,iso}}{\partial Z_j^{meas}} = 2\frac{P^{meas}V_j}{(Z_j^{meas})^2RT_j} \tag{A.18}$$

$$\frac{\partial n_{abs,iso}}{\partial V_i} = \frac{2}{R}\left[\frac{P^{calc}}{Z_i^{calc}T_i} - \frac{P^{meas}}{Z_i^{meas}T_i}\right] \tag{A.19}$$

$$\frac{\partial n_{abs,iso}}{\partial V_j} = \frac{2}{R}\left[\frac{P^{calc}}{Z_j^{calc}T_j} - \frac{P^{meas}}{Z_j^{meas}T_j}\right] \tag{A.20}$$

The volumetric uncertainties δV_i and δV_j will depend on whether the large or the small volume is applied. In any case the respective uncertainties are taken from table 3.1 and the combined uncertainty is determined as

$$\delta V = \left[\sum_{k=1}^{N}\left\{(\delta V_k)^2\right\}\right]^{\frac{1}{2}} \tag{A.21}$$

where the sum is over all contributing volumes. It is finally noted as an experimental curiosity that it is the pressure terms A.11 and A.12 that yield the dominant contribution to the final uncertainty $\delta n_{abs,iso}$ in the current configuration of the Sieverts apparatuses.

A.3 Sorption at elevated temperatures

Let us next consider the situation where two volumes V_i and V_j' are filled with H_2-gas to respective pressures of P_i and P_j. The volume V_j is furthermore partially immersed into a thermal reservoir at an elevated temperature $T > T_{RT}$ while the rest of the system is placed inside a large isothermal reservoir of ambient temperature T_{RT}. We assume that a sample occupies the volume V_{sample} within the volume V_j' so that $V_j = V_j' - V_{sample}$. The two volumes are initially separated by a closed valve. When the valve is opened the gas will flow inside the system to establish a new thermodynamic equilibrium and in this process the sample will sorb some H_2-molecules. The pressure that would establish itself within the combined volume $V_i + V_j - V_{sample}$ in the absence of any -sorbing sample can in turn be predicted from equation A.4. Let us therefore determine the sorbed amount of moles of hydrogen by the sample $n_{k,\ heated}$ after k data-points has been collected. If the molar amount of H_2 molecules present within the system before the valve is opened is n_0 and the amount of moles present when the k'th data-point is collected is n_k we have that the sorbed molar amount of hydrogen by the sample $n_{k,\ heated}$ is given as

$$\begin{aligned}
n_{k,\ heated} &= 2(n_0 - n_k) \\
&= 2(n_{0,+} + n_{0,-} - n_{k,+} - n_{0,-}) \\
&= 2\Bigg(\frac{P_0^{calc}}{Z_-^{calc}RT_a}(1-x)(V_i + V_j - V_{sample}) + \frac{P_0^{calc}}{Z_+^{calc}RT_b}x(V_i + V_j - V_{sample}) \\
&\quad - \frac{P_k^{meas}}{Z_-^{meas}RT_a}(1-x)(V_i + V_j - V_{sample}) - \frac{P_k^{meas}}{Z_+^{meas}RT_b}x(V_i + V_j - V_{sample})\Bigg)
\end{aligned} \tag{A.22}$$

where we the pre-factor 2 is a manifestation of the fact that there are two hydrogen atoms in a H_2-molecule, in the second step have expanded the initial amount of moles n_0 into the amount of moles present in the hot thermal reservoir $n_{0,+}$ and cool thermal reservoir $n_{0,-}$ respectively and ditto for the k'th measurement before we in the final step have utilized the ideal gas law 3.22. If the relation is massaged somewhat further we wind up at the final result given by

$$n_{k,\ heated} = \frac{2}{RT_a}\left[\Omega^{calc}P_0^{calc} - \Omega^{meas}P_0^{meas}\right](V_i + V_j - V_{sample}) \tag{A.23}$$

where we have introduced the dimensionless parameter Ω^{label} given by

$$\Omega^{label} = \frac{1}{Z_-^{label}} \left(1 - x \left(1 - \frac{Z_-^{label} T_a}{Z_+^{label} T_b} \right) \right) \tag{A.24}$$

where $label$ is either $meas$ or $calc$ and P_0^{calc} is the calculated pressure given by equation A.4, P_k^{meas} is the measured pressure in measurement k, T_a is the temperature measured by the thermistor within the manifold in measurement k, T_b is the temperature measured by the thermistor coupled to the sample-holder in measurement k, R is the universal gas constant and $Z_-^{calc} = Z(P_0^{calc}, T_a)$, $Z_+^{calc} = Z(P_0^{calc}, T_b)$, $Z_-^{meas} = Z(P_k^{meas}, T_a)$ and $Z_+^{meas} = Z(P_k^{meas}, T_b)$ are the associated compressibility factors. The effective heated fraction of the volume x is finally given by equation A.6 with application of relation A.8.

Error analysis

Under the assumption that all the measurement errors are independent and randomly distributed the uncertainty in the absorbed amount of moles $\delta n_{abs,heated}$ is given by

$$\begin{aligned}\delta n_{abs,iso} = \Bigg[& \left(\frac{\partial n_{abs,heated}}{\partial P^{calc}} \delta P^{calc} \right)^2 + \left(\frac{\partial n_{abs,heated}}{\partial P^{meas}} \delta P \right)^2 + \left(\frac{\partial n_{abs,heated}}{\partial x} \delta x \right)^2 \\ & + \left(\frac{\partial n_{abs,heated}}{\partial T_a} \delta T \right)^2 + \left(\frac{\partial n_{abs,heated}}{\partial T_b^{calc}} \delta T \right)^2 + \left(\frac{\partial n_{abs,heated}}{\partial Z_-^{calc}} \delta Z \right)^2 \\ & + \left(\frac{\partial n_{abs,heated}}{\partial Z_+^{calc}} \delta Z \right)^2 + \left(\frac{\partial n_{abs,heated}}{\partial Z_-^{meas}} \delta Z \right)^2 + \left(\frac{\partial n_{abs,heated}}{\partial Z_+^{meas}} \delta Z \right)^2 \\ & + \left(\frac{\partial n_{abs,heated}}{\partial V_i} \delta V_i \right)^2 + \left(\frac{\partial n_{abs,heated}}{\partial V_j} \delta V_j \right)^2 \Bigg]^{\frac{1}{2}} \end{aligned} \tag{A.25}$$

where the uncertainties δP, δT and δZ are given by relations 3.4, 3.5 and 3.25 respectively, while the uncertainty in the pressure δP^{calc} is determined as in the calibration document [64]. The derivatives are given as

$$\frac{\partial n_{abs,heated}}{\partial P^{calc}} = \frac{2(V_i + V_j)}{R} \left[\frac{(1-x)}{Z_-^{calc} T_a} + \frac{x}{Z_+^{calc} T_b} \right] \tag{A.26}$$

$$\frac{\partial n_{abs,heated}}{\partial P^{meas}} = -\frac{2(V_i + V_j)}{R} \left[\frac{(1-x)}{Z_-^{meas} T_a} + \frac{x}{Z_+^{meas} T_b} \right] \tag{A.27}$$

$$\frac{\partial n_{abs,heated}}{\partial x} = \frac{2(V_i + V_j}{R}) \left[\frac{P^{calc}}{Z_{+}^{calc} T_b} - \frac{P^{calc}}{Z_{-}^{calc} T_a} + \frac{P^{meas}}{Z_{-}^{meas} T_a} - \frac{P^{meas}}{Z_{+}^{meas} T_b} \right] \tag{A.28}$$

$$\frac{\partial n_{abs,heated}}{\partial T_a} = \frac{2(1-x)(V_i + V_j)}{R T_a^2} \left[\frac{P^{meas}}{Z_{-}^{meas}} - \frac{P^{calc}}{Z_{-}^{calc}} \right] \tag{A.29}$$

$$\frac{\partial n_{abs,heated}}{\partial T_b} = \frac{2x(V_i + V_j)}{R T_b^2} \left[\frac{P^{meas}}{Z_{+}^{meas}} - \frac{P^{calc}}{Z_{+}^{calc}} \right] \tag{A.30}$$

$$\frac{\partial n_{abs,heated}}{\partial Z_{-}^{calc}} = -2 \frac{(1-x) P^{calc} (V_i + V_j)}{(Z_{-}^{calc})^2 R T_a} \tag{A.31}$$

$$\frac{\partial n_{abs,heated}}{\partial Z_{+}^{calc}} = -2 \frac{x P^{calc} (V_i + V_j)}{(Z_{+}^{calc})^2 R T_b} \tag{A.32}$$

$$\frac{\partial n_{abs,heated}}{\partial Z_{-}^{meas}} = 2 \frac{(1-x) P^{meas} (V_i + V_j)}{(Z_{-}^{meas})^2 R T_a} \tag{A.33}$$

$$\frac{\partial n_{abs,heated}}{\partial Z_{+}^{meas}} = 2 \frac{x P^{meas} (V_i + V_j)}{(Z_{+}^{meas})^2 R T_b} \tag{A.34}$$

$$\frac{\partial n_{abs,heated}}{\partial V_i} = \frac{2}{R} \left[\frac{(1-x) P^{calc}}{Z_{-}^{calc} T_a} + \frac{x P^{calc}}{Z_{+}^{calc} T_b} - \frac{(1-x) P^{meas}}{Z_{-}^{meas} T_a} - \frac{x P^{meas}}{Z_{+}^{meas} T_b} \right] \tag{A.35}$$

$$\frac{\partial n_{abs,heated}}{\partial V_j} = \frac{\partial n_{abs,heated}}{\partial V_i} \tag{A.36}$$

The volumetric uncertainties δV_i and δV_j will depend on whether the large or the small volume is applied. In any case the respective uncertainties are taken from table 3.1 and the combined uncertainty is determined as

$$\delta V = \left[\sum_{k=1}^{N} \left\{ (\delta V_k)^2 \right\} \right]^{\frac{1}{2}} \tag{A.37}$$

where the sum is over all contributing volumes. As for the isothermal case it is the pressure terms A.26 and A.27 that yield the dominant contribution to the final uncertainty $\delta n_{abs,heated}$ in the current configuration of the Sieverts apparatuses.

A.4 The molar hydrogen-to-metal ratio

Often the property we are after is the molar hydrogen-to-metal ratio x of the hydride $\mathrm{MH_x}$ which is given as

$$\mathrm{x} = \frac{n_{\mathrm{H}}}{n_{\mathrm{M}}} \tag{A.38}$$

where n_{H} is the absorbed amount of moles by the n_{M} moles of metal M. After N consecutive measurements the total amount of moles that has been absorbed by the sample n_{H} is given by

$$n_{\mathrm{H}} = \sum_{k=1}^{N} \{n_k\} \tag{A.39}$$

where n_k is given by equation A.9 or A.23 depending on whether the sample is at ambient or elevated temperatures.

Error analysis

Once again we place the assumption on the system that the measurement uncertainties are independent and randomly distributed so that the uncertainty $\delta\mathrm{x}$ is given by

$$\delta\mathrm{x} = \left[\left(\frac{\partial\mathrm{x}}{\partial n_{\mathrm{H}}}\delta n_{\mathrm{H}}\right)^2 + \left(\frac{\partial\mathrm{x}}{\partial n_{\mathrm{M}}}\delta n_{\mathrm{M}}\right)^2\right]^{\frac{1}{2}} \tag{A.40}$$

with

$$\begin{aligned}\delta n_{\mathrm{H}} &= \left[\sum_{k=1}^{N}\left\{\left(\frac{\partial n_{\mathrm{H}}}{\partial n_k}\delta n_k\right)^2\right\}\right]^{\frac{1}{2}} \\ &= \left[\sum_{k=1}^{N}\left\{(\delta n_k)^2\right\}\right]^{\frac{1}{2}}\end{aligned} \tag{A.41}$$

and

$$\delta n_{\mathrm{M}} = \left[\left(\frac{\partial n_{\mathrm{M}}}{\partial m}\delta m\right)^2 + \left(\frac{\partial n_{\mathrm{M}}}{\partial M}\delta M\right)^2\right]^{\frac{1}{2}} \tag{A.42}$$

where n_k is the amount of moles of hydrogen absorbed by the sample during measurement k, $\mathrm{n_H}$ is the total amount of moles of hydrogen absorbed by the sample, $\mathrm{n_M}$ is the number of moles of the sorbing metal having mass m and molar mass M. It is finally often assumed that the uncertainty in the molar mass $\delta M = 0$ so that the uncertainty in the stoichiometric concentration of hydrogen in the sample $\delta\mathrm{x}$ is finally given by

$$\delta\mathrm{x} = \frac{1}{n_\mathrm{M}}\left[\sum_{k=1}^{N}\{\delta n_k\} + \frac{\mathrm{x}^2}{M^2}\delta m^2\right]^{\frac{1}{2}} \tag{A.43}$$

A.5 The weight percentage of hydrogen

Similarly we would like to determined the mass percentage of hydrogen present in our hydride η. In this respect we know that

$$\begin{aligned}\eta &= \frac{m_\mathrm{H}}{m_\mathrm{H} + m_\mathrm{M}} \cdot 100\% \\ &= \frac{n_\mathrm{H} M_\mathrm{H}}{n_\mathrm{H} M_\mathrm{H} + n_\mathrm{M} M_\mathrm{M}} \cdot 100\% \\ \eta &= \frac{\mathrm{x} M_\mathrm{H}}{\mathrm{x} M_\mathrm{H} + M_\mathrm{M}} \cdot 100\% \end{aligned} \tag{A.44}$$

where we in the first step have utilized equation 3.7 and in the second have simplified the result somewhat with m_H as the mass of hydrogen, m_M as the mass of sorbing metal, M_H as the molar mass of hydrogen, M_M as the molar mass of the sorbing metal and x as the stoichiometric coefficient of hydrogen in the hydride $\mathrm{MH_x}$.

Error analysis

Under the assumption that all the measurement errors are independent and randomly distributed the uncertainty in the mass percentage of hydrogen η is given by

$$\begin{aligned}
\delta\eta &= \left[\left(\frac{\partial\eta}{\partial \mathrm{x}}\delta\mathrm{x}\right)^2 + \left(\frac{\partial\eta}{\partial M_{\mathrm{H}}}\delta M_{\mathrm{H}}\right)^2 + \left(\frac{\partial\eta}{\partial M_{\mathrm{M}}}\delta M_{\mathrm{M}}\right)^2\right]^{\frac{1}{2}} \\
&= \frac{\partial\eta}{\partial \mathrm{x}}\delta\mathrm{x} \\
\delta\eta &= \left(\frac{M_{\mathrm{H}}}{\mathrm{x}M_{\mathrm{H}} + M_{\mathrm{M}}}\left[1 - \frac{\mathrm{x}M_{\mathrm{H}}}{\mathrm{x}M_{\mathrm{H}} + M_{\mathrm{M}}}\right]\delta\mathrm{x}\right)\cdot 100\% \qquad \text{(A.45)}
\end{aligned}$$

where we in the first step have assumed that $\delta M_{\mathrm{H}} = \delta M_{\mathrm{M}} = 0$ and in the second step have performed the differentiation $\frac{\partial\eta}{\partial \mathrm{x}}$.

Appendix B

Calibration of the BM01A beamline blower

This appendix present the calibrations that was performed for the blower at the Swiss-Norwegian Beamline. Three different substances were in either case heated. The melting-points were used for the calibration. A total of three calibrations was eventually conducted due to different reasons.

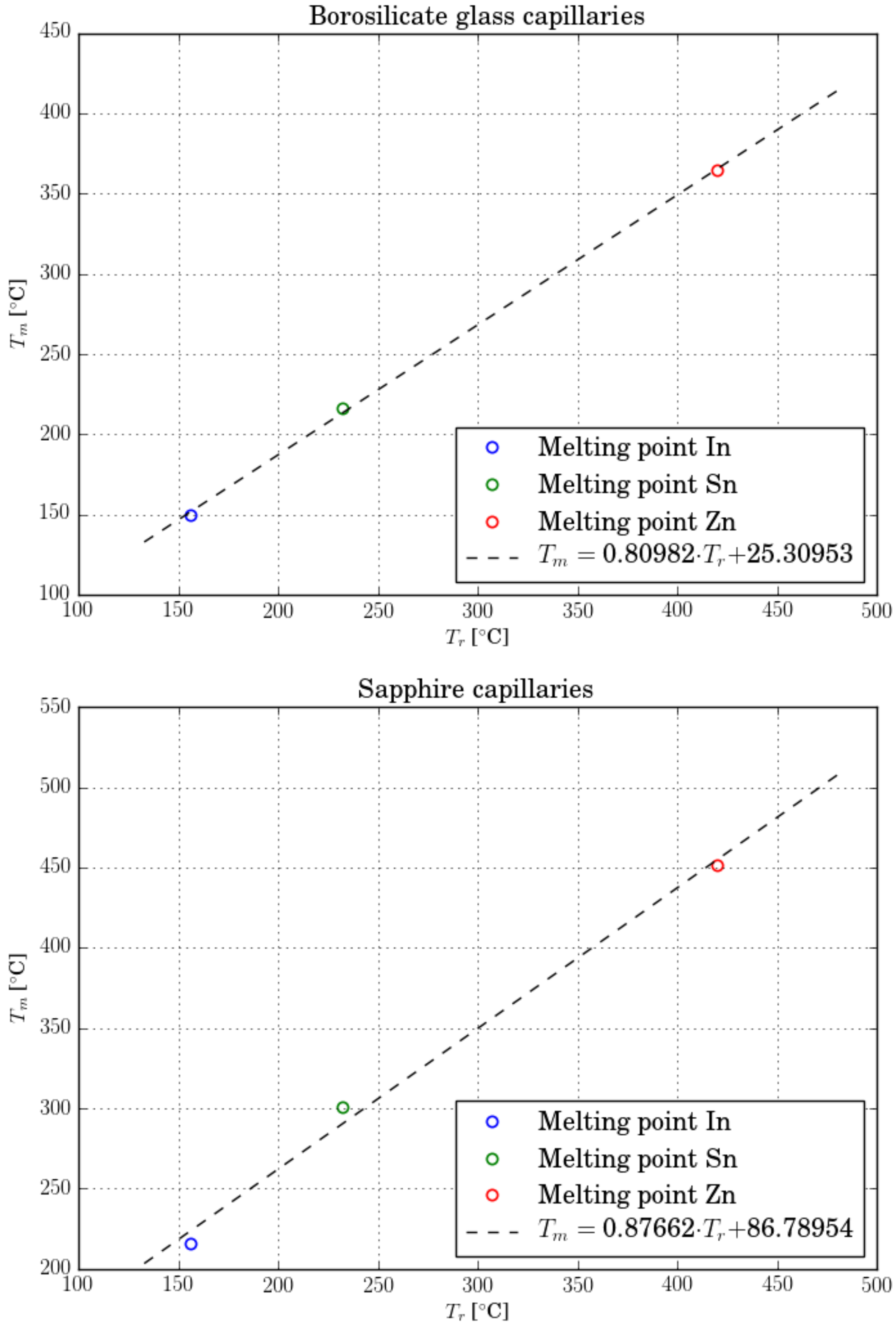

Figure B.1: Calibration curve for the blower at the Swiss-Norwegian Beamline. The real temperature T_r is given by the line of regression from the measured temperature T_m.

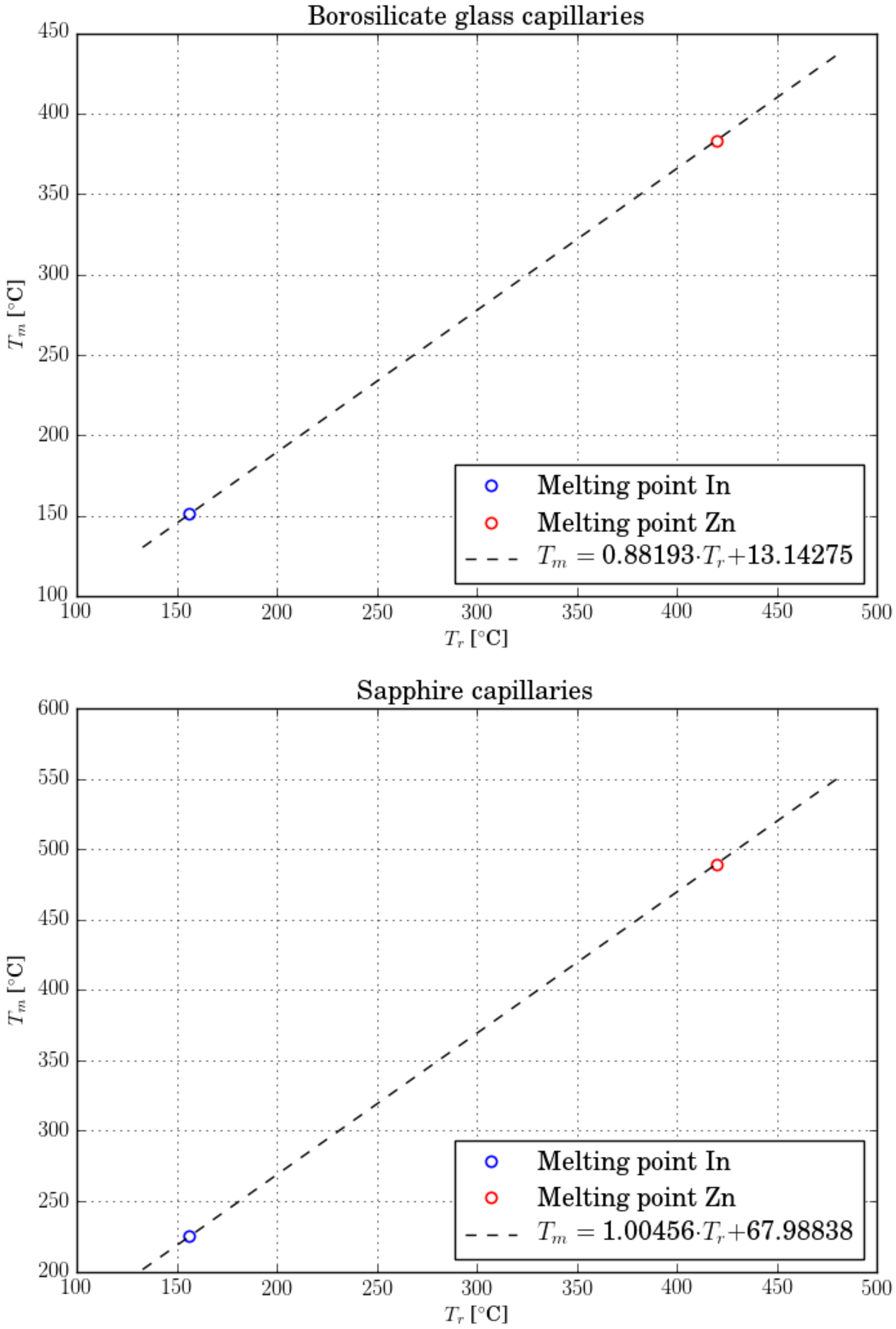

Figure B.2: Calibration curve for the blower at the Swiss-Norwegian Beamline. The real temperature T_r is given by the line of regression from the measured temperature T_m.

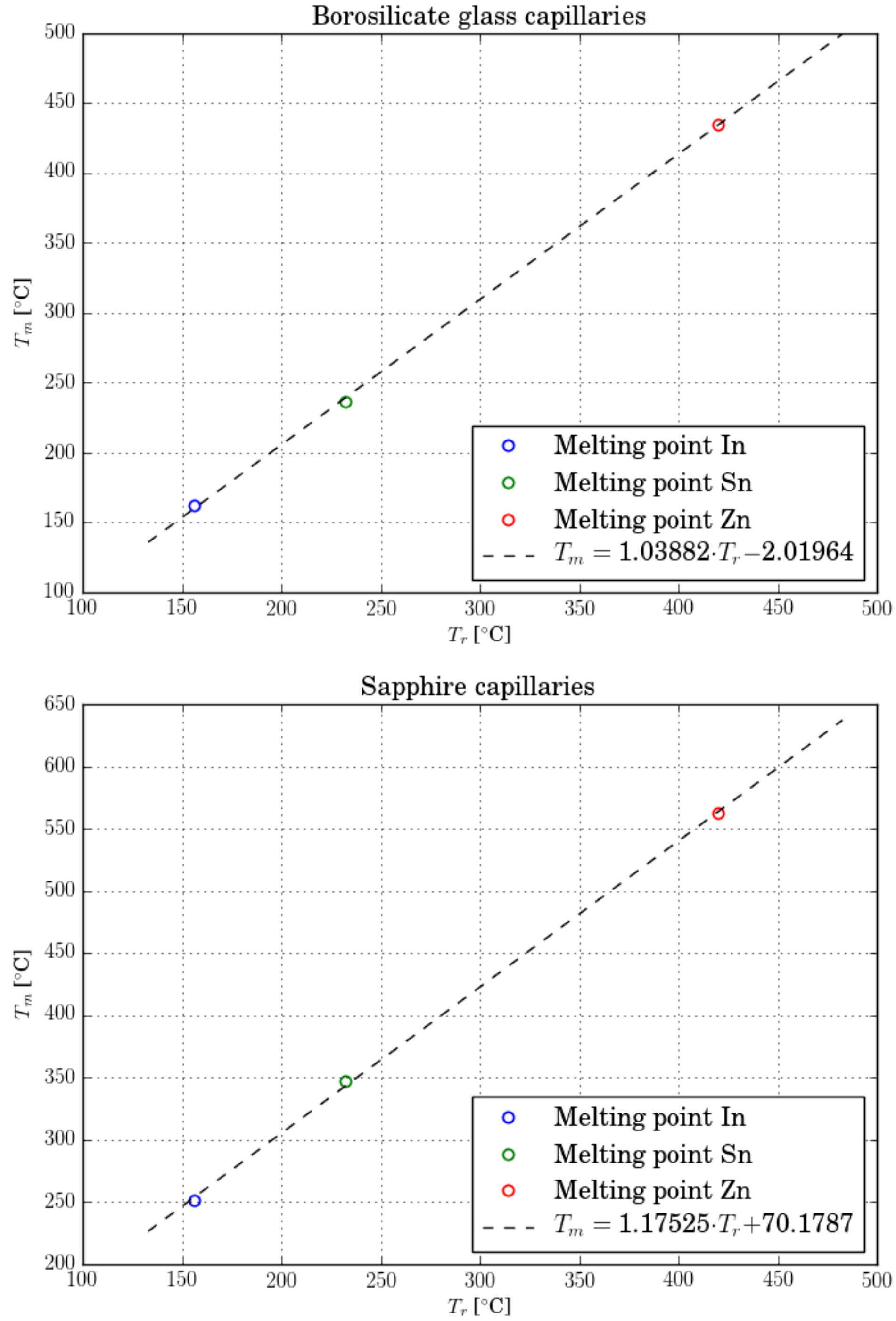

Figure B.3: Calibration curve for the blower at the Swiss-Norwegian Beamline. The real temperature T_r is given by the line of regression from the measured temperature T_m.

Appendix C

Sample preparation tables

This appendix present the sample preparation tables.

Table C.1: The masses of the different elements that were determined with the Sartorius ED124S balance inside the glove-box for the different samples $(\mathrm{Ti}_{0.70}\mathrm{V}_{0.30})_{1\text{-}z}\mathrm{Fe}_{z}$. The change in sample mass throughout the sample preparation $\Delta m = m_{tot} - m'_{tot}$ where m_{tot} is the total mass measured in the glove-box and m'_{tot} is the total mass measured by the Mettler PM460 DeltaRange balance in the laboratory is also shown.

Sample	m_{Ti} [g]	m_{V} [g]	m_{Fe} [g]	m_{tot} [g]	Δm [g]
$\mathrm{Ti}_{0.70}\mathrm{V}_{0.30}$	1.4630	0.6675	-	2.1305	0.0085
	±0.0001	±0.0003	-	±0.0003	-
$(\mathrm{Ti}_{0.70}\mathrm{V}_{0.30})_{0.97}\mathrm{Fe}_{0.03}$	1.3849	0.6313	0.07130	2.0875	0.0235
	±0.0001	±0.0003	±0.0027	±0.0027	-
$(\mathrm{Ti}_{0.70}\mathrm{V}_{0.30})_{0.94}\mathrm{Fe}_{0.06}$	1.503	0.6851	0.1600	2.3481	0.0081
	±0.0001	±0.0003	±0.0012	±0.0012	-
$(\mathrm{Ti}_{0.70}\mathrm{V}_{0.30})_{0.90}\mathrm{Fe}_{0.10}$	1.3466	0.6141	0.2494	2.2101	0.0291
	±0.0001	±0.0003	±0.0008	±0.0009	-
$(\mathrm{Ti}_{0.70}\mathrm{V}_{0.30})_{0.80}\mathrm{Fe}_{0.20}$	1.1401	0.5198	0.4750	2.1349	0.0329
	±0.0002	±0.0004	±0.0004	±0.0006	-
$(\mathrm{Ti}_{0.70}\mathrm{V}_{0.30})_{0.70}\mathrm{Fe}_{0.30}$	1.063	0.4848	0.7594	2.3072	0.0362
	±0.0002	±0.0004	±0.0003	±0.0005	-

Table C.2: The moles of the different elements that were determined through equation 3.7 from the masses in table C.1 for the different samples of $(\mathrm{Ti}_{0.70}\mathrm{V}_{0.30})_{1\text{-z}}\mathrm{Fe}_{\mathrm{z}}$.

Sample	n_{Ti} [mmol]	n_{V} [mmol]	n_{Fe} [mmol]
$\mathrm{Ti}_{0.70}\mathrm{V}_{0.30}$	30.575	13.104	-
	± 0.003	± 0.006	-
$(\mathrm{Ti}_{0.70}\mathrm{V}_{0.30})_{0.97}\mathrm{Fe}_{0.03}$	28.924	12.393	1.28
	± 0.003	± 0.006	± 0.05
$(\mathrm{Ti}_{0.70}\mathrm{V}_{0.30})_{0.94}\mathrm{Fe}_{0.06}$	31.391	13.449	2.69
	± 0.003	± 0.006	± 0.02
$(\mathrm{Ti}_{0.70}\mathrm{V}_{0.30})_{0.90}\mathrm{Fe}_{0.10}$	28.124	12.055	4.466
	± 0.003	± 0.006	± 0.014
$(\mathrm{Ti}_{0.70}\mathrm{V}_{0.30})_{0.80}\mathrm{Fe}_{0.20}$	23.812	10.204	8.505
	± 0.004	± 0.008	± 0.007
$(\mathrm{Ti}_{0.70}\mathrm{V}_{0.30})_{0.70}\mathrm{Fe}_{0.30}$	22.201	9.517	13.600
	± 0.004	± 0.008	± 0.005

Table C.3: The masses of the different elements that were determined with the Mettler Toledo AG204 DeltaRange balance inside the glove-box for the different batches of $\mathrm{Zr}_7\mathrm{Ni}_{10}$. The change in sample mass throughout the sample preparation $\Delta m = m_{TOT} - m'_{TOT}$ where m_{TOT} is the total mass measured in the glove-box and m'_{TOT} is the total mass measured by the Mettler PM460 DeltaRange balance in the laboratory is also shown.

Batch	m_{Zr} [g]	m_{Ni} [g]	m_{TOT} [g]	Δm [g]
#1	0.1307	0.1199	0.251	0.0226
	±0.0015	±0.0016	±0.002	-
#2	0.1304	0.1197	0.250	0.0271
	±0.0015	±0.0016	±0.002	-
#3	0.1304	0.1196	0.250	-
	±0.0015	±0.0016	±0.002	-
#4	0.1305	0.1197	0.250	-0.0162
	±0.0015	±0.0016	±0.002	-

Table C.4: The moles of the different elements that were determined through equation 3.7 from the masses in table C.3 for the different batches of $(\mathrm{Zr_wNi})_{10}$. The corresponding stoichiometric coefficient $\mathrm{w} = \frac{n_{\mathrm{Zr}}}{n_{\mathrm{Ni}}}$ were also determined from the data.

Batch	n_{Zr} [mmol]	n_{Ni} [mmol]
#1	1.433	2.04
	± 0.016	± 0.03
#2	1.430	2.04
	± 0.016	± 0.03
#3	1.430	2.04
	± 0.016	± 0.03
#4	1.431	2.04
	± 0.016	± 0.03

Table C.5: The masses of the samples m_s and Zr_7Ni_{10} catalysts m_c that were measured with the Sartorius ED124S balance inside the glove-box before ball-milling. The change in sample mass throughout the milling $\Delta m = m_{tot} - m'_{tot}$ where m_{tot} is the total mass measured before milling and m'_{tot} is the total mass measured after the milling is also shown.

Sample	m_{sample} [g]	m_c [g]	m_{tot} [g]	$\frac{m_c}{m_{tot}}$ $[\emptyset]$	Δm [g]
$Ti_{0.70}V_{0.30}$	0.082	0.004	0.087	0.0496	-0.008
	± 0.002	± 0.04	± 0.002	±	±0.003
$(Ti_{0.70}V_{0.30})_{0.97}Fe_{0.03}$	0.078	0.0041	0.082	0.0501	-0.009
	±0.002	± 0.05	±0.002	±	±0.003
$(Ti_{0.70}V_{0.30})_{0.94}Fe_{0.06}$	0.212	0.011	0.223	0.0503	-0.0067
	± 0.001	± 0.017	± 0.0010	±	±0.0013
$(Ti_{0.70}V_{0.30})_{0.90}Fe_{0.10}$	0.040	0.0021	0.043	0.0494	-0.004
	± 0.005	± 0.09	± 0.005	±	±0.007
$(Ti_{0.70}V_{0.30})_{0.80}Fe_{0.20}$	0.041	0.0022	0.043	0.0509	-0.007
	± 0.005	± 0.09	± 0.005	±	±0.007
$(Ti_{0.70}V_{0.30})_{0.70}Fe_{0.30}$	0.044	0.0022	0.047	0.0471	-0.021
	± 0.004	± 0.09	± 0.004	±	±0.006
$Ti_{0.70}V_{0.30}H_x$	0.1471	0.0077	0.1548	0.0497	-0.002
	± 0.0013	± 0.03	± 0.0012	±	±0.012
$(Ti_{0.70}V_{0.30})_{0.97}Fe_{0.03}H_x$	0.1520	0.008	0.1600	0.0500	-
	± 0.0013	± 0.02	± 0.0012	±	-
$(Ti_{0.70}V_{0.30})_{0.94}Fe_{0.06}H_x$	0.1129	0.006	0.1188	0.0505	-0.004
	± 0.0017	± 0.03	± 0.0016	±	±0.002
$(Ti_{0.70}V_{0.30})_{0.90}Fe_{0.10}H_x$	0.1133	0.006	0.1193	0.0503	-0.003
	± 0.0017	± 0.03	± 0.0016	±	±0.002
$(Ti_{0.70}V_{0.30})_{0.80}Fe_{0.20}H_x$	0.093	0.0049	0.098	0.0500	-0.009
	± 0.002	± 0.04	± 0.002	±	±0.003
$(Ti_{0.70}V_{0.30})_{0.70}Fe_{0.30}H_x$	0.1236	0.0066	0.1301	0.0507	-0.006
	± 0.0015	± 0.03	± 0.0015	±	±0.002

Appendix D

Rietveld refinements

This appendix present the Rietveld refinements that has been conducted throughout this thesis.

D.1 Lab PXD patterns of the alloys

Table D.1: The fitted parameters from GSAS for the $Ti_{0.70}V_{0.30}$ XRD pattern that was measured on the Bruker AXS D8 Advance diffractometer at IFE. The unweighted profile factor was determined to $R_p = 0.0162$ while the weighted profile factor was $R_{wp} = 0.0264$. The goodness-of-fit was similarly determined to $\chi^2 = 6.858$. The scale factor was found to be S=821980. Zero-offset 0.0420263°. Shifted Chebyschev with 16 parameters background. Absorption: 11.432.

Phase	BCC		HCP	
S_{rel} [$\emptyset$]	1.0		0.37440	
wt.% [$\emptyset$]	0.73		0.27	
	±0.01		±0.02	
a [Å]	3.1794		2.9576	
	±0.0003		±0.0003	
b [Å]	3.1794		2.9576	
	±0.0003		±0.0003	
c [Å]	3.1794		4.7368	
	±0.0003		±0.0006	
V [Å^3]	32.14		35.88	
	±0.01		±0.01	
α [deg]	90		90	
β [deg]	90		90	
γ [deg]	90		120	
G_U [$\emptyset$]	4328.44		3431.97	
G_V [$\emptyset$]	-3592.76		-2856.98	
G_W [$\emptyset$]	920.524		596.958	
L_X [$\emptyset$]	0		0	
L_Y [$\emptyset$]	0		0	
U_{ISO}	0.07672		0.05389	
Atom	Ti	V	Ti	V
x	0	0	$\frac{1}{3}$	$\frac{1}{3}$
y	0	0	$\frac{2}{3}$	$\frac{2}{3}$
z	0	0	$\frac{1}{4}$	$\frac{1}{4}$

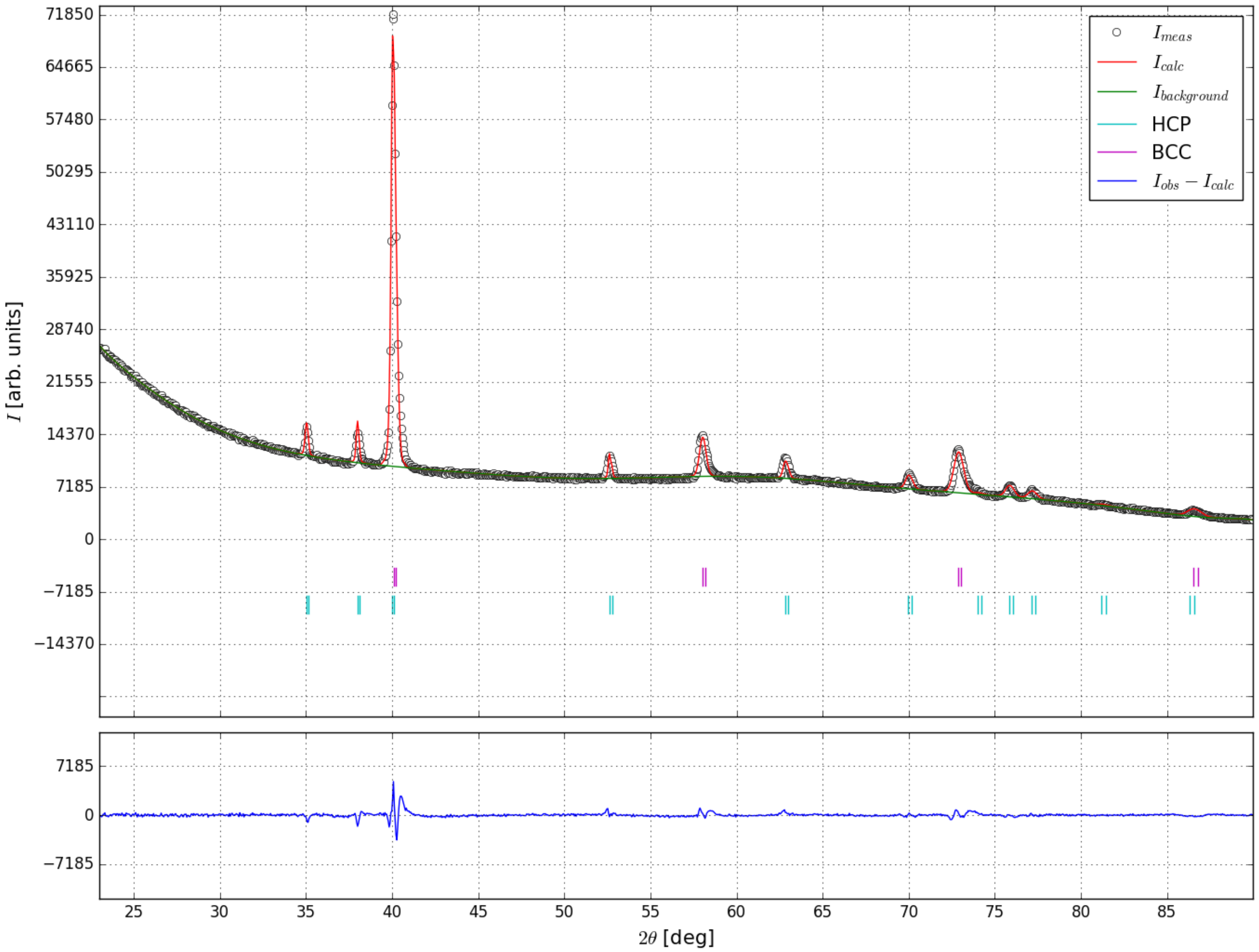

Figure D.1: The Lab PXD intensities I_{obs} for $\mathrm{Ti}_{0.70}\mathrm{V}_{0.30}$ measured on the Bruker AXS D8 Advance diffractometer at IFE shown alongside the background $I_{background}$ and the calculated intensities I_{calc} that was fitted to the pattern in GSAS. The fitted parameters of the model is given in table D.1.

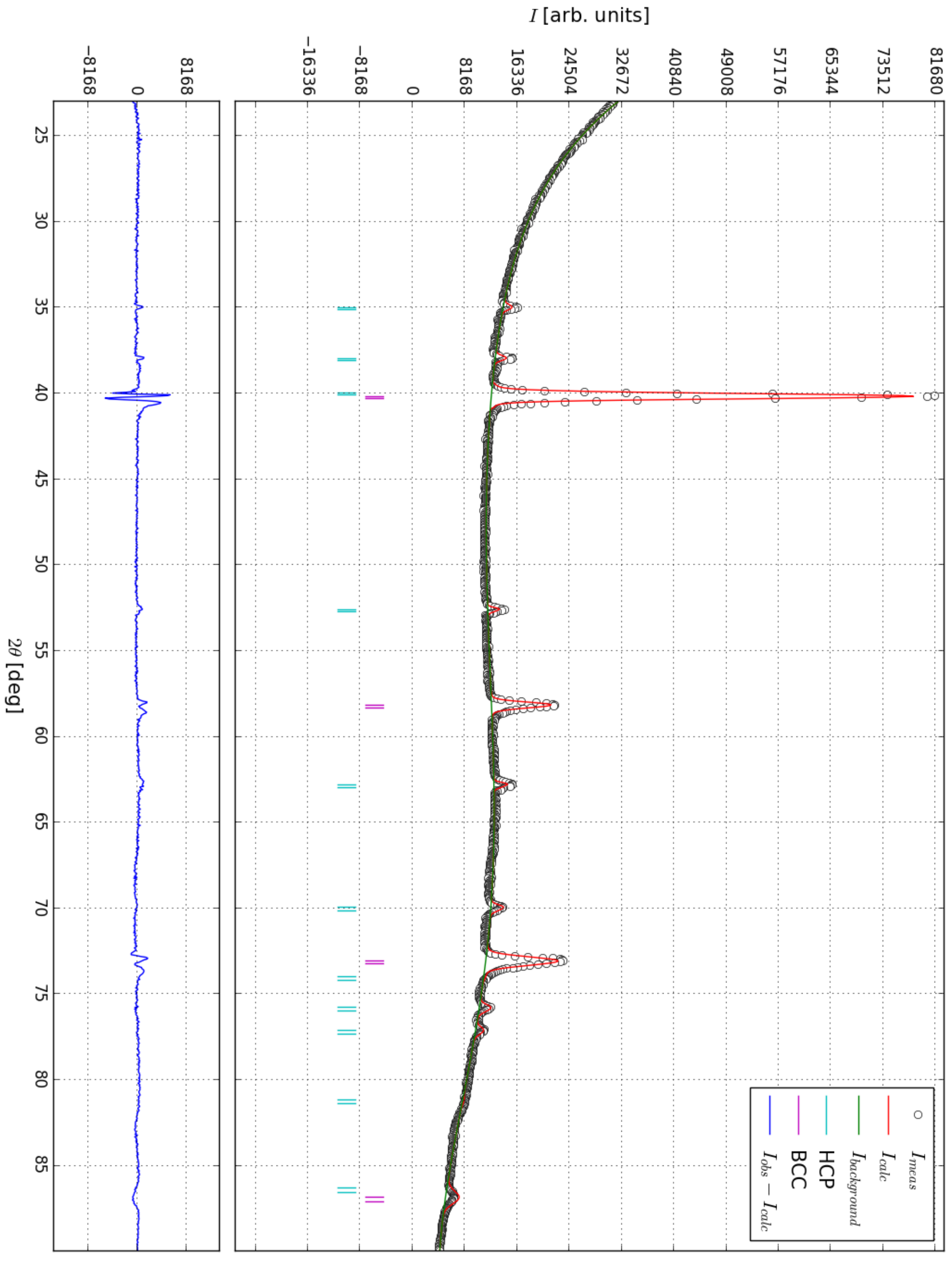

Figure D.2: The Lab PXD intensities I_{obs} for $(\mathrm{Ti}_{0.70}\mathrm{V}_{0.30})_{0.97}\mathrm{Fe}_{0.03}$ measured on the Bruker AXS D8 Advance diffractometer at IFE shown alongside the background $I_{background}$ and the calculated intensities I_{calc} that was fitted to the pattern in GSAS. The fitted parameters of the model is given in table D.2.

Table D.2: The fitted parameters from GSAS for the $(Ti_{0.70}V_{0.30})_{0.97}Fe_{0.03}$ XRD pattern that was measured on the Bruker AXS D8 Advance diffractometer at IFE. The unweighted profile factor was determined to $R_p = 0.0167$ while the weighted profile factor was $R_{wp} = 0.0277$. The goodness-of-fit was similarly determined to $\chi^2 = 10.39$. The scale factor was found to be S=1434800. Zero-offset 0.0342144°. Shifted Chebyschev with 16 parameters background. Absorption: 16.892.

Phase	BCC		HCP	
S_{rel} [$\emptyset$]	1.0		0.13071	
wt.% [$\emptyset$]	0.88		0.12	
	±0.01		±0.01	
a [Å]	3.1710		2.9577	
	±0.0003		±0.0005	
b [Å]	3.1710		2.9577	
	±0.0003		±0.0005	
c [Å]	3.1710		4.7372	
	±0.0003		±0.0012	
V [Å^3]	31.884		35.890	
	±0.007		±0.011	
α [deg]	90		90	
β [deg]	90		90	
γ [deg]	90		120	
G_U [$\emptyset$]	3274.76		3203.61	
G_V [$\emptyset$]	-2450.74		-3331.26	
G_W [$\emptyset$]	709.799		906.003	
L_X [$\emptyset$]	0		0	
L_Y [$\emptyset$]	0		0	
U_{ISO}	0.05751		0.01944	
Atom	Ti	V	Ti	V
x	0	0	$\frac{1}{3}$	$\frac{1}{3}$
y	0	0	$\frac{2}{3}$	$\frac{2}{3}$
z	0	0	$\frac{1}{4}$	$\frac{1}{4}$

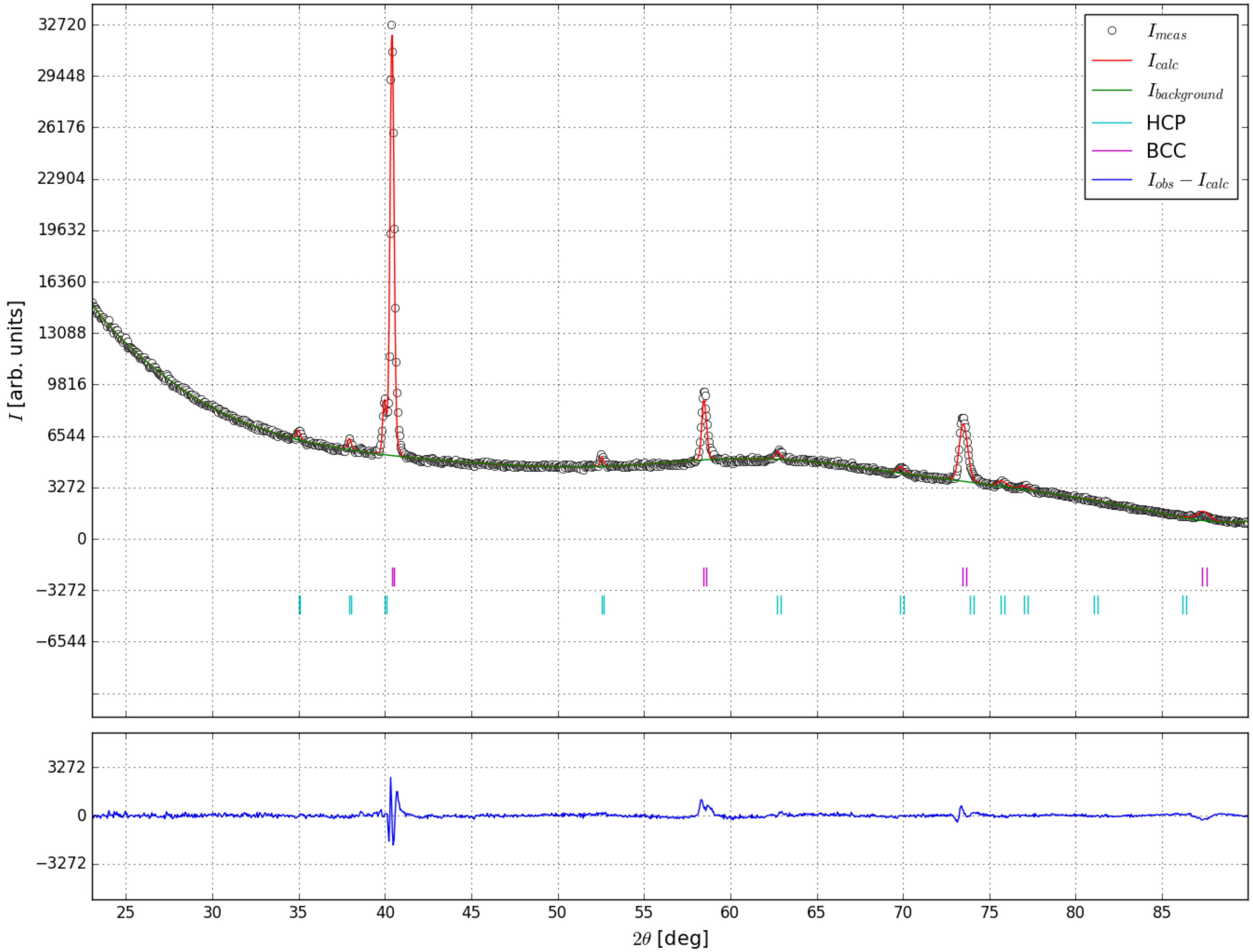

Figure D.3: The Lab PXD intensities I_{obs} for $(\mathrm{Ti}_{0.70}\mathrm{V}_{0.30})_{0.94}\mathrm{Fe}_{0.06}$ measured on the Bruker AXS D8 Advance diffractometer at IFE shown alongside the background $I_{background}$ and the calculated intensities I_{calc} that was fitted to the pattern in GSAS. The fitted parameters of the model is given in table D.3.

Table D.3: The fitted parameters from GSAS for the $(Ti_{0.70}V_{0.30})_{0.94}Fe_{0.06}$ XRD pattern that was measured on the Bruker AXS D8 Advance diffractometer at IFE. The unweighted profile factor was determined to $R_p = 0.0183$ while the weighted profile factor was $R_{wp} = 0.0294$. The goodness-of-fit was similarly determined to $\chi^2 = 4.674$. The scale factor was found to be S=541570. Zero-offset 0.0334392°. Shifted Chebyschev with 16 parameters background. Absorption: 17.4565.

Phase	BCC		HCP	
S_{rel} [∅]	1.0		0.12594	
wt.% [∅]	0.89		0.11	
	±0.01		±0.01	
a [Å]	3.1571		2.9616	
	±0.0003		±0.0006	
b [Å]	3.1571		2.9616	
	±0.0003		±0.0006	
c [Å]	3.1571		4.7444	
	±0.0003		±0.0016	
V [Å^3]	31.468		36.039	
	±0.009		±0.013	
α [deg]	90		90	
β [deg]	90		90	
γ [deg]	90		120	
G_U [∅]	4328.54		3869.95	
G_V [∅]	-3959.65		-3533.2	
G_W [∅]	943.727		823.132	
L_X [∅]	0		0	
L_Y [∅]	0		0	
U_{ISO}	0.06553		0.03824	
Atom	Ti	V	Ti	V
x	0	0	$\frac{1}{3}$	$\frac{1}{3}$
y	0	0	$\frac{2}{3}$	$\frac{2}{3}$
z	0	0	$\frac{1}{4}$	$\frac{1}{4}$

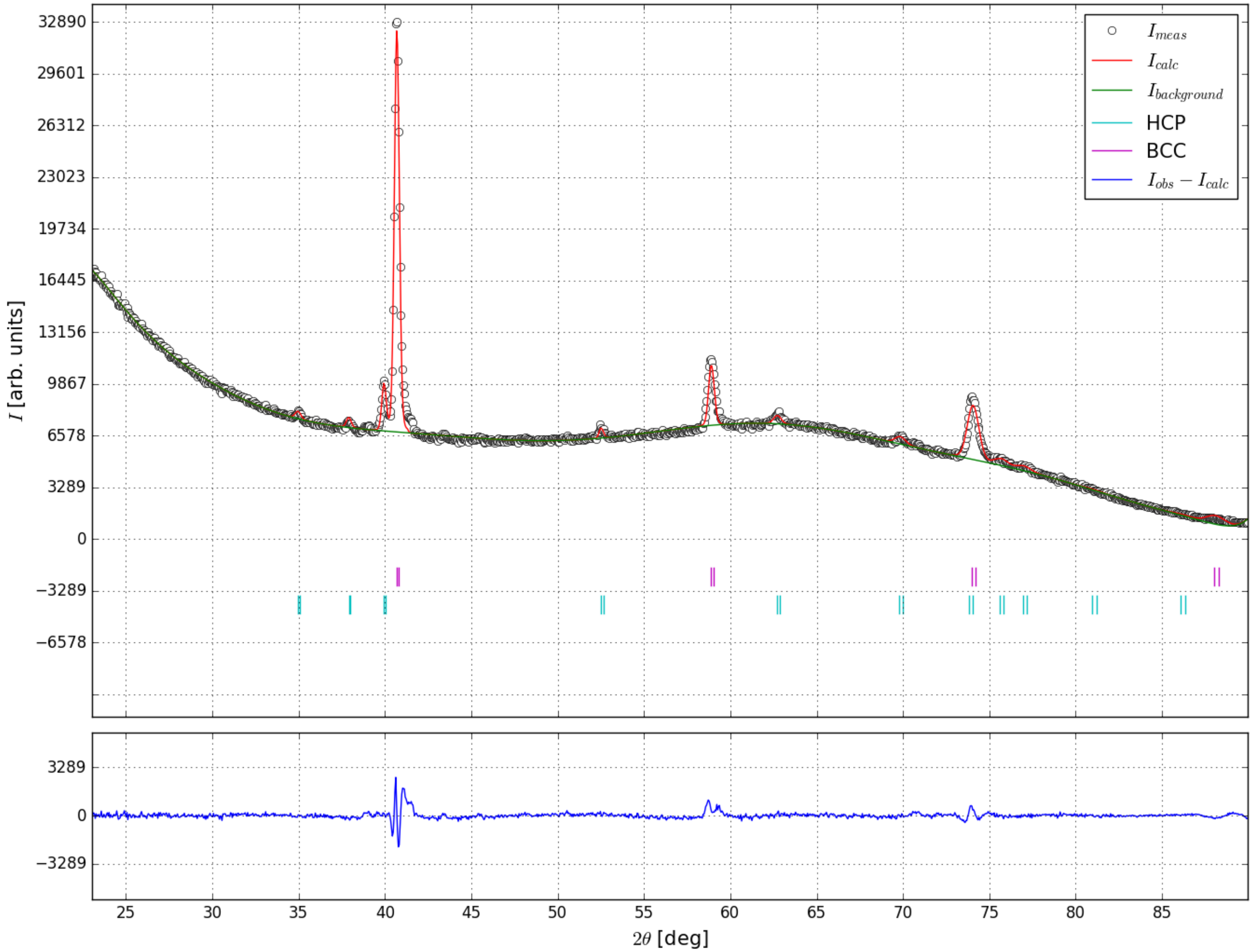

Figure D.4: The Lab PXD intensities I_{obs} for $(\mathrm{Ti}_{0.70}\mathrm{V}_{0.30})_{0.90}\mathrm{Fe}_{0.10}$ measured on the Bruker AXS D8 Advance diffractometer at IFE shown alongside the background $I_{background}$ and the calculated intensities I_{calc} that was fitted to the pattern in GSAS. The fitted parameters of the model is given in table D.4.

Table D.4: The fitted parameters from GSAS for the $(Ti_{0.70}V_{0.30})_{0.90}Fe_{0.10}$ XRD pattern that was measured on the Bruker AXS D8 Advance diffractometer at IFE. The unweighted profile factor was determined to $R_p = 0.0177$ while the weighted profile factor was $R_{wp} = 0.0286$. The goodness-of-fit was similarly determined to $\chi^2 = 5.700$. The scale factor was found to be S=612090. Zero-offset 0.0325081°. Shifted Chebyschev with 16 parameters background. Absorption: 18.216.

Phase	BCC		HCP	
S_{rel} $[\emptyset]$	1.0		0.10220	
wt.% $[\emptyset]$	0.91		0.09	
	±0.01		±0.01	
a [Å]	3.1364		2.9632	
	±0.0005		±0.0008	
b [Å]	3.1364		2.9632	
	±0.0005		±0.0008	
c [Å]	3.1364		4.748	
	±0.0005		±0.003	
V [Å^3]	30.853		36.102	
	±0.013		±0.020	
α [deg]	90		90	
β [deg]	90		90	
γ [deg]	90		120	
G_U $[\emptyset]$	9999.94		11471.5	
G_V $[\emptyset]$	-9188.59		-10060.1	
G_W $[\emptyset]$	2176.9		2249.18	
L_X $[\emptyset]$	0		0	
L_Y $[\emptyset]$	0		0	
U_{ISO}	0.05831		0.00546	
Atom	Ti	V	Ti	V
x	0	0	$\frac{1}{3}$	$\frac{1}{3}$
y	0	0	$\frac{2}{3}$	$\frac{2}{3}$
z	0	0	$\frac{1}{4}$	$\frac{1}{4}$

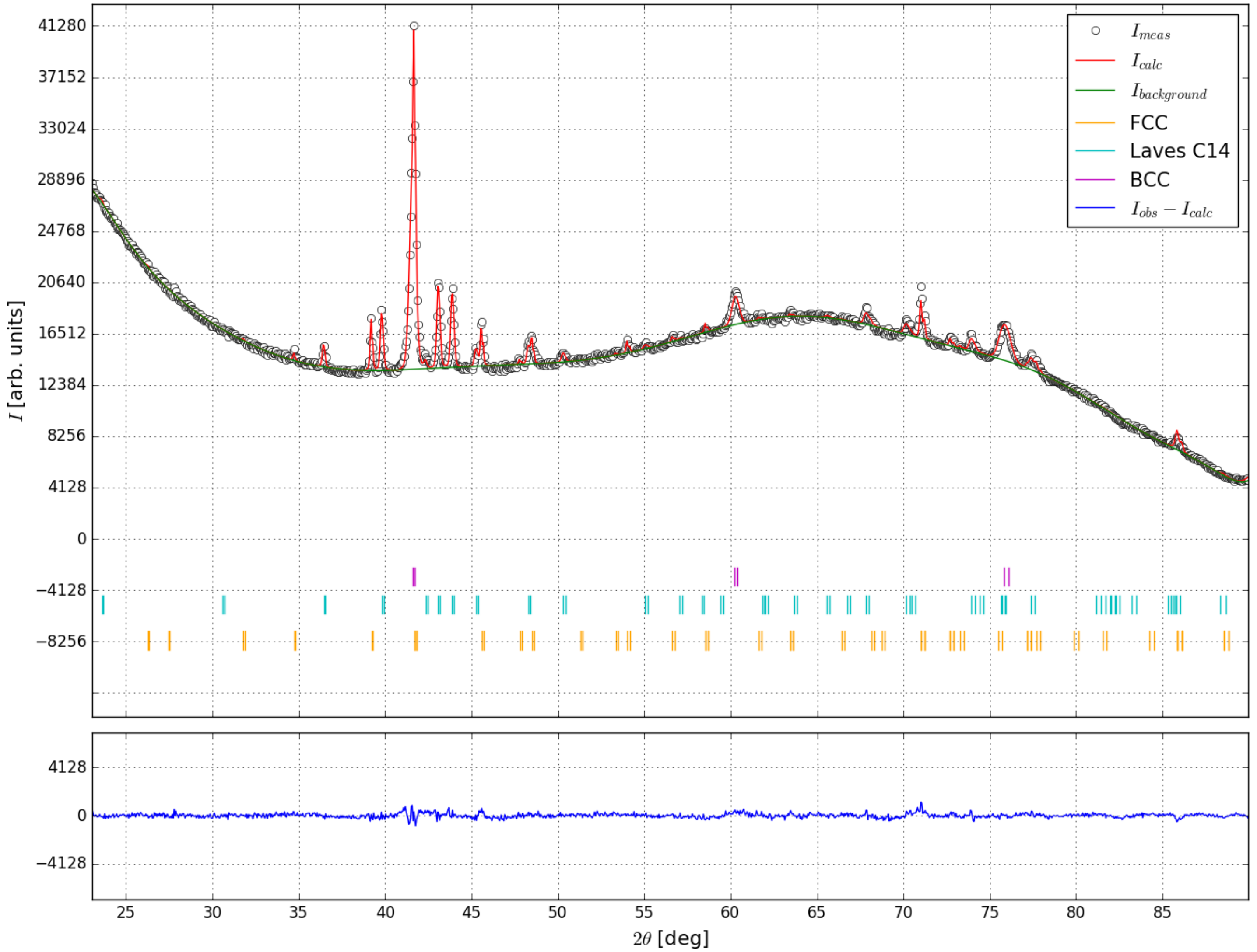

Figure D.5: The Lab PXD intensities I_{obs} for $(\mathrm{Ti}_{0.70}\mathrm{V}_{0.30})_{0.70}\mathrm{Fe}_{0.30}$ measured on the Bruker AXS D8 Advance diffractometer at IFE shown alongside the background $I_{background}$ and the calculated intensities I_{calc} that was fitted to the pattern in GSAS. The fitted parameters of the model is given in table D.5.

Table D.5: The fitted parameters from GSAS for the $(Ti_{0.70}V_{0.30})_{0.70}Fe_{0.30}$ XRD pattern that was measured on the Bruker AXS D8 Advance diffractometer at IFE. The unweighted profile factor was determined to $R_p = 0.0094$ while the weighted profile factors was $R_{wp} = 0.0124$. The goodness-of-fit was similarly determined to $\chi^2 = 2.407$. The scale factor was determined to $S = 450610$. Zero offset 0.0250299°. Shifted Chebyschev with 16 parameters for background.

Phase	BCC			Laves C14						FCC			
S_{rel} [∅]	1.0			0.13972						0.013835			
wt.% [∅]	0.392			0.336						0.272			
	±0.001			±0.003						±0.003			
a [Å]	3.0710			4.9297						11.2571			
	±0.0001			±0.0002						±0.0003			
b [Å]	3.0710			4.9297						11.2571			
	±0.00008			±0.0002						±0.0003			
c [Å]	3.0710			8.0117						11.2571			
	±0.00008			±0.000						±0.0003			
α [deg]	90			90						90			
β [deg]	90			90						90			
γ [deg]	90			120						90			
V [Å^3]	28.962			168.618						1426.508			
	±0.003			±0.017						±0.106			
G_U [∅]	5749.67			0						86.684			
G_V [∅]	-5094.52			272.47						-28.4592			
G_W [∅]	1347.2			-76.5049						1.82234			
L_X [∅]	0			0						0			
L_Y [∅]	0			0						0			
U_{ISO}	0.04945			0.05700						0.05195			
Atom	Ti	V	Fe	Ti	V	Fe	V	Fe	V	Ti	Fe	Ti	O
x	0	0	0	$\frac{1}{3}$	$\frac{1}{3}$	0	0	$\frac{83}{100}$	$\frac{83}{100}$	$\frac{47}{50}$	$\frac{293}{1000}$	$\frac{1}{2}$	0
y	0	0	0	$\frac{2}{3}$	$\frac{2}{3}$	0	0	$\frac{33}{50}$	$\frac{33}{50}$	$\frac{1}{8}$	$\frac{293}{1000}$	$\frac{1}{2}$	0
z	0	0	0	$\frac{63}{1000}$	$\frac{63}{1000}$	0	0	$\frac{1}{4}$	$\frac{1}{4}$	$\frac{1}{8}$	$\frac{293}{1000}$	$\frac{1}{2}$	0

D.2 Lab PXD patterns of hydrides

Table D.6: The fitted parameters from GSAS for the XRD pattern of $Ti_{0.70}V_{0.30}H_x$ that was measured on the Bruker AXS D8 Advance diffractometer at IFE. The unweighted profile factor was determined to $R_p = 0.0160$ while the weighted profile factor was $R_{wp} = 0.0213$. The goodness-of-fit was similarly determined to $\chi^2 = 5.486$. The scale factor was found to be S=505940. Zero-offset 0.1690750°. Shifted Chebyschev with 8 parameters background. Absorption: 11.406.

Phase	FCC		
S_{rel} [∅]	1.0		
wt.% [∅]	1.0		
	-		
a [Å]	4.4032 ±0.0014		
b [Å]	4.4032 ±0.0014		
c [Å]	4.4032 ±0.0014		
V [Å^3]	85.369 ±0.079		
α [deg]	90		
β [deg]	90		
γ [deg]	90		
G_U [∅]	0		
G_V [∅]	6622.08		
G_W [∅]	-1592.96		
L_X [∅]	0		
L_Y [∅]	195.387		
U_{ISO}	0.02942		
Atom	Ti	V	H
x	0	0	$\frac{1}{4}$
y	0	0	$\frac{1}{4}$
z	0	0	$\frac{1}{4}$

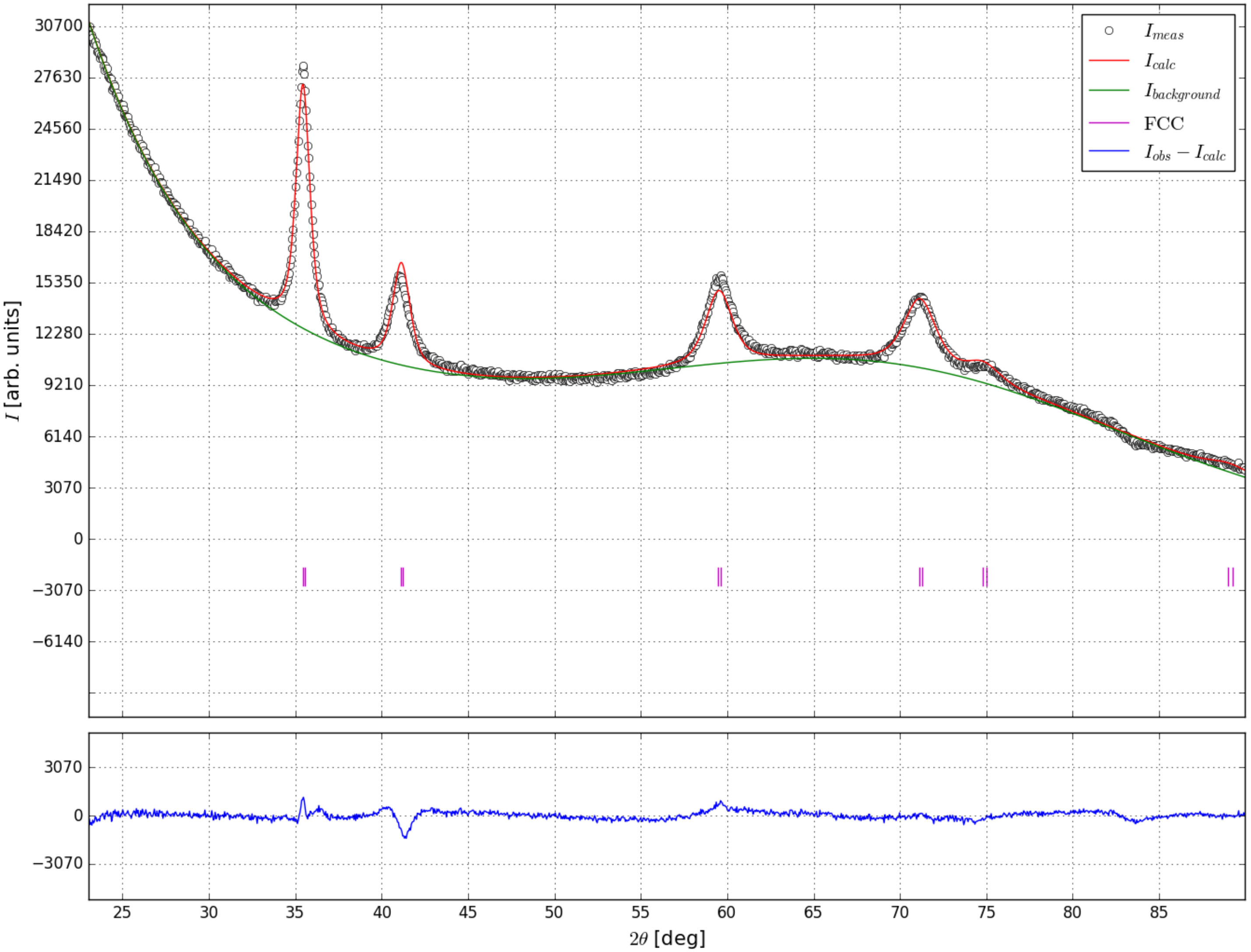

Figure D.6: The Lab PXD intensities I_{obs} for $\mathrm{Ti}_{0.70}\mathrm{V}_{0.30}\mathrm{H}_{\mathrm{x}}$ measured on the Bruker AXS D8 Advance diffractometer at IFE shown alongside the background $I_{background}$ and the calculated intensities I_{calc} that was fitted to the pattern in GSAS. The fitted parameters of the model is given in table D.6.

D.3 Lab PXD patterns of catalysts

Table D.7: The fitted parameters from GSAS for the XRD pattern of the first prepared batch of Zr_7Ni_{10} that was measured on the Bruker AXS D8 Advance diffractometer at IFE. The unweighted profile factor was determined to $R_p = 0.0344$ while the weighted profile factor was $R_{wp} = 0.0439$. The goodness-of-fit was similarly determined to $\chi^2 = 19.11$. The scale factor was found to be S=26866. Zero-offset 0.0402658°. Shifted Chebyschev with 16 parameters background. Absorption: 11.406.

Phase	Orthorombic
S_{rel} $[\emptyset]$	1.0
wt.% $[\emptyset]$	1.0
	-
a [Å]	12.356
	±0.004
b [Å]	9.171
	±0.005
c [Å]	9.201
	±0.004
V [Å^3]	1042.517
	±0.817
α [deg]	90
β [deg]	90
γ [deg]	90
G_U $[\emptyset]$	14223.4
G_V $[\emptyset]$	-10324.1
G_W $[\emptyset]$	2559.04
L_X $[\emptyset]$	0
L_Y $[\emptyset]$	0
U_{ISO}	0.03325

Atom	Ni	Ni	Ni	Zr	Zr	Zr	Zr
x	0.144380	0.355070	0	0	0.2500	0.306340	0
y	0.011150	0.291570	0.107550	0.312190	0.254660	0	0
z	0.208220	0.008330	0.394230	0.188470	0.2500	0	0

Table D.8: The fitted parameters from GSAS for the XRD pattern of the second prepared batch of Zr_7Ni_{10} that was measured on the Bruker AXS D8 Advance diffractometer at IFE. The unweighted profile factor was determined to $R_p = 0.0485$ while the weighted profile factor was $R_{wp} = 0.0653$. The goodness-of-fit was similarly determined to $\chi^2 = 23.67$. The scale factor was found to be S=14457. Zero-offset 0.0497335°. Shifted Chebyschev with 16 parameters background. Absorption: 11.406.

Phase	Orthorombic						
S_{rel} $[\emptyset]$	1.0						
wt.% $[\emptyset]$	1.0						
	-						
a [Å]	12.360						
	±0.005						
b [Å]	9.161						
	±0.004						
c [Å]	9.206						
	±0.004						
V [Å^3]	1042.462						
	±1.023						
α [deg]	90						
β [deg]	90						
γ [deg]	90						
G_U $[\emptyset]$	11820.7						
G_V $[\emptyset]$	-9282.39						
G_W $[\emptyset]$	2228.26						
L_X $[\emptyset]$	0						
L_Y $[\emptyset]$	0						
U_{ISO}	0.04183						
Atom	Ni	Ni	Ni	Zr	Zr	Zr	Zr
x	0.144380	0.355070	0	0	0.2500	0.306340	0
y	0.011150	0.291570	0.107550	0.312190	0.254660	0	0
z	0.208220	0.008330	0.394230	0.188470	0.2500	0	0

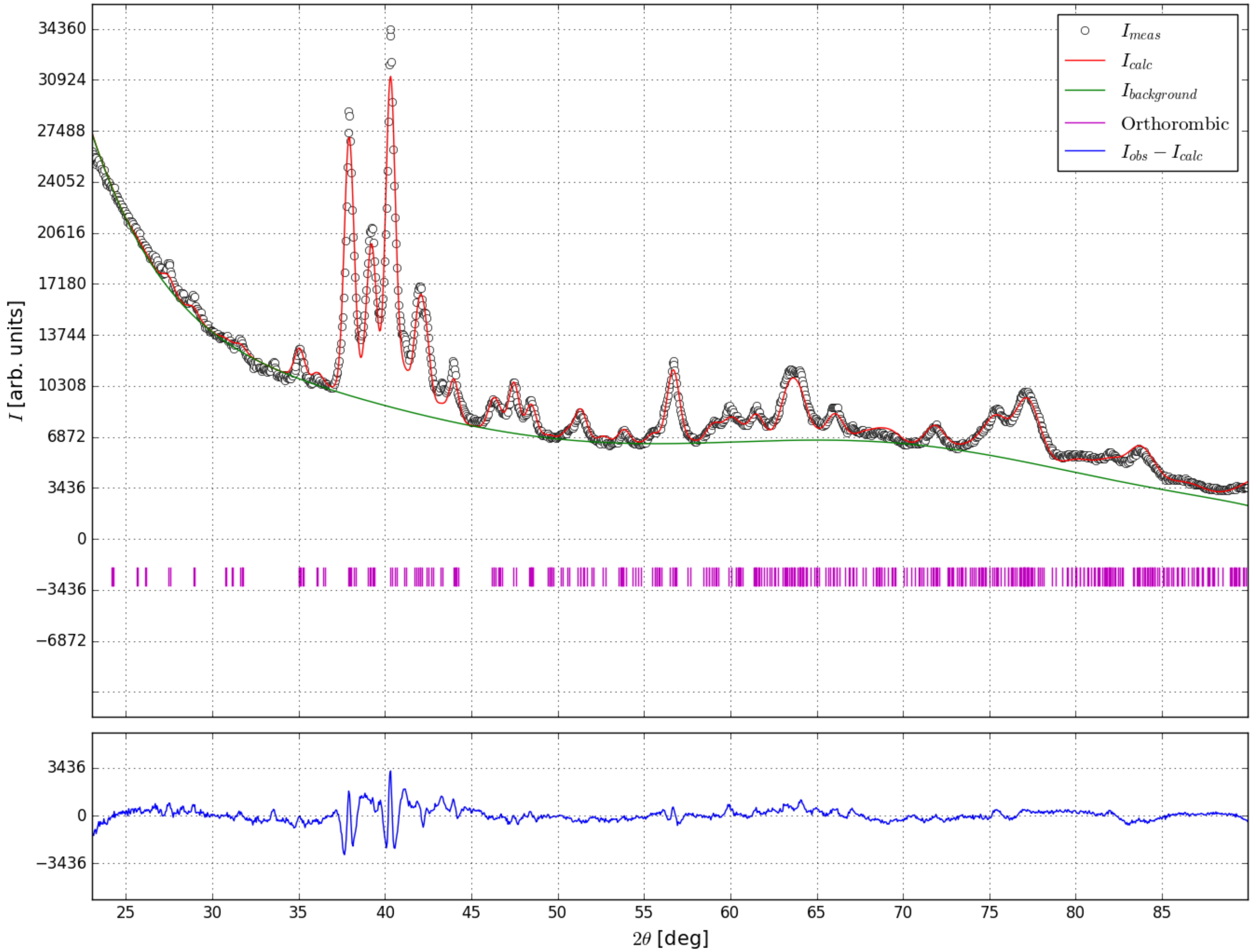

Figure D.7: The Lab PXD intensities I_{obs} for Zr_7Ni_{10} measured on the Bruker AXS D8 Advance diffractometer at IFE shown alongside the background $I_{background}$ and the calculated intensities I_{calc} that was fitted to the pattern in GSAS. The fitted parameters of the model is given in table D.7.

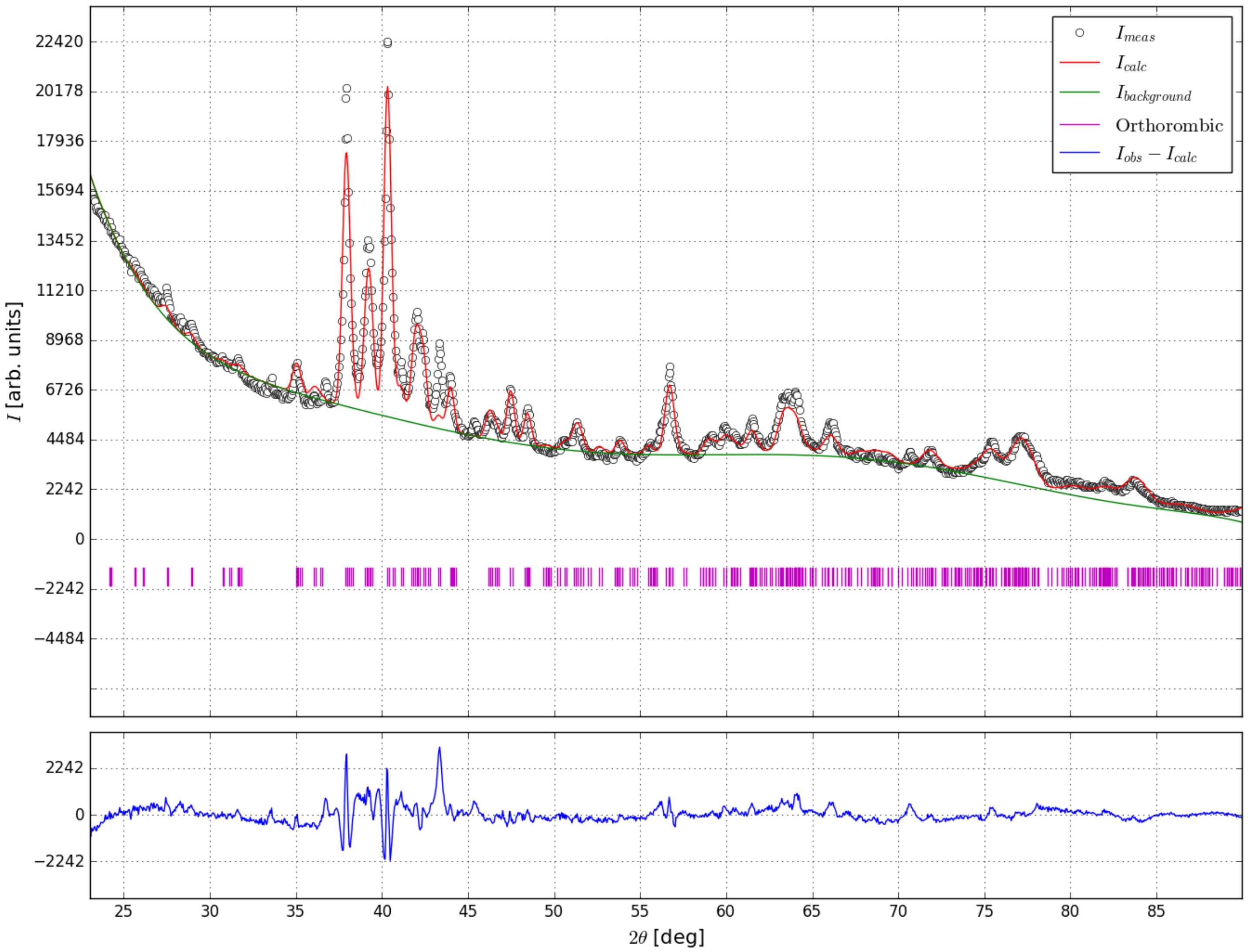

Figure D.8: The Lab PXD intensities I_{obs} for Zr_7Ni_{10} measured on the Bruker AXS D8 Advance diffractometer at IFE shown alongside the background $I_{background}$ and the calculated intensities I_{calc} that was fitted to the pattern in GSAS. The fitted parameters of the model is given in table D.8.

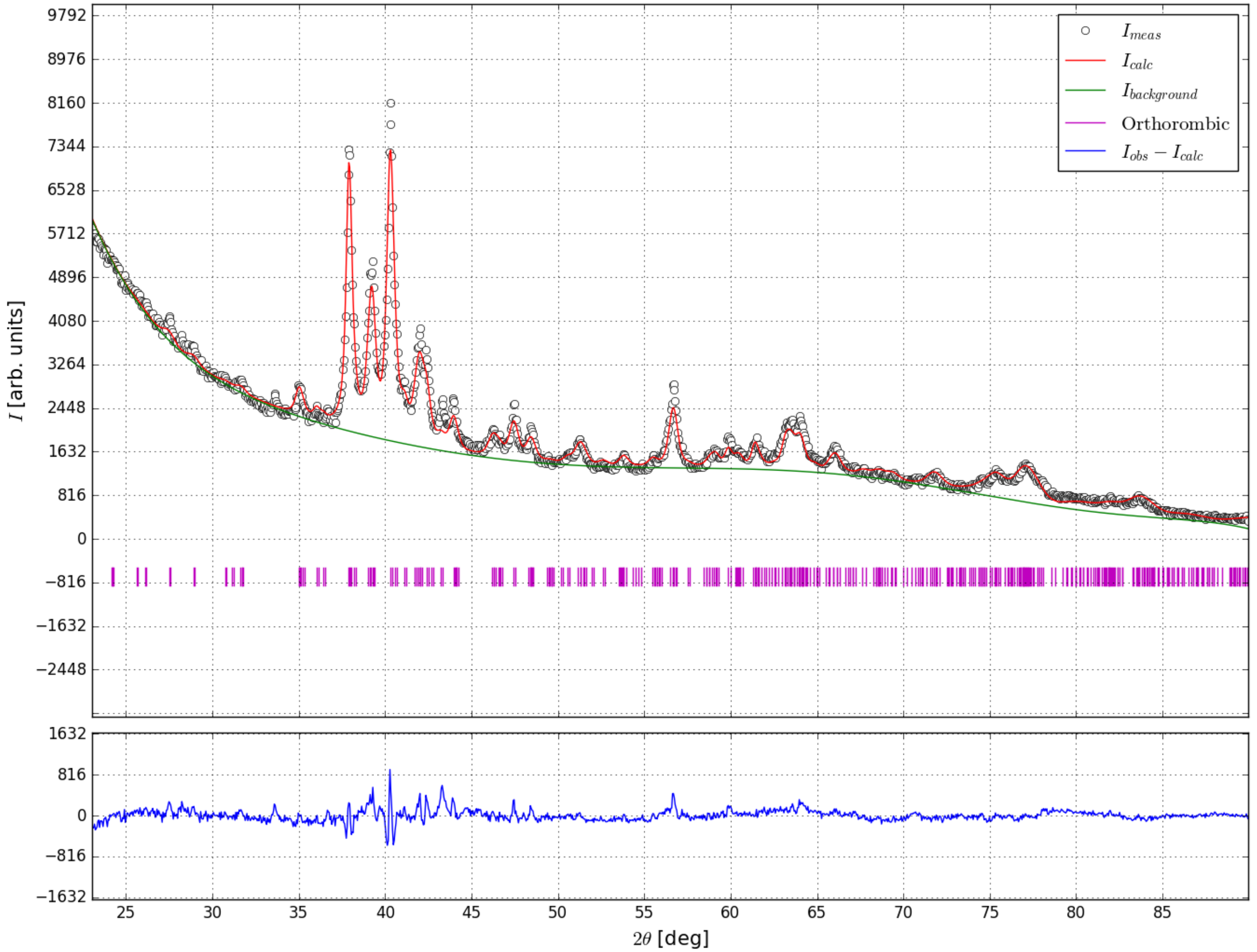

Figure D.9: The Lab PXD intensities I_{obs} for Zr_7Ni_{10} measured on the Bruker AXS D8 Advance diffractometer at IFE shown alongside the background $I_{background}$ and the calculated intensities I_{calc} that was fitted to the pattern in GSAS. The fitted parameters of the model is given in table D.9.

Table D.9: The fitted parameters from GSAS for the XRD pattern of the second prepared batch of Zr_7Ni_{10} that was measured on the Bruker AXS D8 Advance diffractometer at IFE. The unweighted profile factor was determined to $R_p = 0.0398$ while the weighted profile factor was $R_{wp} = 0.0523$. The goodness-of-fit was similarly determined to $\chi^2 = 5.382$. The scale factor was found to be $S = 7397.8$. Zero-offset 0.0684766°. Shifted Chebyschev with 8 parameters background. Absorption: 11.406.

Phase	Orthorombic						
S_{rel} [$\emptyset$]	1.0						
wt.% [$\emptyset$]	1.0						
	-						
a [Å]	12.3670						
	±0.0016						
b [Å]	9.1756						
	±0.0014						
c [Å]	9.2063						
	±0.0014						
V [Å^3]	1044.686						
	±0.263						
α [deg]	90						
β [deg]	90						
γ [deg]	90						
G_U [$\emptyset$]	1872.09						
G_V [$\emptyset$]	-1752.82						
G_W [$\emptyset$]	376.939						
L_X [$\emptyset$]	30.9141						
L_Y [$\emptyset$]	0						
U_{ISO}	0.05464						
Atom	Ni	Ni	Ni	Zr	Zr	Zr	Zr
x	0.144380	0.355070	0	0	0.2500	0.306340	0
y	0.011150	0.291570	0.107550	0.312190	0.254660	0	0
z	0.208220	0.008330	0.394230	0.188470	0.2500	0	0

D.4 SR-PXD patterns of absorption experiment

Table D.10: The fitted parameters from GSAS for the $(Ti_{0.70}V_{0.30})_{0.90}Fe_{0.10}$+5wt.% Zr_7Ni_{10} that was measured during the absorption experiment shown in figure 4.16. The unweighted profile factor was determined to $R_p = 0.0622$ while the weighted profile factor was $R_{wp} = 0.0913$. The goodness-of-fit was similarly determined to $\chi^2 = 1287000$. The scale factor was found to be S=149930. Zero-offset -0.0161493°. User defined background with 16 parameters background. Absorption: 3.0977.

Phase	BCC		HCP	
S_{rel} [$\emptyset$]	1.0		0.082623	
wt.% [$\emptyset$]	0.924 ±0.001		0.076 ±0.002	
a [Å]	3.13588 ±0.00007		2.9597 ±0.0003	
b [Å]	3.13588 ±0.00007		2.9597 ±0.0003	
c [Å]	3.13588 ±0.00007		4.742 ±0.001	
V [Å^3]	30.837 ±0.002		35.971 ±0.008	
α [deg]	90		90	
β [deg]	90		90	
γ [deg]	90		120	
G_U [$\emptyset$]	0		0	
G_V [$\emptyset$]	242.965		85.4945	
G_W [$\emptyset$]	-19.9898		5.0465	
L_X [$\emptyset$]	0		0	
L_Y [$\emptyset$]	32.7734		37.612	
U_{ISO}	0.02306		0.01644	
Atom	Ti	V	Ti	V
x	0	0	$\frac{1}{3}$	$\frac{1}{3}$
y	0	0	$\frac{2}{3}$	$\frac{2}{3}$
z	0	0	$\frac{1}{4}$	$\frac{1}{4}$

Table D.11: The fitted parameters from GSAS for the $(Ti_{0.70}V_{0.30})_{0.90}Fe_{0.10}$+5wt.% Zr_7Ni_{10} that was measured during the absorption experiment shown in figure 4.16. The unweighted profile factor was determined to $R_p = 0.0776$ while the weighted profile factor was $R_{wp} = 0.1176$. The goodness-of-fit was similarly determined to $\chi^2 = 1896000$. The scale factor was found to be S=129960. Zero-offset -0.071001°. User defined background with 16 parameters background. Absorption: 3.0977.

Phase	BCC			HCP			FCC			
S_{rel} [$\emptyset$]	1.0			0.12622			0.0071686			
wt.% [$\emptyset$]	0.876			0.111			0.013075			
	±0.001			±0.004			±0.002			
a [Å]	3.1437			2.9676			4.220			
	±0.0003			±0.0005			±0.005			
b [Å]	3.1437			2.9676			4.220			
	±0.0003			±0.0005			±0.005			
c [Å]	3.1437			4.7526			4.220			
	±0.0003			±0.0015			±0.005			
α [deg]	90			90			90			
β [deg]	90			90			90			
γ [deg]	90			120			90			
V [Å^3]	31.068			36.248			75.166			
	±0.008			±0.013			±0.249			
G_U [$\emptyset$]	0			0			0			
G_V [$\emptyset$]	437.354			197.706			4143.94			
G_W [$\emptyset$]	-27.7729			30.77			-508.42			
L_X [$\emptyset$]	0			0			0			
L_Y [$\emptyset$]	0			0			0			
U_{ISO}	0.03563			0.04528			0.02500			
Atom	Ti	V	Fe	Ti	V	Fe	Ti	V	Fe	H
x	0	0	0	$\frac{1}{3}$	$\frac{1}{3}$	$\frac{1}{3}$	0	0	0	$\frac{1}{4}$
y	0	0	0	$\frac{2}{3}$	$\frac{2}{3}$	$\frac{2}{3}$	0	0	0	$\frac{1}{4}$
z	0	0	0	$\frac{1}{4}$	$\frac{1}{4}$	$\frac{1}{4}$	0	0	0	$\frac{1}{4}$

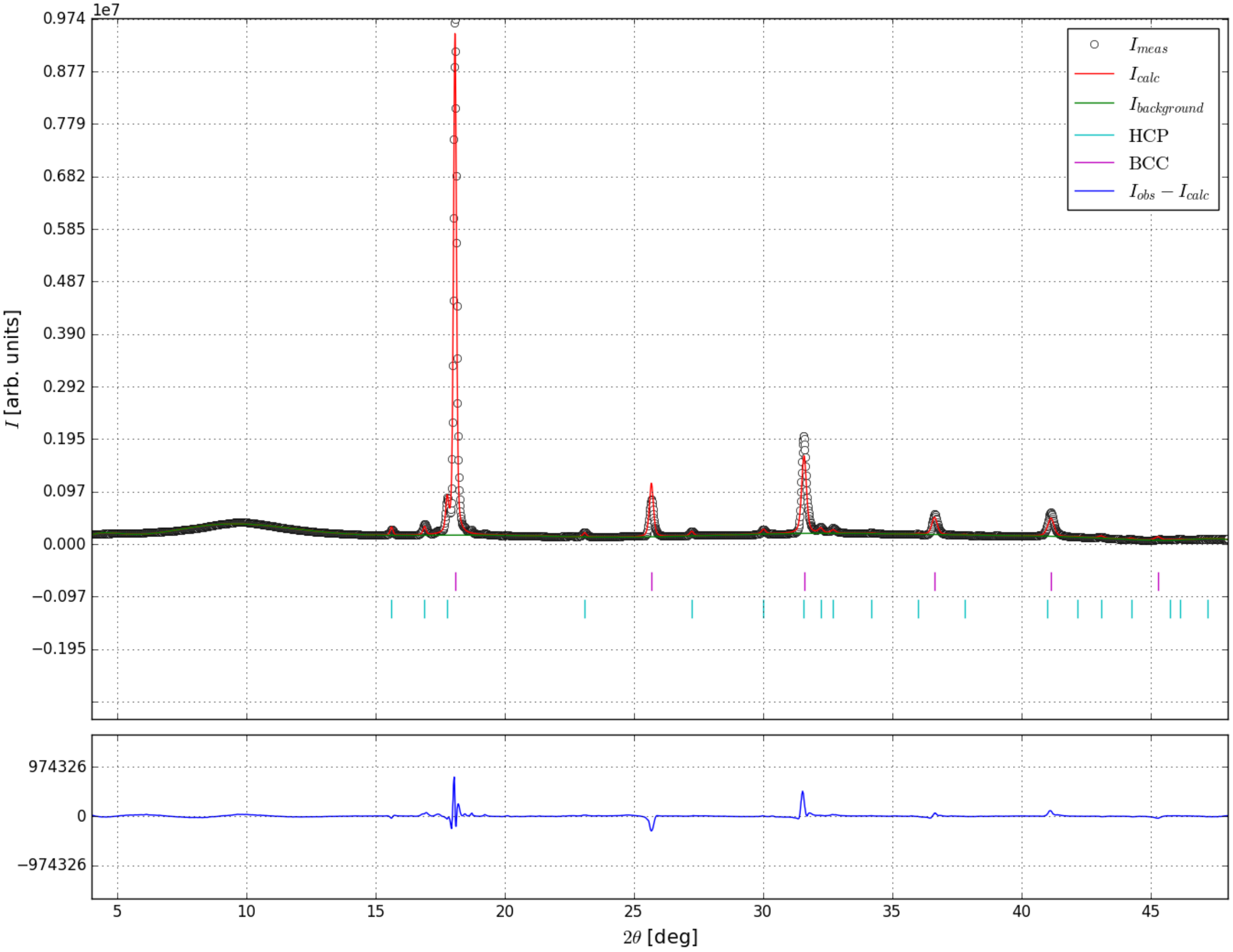

Figure D.10: The SR-PXD intensities I_{obs} for $(Ti_{0.70}V_{0.30})_{0.90}Fe_{0.10}$+5wt.% Zr_7Ni_{10} that was measured during the absorption experiment shown in figure 4.16 alongside the background $I_{background}$ and the calculated intensities I_{calc} that was fitted to the pattern in GSAS. The fitted parameters of the model is given in table D.10.

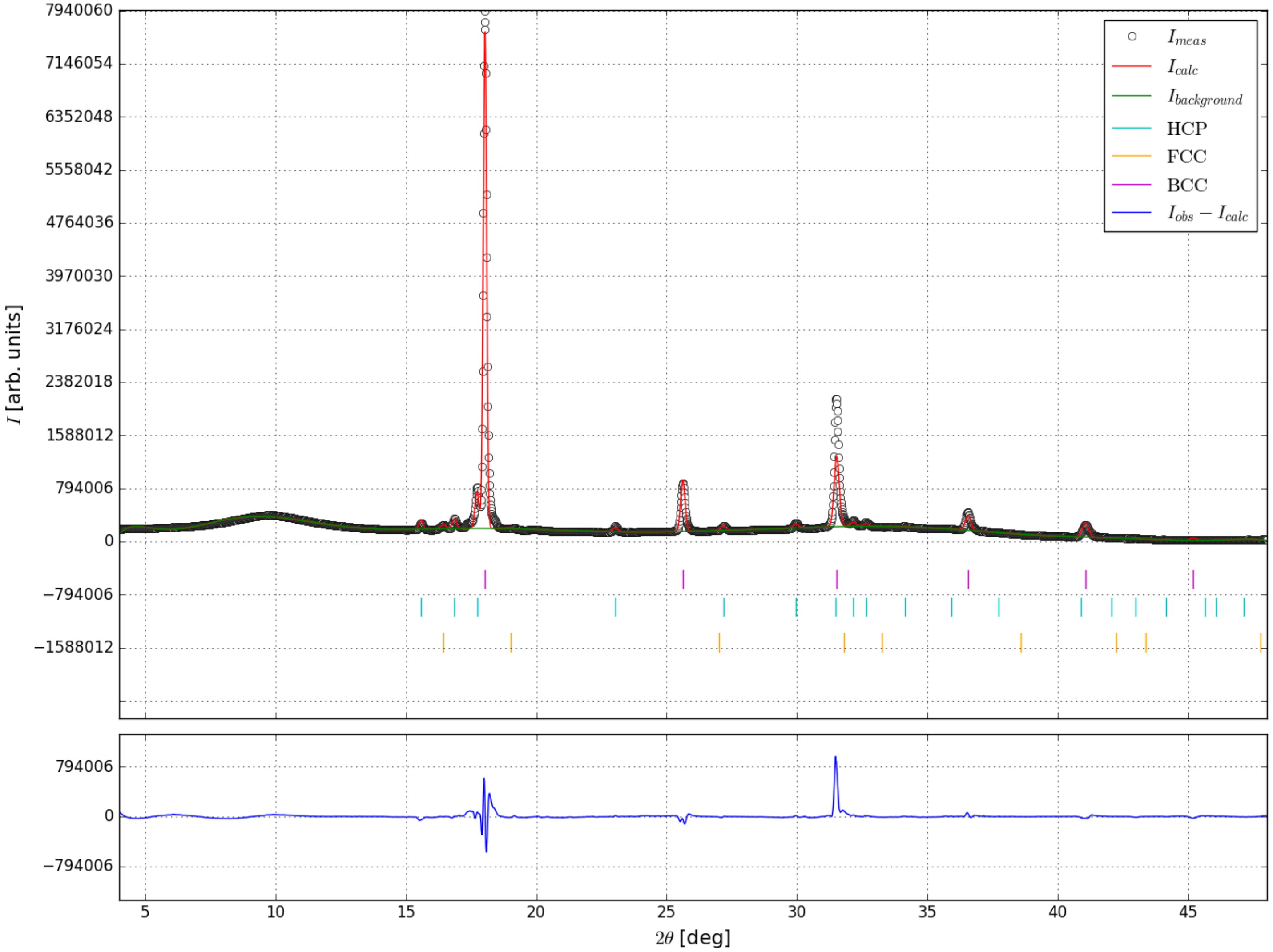

Figure D.11: The SR-PXD intensities I_{obs} for $(\mathrm{Ti}_{0.70}\mathrm{V}_{0.30})_{0.90}\mathrm{Fe}_{0.10}$+5wt.% $\mathrm{Zr}_7\mathrm{Ni}_{10}$ that was measured during the absorption experiment shown in figure 4.16 alongside the background $I_{background}$ and the calculated intensities I_{calc} that was fitted to the pattern in GSAS. The fitted parameters of the model is given in table D.11.

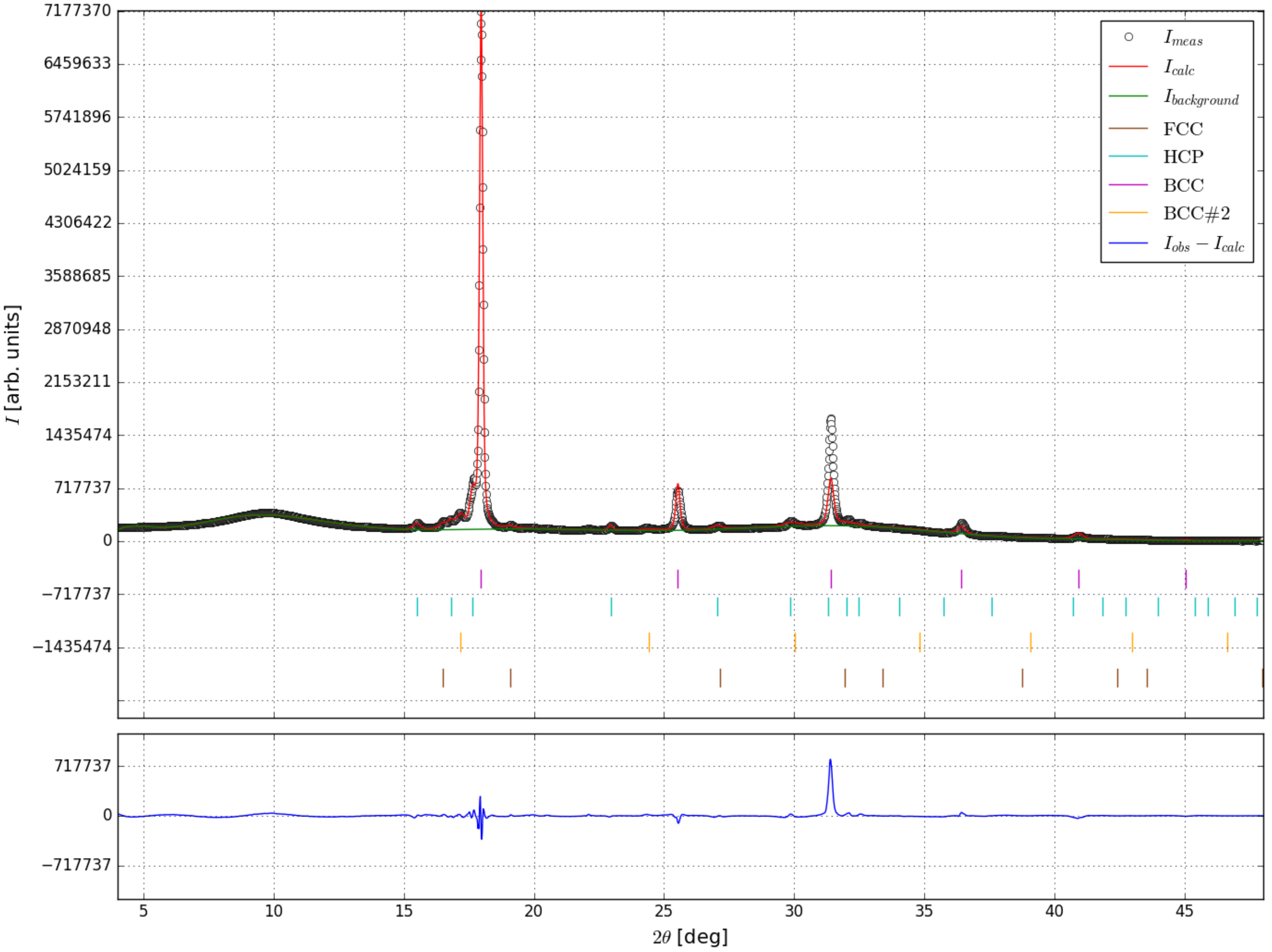

Figure D.12: The SR-PXD intensities I_{obs} for $(\mathrm{Ti}_{0.70}\mathrm{V}_{0.30})_{0.90}\mathrm{Fe}_{0.10}$+5wt.% $\mathrm{Zr}_7\mathrm{Ni}_{10}$ that was measured during the absorption experiment shown in figure 4.16 alongside the background $I_{background}$ and the calculated intensities I_{calc} that was fitted to the pattern in GSAS. The fitted parameters of the model is given in table D.12.

Table D.12: The fitted parameters from GSAS for the $(Ti_{0.70}V_{0.30})_{0.90}Fe_{0.10}$+5wt.% Zr_7Ni_{10} that was measured during the absorption experiment shown in figure 4.16. The unweighted profile factor was determined to $R_p = 0.0621$ while the weighted profile factor was $R_{wp} = 0.0973$. The goodness-of-fit was similarly determined to $\chi^2 = 1193000$. The scale factor was found to be S=165830. Zero-offset -0.0036067°. User defined background with 16 parameters background. Absorption: 3.0977.

Phase	BCC			HCP			BCC #2				FCC			
S_{rel} [$\emptyset$]	1.0			0.11157			0.048436				0.018462			
wt.% [$\emptyset$]	0.830			0.093			0.045				0.032			
	±0.001			±0.004			±0.002				±0.002			
a [Å]	3.1552			2.9838			3.2973				4.203			
	±0.0004			±0.0011			±0.0015				±0.004			
b [Å]	3.1552			2.9838			3.2973				4.203			
	±0.0004			±0.0011			±0.0015				±0.004			
c [Å]	3.1552			4.7666			3.2973				4.203			
	±0.0004			±0.0031			±0.0015				±0.004			
α [deg]	90			90			90				90			
β [deg]	90			90			90				90			
γ [deg]	90			120			90				90			
V [Å^3]	31.409			36.752			35.849				75.166			
	±0.012			±0.021			±0.050				±0.249			
G_U [$\emptyset$]	3842.25			65736.7			0				0			
G_V [$\emptyset$]	-1328.68			-24209.9			9388.02				227.218			
G_W [$\emptyset$]	132.023			2260.46			-1164.66				-126.69			
L_X [$\emptyset$]	0			0			0				0			
L_Y [$\emptyset$]	45.6199			30.4102			0				192.998			
U_{ISO}	0.05310			0.04356			0.02500				0.02500			
Atom	Ti	V	Fe	Ti	V	Fe	Ti	V	Fe	H	Ti	V	Fe	H
x	0	0	0	$\frac{1}{3}$	$\frac{1}{3}$	$\frac{1}{3}$	0	0	0	0	0	0	0	$\frac{1}{4}$
y	0	0	0	$\frac{2}{3}$	$\frac{2}{3}$	$\frac{2}{3}$	0	0	0	$\frac{1}{2}$	0	0	0	$\frac{1}{4}$
z	0	0	0	$\frac{1}{4}$	$\frac{1}{4}$	$\frac{1}{4}$	0	0	0	$\frac{1}{4}$	0	0	0	$\frac{1}{4}$

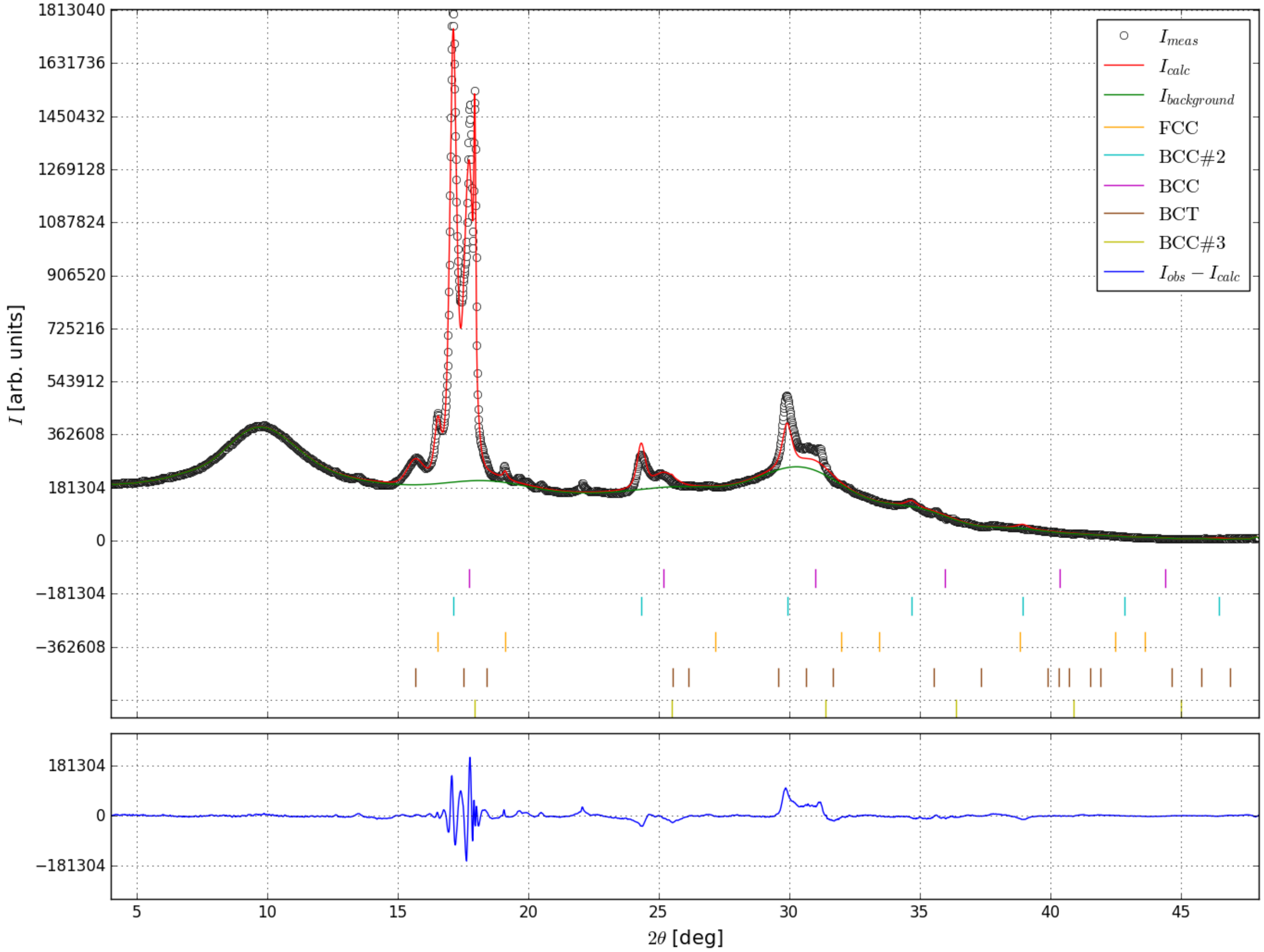

Figure D.13: The SR-PXD intensities I_{obs} for $(Ti_{0.70}V_{0.30})_{0.90}Fe_{0.10}$+5wt.% Zr_7Ni_{10} that was measured during the absorption experiment shown in figure 4.16 alongside the background $I_{background}$ and the calculated intensities I_{calc} that was fitted to the pattern in GSAS. The fitted parameters of the model is given in table D.13.

Table D.13: The fitted parameters from GSAS for the $(Ti_{0.70}V_{0.30})_{0.90}Fe_{0.10}$+5wt.% Zr_7Ni_{10} that was measured during the absorption experiment shown in figure 4.16. The unweighted profile factor was determined to $R_p = 0.0391$ while the weighted profile factor was $R_{wp} = 0.0642$. The goodness-of-fit was similarly determined to $\chi^2 = 489900$. The scale factor was found to be S=125310. Zero-offset -0.0313618°. User defined background with 36 parameters background. Absorption: 3.0977.

Phase	FCC				BCT				BCC #2				BCC			BCC #3		
S_{rel} [∅]	1.5126				1.4272				1.0271				1.0			0.82045		
wt.% [∅]	0.409 ±0.019				0.193 ±0.014				0.14955 ±0.002				0.130 ±0.002			0.11946 ±0.0013		
a [Å]	4.1921 ±0.0014				3.078 ±0.004				3.1928 ±0.0004				3.1542 ±0.0003			3.3050 ±0.0003		
b [Å]	4.1921 ±0.0014				3.078 ±0.004				3.1928 ±0.0004				3.1542 ±0.0003			3.3050 ±0.0003		
c [Å]	4.1921 ±0.0014				4.566 ±0.013				3.1928 ±0.0004				3.1542 ±0.0003			3.3050 ±0.0003		
α [deg]	90				90				90				90			90		
β [deg]	90				90				90				90			90		
γ [deg]	90				90				90				90			90		
V [Å^3]	73.668 ±0.072				43.272 ±0.160				32.546 ±0.021				31.382 ±0.009			36.100 ±0.010		
G_U [∅]	0				0				0				0			0		
G_V [∅]	284.849				35767.5				16367.7				88.7773			284.849		
G_W [∅]	37.1196				-4046.6				-2286.35				-1.91255			37.1196		
L_X [∅]	0				0				0				0			0		
L_Y [∅]	105.389				0				77.9915				0			105.389		
U_{ISO}	0.57820				0.54819				0.11635				0.39792			0.08140		
Atom	Ti	V	Fe	H	Ti	V	Fe	H	Ti	V	Fe	H	Ti	V	Fe	Ti	V	Fe
x	0	0	0	$\frac{1}{4}$	0	0	0	0	0	0	0	0	0	0	0	0	0	0
y	0	0	0	$\frac{1}{4}$	0	0	0	$\frac{1}{2}$	0	0	0	$\frac{1}{2}$	0	0	0	0	0	0
z	0	0	0	$\frac{1}{4}$	0	0	0	$\frac{1}{4}$	0	0	0	$\frac{1}{4}$	0	0	0	0	0	0

D.5 SR-PXD patterns of the alloys

Table D.14: The fitted parameters from GSAS for the $Ti_{0.70}V_{0.30}$ XRD pattern that was collected at ESRF. The unweighted profile factor was determined to $R_p = 0.0401$ while the weighted profile factor was $R_{wp} = 0.0840$. The goodness-of-fit was similarly determined to $\chi^2 = 2023$. The scale factor was found to be S=6.0985. Zero-offset -0.16230. Shifted Chebyschev with 16 parameters background.

Phase	BCC		BCC #2		HCP	
S_{rel} [∅]	1.0		0.31136		0.10621	
Wt. frac. [∅]	0.655		0.204		0.141	
	±0.001		±0.008		±0.002	
a [Å]	3.18365		3.1679		2.95844	
	±0.00008		±0.0005		±0.00007	
b [Å]	3.18365		3.1679		2.95844	
	±0.00008		±0.0005		±0.00007	
c [Å]	3.18365		3.1679		4.73545	
	±0.00008		±0.0005		±0.00013	
V [Å^3]	32.268		31.790		35.894	
	±0.002		±0.015		±0.002	
α [deg]	90		90		90	
β [deg]	90		90		90	
γ [deg]	90		90		120	
G_U [∅]	281.565		250.550		462.962	
G_V [∅]	-4.79878		-31.3341		-204.811	
G_W [∅]	11.6055		44.4803		38.4342	
L_X [∅]	0		0		0	
L_Y [∅]	17.6358		31.1883		22.1594	
U_{ISO}	0.00796		0.02500		-0.00448	
Atom	Ti	V	Ti	V	Ti	V
x	0	0	0	0	$\frac{1}{3}$	$\frac{1}{3}$
y	0	0	0	0	$\frac{2}{3}$	$\frac{2}{3}$
z	0	0	0	0	$\frac{1}{4}$	$\frac{1}{4}$

Table D.15: The fitted parameters from GSAS for the $(Ti_{0.70}V_{0.30})_{0.97}Fe_{0.03}$ XRD pattern that was collected at ESRF. The unweighted profile factor was determined to $R_p = 0.0312$ while the weighted profile factors was $R_{wp} = 0.0466$. The goodness-of-fit was similarly determined to $\chi^2 = 699.9$. the scale was determined to $S = 5.954400$

Phase	BCC			BCC #2			HCP			FCC		
S_{rel} $[\emptyset]$	1.0			0.249780			0.044518			0.013147		
wt.% $[\emptyset]$	1.0			0.249780			0.044518			0.013147		
a [Å]	3.175766			3.160893			2.959015			4.273150		
b [Å]	3.175766			3.160893			2.959015			4.273150		
c [Å]	3.175766			3.160893			4.736785			4.273150		
α [deg]	90			90			90			90		
β [deg]	90			90			90			90		
γ [deg]	90			90			120			90		
G_U $[\emptyset]$	256.306			205.1320			307.6570			205.1320		
G_V $[\emptyset]$	-14.6212			4.83261			-139.7310			4.83261		
G_W $[\emptyset]$	11.7039			28.8402			31.1600			6.75006		
L_X $[\emptyset]$	0			0			0			0		
L_Y $[\emptyset]$	17.7637			20.8906			25.0708			20.8906		
U_{ISO}	0.00182			0.02500			-0.01421			0.02500		
Atom	Ti	V	Fe	Ti	V	Fe	Ti	V	Fe	Ti	V	Fe
x	0	0	0	0	0	0	$\frac{1}{3}$	$\frac{1}{3}$	$\frac{1}{3}$	0	0	0
y	0	0	0	0	0	0	$\frac{2}{3}$	$\frac{2}{3}$	$\frac{2}{3}$	0	0	0
z	0	0	0	0	0	0	$\frac{1}{4}$	$\frac{1}{4}$	$\frac{1}{4}$	0	0	0

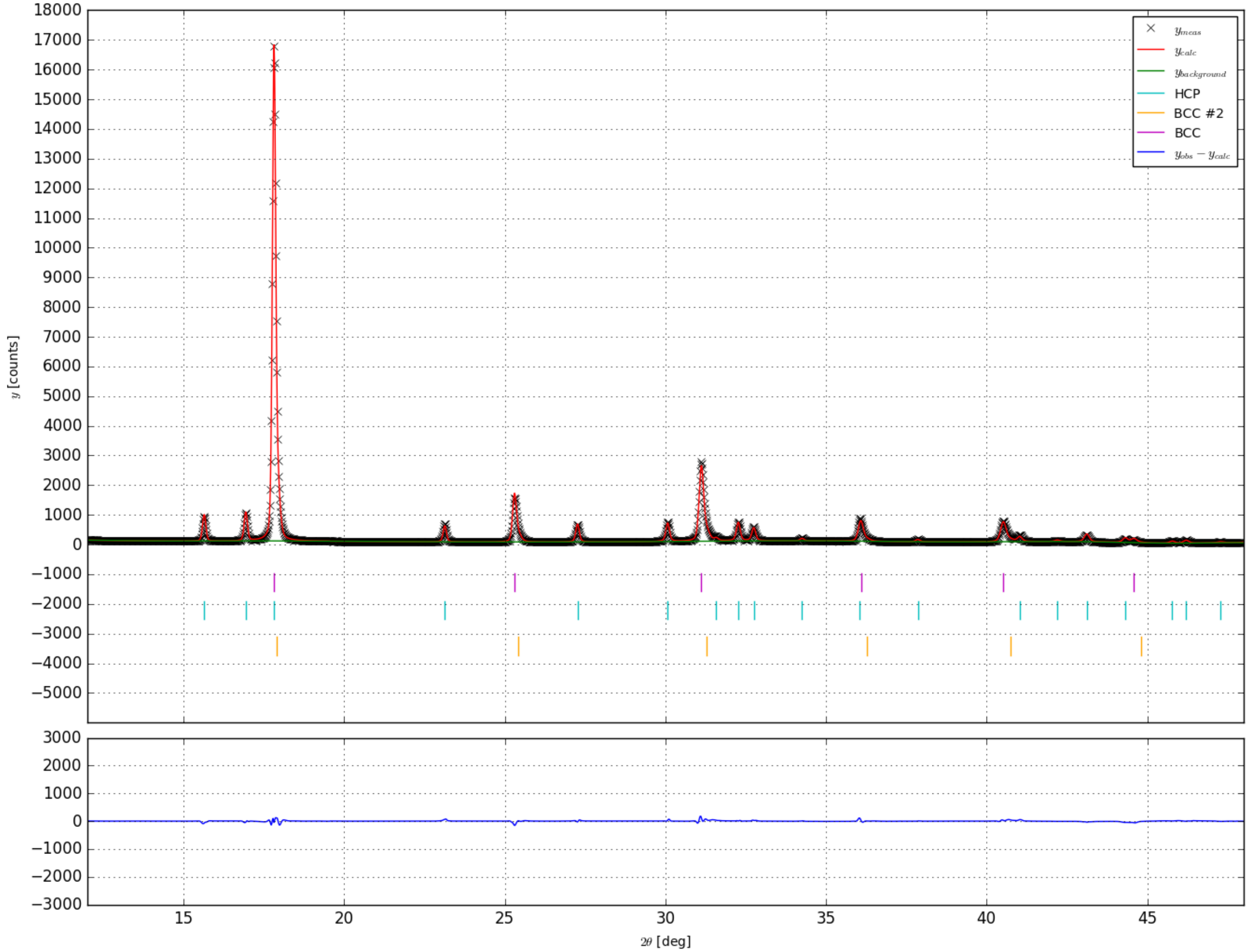

Figure D.14: The SR-PXD intensities y_{obs} for $\mathrm{Ti}_{0.70}\mathrm{V}_{0.30}$ measured at ESRF shown alongside the background $y_{background}$ and the calculated intensities y_{calc} that was fitted to the pattern in GSAS. The fitted parameters of the model is shown for reference in table D.14.

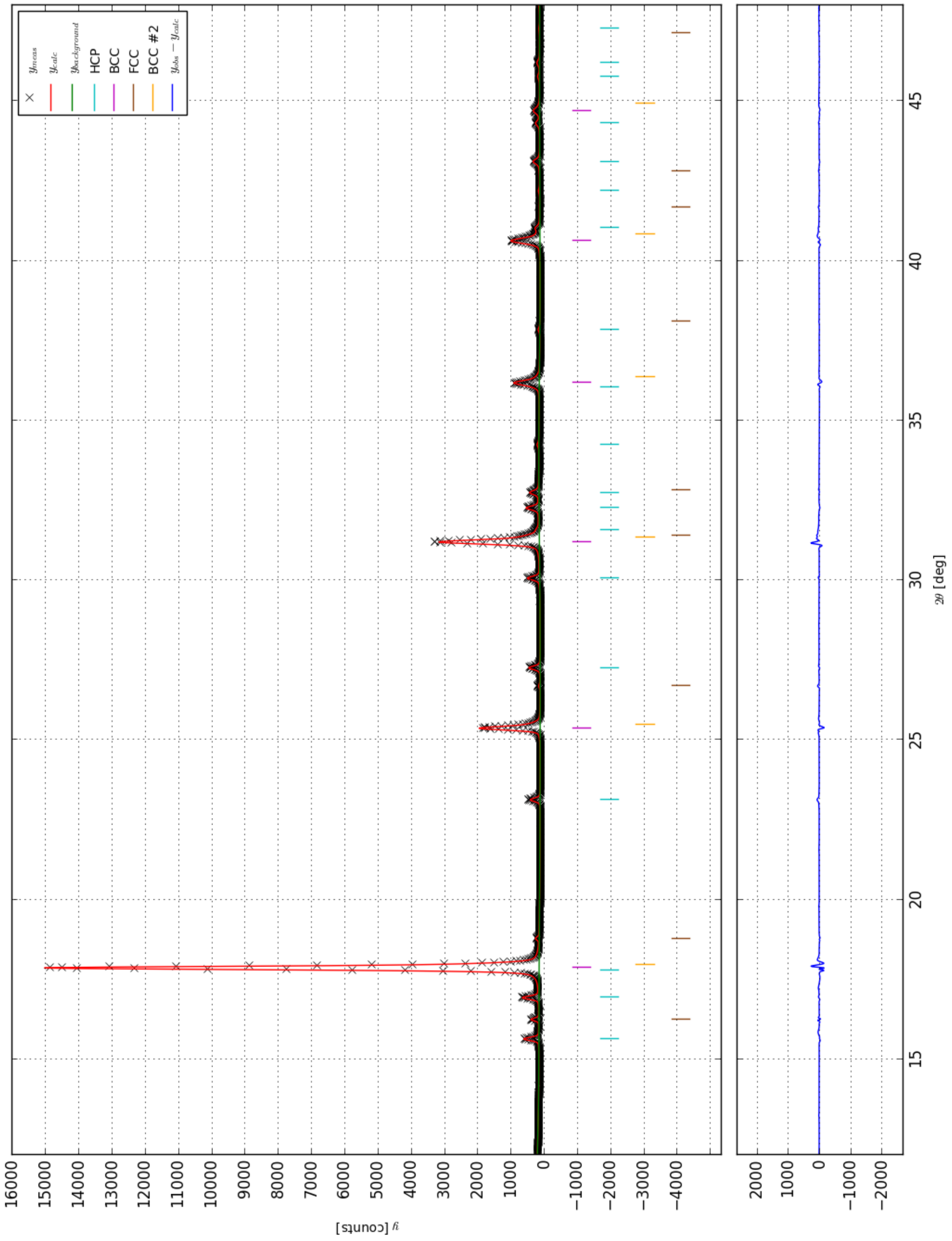

Figure D.15: The SR-PXD intensities y_{obs} for $(\mathrm{Ti}_{0.70}\mathrm{V}_{0.30})_{0.97}\mathrm{Fe}_{0.03}$ measured at ESRF shown alongside the background $y_{background}$ and the calculated intensities y_{calc} that was fitted to the pattern in GSAS. The fitted parameters of the model is shown for reference in table D.15.

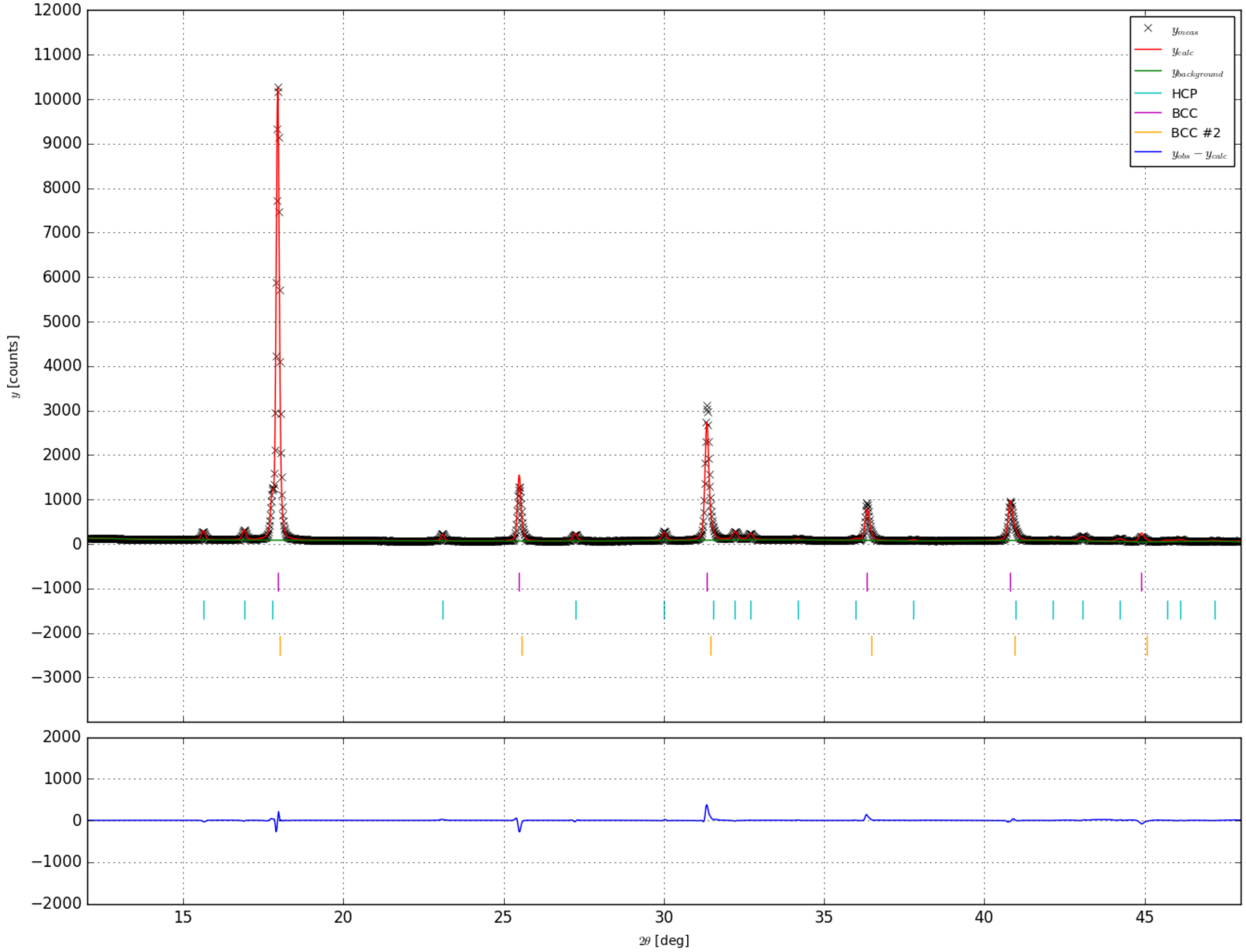

Figure D.16: The SR-PXD intensities y_{obs} for $(\mathrm{Ti}_{0.70}\mathrm{V}_{0.30})_{0.94}\mathrm{Fe}_{0.06}$ measured at ESRF shown alongside the background $y_{background}$ and the calculated intensities y_{calc} that was fitted to the pattern in GSAS. The fitted parameters of the model is shown for reference in table D.16.

Table D.16: The fitted parameters from GSAS for the $(\mathrm{Ti}_{0.70}\mathrm{V}_{0.30})_{0.94}\mathrm{Fe}_{0.06}$ XRD pattern that was collected at ESRF. The unweighted profile factor was determined to $R_p = 0.0428$ while the weighted profile factors was $R_{wp} = 0.0845$. The goodness-of-fit was similarly determined to $\chi^2 = 1508$. The scale factor was determined to $S = 3.9688$. Zero-offset 1.01722. Shifted Chebyshev with 16 parameters background.

Phase	BCC		HCP		BCC #2	
S_{rel} $[\emptyset]$	1.0		0.15218		0.13009	
a [Å]	3.162787		2.963083		3.152516	
b [Å]	3.162787		2.963083		3.152516	
c [Å]	3.162787		4.747273		3.152516	
α [deg]	90		90		90	
β [deg]	90		90		90	
γ [deg]	90		120		90	
G_U $[\emptyset]$	41.6027		1226.8800		87.2146	
G_V $[\emptyset]$	24.8350		-538.3170		8.22154	
G_W $[\emptyset]$	10.7402		69.8492		29.2228	
L_X $[\emptyset]$	0		0		0	
L_Y $[\emptyset]$	15.3560		36.1512		22.5588	
U_{ISO}	-0.00223		-0.02459		-0.01451	
Atom	Ti	V	Ti	V	Ti	V
x	0	0	$\frac{1}{3}$	$\frac{1}{3}$	0	0
y	0	0	$\frac{2}{3}$	$\frac{2}{3}$	0	0
z	0	0	$\frac{1}{4}$	$\frac{1}{4}$	0	0

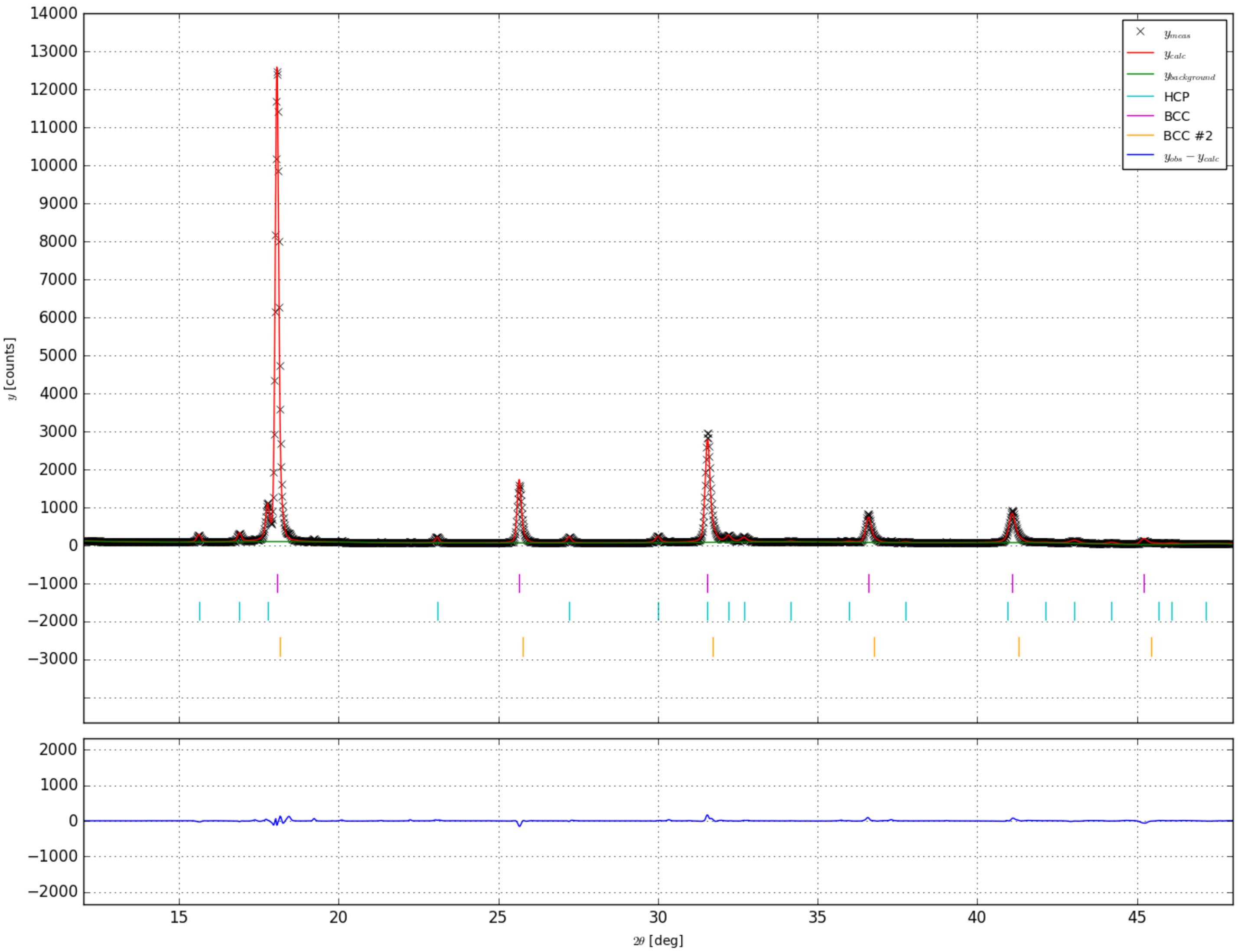

Figure D.17: The SR-PXD intensities y_{obs} for $(Ti_{0.70}V_{0.30})_{0.90}Fe_{0.10}$ measured at ESRF shown alongside the background $y_{background}$ and the calculated intensities y_{calc} that was fitted to the pattern in GSAS. The fitted parameters of the model is shown for reference in table D.17.

Table D.17: The fitted parameters from GSAS for the $(Ti_{0.70}V_{0.30})_{0.90}Fe_{0.10}$ XRD pattern that was collected at ESRF. The unweighted profile factor was determined to $R_p = 0.0404$ while the weighted profile factors was $R_{wp} = 0.0832$. The goodness-of-fit was similarly determined to $\chi^2 = 1598$. The scale factor was determined to $S = 5.7843$. Zero-offset 0.67719. Shifted Chebyshev with 16 parameters background.

Phase	BCC		BCC #2		HCP	
S_{rel} $[\emptyset]$	1.0		0.13288		0.12300	
a [Å]	3.141750		3.126755		2.963816	
b [Å]	3.141750		3.126755		2.963816	
c [Å]	3.141750		3.126755		4.748923	
α [deg]	90		90		90	
β [deg]	90		90		90	
γ [deg]	90		90		120	
G_U $[\emptyset]$	499.042		623.231		1972.5	
G_V $[\emptyset]$	-85.6188		-158.57		-882.597	
G_W $[\emptyset]$	22.0309		70.7101		103.234	
L_X $[\emptyset]$	0		0		0	
L_Y $[\emptyset]$	15.6927		28.9288		53.425	
U_{ISO}	0.00380		-0.00828		-0.02031	
Atom	Ti	V	Ti	V	Ti	V
x	0	0	0	0	$\frac{1}{3}$	$\frac{1}{3}$
y	0	0	0	0	$\frac{2}{3}$	$\frac{2}{3}$
z	0	0	0	0	$\frac{1}{4}$	$\frac{1}{4}$

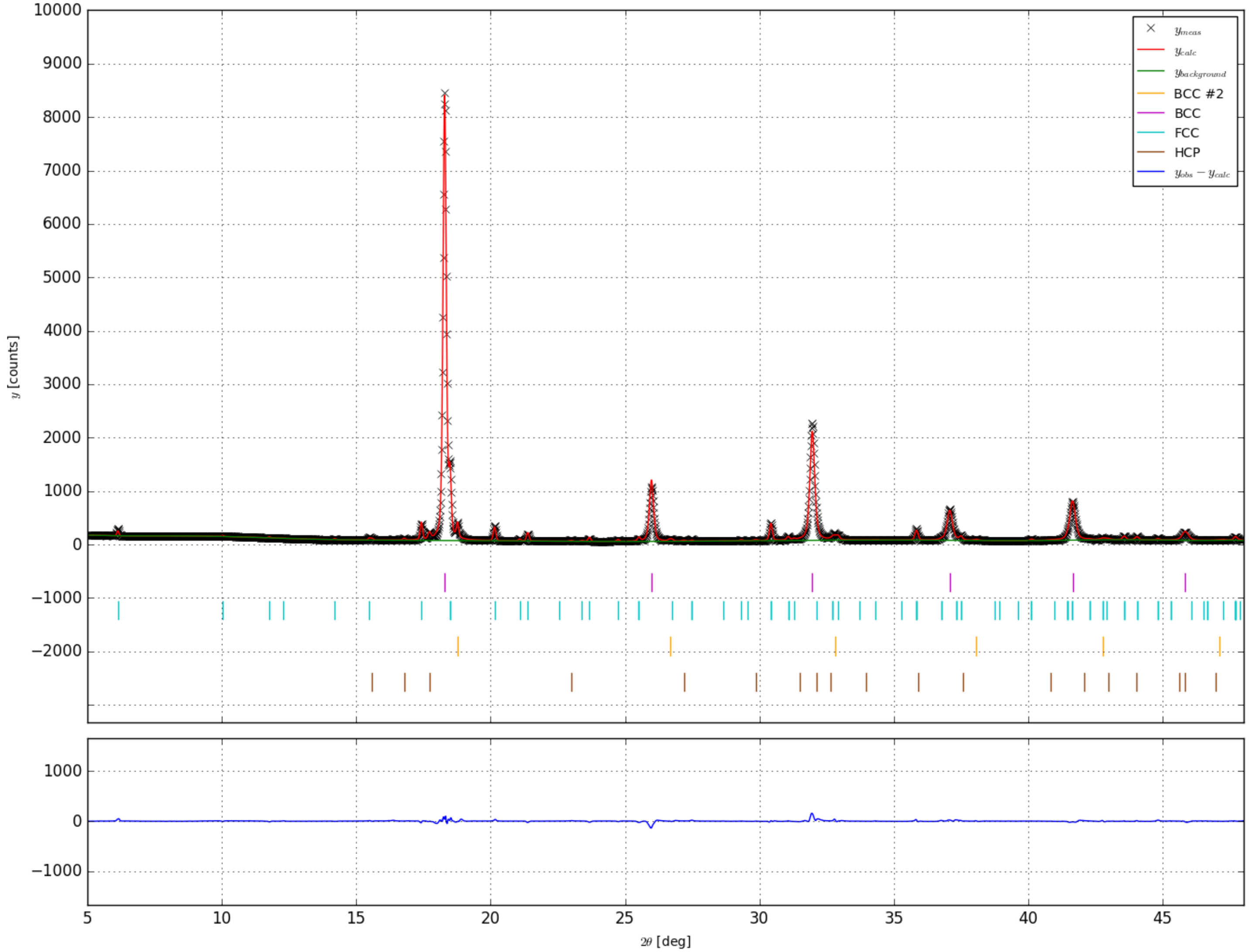

Figure D.18: The SR-PXD intensities y_{obs} for $(\mathrm{Ti}_{0.70}\mathrm{V}_{0.30})_{0.80}\mathrm{Fe}_{0.20}$ measured at ESRF shown alongside the background $y_{background}$ and the calculated intensities y_{calc} that was fitted to the pattern in GSAS. The fitted parameters of the model is shown for reference in table D.18.

Table D.18: The fitted parameters from GSAS for the $(Ti_{0.70}V_{0.30})_{0.80}Fe_{0.20}$ XRD pattern that was collected at ESRF. The unweighted profile factor was determined to $R_p = 0.0346$ while the weighted profile factors was $R_{wp} = 0.0550$. The goodness-of-fit was similarly determined to $\chi^2 = 584.1$. The scale factor was $S = 4.3498$. Zero-offset -0.48534. Shifted Chebyschev with 16 parameters for background.

Phase	BCC			BCC #2			HCP			FCC		
S_{rel} [∅]	1.0			0.023317			0.014968			0.003275		
Wt. frac [∅]	0.8300			0.0194			0.0150			0.1383		
	±0.0001			±0.0006			±0.0008			±0.0014		
a [Å]	3.10149			3.02331			2.9666			11.2738		
	±0.00006			±0.00018			±0.0005			±0.0003		
b [Å]	3.10149			3.02331			2.9666			11.2738		
	±0.00006			±0.00018			±0.0005			±0.0003		
c [Å]	3.10149			3.02331			4.7769			11.2738		
	±0.00006			±0.00018			±0.0014			±0.0003		
V [Å^3]	29.834			27.634			36.407			1432.871		
	±0.002			±0.005			±0.010			±0.010		
α [deg]	90			90			90			90		
β [deg]	90			90			90			90		
γ [deg]	90			90			120			90		
G_U [∅]	2.92022			15.15			303.949			0		
G_V [∅]	139.698			130.453			172.408			39.631		
G_W [∅]	-1.83691			-15.7043			-5.18342			10.0082		
L_X [∅]	0			0			0			0		
L_Y [∅]	34.8893			37.5069			0			11.5227		
U_{ISO}	-0.00835			-0.01795			-0.01293			-		
Atom	Ti	V	Fe	Ti	V	Fe	Ti	V	Fe	Ti	Fe	O
x	0	0	0	0	0	0	$\frac{1}{3}$	$\frac{1}{3}$	$\frac{1}{3}$	-	-	-
y	0	0	0	0	0	0	$\frac{2}{3}$	$\frac{2}{3}$	$\frac{2}{3}$	-	-	-
z	0	0	0	0	0	0	$\frac{1}{4}$	$\frac{1}{4}$	$\frac{1}{4}$	-	-	-

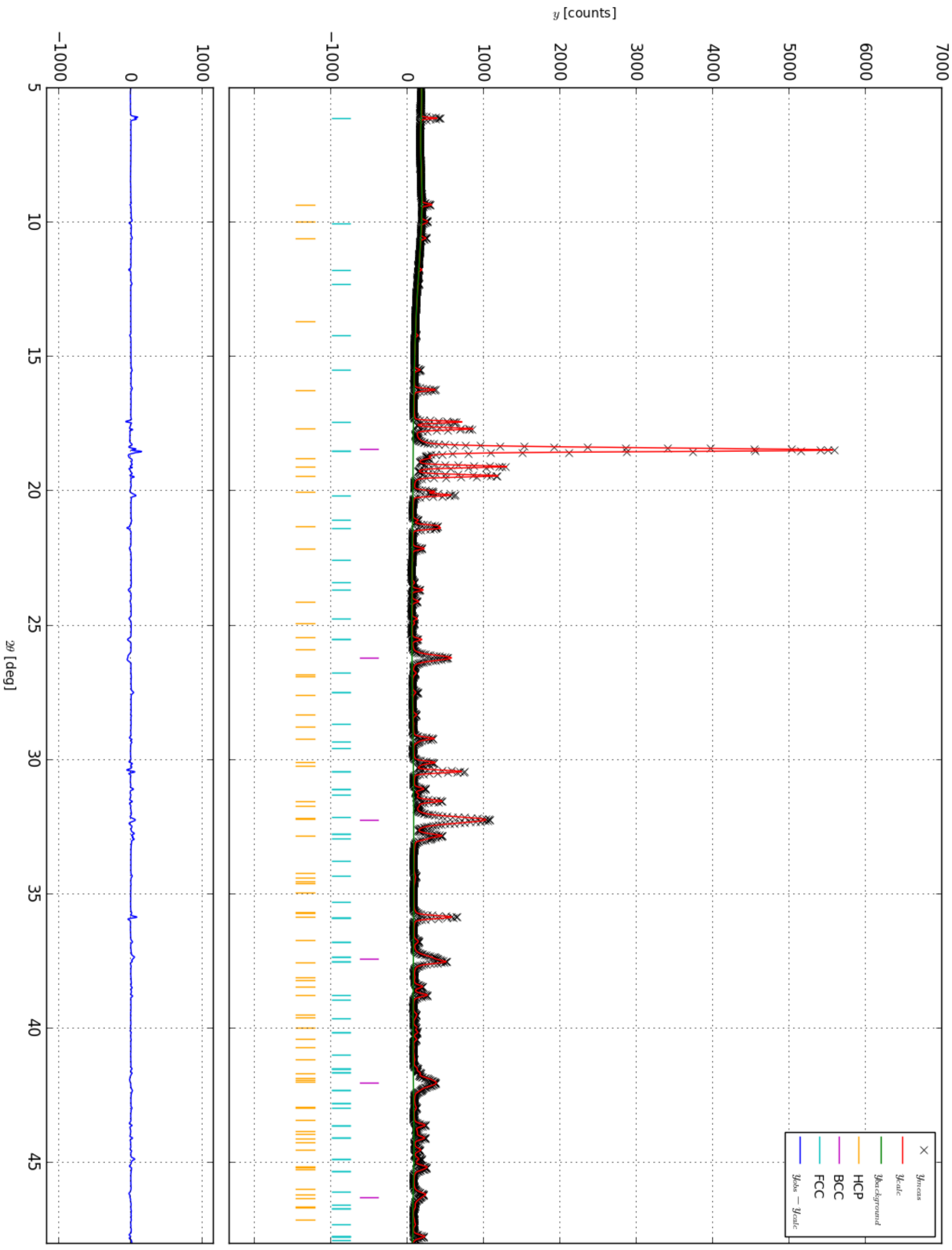

Figure D.19: The SR-PXD intensities y_{obs} for $(\mathrm{Ti}_{0.70}\mathrm{V}_{0.30})_{0.70}\mathrm{Fe}_{0.30}$ measured at ESRF shown alongside the background $y_{background}$ and the calculated intensities y_{calc} that was fitted to the pattern in GSAS. The fitted parameters of the model is shown for reference in table D.19.

Table D.19: The fitted parameters from GSAS for the $(Ti_{0.70}V_{0.30})_{0.70}Fe_{0.30}$ XRD pattern that was collected at ESRF. The unweighted profile factor was determined to $R_p = 0.0374$ while the weighted profile factors was $R_{wp} = 0.0593$. The goodness-of-fit was similarly determined to $\chi^2 = 714.9$. The scale factor was determined to $S = 2.4591$. Zero offset 0.40105. Shifted Chebyschev with 20 parameters for background.

Phase	BCC			C14 Laves						FCC			
S_{rel} [$\emptyset$]	1.0			0.087406						0.0091645			
Wt. frac. [$\emptyset$]	0.50122			0.2684						0.230			
	±0.0001			±0.0019						±0.002			
a [Å]	3.07307			4.93242						11.2618			
	±0.00008			±0.00012						±0.0002			
b [Å]	3.07307			4.93242						11.2618			
	±0.00008			±0.00012						±0.0002			
c [Å]	3.07307			8.0163						11.2618			
	±0.00008			±0.0003						±0.0002			
α [deg]	90			90						90			
β [deg]	90			90						90			
γ [deg]	90			120						90			
V [Å^3]	29.021			168.898						1428.33			
	±0.002			±0.009						±0.09			
G_U [$\emptyset$]	148.482			22.4738						0			
G_V [$\emptyset$]	314.418			3.44948						64.6940			
G_W [$\emptyset$]	-23.3922			11.396300						2.93002			
L_X [$\emptyset$]	0			0						0			
L_Y [$\emptyset$]	39.7255			20.7719						8.35146			
U_{ISO}	-0.00664			-0.01160						-0.01587			
Atom	Ti	V	Fe	Ti	V	Fe	V	Fe	V	Ti	Fe	Ti	O
x	0	0	0	$\frac{1}{3}$	$\frac{1}{3}$	0	0	$\frac{83}{100}$	$\frac{83}{100}$	$\frac{47}{50}$	$\frac{293}{1000}$	$\frac{1}{2}$	0
y	0	0	0	$\frac{2}{3}$	$\frac{2}{3}$	0	0	$\frac{33}{50}$	$\frac{33}{50}$	$\frac{1}{8}$	$\frac{293}{1000}$	$\frac{1}{2}$	0
z	0	0	0	$\frac{63}{1000}$	$\frac{63}{1000}$	0	0	$\frac{1}{4}$	$\frac{1}{4}$	$\frac{1}{8}$	$\frac{293}{1000}$	$\frac{1}{2}$	0

D.6 SR-PXD patterns of hydrides

Table D.20: The fitted parameters from GSAS for the $(Ti_{0.70}V_{0.30})_{0.80}Fe_{0.20}$ that was measured . The unweighted profile factor was determined to $R_p = 0.0495$ while the weighted profile factor was $R_{wp} = 0.0646$. The goodness-of-fit was similarly determined to $\chi^2 = 1074$. The scale factor was set to S=367.12. Zero-offset -0.0068484°. User defined background with 16 parameters background. Absorption: 4.02983.

Phase	BCC				BCT				FCC			
S_{rel} [$\emptyset$]	1.0				0.27260				0.0027202			
wt.% [$\emptyset$]	0.725				0.186				0.0895			
	±0.001				±0.002				±0.0013			
a [Å]	3.1889				2.950				11.3549			
	±0.0006				±0.002				±0.0008			
b [Å]	3.1889				2.950				11.3549			
	±0.0006				±0.002				±0.0008			
c [Å]	3.1889				4.521				11.3549			
	±0.0006				±0.006				±0.0008			
α [deg]	90				90				90			
β [deg]	90				90				90			
γ [deg]	90				90				90			
V [Å^3]	32.428				39.350				1464.014			
	±0.018				±0.064				±0.315			
G_U [$\emptyset$]	7726.38				18250.3				25.7278			
G_V [$\emptyset$]	12533.7				-9155.73				251.858			
G_W [$\emptyset$]	1790.28				30.77				-1.63452			
L_X [$\emptyset$]	0				0				0			
L_Y [$\emptyset$]	48.7505				0				13.6293			
U_{ISO}	0.05237				0.02170				0.01727			
Atom	Ti	V	Fe	H	Ti	V	Fe	H	Ti	Fe	Ti	O
x	0	0	0	0	0	0	0	0	$\frac{47}{50}$	$\frac{293}{1000}$	$\frac{1}{2}$	0
y	0	0	0	$\frac{1}{2}$	0	0	0	$\frac{1}{2}$	$\frac{1}{8}$	$\frac{293}{1000}$	$\frac{1}{2}$	0
z	0	0	0	$\frac{1}{4}$	0	0	0	$\frac{1}{4}$	$\frac{1}{8}$	$\frac{293}{1000}$	$\frac{1}{2}$	0

Table D.21: The fitted parameters from GSAS for the $(Ti_{0.70}V_{0.30})_{0.70}Fe_{0.30}H_x$ XRD pattern that was collected at ESRF. The unweighted profile factor was determined to $R_p = 0.0647$ while the weighted profile factors was $R_{wp} = 0.0878$. The goodness-of-fit was similarly determined to $\chi^2 = 1394$. The scale factor was determined to $S = 174.15$. Zero offset -0.0099358°. User defined background with 16 parameters.

Phase	BCC				C14 Laves						FCC			
S_{rel} [∅]	1.0				0.085037						0.0089332			
Wt. frac. [∅]	0.536				0.250						0.215			
	±0.001				±0.0013						±0.0012			
a [Å]	3.2145				4.9962						11.3094			
	±0.0002				±0.0002						±0.0002			
b [Å]	3.2145				4.9962						11.3094			
	±0.0002				±0.0002						±0.0002			
c [Å]	3.2145				8.1543						11.3094			
	±0.0002				±0.0007						±0.0002			
α [deg]	90				90						90			
β [deg]	90				90						90			
γ [deg]	90				120						90			
V [Å^3]	33.215				176.276						1446.501			
	±0.007				±0.018						±0.091			
G_U [∅]	0				1606.07						0			
G_V [∅]	1927.49				-512.376						54.66			
G_W [∅]	-259.003				75.4492						13.7638			
L_X [∅]	0				0						0			
L_Y [∅]	145.757				26.2251						13.5599			
U_{ISO}	0.02956				0.00347						0.00463			
Atom	Ti	V	Fe	H	Ti	V	Fe	V	Fe	V	Ti	Fe	Ti	O
x	0	0	0	0	$\frac{1}{3}$	$\frac{1}{3}$	0	0	$\frac{83}{100}$	$\frac{83}{100}$	$\frac{47}{50}$	$\frac{293}{1000}$	$\frac{1}{2}$	0
y	0	0	0	$\frac{1}{2}$	$\frac{2}{3}$	$\frac{2}{3}$	0	0	$\frac{33}{50}$	$\frac{33}{50}$	$\frac{1}{8}$	$\frac{293}{1000}$	$\frac{1}{2}$	0
z	0	0	0	$\frac{1}{4}$	$\frac{63}{1000}$	$\frac{63}{1000}$	0	0	$\frac{1}{4}$	$\frac{1}{4}$	$\frac{1}{8}$	$\frac{293}{1000}$	$\frac{1}{2}$	0

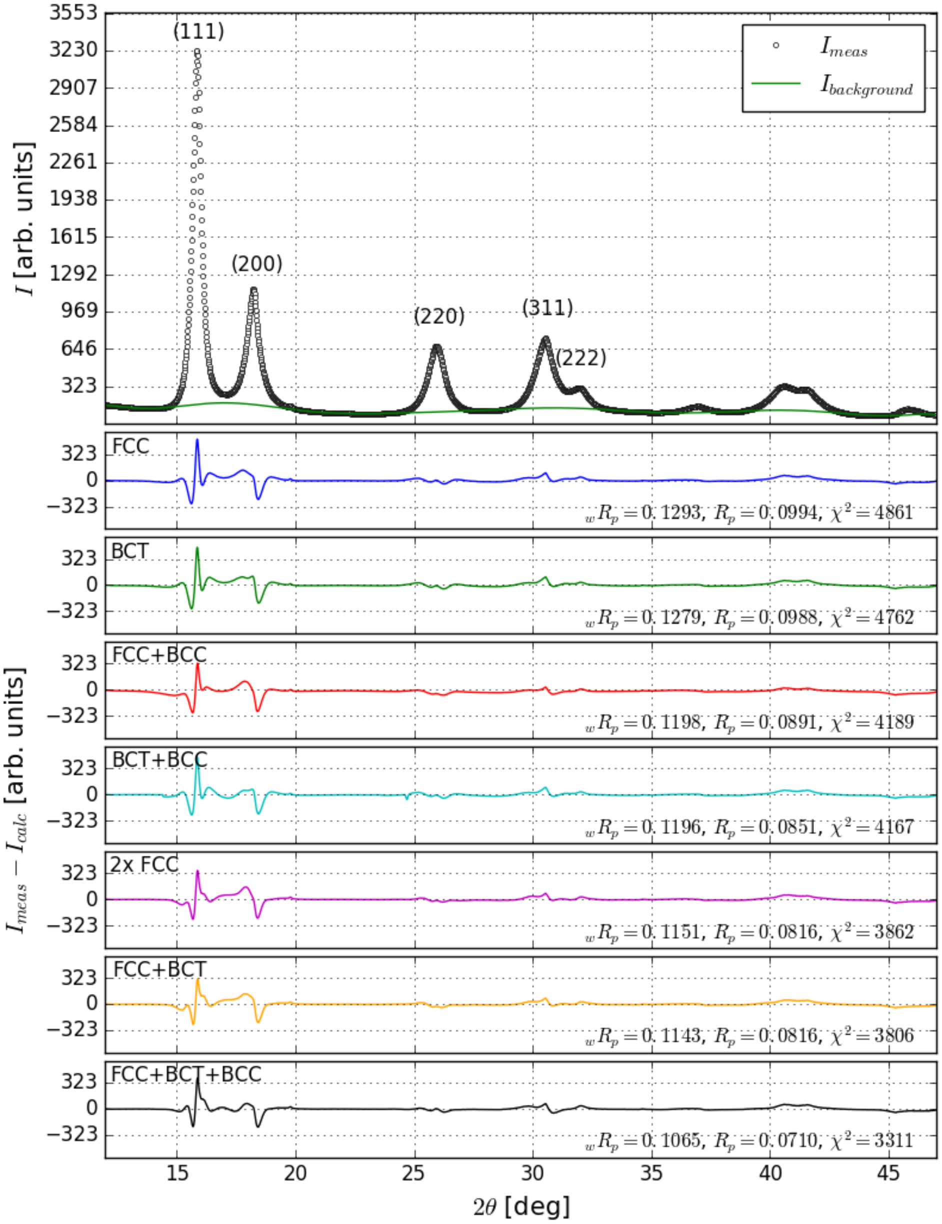

Figure D.20: The measured SR-PXD pattern of the hydride $(Ti_{0.70}V_{0.30})_{0.97}Fe_{0.03}H_x$ that was synthesised following the procedure outlined in table 4.2 shown alongside the background $I_{background}$ and the intensity deviation $I_{meas} - I_{calc}$ between the measured scattering intensity I_{meas} and the calculated intensity I_{calc} determined through Rietveld refinement for several different solution candidates. The statistical parameters R_p, ${}_wR_p$ and χ^2 of the refinements are also indicated.

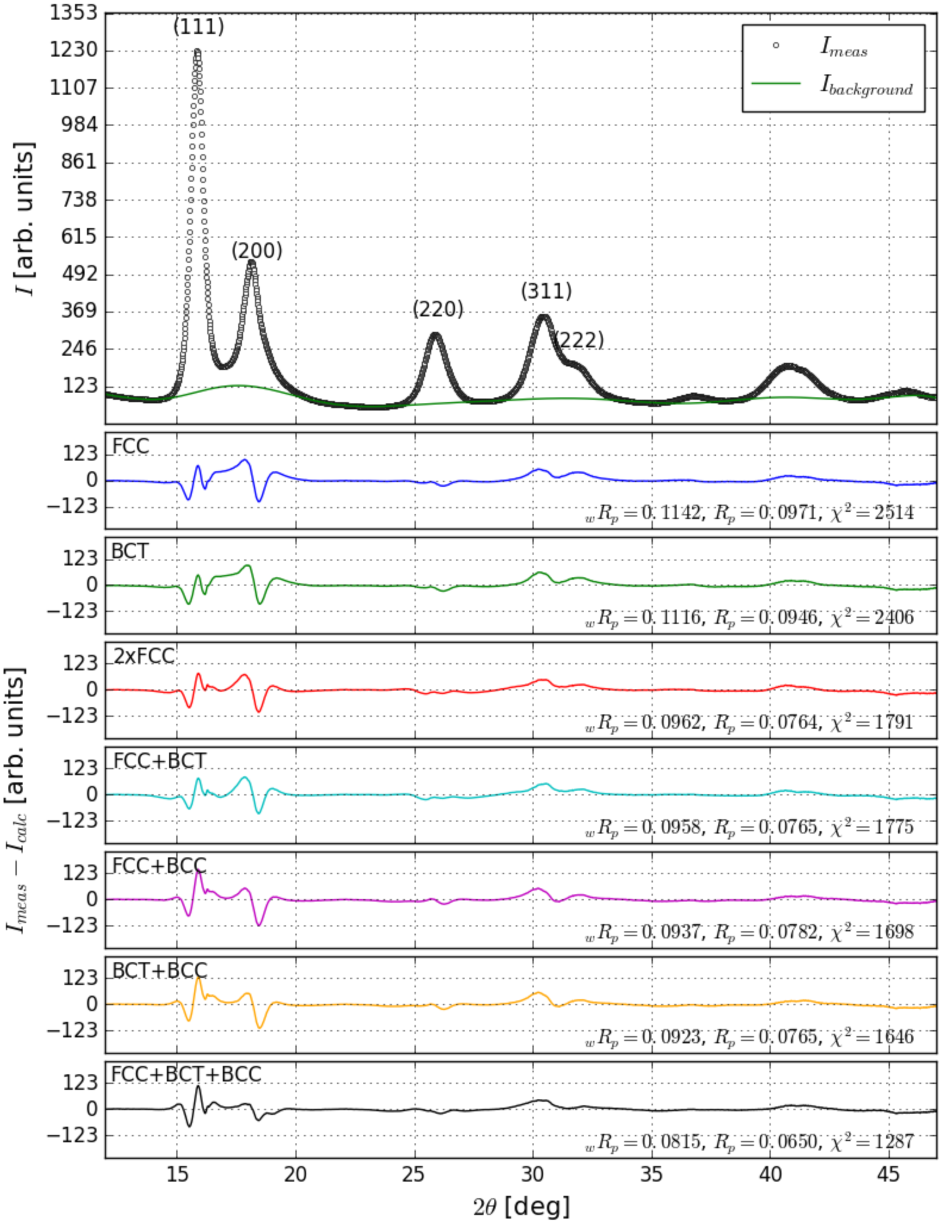

Figure D.21: The measured SR-PXD pattern of the hydride $(Ti_{0.70}V_{0.30})_{0.94}Fe_{0.06}H_x$ that was synthesised following the procedure outlined in table 4.2 shown alongside the background $I_{background}$ and the intensity deviation $I_{meas} - I_{calc}$ between the measured scattering intensity I_{meas} and the calculated intensity I_{calc} determined through Rietveld refinement for several different solution candidates. The statistical parameters R_p, $_wR_p$ and χ^2 of the refinements are also indicated.

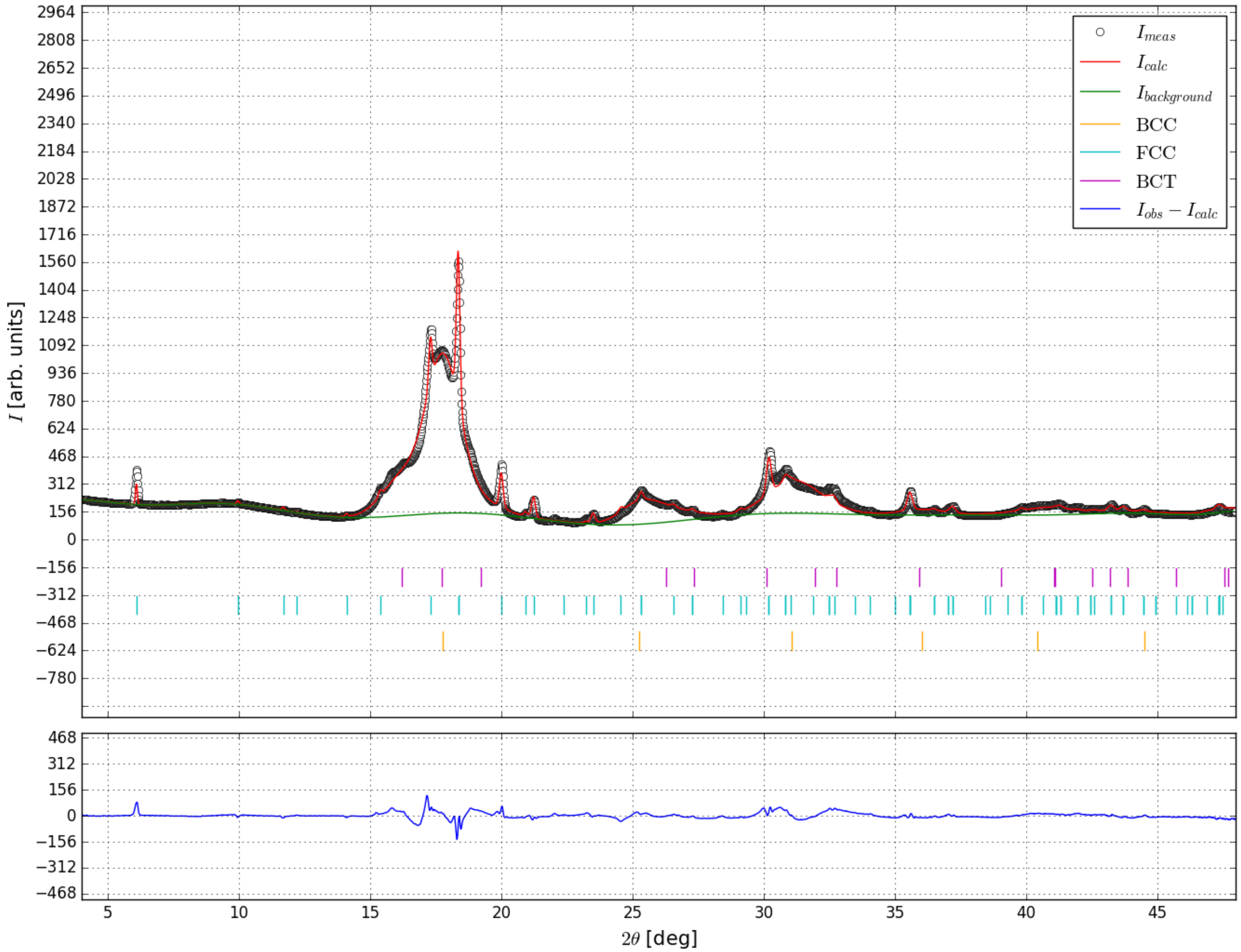

Figure D.22: The SR-PXD intensities I_{obs} for $(\mathrm{Ti}_{0.70}\mathrm{V}_{0.30})_{0.80}\mathrm{Fe}_{0.20}$ that was measured during the absorption experiment shown in figure 4.16 alongside the background $I_{background}$ and the calculated intensities I_{calc} that was fitted to the pattern in GSAS. The fitted parameters of the model is given in table D.20.

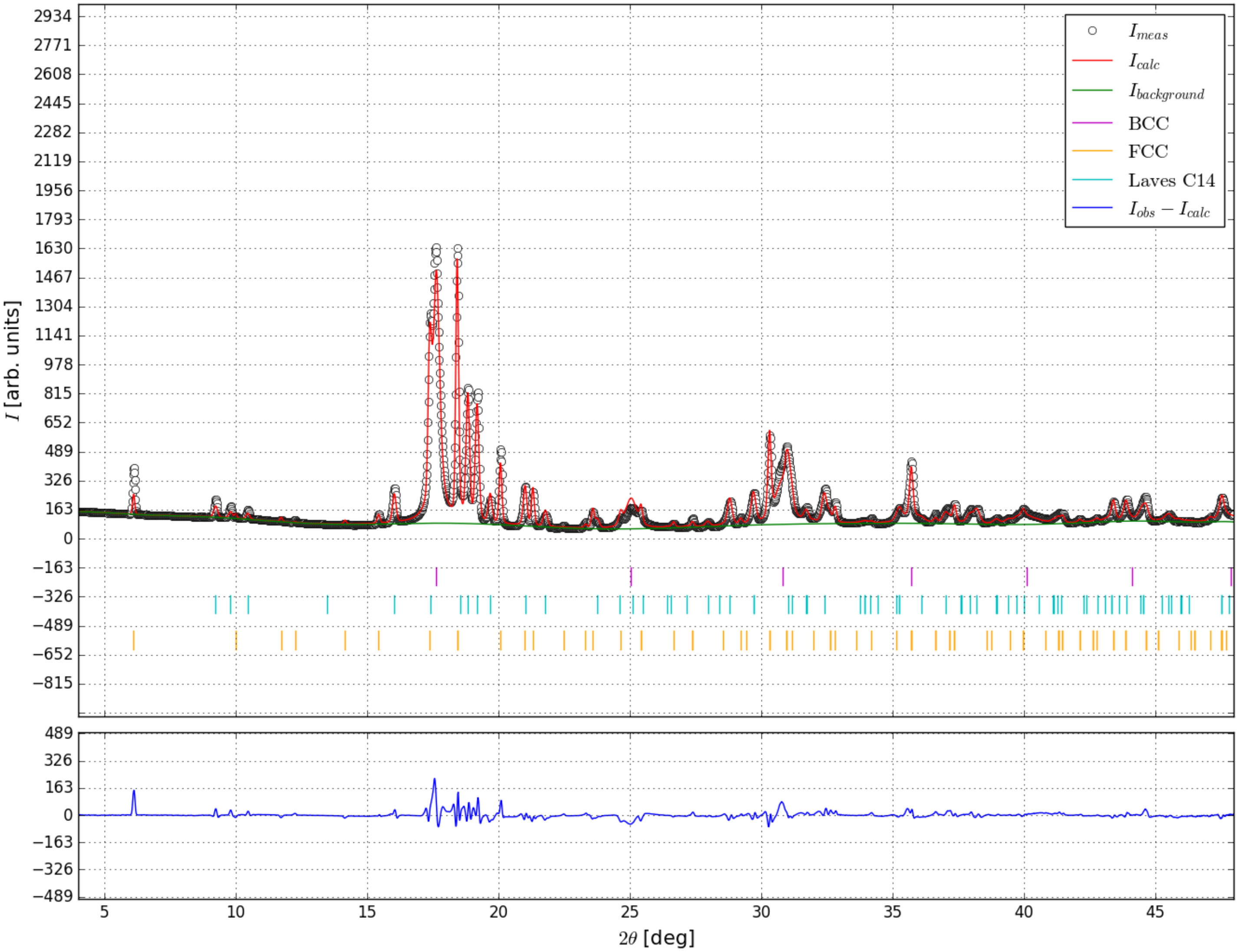

Figure D.23: The SR-PXD intensities y_{obs} for $(\mathrm{Ti}_{0.70}\mathrm{V}_{0.30})_{0.70}\mathrm{Fe}_{0.30}\mathrm{H}_{\mathrm{x}}$ measured at ESRF shown alongside the background $y_{background}$ and the calculated intensities y_{calc} that was fitted to the pattern in GSAS. The fitted parameters of the model is shown for reference in table D.21.

Appendix E

Kissinger analyses

This appendix hold the Kissinger analyses that has been performed on the collected TG/DSC data. The analyses are conducted as described in subsection 3.2.4 and the results are discussed in subsection 4.5.2.

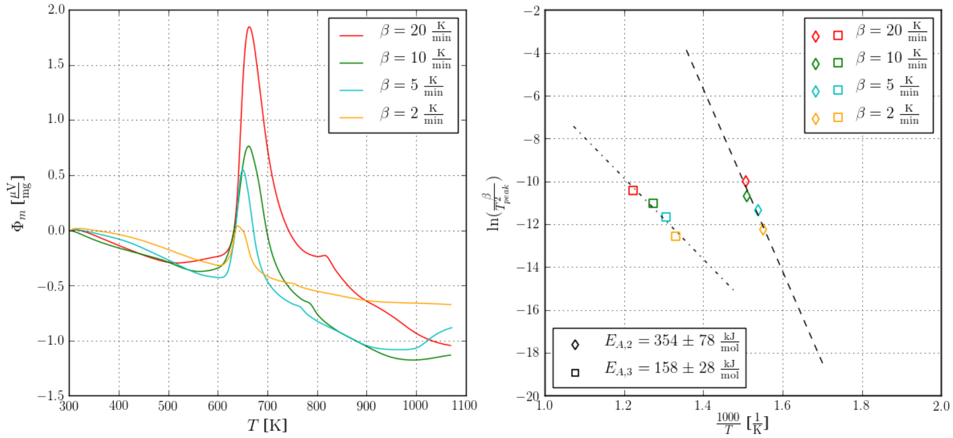

Figure E.1: Kissinger analysis performed on the DSC measurements of $Ti_{0.70}V_{0.30}H_x$ at different heating rates β. The left figure show the measured heat flow signals Φ_m while the right figure show the corresponding Kissinger plot. The *apparent* activation energies $E_{A,2}$ and $E_{A,3}$ were determined following the procedure outlined in subsection 3.2.4. It should be noted that the peaks are endothermic reactions.

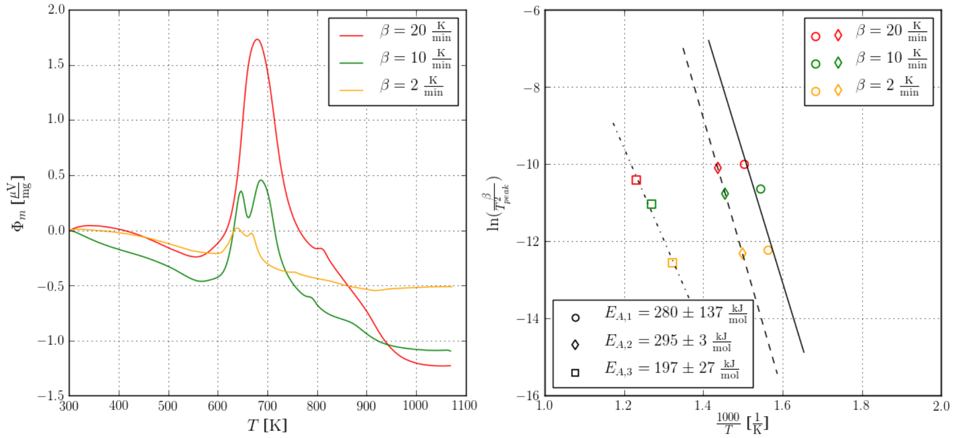

Figure E.2: Kissinger analysis performed on the DSC measurements of $(Ti_{0.70}V_{0.30})_{0.97}Fe_{0.03}H_x$ at different heating rates β. The left figure show the measured heat flow signals Φ_m while the right figure show the corresponding Kissinger plot. The *apparent* activation energies $E_{A,1}$, $E_{A,2}$ and $E_{A,3}$ were determined following the procedure outlined in subsection 3.2.4. It should be noted that the peaks are endothermic reactions.

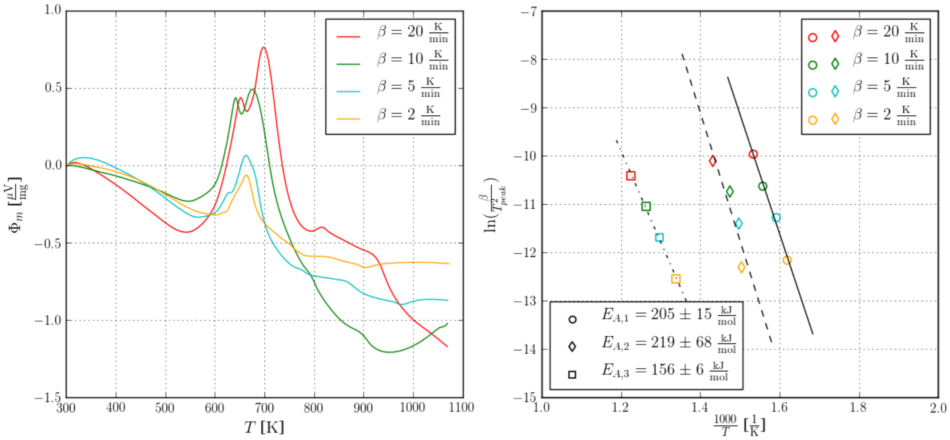

Figure E.3: Kissinger analysis performed on the DSC measurements of $(Ti_{0.70}V_{0.30})_{0.94}Fe_{0.06}H_x$ at different heating rates β. The left figure show the measured heat flow signals Φ_m while the right figure show the corresponding Kissinger plot. The *apparent* activation energies $E_{A,1}$, $E_{A,2}$ and $E_{A,3}$ were determined following the procedure outlined in subsection 3.2.4. It should be noted that the peaks are endothermic reactions.

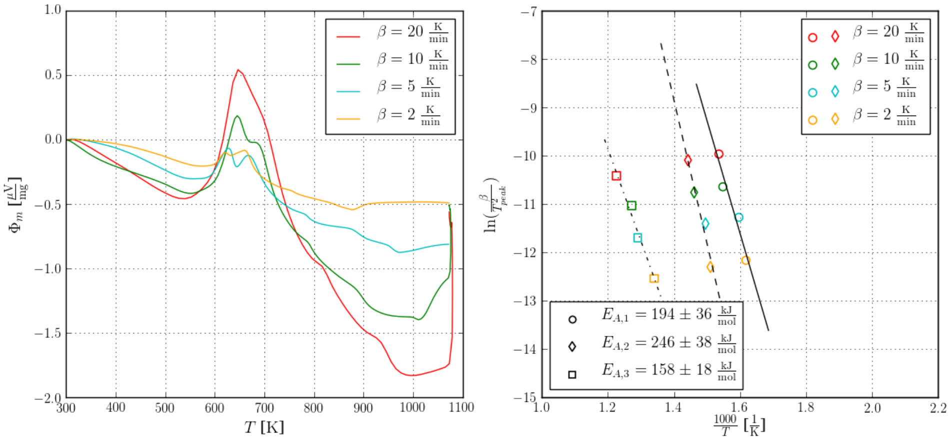

Figure E.4: Kissinger analysis performed on the DSC measurements of $(Ti_{0.70}V_{0.30})_{0.90}Fe_{0.10}H_x$ at different heating rates β. The left figure show the measured heat flow signals Φ_m while the right figure show the corresponding Kissinger plot. The *apparent* activation energies $E_{A,1}$, $E_{A,2}$ and $E_{A,3}$ were determined following the procedure outlined in subsection 3.2.4. It should be noted that the peaks are endothermic reactions.

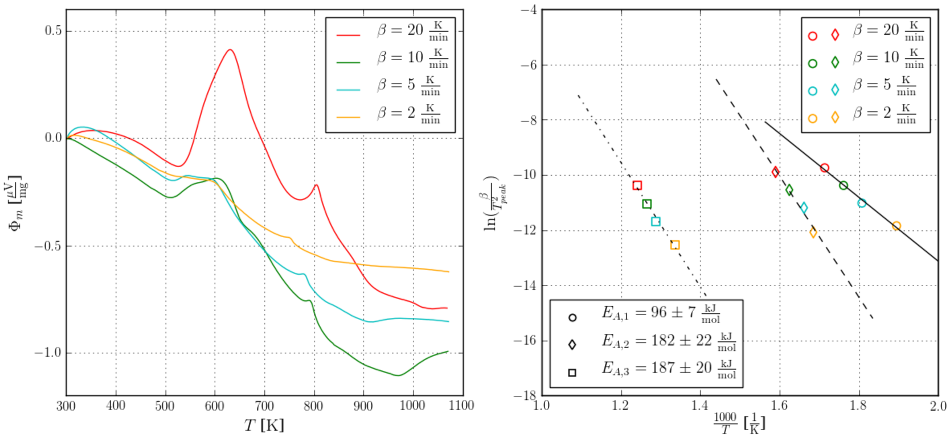

Figure E.5: Kissinger analysis performed on the DSC measurements of $(Ti_{0.70}V_{0.30})_{0.80}Fe_{0.20}H_x$ at different heating rates β. The left figure show the measured heat flow signals Φ_m while the right figure show the corresponding Kissinger plot. The *apparent* activation energies $E_{A,1}$, $E_{A,2}$ and $E_{A,3}$ were determined following the procedure outlined in subsection 3.2.4. It should be noted that the peaks are endothermic reactions.

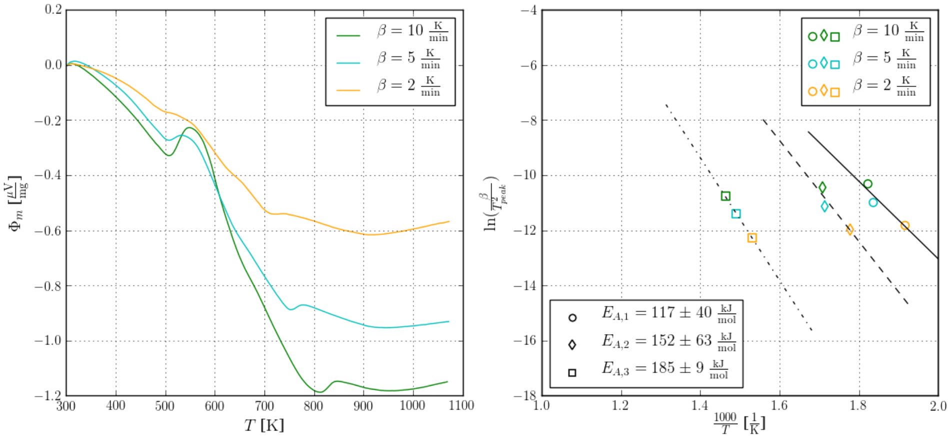

Figure E.6: Kissinger analysis performed on the DSC measurements of $(Ti_{0.70}V_{0.30})_{0.70}Fe_{0.30}H_x$ at different heating rates β. The left figure show the measured heat flow signals Φ_m while the right figure show the corresponding Kissinger plot. The *apparent* activation energies $E_{A,1}$, $E_{A,2}$ and $E_{A,3}$ were determined following the procedure outlined in subsection 3.2.4. It should be noted that the peaks are endothermic reactions.

Bibliography

[1] The International Energy Agency. Key World Energy Statistics. Technical report, The International Energy Agency, 2015.

[2] The International Panel on Climate Change. Climate change 2014 Synthesis Report Summary for Policymakers. Technical report, The International Panel on Climate Change, 2014.

[3] European Commission. 2030 energy strategy. `http://ec.europa.eu/energy/en/topics/energy-strategy/2030-energy-strategy`, February 2016. Accessed: 2016-02-17.

[4] The European Wind Energy Association. Wind in Power - 2015 European Statistics. Technical report, EWEA, 2016.

[5] Solar Power Europe. Global Market Outlook for Solar Power / 2015-2019. Technical report, SPE, 2015.

[6] Yaşar Demirel. *Energy and Energy Types*, pages 27–70. Springer London, London, 2012.

[7] National Institute of Standards and Technology. IEA Energy Technology Essentials - Hydrogen Production & Distribution. `https://www.iea.org/publications/freepublications/publication/essentials5.pdf`, 2007. Accessed: 2016-12-11.

[8] Michael Grätzel. Photoelectrochemical cells. *Nature*, 414(6861):338–344, 2001.

[9] Oscar Khaselev and John A Turner. A monolithic photovoltaic-photoelectrochemical device for hydrogen production via water splitting. *Science*, 280(5362):425–427, 1998.

[10] NEL. Nel A Atmospheric Electrolyser. `http://nelhydrogen.com/product/a-range/`, 2016. Accessed: 2016-12-11.

[11] Brian CH Steele and Angelika Heinzel. Materials for fuel-cell technologies. *Nature*, 414(6861):345–352, 2001.

[12] National Institute of Standards and Technology. Thermophysical properties of fluid systems. `http://webbook.nist.gov/chemistry/fluid/`, 2016. Accessed: 2016-12-11.

[13] Rahul Krishna, ALC Ferreira, Ananth Rajkumar, Elby Titus, JMG Sousa, João Campos Gil, Jose Gracio, Maryam Salimian, Olena Okhay, and Sivakumar Rajendran. *Hydrogen storage for energy application.* INTECH Open Access Publisher, 2012.

[14] Toyota Motor Corp. Technology file - High-pressure hydrogen tanks. `http://www.toyota-global.com/innovation/environmental_technology/technology_file/`, 2016. Accessed: 2016-12-12.

[15] Air Liquide Norway AS. Gas Encyclopedia - Hydrogen. `http://encyclopedia.airliquide.com/Encyclopedia.asp?GasID=36#LiquidGasConversion`, 2016. Accessed: 2016-02-12.

[16] National Aeronautics and Space Administration (NASA). Liquid Hydrogen–the Fuel of Choice for Space Exploration. `http://www.nasa.gov/topics/technology/hydrogen/hydrogen_fuel_of_choice.html`, July 2010. Accessed: 2016-02-17.

[17] Michael Hirscher, Barbara Panella, and Barbara Schmitz. Metal-organic frameworks for hydrogen storage. *Microporous and mesoporous materials*, 129(3):335–339, 2010.

[18] Louis Schlapbach and Andreas Züttel. Hydrogen-storage materials for mobile applications. *Nature*, 414(6861):353–358, 2001.

[19] C Li, P Peng, DW Zhou, and L Wan. Research progress in libh 4 for hydrogen storage: a review. *international journal of hydrogen energy*, 36(22):14512–14526, 2011.

[20] London Metal Exchange. Current metals prices and metals news. `https://www.metalprices.com/`, 2016. Accessed: 2016-12-05.

[21] Westbrook Resources Ltd. Ferrovanadium. `http://www.wbrl.co.uk/ferro-vanadium.html`, 2016. Accessed: 2016-12-12.

[22] AJ Maeland, GG Libowitz, and JP Lynch. Hydride formation rates of titanium-based bcc solid solution alloys. *Journal of the Less Common Metals*, 104(2):361–364, 1984.

[23] A Martínez and DS dos Santos. Hydrogen absorption/desorption properties in the ticrv based alloys. *Materials Research*, 15(5):809–812, 2012.

[24] Thomas Bibienne, Jean-Louis Bobet, and Jacques Huot. Crystal structure and hydrogen storage properties of body centered cubic 52ti–12v–36cr alloy doped with zr 7 ni 10. *Journal of Alloys and Compounds*, 607:251–257, 2014.

[25] Crystal lattice and Unit Cell. `https://amazingsolids.files.wordpress.com/2013/06/9.jpg`, June 2013. Accessed: 2016-10-19.

[26] G. L. Squires. *Thermal Neutron Scattering*. Cambridge University Press, 2012.

[27] John Lilley. *Nuclear Physics - Principles and Applications*. John Wiley & Sons, Ltd., 2001.

[28] PC Hemmer. *Kvantemekanikk*. Fagbokforlaget, 5 edition, 2015.

[29] Matthew D. Schwartz. *Quantum Field Theory and the Standard Model*. Cambridge University Press, 1 edition, 2014.

[30] Simon Jacques Paul Barnes and Martin Vickers. Powder Diffraction. `http://pd.chem.ucl.ac.uk/pdnn/diff2/kinemat2.htm`, 1997-2006. Accessed: 2016-03-07.

[31] Karl J Gross, KR Carrington, S Barcelo, A Karkamkar, J Purewal, S Ma, HC Zhou, P Dantzer, K Ott, T Burrell, et al. Recommended best practices for the characterization of storage properties of hydrogen storage materials. *National Renewable Energy Laboratory*, 2012.

[32] Daniel V. Schroeder. *An Introduction to Thermal Physics*. Pearson Education Limited, 1 edition, 2014.

[33] M Ron. The normalized pressure dependence method for the evaluation of kinetic rates of metal hydride formation/decomposition. *Journal of alloys and compounds*, 283(1):178–191, 1999.

[34] Sergey Vyazovkin, Alan K Burnham, José M Criado, Luis A Pérez-Maqueda, Crisan Popescu, and Nicolas Sbirrazzuoli. Ictac kinetics committee recommendations for performing kinetic computations on thermal analysis data. *Thermochimica Acta*, 520(1):1–19, 2011.

[35] David R. Lide. *CRC Handbook of Chemistry and Physics*. CRC Press, 1995.

[36] RM Wood. The lattice constants of high purity alpha titanium. *Proceedings of the Physical Society*, 80(3):783, 1962.

[37] J Spreadborough and JW Christian. The measurement of the lattice expansions and debye temperatures of titanium and silver by x-ray methods. *Proceedings of the Physical Society*, 74(5):609, 1959.

[38] Pavel Karen, *, Emmanuelle Suard, and Franois Fauth. Crystal structure of stoichiometric yba2fe3o8. *Inorganic Chemistry*, 44(23):8170–8172, 2005. PMID: 16270946.

[39] EA Owen and EL Yates. Xli. precision measurements of crystal parameters. *The London, Edinburgh, and Dublin Philosophical Magazine and Journal of Science*, 15(98):472–488, 1933.

[40] ME Straumanis and DC Kim. Lattice constants, thermal expansion coefficients, densities, and perfection of structure of pure iron and of iron loaded with hydrogen. *Z METALLKUNDE*, 60(4):272–277, 1969.

[41] R. Kohlhaas, P. Duenner, and N. Schmitz-Pranghe. Ueber die temperaturabhaengigkeit der gitterparameter von eisen, kobalt und nickel im bereich hoher temperaturen. *Zeitschrift fuer Angewandte Physik 23*, 23:245–249, 1967.

[42] Arnulf J Maeland, Thomas RP Gibb Jr, and David P Schumacher. A novel hydride of vanadium1. *Journal of the American Chemical Society*, 83(17):3728–3729, 1961.

[43] Arnulf J Maeland. Investigation of the vanadiumhydrogen system by x-ray diffraction techniques1, 2. *The Journal of Physical Chemistry*, 68(8):2197–2200, 1964.

[44] James J Reilly and Richard H Wiswall. Higher hydrides of vanadium and niobium. *Inorganic Chemistry*, 9(7):1678–1682, 1970.

[45] SS Sidhu, LeRoy Heaton, and DD Zauberis. Neutron diffraction studies of hafnium–hydrogen and titanium–hydrogen systems. *Acta Crystallographica*, 9(7):607–614, 1956.

[46] Joanne L Murray. The ti- v (titanium-vanadium) system. *Bulletin of Alloy Phase Diagrams*, 2(1):48–55, 1981.

[47] Tatsuya Hagi, Yoshitsugu Sato, Masabumi Yasuda, and Kazuhide Tanaka. Structure and phase diagram of ti–v–h system at room temperature. *Transactions of the Japan institute of metals*, 28(3):198–204, 1987.

[48] S Suwarno, JK Solberg, JP Maehlen, RV Denys, B Krogh, E Ochoa-Fernández, BT Børresen, E Rytter, IE Gabis, and VA Yartys. Non-isothermal kinetics and in situ sr xrd studies of hydrogen desorption from dihydrides of binary ti–v alloys. *international journal of hydrogen energy*, 38(34):14704–14714, 2013.

[49] Akio Kagawa. Absorption of hydrogen by vanadium-titanium alloys. , 25(45):233–239, 1995.

[50] JF Lynch, AJ Maeland, and GG Libowitz. Lattice parameter variation and thermodynamics of dihydride formation in the vanadium-rich vtife/h2 system. *Zeitschrift für Physikalische Chemie*, 145(1_2):51–59, 1985.

[51] S Ono, K Nomura, and Y Ikeda. The reaction of hydrogen with alloys of vanadium and titanium. *Journal of the Less Common Metals*, 72(2):159–165, 1980.

[52] Junko Matsuda and Etsuo Akiba. Lattice defects in v–ti bcc alloys before and after hydrogenation. *Journal of Alloys and Compounds*, 581:369–372, 2013.

[53] AJ Maeland, GG Libowitz, JF Lynch, and G Rak. Hydride formation rates of bcc group v metals. *Journal of the Less Common Metals*, 104(1):133–139, 1984.

[54] S Suwarno, JK Solberg, JP Maehlen, B Krogh, and VA Yartys. Influence of cr on the hydrogen storage properties of ti-rich ti–v–cr alloys. *international journal of hydrogen energy*, 37(9):7624–7628, 2012.

[55] Lydia Pickering, Jing Li, Daniel Reed, Alexander I Bevan, and David Book. Ti–v–mn based metal hydrides for hydrogen storage. *Journal of Alloys and Compounds*, 580:S233–S237, 2013.

[56] E Akiba and H Iba. Hydrogen absorption by laves phase related bcc solid solution. *Intermetallics*, 6(6):461–470, 1998.

[57] A Kagawa, E Ono, T Kusakabe, and Y Sakamoto. Absorption of hydrogen by vanadium-rich v ti-based alloys. *Journal of the Less Common Metals*, 172:64–70, 1991.

[58] Sartorius Mechatronics. Operating Instructions: Sartorius Extend Series Sartorius Gem and Gold Extend - Electronic Analytical and Precision Balances and Precious Metal Scales. Technical report, Sartorius AG, 2005.

[59] Mettler Toledo. Operating instructions: Mettler Toledo AG balances. Technical report, Mettler Toledo GmbH, 2004.

[60] Mettler Toledo. Operating instructions: Mettler Toledo AM/PM Balances. Technical report, Mettler Toledo GmbH, 1999.

[61] The European Synchrotron. What is a synchrotron? `http://www.esrf.eu/about/synchrotron-science/synchrotron`, 2016. Accessed: 2016-11-21.

[62] Vadim Dyadkin, Philip Pattison, Vladimir Dmitriev, and Dmitry Chernyshov. A new multipurpose diffractometer pilatus@ snbl. *Journal of synchrotron radiation*, 23(3), 2016.

[63] NPTEL National Programme on Technology Enhanced Learning. Scanning electron microscope. `http://nptel.ac.in/courses/102103044/18`, 2016. Accessed: 2016-12-11.

[64] Magnus Moe Nygård. Calibration of the Sieverts apparatus at IFE. Technical report, The Institute for Energy Technology, 2016.

[65] Sartorius Mechatronics. Sartorius Extend. ED124S. Technical report, Sartorius AG, 2009.

[66] Arthur Reichmuth. Estimating Weighing Uncertainty From Balance Data Sheet Specifications. Technical report, Mettler Toledo, 2000.

[67] Allen C Larson and Robert B Von Dreele. Gsas. *General Structure Analysis System. LANSCE, MS-H805, Los Alamos, New Mexico*, 1994.

[68] HM Rietveld. Line profiles of neutron powder-diffraction peaks for structure refinement. *Acta Crystallographica*, 22(1):151–152, 1967.

[69] HaM Rietveld. A profile refinement method for nuclear and magnetic structures. *Journal of applied Crystallography*, 2(2):65–71, 1969.

[70] G Caglioti, A t Paoletti, and FP Ricci. Choice of collimators for a crystal spectrometer for neutron diffraction. *Nuclear Instruments*, 3(4):223–228, 1958.

[71] Eric W Lemmon, Marcia L Huber, and Jacob W Leachman. Revised standardized equation for hydrogen gas densities for fuel consumption applications. *Journal of research of the National Institute of Standards and Technology*, 113(6):341, 2008.

[72] Marcin Wojdyr. Fityk: a general-purpose peak fitting program. *Journal of Applied Crystallography*, 43(5):1126–1128, 2010.

[73] John R. Taylor. *Error analysis*. University Science Books, 1997.

[74] Bertram Eugene Warren. *X-ray Diffraction*. Addison-Wesley, 1969.

[75] Maxime Dupraz, Guillaume Beutier, David Rodney, Dan Mordehai, and Marc Verdier. Signature of dislocations and stacking faults of face-centred cubic nanocrystals in coherent x-ray diffraction patterns: a numerical study. *Journal of applied crystallography*, 48(3):621–644, 2015.

[76] JD Makinson, JS Lee, SH Magner, RJ De Angelis, WN Weins, and AS Hieronymus. X-ray diffraction signatures of defects in nanocrystalline materials. *Advances in X-ray Analysis*, 42:407–411, 2000.

[77] Levente Balogh, Gábor Ribárik, and Tamás Ungár. Stacking faults and twin boundaries in fcc crystals determined by x-ray diffraction profile analysis. *Journal of applied physics*, 100(2):023512, 2006.

Norges miljø- og biovitenskapelig universitet
Noregs miljø- og biovitskapelege universitet
Norwegian University of Life Sciences

Postboks 5003
NO-1432 Ås
Norway